Hydrodynamic modeling and experimental characterization of the plasmonic and thermoelectric terahertz response of field-effect transistors with integrated broadband antennas in AlGaN/GaN HEMTs and CVD-grown graphene

Dissertation
zur Erlangung des Doktorgrades
der Naturwissenschaften

vorgelegt beim Fachbereich Physik
der Johann Wolfgang Goethe-Universität
in Frankfurt am Main

von
Maris Bauer
aus Frankfurt am Main

Frankfurt am Main 2017
(D30)

vom Fachbereich Physik der

Johann Wolfgang Goethe-Universität als Dissertation angenommen.

Dekan: Prof. Dr. Michael Lang

Gutachter:
Prof. Dr. Hartmut Roskos
Prof. Dr.-Ing. Viktor Krozer
Prof. Dr.-Ing. Peter Haring Bolívar

Datum der Disputation: 18.10.2018

"Wer versteht schon alles, was er so schreibt?"

Für meinen Vater

Abstract

Terahertz (THz) physics are an emerging field of research dealing with electromagnetic radiation in the far-infrared to microwave region. The development of innovative technologies for the generation and detection of THz radiation has only in the recent past led to a tremendous rise of both fundamental research as well as investigation of possible fields of application for THz radiation. The most prominent reason has long been the scarce accessibility of the THz region of the electromagnetic spectrum - commonly loosely located between 0.1 and 30 THz - to broad research, and it was mostly limited to astronomy and high energy physics facilities. Over the recent years, numerous novel concepts on both the source and detector side have been proposed and successfully implemented to overcome this so-called THz gap. New technology has become available and paved the way for wide-spread experimental laboratory work and accompanying theoretical investigations. First application studies have emerged and in some cases even commercial development of the field of THz physics is on the rise.

Despite these enormous progresses, a continuing demand for more efficient THz detectors still impels current technological research. Relatively low source powers are often a major limiting factor and the request for new detection concepts, their understanding and implementation, as well as the optimization on a device basis has been and still remains in place. One of these concepts is the use of field-effect transistors (FETs) high above their conventional cut-off frequencies as electronic THz detectors. The concept has been proposed in a number of theoretical publications by M. Dyakonov and M. Shur in the early 1990's, who pioneered to show that under certain boundary conditions, non-linear collective excitations of the charge carrier system of a two-dimensional electron gas (2DEG) by incident THz radiation can exhibit rectifying behaviour - a detection principle, which has become known as plasma wave or plasmonic mixing. Up until this day, the concept has been successfully implemented in many device realizations - most advanced in established silicon CMOS technology - and stands on the edge of becoming commercially available on a large scale.

The main direction of the work presented in this thesis was the modeling and experimental characterization of antenna-coupled FETs for THz detection - termed *TeraFET*s in this and the author's previous works - which have been implemented in different material systems. The materials presented in this thesis are AlGaN/GaN HEMTs and graphene FETs. In a number of scientific collaborations, TeraFETs were designed based on a hydrodynamic transport model, fabricated in the respective materials, and characterized mainly in the lower THz frequency region from 0.2 to 1.2 THz.

The theoretical description of the plasma wave mixing mechanism in TeraFETs, as initiated by Dyakonov and Shur, was based on a fluid-dynamic transport model for charge carriers in the transistor channel. The THz radiation induces propagating charge density oscillations (plasma waves) in the 2DEG, which via non-linear self-mixing cause rectification of the incident THz signals. Over the course of this work, it became evident in the on-going detector characterization experiments that this original theoretical model of the detection process widely applied in the respective literature does not suffice to describe some of the experimental findings in TeraFET detection signals. Thorough measurements showed signal contributions, which are identified in this work to be of thermoelectric origin arising from an inherent asymmetric local heating of charge carriers in the devices. Depending on the material, these contributions constituted a mere side effect to plasmonic detection (AlGaN/GaN) or even reached a comparable magnitude (graphene FETs). To include these effects in the detector model, the original reduced fluid-dynamic description was extended to a hydrodynamic transport model. The model yields at the current stage a reasonable qualitative agreement to the measured THz detection signals.

This thesis presents the formulation of a hydrodynamic charge carrier transport model and its specific implementation in a circuit simulation tool. A second modeling aspect is that the transport equations cover only the intrinsic plasmonic detection process in the active gated part of the TeraFET's transistor channel. In order to model and simulate the behavior of real devices, extrinsic detector parts such as ungated channel regions, parasitic resistances and capacitances, integrated antenna impedance, and others must be considered. The implemented detector model allows to simulate THz detection in real devices with the above influences included.

Besides presentation of the detector model, experimental THz characterization of the fabricated TeraFETs is presented in this work. Careful device design yielded record detection performance for detectors in both investigated materials. The respective results are shown and the experimental observations of the thermoelectric effect in TeraFETs are compared to modeling results. It is the goal of this work to provide a framework for further theoretical and experimental studies of the plasmonic and thermoelectric effect in TeraFETs, which could eventually lead to a new type of THz detectors particularly exploiting the thermoelectric effect to enhance the sensitivity of today's plasmonic TeraFETs.

Zusammenfassung

Die Terahertz-(THz)-Physik ist ein aufstrebendes Forschungsfeld, welches sich mit elektromagnetischer Strahlung vom Ferninfraroten bis hin zum Mikrowellenbereich befasst. Die Entwicklung innovativer Technologien zur Erzeugung und Detektion von THz-Strahlung führte erst in der jüngeren Vergangenheit zu einem gewaltigen Anstieg von Grundlagenforschung sowie der Auslotung möglicher Anwendungsfelder von THz Strahlung. Der vorrangige Grund war die lange Zeit spärliche Zugänglichkeit des THz-Bereichs - üblicherweise lose veranlagt zwischen 0.1 und 30 THz - für breite Forschung und der Bereich war hauptsächlich beschränkt auf Einrichtungen der Astronomie und der Hochenergiephysik. In den letzten Jahren wurden zahlreiche neuartige Konzepte sowohl auf der Seite von Quellen als auch Detektoren vorgeschlagen und erfolgreich implementiert um diese sogenannte THz-Lücke zu überwinden. Neue Technologie wurde zugänglich und ebnete den Weg für breit angelegte experimentelle Laborarbeit und begleitende theoretische Untersuchungen. Erste Anwendungsstudien wurden durchgeführt und in einigen Fällen ist sogar die kommerzielle Erschließung der THz Physik auf dem Vormarsch.

Trotz dieses enormen Fortschritts wird die technologische Forschung noch immer durch die anhaltende Nachfrage nach effizienteren THz-Detektoren angetrieben. Oftmals sind geringe Ausgangsleistungen von Quellen der vorherrschende, limitierende Faktor und die Anforderung an neue Detektionskonzepte, deren Verständnis und Implementierung, sowie die Optimierung auf Bauelementebene, waren und sind stets vorhanden. Eines dieser Konzepte ist die Anwendung von Feldeffekttransistoren (FETs) weit über deren herkömmlichen Cut-off Frequenzen als elektronische THz-Detektoren. Das Konzept wurde in einer Reihe von theoretischen Beiträgen von M. Dyakonov und M. Shur anfang der neunziger Jahre vorgeschlagen, als diese erstmals zeigten, dass unter bestimmten Randbedingungen nichtlineare kollektive Anregungen des Ladungsträgersystems eines zweidimensionalen Elektronengases (2DEG) durch die einfallende THz-Strahlung gleichrichtend wirken können - das Detektionsprinzip wurde bekannt unter dem Namen Plasmawellen- oder plasmonisches Mischen. Bis heute wurde das Konzept in zahlreichen konkreten Bauelementen erfolgreich implementiert - am weitesten fortgeschritten in etablierter Silizium CMOS Technologie - und steht vor dem Sprung in großem Maße kommerziell verfügbar zu werden.

Die zentrale Ausrichtung der in dieser Arbeit vorgestellten Aktivitäten war die Modellierung und experimentelle Charakterisierung antennengekopplter FETs für die THz Detektion - in dieser und in früheren Arbeiten des Autors *TeraFETs* genannt - welche in verschiedenen Materialsystemen implementiert wurden. Die in dieser Arbeit vorgestellten Materialien sin AlGaN/GaN HEMTs und Graphene-FETs. In einer Reihe wissenschaftlicher Zusammenarbeiten wurden TeraFETs auf der Basis eines

hydrodynamischen Transportmodells entworfen, in den entsprechenden Materialien hergestellt und hauptsächlich im unteren THz-Frequenzbereich von 0.2 bis 1.2 THz charakterisiert.

Die theoretische Beschreibung des Mechanismus des Mischens mit Plasmawellen in TeraFETs, wie ursprünglich von Dyakonov und Shur angestoßen, basierte auf einem fluiddynamischen Transportmodel für Ladungsträger innerhalb des Transistorkanals. Die THz Strahlung induziert laufende Ladungsträgerdichtewellen (Plasmawellen) innerhalb des 2DEGs, welche durch nicht-lineares Selbstmischen eine nichtlineare Gleichrichtung des einfallenden THz-Signals bewirken. Im Verlaufe dieser Arbeit zeigte sich im Zuge der Detektionsexperimente, dass dieses weitverbreitete, ursprüngliche, theoretische Model des Detektionsmechanismus nicht aussreicht einige der experimentellen Befunde in den Detektionssignalen zu erklären. In gründlichen Messungen zeigten sich Signalbeiträge, welche in dieser Arbeit als thermoelektrisch identifiziert werden, ausgelöst durch ein inhärentes, lokales Anheizen von Ladungsträgern in dem Bauelement. In Abhängigkeit des Materials stellten diese Beiträge lediglich einen Nebeneffekt zur plasmonischen Detektion dar (AlGaN/GaN) oder erreichten eine vergleichbare Stärke (Graphen FETs). Um diese Effekte in das Detektormodell zu intergrieren wurde das ursprüngliche fluiddynamische Modell zu einem hydrodynamischen Transportmodell erweitert. Das Modell erzielt in der jetzigen Form eine vernünftige, qualitative Übereinstimmung mit den gemessenen THz-Detektionssignalen.

In dieser Arbeit wird die Formulierung eines hydrodynamischen Ladungsträgertransportmodells und dessen spezifische Implementierung in einem Schaltkreis-Simulationstool dargestellt. Ein weiterer Aspekt der Modellierung ist, dass die Transportgleichungen nur den intrinsischen plasmonischen Detektionsprozess in dem aktiven gegateten Teil des Transistorkanals abdecken. Um realistische Bauelemente zu modelieren und zu simulieren müssen extrinsische Elemente, wie z.B. ungegatete Teile des Kanals, parasitäre Widerstände und Kapazitäten, die Impedanz der integrierten Antenne u.a. berücksichtigt werden. Das implementierte Detektormodell erlaubt eine Simulation der THz-Detektion in realen Bauelementen unter Berücksichtigung dieser Einflüsse.

Neben der Darstellung des Detektormodells wird die experimentelle Charakterisierung der hergestellten TeraFETs präsentiert. Ein gründliches Design der Detektoren führte zu Rekordwerten der Detektionsleistung in beiden dargestellten Materialien. Die entsprechenden Messergebnisse werden gezeigt und die experimentelle Beobachtung des thermoelektrischen Effekts in TeraFETs verglichen mit Ergebnissen der Modellierung. Es ist das Ziel dieser Arbeit ein Rahmenwerk für weitere theoretische und experimentelle Studien des plasmonischen Mischens und des thermoelektrischen Effekts in TeraFETs zu liefern, welche letztendlich zu einer neuen Art von THz Detektoren führen könnten, welche im Speziellen den thermoelektrischen Effekt ausnutzen um die Sensitivität heutiger plasmonischer TeraFETs zu erhöhen.

Contents

Abstract **iv**

Zusammenfassung **vi**

1 Introduction **1**

1.1 Detection mechanisms in TeraFETs 1
1.2 Hydrodynamic transport model and circuit implementation 3
1.3 Fabrication and experimental characterization of TeraFETs 5
1.4 Structure of this thesis 5

2 Plasma wave mixing model **7**

2.1 Foundation of the concept of plasma wave mixing 7
2.2 One-dimensional treatment of charge carrier transport 9
2.3 Intrinsic channel impedance and THz response 11
2.3.1 Channel impedance and carrier velocity 11
2.3.2 THz response 14
2.4 Detection regimes 16
2.4.1 Classical resistive mixing 17
2.4.2 Distributed resistive mixing 18
2.4.3 Plasmonic mixing 19
2.5 Asymmetric boundary conditions 21
2.6 Transmission line equivalent circuit description 23

3 Hydrodynamic model **26**

3.1 The Boltzmann transport equation 26
3.1.1 The distribution function 28
3.1.2 The method of moments 29
3.1.3 Balance equations 30
3.2 Transport models 31
3.2.1 Charge continuity equation 31
3.2.2 The drift-diffusion model 32
3.2.3 Hot carriers 33
3.2.4 The hydrodynamic transport model 35
3.3 Comparison of the Dyakonov-Shur and the hydrodynamic transport model 36

4 Circuit model implementation **39**

4.1 The intrinsic distributed channel 40
4.1.1 Gate capacitance 40
4.1.2 Drift current 42
4.1.3 Convection current 42
4.1.4 Diffusion current 43
4.1.5 Carrier temperature 43
4.2 Verification of the model implementation 44
4.2.1 Charge control model 44
4.2.2 Parameter extraction from DC resistance 46
4.2.3 Comparison of analytic calculations and numerical circuit simulations 47

5 Simulations **52**

5.1 Detection sensitivity in the resonant plasmonic mixing regime 52
5.2 Circuit simulations with ungated access regions 56
5.2.1 Power distribution 56
5.2.2 Influence on plasmonic mixing efficiency 60

6 TeraFET characterization **62**

6.1 TeraFET figures of merit 63
6.1.1 NEP and thermal noise of zero-biased TeraFETs 64
6.1.2 Optical versus electrical responsivity and NEP 66
6.2 Experimental setups 68
6.2.1 DC measurements 68
6.2.2 THz sources 69
6.2.3 Detector module 73
6.3 AlGaN/GaN TeraFETs 74
6.3.1 First detector generation, variation of gate width 75
6.3.2 Improved detectors, bow-tie and log-spiral design 78
6.3.3 Highly sensitive broadband AlGaN/GaN TeraFETs 84
6.4 Graphene TeraFETs 88
6.4.1 Differences for graphene TeraFET model 89
6.4.2 Graphene DC parameter extraction and modifications of transport model 90
6.4.3 THz detection with graphene TeraFETs 95

7 Thermoelectrics in TeraFETs **98**

7.1 Origin of thermoelectric signals in TeraFETs 100
7.1.1 Derivation of Seebeck coefficient from transport equations . . 100
7.1.2 Direction of thermoelectric signals 102
7.2 Experimental evidences 104
7.2.1 AlGaN/GaN TeraFETs 105
7.2.2 Graphene TeraFETs 109

8 Summary and Outlook **115**

Appendices

A Plasma wave mixing model **121**

A.1 Plasma velocity and plasma wavevector . . . 121
A.2 THz response . . . 123
A.2.1 Quasi-static TeraFET response . . . 124

B Derivation of transport models from the Boltzmann transport equation **126**

B.1 Method of moments . . . 126
B.1.1 Charge carrier density . . . 127
B.1.2 Carrier momentum density and drift velocity . . . 128
B.1.3 Energy density . . . 128
B.2 Transport models . . . 129
B.2.1 Charge continuity equation . . . 129
B.2.2 Drift-diffusion model . . . 130
B.2.3 Hydrodynamic transport model . . . 131
B.3 Diffusion constant and Seebeck coefficient . . . 133

C Graphene TeraFET model **135**

C.1 Cyclotron mass . . . 135

List of own publications **136**

Bibliography **138**

Zusammenfassung **149**

Chapter 1

Introduction

Field-effect transistors (FETs) can act as rectifying detectors for incident electromagnetic radiation, in particular at high frequencies. Depending on the regime of radiation frequencies and specific device design, several physical detection mechanism can take place in the FET's channel. In this thesis, two main mechanisms of rectification in FET-based THz detectors are discussed - non-linear plasma wave mixing as well as diffusive charge carrier transport, mainly, the hot electron thermoelectric effect. A respective detector model based on a macroscopic hydrodynamic model to describe the intrinsic charge carrier transport in the FET channel was developed and is presented. The model, which extends the commonly employed fluid-dynamic description of plasma wave mixing, was translated into a transmission line equivalent circuit picture and implemented in a numerical circuit simulation software environment allowing to perform numerical modeling and simulation of the photoresponse of FET-based THz detectors. Based on these considerations, a number of broadband THz detectors were implemented in different materials, namely AlGaN/GaN HEMTs and single-layer CVD-grown graphene FETs. Results of the respective THz characterization experiments are presented and compared to simulations with the numerical model. In both materials, record sensitivities for FET-based THz detectors were obtained .

1.1 Detection mechanisms in TeraFETs

Dyakonov and Shur in the early to mid-1990s discussed theoretically that the two-dimensional electron gas (2DEG) in a semiconductor FET under appropriate radiation coupling boundary conditions can act as a cavity for charge density (plasma) waves induced by an incoming high frequency (HF) signal [18]. The detection mechanism then relies on non-linear self-mixing properties of the plasma waves launched into the transistor channel from either the drain or source terminals. It can be described with the help of a fluid-dynamic picture of charge carrier transport. This led to the term *plasma wave detectors* or *plasmonic detectors* in the literature. From a more general point of view, depending on the regime of applied frequencies, the principle manifests as classical *resistive mixing* (for low frequencies) or *distributed resistive mixing* (for high frequencies). For further increasing frequencies towards the THz spectral region,

significant enhancement of distributed resistive mixing by self-mixing properties of induced plasma waves can occur [19]. It was in particular shown that for typical semiconductor structures and materials, the frequencies for an efficient enhancement of detection can lie in the THz region. The plasma wave detection mechanism and the description by fluid dynamics has been extensively discussed over the past two decades and numerous detector implementations have been demonstrated to yield sensitivities well comparable to competing detector technologies for the THz region [20]–[22].

Another fundamental physical mechanism which can take place in TeraFETs is the generation of diffusion currents. These currents can be the result of spatial gradients in carrier density or carrier temperature in the channel induced by the incoming radiation. In the latter case, the induced diffusion signal is thermoelectric[23]. Employing FETs as efficient plasmonic detectors for electromagnetic radiation requires the implementation of asymmetric boundary conditions to ensures that the plasma waves are launched into the channel from one terminal only and no counteracting signal is created by a reverse wave from the other terminal [2], [24], [25]. As a direct consequence of this built-in asymmetry, a non-uniform distribution of incident radiation power builds up over the transistor channel. When the carrier ensemble is sufficiently decoupled from the crystal lattice, charge carriers can be locally heated on one end of the channel, while remaining at equilibrium temperature at the other end. This situation is achieved, e.g., when energy is distributed within the carrier electronic system by multiple carrier-carrier collisions rather than by phonon scattering to the lattice. A spatial gradient in carrier temperature is the result and hot carriers will then tend to diffuse from the heated to the cold end of the channel and a significant hot-electron thermoelectric current can be observed [23], [26]–[29]. Such signals in TeraFETs have already been observed in a small number of experimental studies [5], [11], [12], [30]–[32] and were to some extent addressed in theoretical discussions [33], [34]. However, a detailed modeling of the effect in the scope of THz detection with TeraFETs is not yet available in the literature.

Following the same principle as discussed above, the local modulation of carrier density can lead to a signal contribution due to diffusion of carriers along the density gradient from channel regions of higher to lower density. We find, however, that this effect plays only a minor role in TeraFETs and it is not treated in further detail in this thesis. Note that in a thermodynamic picture, the product of carrier density and temperature can be associated with the hydrodynamic pressure via the relation $P = nk_BT_C$ well known from ideal gas theory. Common state-of-the-art fluid-dynamic TeraFET models found in the literature omit pressure terms and therefore do not consider diffusive current contributions to the TeraFET detection signals [18], [35], [36].

There are mainly two reasons why thermoelectric detection has so-far mostly been omitted in discussions on plasmonic detection models for TeraFETs in the literature. First, the additional contributions are small compared to the plasma wave rectification signals in TeraFET fabricated in most conventional semiconductor materials. The most efficient detectors have been fabricated in Si-CMOS [24], [37], which is foremost due to the advanced maturity of the technology[21]. No signal contributions which could be related to diffusion of charge carriers had become

evident in the multitude of THz detection experiments. However, during the course of investigation of TeraFETs in new material systems, in AlGaN/GaN HEMTs and particularly in graphene FETs, could the effect be observed in THz detection experiments to a significant level at room temperature.

A second aspect is that thermoelectric signals in conventional semiconductor TeraFETs appear most prominently at detector operation points (in terms of applied gate bias voltage) which are quite far away from operation points of best plasmonic detection sensitivity - usually close to the transistor's threshold voltage. At gate biases where the plasmonic signals are dominating, thermoelectric contributions to the signal can easily be masked by the plasma wave mixing signal. However, since the plasmonic detector response falls off to zero rapidly with increasing gate voltage above threshold,[1] the diffusive currents can appear as an isolated detection signal at high gate bias TeraFET operation.

The thermoelectric signals in the AlGaN/GaN TeraFETs investigated over the course of this work were about one order of magnitude lower than the plasma wave mixing signals. In the graphene TeraFETs, on the other hand, the situation is fundamentally different. A highly efficient decoupling of the heated carrier ensemble from the crystal lattice [27]–[29], [38] leads to pronounced thermoelectric signals on the same order as the maximum plasmonic response. Even an enhancement of the plasmonic detection is obtained. This promising observation motivates further investigation of the thermoelectric effect in TeraFETs and could in the future eventually lead to a new type of THz detector exploiting mainly the thermoelectric detection principle.

1.2 Hydrodynamic transport model and circuit implementation

The plasma wave detection mechanism in TeraFETs can be described by a set of hydrodynamic transport equations[18], [39], [40]. The formation of gated plasmons in the transistor channel is associated with a simultaneous modulation of charge carrier density and velocity. This collective excitation of charge carrier density waves is the basis for non-linear self-mixing and thereby rectification of HF radiation in an FET channel. The governing hyperbolic coupled differential equations can in principle be solved by, e.g., FDTD approaches. However, a "real" detector implemented in a physical device - as opposed to a theoretical intrinsic FET channel - in general contains a number of extrinsic device elements. Such elements may be, e.g., ungated (*access*) regions of the channel and other parasitic resistances, intentionally or inadvertently implemented parasitic capacitances, integrated radiation coupling antennas. The sum of all these external components determines the boundary conditions and efficiency of power transfer to the rectifying intrinsic detector element. While common detector models in the literature rely on precisely defined boundary conditions, for

[1] In the context of this thesis, in the case of negative threshold or Dirac voltages, the terms *high* and *increasing* gate bias voltage refer to "less negative" values. This is in particular important for the normally-open AlGaN/GaN HEMTs.

which analytic solutions to the governing model equations for the intrinsic detection mechanism exist, such solutions are in general not available in a real device situation.

The hydrodynamic model equations only describe the *intrinsic* processes in the detector's "active" gated channel region. Although the approximate behavior of real devices can in some cases be modeled remarkably well by analysis of the hydrodynamic equations alone, it is apparent that in order to design or model a real device, the HF influence of extrinsic components must be incorporated in a realistic device model. In particular, the power transfer from the integrated antennas to the active device regions must be considered. It was shown before that second order analysis of the transport equations can yield an analytical expression for the intrinsic TeraFET's photoresponse given as the product of a frequency independent quasi-static term and a frequency-dependent factor accounting for plasmonic enhancement and its form depending on the specific boundary conditions of radiation coupling [18], [41], [42]. It was then proposed that approximate modeling of the THz response of a real detector can be achieved by additional multiplication of several frequency-dependent factors considering power transfer to the active transistor region depending on the HF behavior of the complex impedances of intrinsic and extrinsic device components [42][43, ch. 3]. To achieve optimal transfer of incident radiation power to the rectifying transistor region, impedance matching of extrinsic and intrinsic device elements in due consideration of the above influences should be aimed for.

In this thesis we present a somewhat different approach, namely the implementation of the hydrodynamic transport equation in a circuit simulation environment. In this way, extrinsic device components can be included in a numerical HF device simulation, even when simple analytic expressions for the above HF factors or specific boundary conditions do not exist. It can be easily shown that the set of differential equations of the hydrodynamic transport model can be translated into a mathematically similar set of differential voltage and current equations known from transmission line theory of electrodynamics [44]. It was therefore suggested to model the transistor channel of a TeraFET as a distributed RCL transmission line [45]–[50]. The implementation in a circuit simulation environment then allows to include extrinsic detector components such as parasitic resistances and capacitances, ungated channel regions, integrated antenna structures, and a specific radiation coupling situation can be modeled to yield a realistic device simulation for real TeraFET detectors. In the course of this work, a transmission line equivalent circuit model was implemented in a commercial circuit simulation software.[2] The implementation of the hydrodynamic transport model - in particular including thermoelectric signal contributions - is presented in this thesis. Simulation results for intrinsic detection are cross-verified with an analytic device model and full device simulations are compared to THz detection measurements.

[2]Keysight Advanced Design System (ADS) [51]

1.3 Fabrication and experimental characterization of TeraFETs

In the course of the presented work, highly sensitive THz detectors employing FETs with integrated antennas - we term these devices *TeraFETs*[3] - were designed and fabricated in different materials, namely, AlGaN/GaN HEMTs and CVD-grown single-layer graphene FETs. The integrated planar antenna structures were laid out for broadband detection mainly operating in the region between 0.1 and 1.2 THz. Careful device design considering optimized power coupling, electrical stabilization of the detector environment, reduction of parasitic elements by improvements in device fabrication technology, as well as thorough experimental characterization led to record measured sensitivities for TeraFETs in the respective materials, in particular, with respect to broadband detection. The devices were fabricated in successful collaborations with Ferdinand-Braun-Institut, Leibniz-Institut für Höchstfrequenztechnik (FBH), Berlin, Germany (AlGaN/GaN HEMTs), and with Chalmers University of Technology, Göteborg, Sweden (graphene FETs).

Based on experimental observations emerging in the course of the THz characterization of the above TeraFETs, we will show in this thesis that the implementation of optimal boundary conditions for an efficient plasma wave-based non-linear rectification - i.e., asymmetric coupling of the incident radiation to the transistor terminals - in turn gives rise to significant thermoelectric signals due to local heating of charge carriers in the FET channel. With the help of the implemented hydrodynamic detector model including diffusion terms, the measurement results are discussed and reproduced qualitatively, which suggests that an extension of state-of-the-art TeraFET models commonly found in the literature is required to account for this additional detection mechanism in TeraFETs.

Some of the presented results from THz measurements have in parts been published prior to the writing of this thesis. The respective references are Refs. [2], [3], [9]–[11], [13], [15] for the AlGaN/GaN HEMTs and Refs. [5], [10], [12] for the graphene FETs.

1.4 Structure of this thesis

This thesis is structured as follows. Chapter 2 presents the basic theory and gives some discussion of the intrinsic plasma wave-based detection mechanism. The fluid-dynamic transport description as employed by Dyakonov and Shur [18] is presented and some important equations for fundamental quantities, such as channel impedance and plasmonic efficiency factor, are derived. The requirement and consequences of asymmetric boundary conditions are discussed and motivate the extension of the detector model by diffusive transport contributions. An transmission line equivalent circuit description of the model equations is introduced.

[3]We introduce the term *TeraFETs* to emphasize the distinction between the intrinsic detector element, i.e., an FET channel, and real physical detectors designed for THz detection and consisting of an antenna-integrated FET including extrinsic detector elements.

Chapter 3 presents the formulation of a comprehensive hydrodynamic transport model from basic transport theory. Model equations for charge carrier density, current density and energy density are obtained from the fundamental Boltzmann transport equation by application of the method of moments. A final comparison of the fluid-dynamic transport description from Ref. [18] with the derived hydrodynamic model equations confirms, that the latter extends the transport description by diffusive terms.

In Chapter 4, the implementation of the hydrodynamic transport model in a transmission line equivalent circuit picture in a commercial circuit simulation software [51] is presented and some details of the implementation are addressed. The software allows numerical simulation of DC device parameters and THz rectification. Simulation results are verified by comparison with results obtained from analytic expressions derived in Chapter 2. Both the numerical simulations with the circuit model as well as the analytic calculation results were based on realistic device parameters extracted from DC characteristics of fabricated devices. A fitting procedure for parameter extraction from DC measured drain-source resistances of the TeraFETs is presented considering the example of a GaN-based detector.

Chapter 5 presents simulation results obtained with the implemented device model, in particular, with respect to the intrinsic plasmonic enhancement factors and the inclusion of ungated channel regions in the detector's equivalent circuit. The concept of resonant plasmonic enhancement is investigated in some detail. Power distribution over the transistor elements is investigated and the influence of power loss to ungated channel regions on the efficiency of plasmonic rectification is discussed.

Experimental results of THz characterization experiments with the fabricated AlGaN/GaN and graphene TeraFETs are presented in Chapter 6. Important figures of merit for the evaluation of THz detectors are introduced and the employed experimental setup is outlined. Three generations of AlGaN/GaN TeraFETs are presented, which on the basis of extensive experimental and theoretical studies and constant design optimization eventually yielded highly sensitive broadband detectors in the frequency region of 0.2 to 1.2 THz. The detectors exhibited record performance for GaN-based TeraFETs and the respective measurement results are presented. The achieved results are currently being prepared for an invited publication [1]. CVD-grown Graphene TeraFETs were produced roughly based on the design of the AlGaN/GaN TeraFETs. The detectors also yielded record sensitivities for graphene TeraFETs at 590 GHz[5]. The measurements are presented and necessary modifications to the model implementation for graphene FETs are discussed.

Significant thermoelectric contributions to the THz detection signals were observed in both materials. These experimental findings are summarized in Chapter 7 together with some further discussion. Comparison of the measurement results with device simulations show that implemented model including thermoelectric contributions can account for the observed signals on a good qualitative level.

Chapter 2

Plasma wave mixing model

In this chapter we present the underlying theoretical model which is employed to describe the plasma wave-based rectification of THz radiation in FETs. The model is presented following the original formulation of Dyakonov and Shur [18]. We investigate the detection regimes of classical resistive, distributed resistive and plasmonic mixing [19] and discuss the requirement and consequences of asymmetric boundary conditions of radiation coupling. Finally, we present a transmission line equivalent formulation of the detector model, whose implementation in a circuit model-based device simulation is shown in Chapter 4.

2.1 Foundation of the concept of plasma wave mixing

It has long been known from basic electronic transport theory in semiconductors that charge carrier dynamics can be well described by fluid dynamic transport models. In an early work, Bloch introduced the concept of using a hydrodynamic treatment based on the Thomas-Fermi atomic model to describe the dynamics of charge carriers as an electron (Fermi-)gas in a semiconductor [52]. He showed that the governing equations of motion are indeed Euler's equation of motion together with the fundamental continuity equation. This system of equations had originally been developed in the 18th century for the description of fluid dynamical processes of gases and liquids [53]. Hydrodynamic and related macroscopic transport models today find wide application in the analysis of semiconductor devices. The basis of these models is to describe carrier transport by averaged macroscopic quantities of the system of charge carriers instead of the individual particles, e.g., the carrier density, current density, and energy density [54], [55].

Due to the identity of description of fluids and charge carriers in semiconductors, many wave-like phenomena known from fluid dynamics have corresponding analogies in carrier transport problems. In particular in FETs, the excitation of propagating collective charge density oscillations in the 2DEG of a semiconductor, so-called *plasma waves*, is possible and resembles to a large extent the physics of shallow water waves [39]. Originally, the general concept of plasma waves has been developed for three-dimensional systems by Tonks and Langmuir in the late 1920s [56] and was

discussed for bulk metals in great detail by Raimes in Ref. [57] and some references given therein. The electron ensemble in a semiconductor in equilibrium constitutes a uniform distribution of charge carriers in the periodic background potential of positively charged crystal ions. When an external field is applied for a short time, the electron gas is shifted relative to the background and, in order to restore the original distribution, a polarization field is induced, which drives the electrons back to their initial position. Because of their finite inertia, charges can overshoot this initial position and when the external force is periodic, collective longitudinal oscillations of charge carriers around their initial position can evolve.

An according formalism for lower dimensional systems, e.g., in semiconductor inversion layers, was first developed in the late 1960s by Stern [58] and discussed in further detail by Chaplik [59], [60] and Ando [61]. It was found that a linear dispersion relation can exist in these semiconductor structures. In 1977, absorption of infrared radiation in silicon inversion layers was first experimentally observed by Allen [62] and later discussed in great detail by Chaplik [60]. In these original works, a necessary spatial modulation of the electric field was realized by metallic grating structures to allow matching of the plasmon wavevectors to the incident radiation.

In the early to mid-1990s, Dyakonov and Shur showed in a number of pioneering works [18], [39], [40] that the same mechanism can take place in the 2DEG of a FET. They employed a reduced[4] fluid dynamic transport model for shallow water waves to describe the charge carrier transport by propagating plasma waves in the channel [39] and demonstrated theoretically that non-linear self-mixing properties of the waves can be used for an efficient detection of radiation in the THz region [18]. The concept was divided into two main regimes of detector operation.

- *Resonant detection*: When the waves launched from one side of the transistor are reflected off the second terminal, a standing wave pattern inside the channel acting as a resonant cavity can develop, and a strong enhancement of the detection mechanism by some orders of magnitude was expected [18]. Very few experimental investigations of this proposed phenomenon are at all available and it seems evident that an appropriate implementation of a real device is difficult to achieve with common semiconductor technologies. At least for conventional materials, extremely small device dimensions, cryogenic cooling of the detector [63]–[65] or drawing of an additional drain-source current is required [66]. The theoretical predictions from Ref. [18] have led to a questionable premise in the search for resonant plasmons in FETs. Although strong resonant enhancement of the mixing principle itself can exists, we will discuss in Chapter 5 that a pronounced enhancement of detection sensitivity cannot be expected for resonant plasmonic detection due to resonant power coupling at these frequencies.

- *Non-resonant/ broadband detection*: When the transistor channel is much longer than the typical decay length of the plasma waves, the detector operates in the so-called non-resonant detection regime [18]. The non-linear mixing happens on

[4]It will be worked out in Chapter 3 that the model is a “reduced” one in the sense that pressure terms and the effect of local heating of charge carriers are not considered in the formalism.

a rather short range in the channel and the remaining parts of the channel act as parasitic resistance and AC shunt capacitances for the incoming radiation. Naturally, this mechanism is not restricted to an exact resonance frequency and allows broadband detection of electromagnetic radiation [13], [24], [48], [67]–[70]. Also, no cooling is needed to achieve nearly state-of-the-art detector sensitivities for the THz region and TeraFETs can be efficiently operated at room temperature[20], [43], [71].

While the fundamental mechanism of the plasmonic detection process is largely understood, modeling and realization of an actual device remains a challenging task. Parasitic effects of the surrounding of the intrinsic gated transistor region as well as integration of an antenna structure for radiation coupling and efficient implementation of boundary conditions plays a crucial role for the TeraFET's efficiency. These aspects can to some extent be incorporated in an analytical device model by simple considerations of an equivalent circuit model of the detector. However, the analytical model, which will be presented in this chapter, relies on assumptions of exactly matched boundary conditions for the coupling of the incoming radiation, otherwise, the underlying equations may lose their validity. These boundary conditions are hardly ever perfectly met in real detectors, in particular when broadband operation is desired. This is one of the main reasons why implementation of the model in a circuit simulator can be advantageous to model non-ideal boundary conditions in a device simulation.

This following sections reviews the use of a reduced fluid dynamic model for the description of charge carrier transport in an FET's 2DEG. We will then show in Chapter 3 that this reduced form of Euler's equation together with the charge continuity equation is contained within a full hydrodynamic transport description [54, p. 201], which can be derived from the fundamental Boltzmann transport equation, and which contains additional density diffusive and thermoelectric current densities.

2.2 One-dimensional treatment of charge carrier transport

Assume a simplified transistor layout as depicted in Fig. 2.1. A 2DEG can form in an inversion layer at the boundary of the bulk semiconductor and the gate dielectric barrier. Application of a voltage to the gate metal contact controls the electrostatic potential in the inversion layer and thereby the charge carrier density in the 2DEG. While a real transistor is (except for intentionally designed low-dimensional structures) a three dimensional structure, it can be shown that the charge carrier dynamics in the context of FETs employed as high frequency detectors can be described by a one dimensional transport model. First, the device is assumed to be fully symmetric in the y-direction with respect to the x-z-plane. Second, it is assumed that the longitudinal electric field in the channel varies only gradually compared to the local gate-to-channel potential along the along the y-direction. This so-called gradual channel approximation is valid for non-saturation operation oft the transistor and in general for small gate-to-channel separations d, which is the case for typical semiconductor FETs where d is on the order of a few up to a few tens of nanometers.

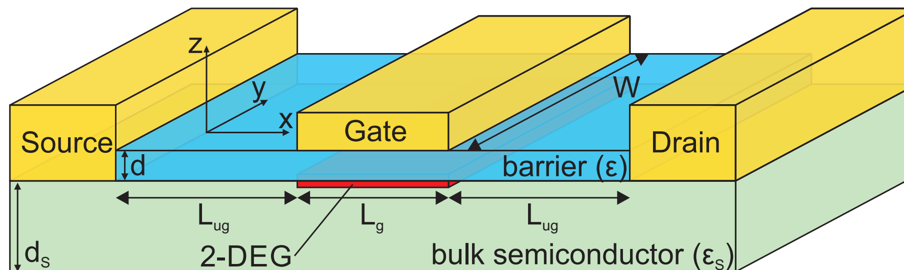

Fig. 2.1: Simplified schematic of a field-effect transistor (FET) and labeling of characteristic device geometrical parameters. Description of carrier transport is reduced to a one-dimensional treatment along the x-direction.

With these two assumptions, the carrier transport in the device can be described by a one-dimensional model along the x-direction. Note that this assumption implies that there exist no significant oblique contributions to the plasma waves in the channel, in particular no turbulence effects. It has been discussed to some extent that this may not be the case for high field or high drain current situations [33], [72].

When the carrier transport in a semiconductor device is non-ballistic, i.e., when carriers experience a multitude of collisions during transit and the mean free path between two consecutive scattering events is short compared to the device dimension, fluid dynamic transport models apply [54]. In particular for most semiconductor FETs, a high density of carriers ($\sim 10^{12}$ cm^{-1}) in the 2DEG leads to frequent electron-electron (e-e) collisions and to a distribution of excess energy in the carrier ensemble, which justifies the application of a hydrodynamic description [39]. Dyakonov and Shur investigated the possibility of frequency conversion in such electronic systems by applying analogies of instability mechanism known from the behavior of shallow water waves or sound waves in organ pipes [18], [39], [40], [73].

Fluid dynamic motion can be described by Euler's equation of motion together with the equation for charge continuity. When pressure terms are neglected and a phenomenological friction term is added, the transport model can be formulated as[5,6]

$$\partial_t v + v\partial_x v - \frac{q}{m}\partial_x \phi + \frac{v}{\tau_\mathrm{p}} = 0 \tag{2.1}$$

$$\partial_t n + \partial_x (nv) = 0 \tag{2.2}$$

In the model, v is the average carrier drift velocity, n the carrier density, and ϕ is the gate-to-channel potential. The constants q, m, and τ_p are the elementary charge, the effective carrier mass, and the momentum scattering time, respectively. When the potential ϕ is modulated by an oscillating external signal, collective charge density oscillations will be induced in the channel, which, by non-linear self-mixing, can

[5] In this text, the abbreviated notations $\partial_t \equiv \partial/\partial t$ and $\partial_x \equiv \partial/\partial x$ are used denoting partial derivatives with respect to time t and x-coordinate, respectively

[6] The model is formulated in terms of carrier density and drift velocity n and v, respectively. It can be rewritten in terms of the current density $j = -qnv$ and then be directly implemented in a circuit simulator (see Chapters 3 and 4).

rectify the incoming signal and induce a measurable DC current (or voltage) response in the device.

2.3 Intrinsic channel impedance and THz response

In this section, some important physical quantities for the discussion of plasma wave mixing in TeraFETs are derived. The discussion is limited to the intrinsic gated region of the transistor channel, since influences of extrinsic detector elements cannot be easily treated in analytic form. While extension of a quasi-static rectification picture by HF factors to account for changes of HF device impedances at high frequencies, matching of integrated antennas, etc. has been proposed before [42], calculation of channel impedance, carrier density and velocity as well as plasmonic enhancement of resistive mixing rely on defined boundary conditions to yield analytic expressions for these quantities (see below). For non-ideal coupling situations, analytic solutions to the transport equations Eqs. (2.1) and (2.2) in general do not exist. Furthermore, power distribution over the device plays a crucial role for the efficiency of the rectification mechanism and must be considered in device design and modeling and will be investigated in Chapter 5. Nevertheless, comparison of analytically derived results for the intrinsic detector element served as a benchmark for the verification of the model implementation presented in Chapter 4. The discussion in this and the following sections are mainly based on Refs. [18], [19], [42], [43]. Some details on the underlying calculations are given in Appendix A.

2.3.1 Channel impedance and carrier velocity

Analysis of plasma wave mixing in TeraFETs described by the fluid-dynamic model is commonly performed by harmonic expansion of the applied oscillating signal and related quantities in terms of the oscillation angular frequency ω. An analysis to the first order in ω of the transport equations Eqs. (2.1) and (2.2) leads to a wave-equation

$$k^2\phi_1 + \partial_x^2\phi_1 = 0 \tag{2.3}$$

for the oscillating component $\phi_1 \propto e^{i(\omega t - kx)}$ of the channel potential.[7] The solutions are propagating charge density (plasma) waves with angular frequency ω, plasma velocity

$$s = \sqrt{\frac{q}{m} n_0 \frac{\partial \phi}{\partial n}} \tag{2.4}$$

and complex wavevector

$$k = \frac{\omega}{s}\sqrt{1 - \frac{i}{\omega\tau_{\mathrm{p}}}} \tag{2.5}$$

Eq. (2.5) shows that the gated plasma waves obey a linear dispersion relation for $\omega\tau_{\mathrm{p}} >> 1$, the so-called *plasmonic mixing regime* (see Section 2.4.3). The channel

[7] The subscript denotes the order in frequency ω in the harmonic expansion.

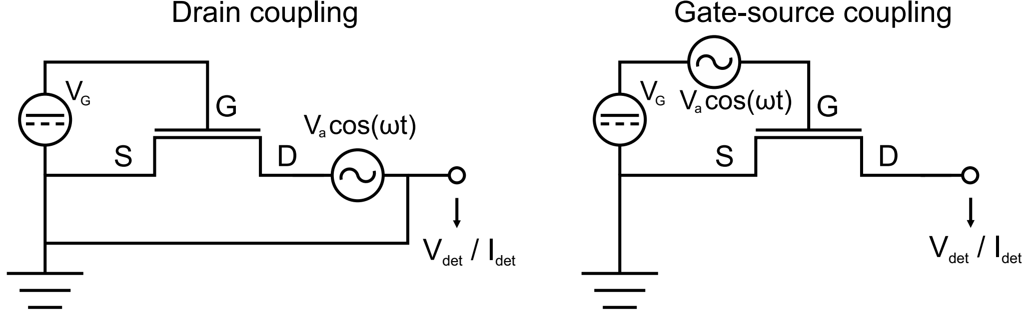

Fig. 2.2: Equivalent circuit for drain coupling (left) and gate-source coupling (right) boundary conditions.

potential is related to the local gate voltage-controlled charge carrier density in the channel by Poisson's equation and can be expressed for the first order in ω in a long-wavelength approximation (see Appendix A.1) as [42]

$$\phi_1(x,t) = -n_1(x,t)\frac{\partial \phi}{\partial n} \tag{2.6}$$

Asymmetric boundary conditions are required for an efficient detection of incoming radiation (for more details, see Section 2.5 below). Although plasma oscillations can still form in fully symmetrically excited FET channels, no net measurable voltage (or current) response to the incident radiation can build up. Full asymmetry is achieved, e.g., when one end of the channel is subjected to the full amplitude of the applied excitation signal $V_\mathrm{a}\cos(\omega t)$ while the other end of the channel is pinned to zero amplitude

$$\begin{aligned} \phi_1(x=0) &= 0 \\ \phi_1(x=L_\mathrm{g}) &= V_\mathrm{a} \end{aligned} \tag{2.7}$$

The picture of charge density waves launched into the transistor channel by the incoming radiation from one end, in this case the drain side at $x = L_\mathrm{g}$, is established. This coupling scheme is therefore referred to as *drain coupling*. A schematic illustration of the situation is shown in Fig. 2.2 on the left. With given boundary conditions, the solutions to the wave equation Eq. (2.3) are uniquely determined. The amplitude of the modulation of the channel potential is then directly related to the first order gate-to-channel voltage amplitude V_1 and can with respect to Eq. (2.7) be calculated as [42]

$$V_1(x) = -V_a\frac{\sin(kx)}{\sin(kL_\mathrm{g})} \tag{2.8}$$

The velocity of charge carriers is modulated by the external oscillation signal and becomes

$$\begin{aligned} v_1(x) &= V_\mathrm{a}\frac{q\omega}{iks^2m}\frac{\cos(kx)}{\sin(kL_\mathrm{g})} \\ &= V_\mathrm{a}\frac{\omega}{ikn_0}\frac{\partial n}{\partial \phi}\frac{\cos(kx)}{\sin(kL_\mathrm{g})} \end{aligned} \tag{2.9}$$

From the carrier velocity, the current density can be calculated via the well-known

relation $j_1 = -qn_0v_1$ and the AC impedance of the channel is simply given as the ratio of voltage and total current $I = j_1W$ at the drain[8]

$$\begin{aligned} Z_\mathrm{g} = \left.\frac{V_1(x)}{j_1(x)W}\right|_{x=L_\mathrm{g}} &= \frac{iks^2m}{\omega q^2 n_0 W}\tan(kL_\mathrm{g}) \\ &= \frac{ikn_0}{\omega W}\frac{\partial n}{\partial \phi}\tan(kL_\mathrm{g}) \end{aligned} \tag{2.10}$$

Figure 2.2 on the right shows coupling conditions as proposed in the original works of Dyakonov and Shur [18]. The incoming radiation is coupled to the FET between the gate and source while the detected signal is again read out at the drain end of the channel. These boundary conditions are commonly referred to as *gate-source coupling* and are defined as

$$\begin{aligned} \phi_1(x=0) &= V_a \\ v_1(x=L_\mathrm{g}) &= 0 \end{aligned} \tag{2.11}$$

with full oscillation of the gate-to-channel potential at the source side and vanishing first order velocity component at the drain end of the channel. Following a similar derivation as above, the gate-to-channel voltage and carrier velocity are calculated as

$$V_{1,\mathrm{GS}}(x) = -V_\mathrm{a}\frac{\cos(k(L_\mathrm{g}-x))}{\cos(kL_\mathrm{g})} \tag{2.12}$$

$$v_{1,\mathrm{GS}}(x) = V_\mathrm{a}\frac{q\omega}{iks^2m}\frac{\sin(k(L_\mathrm{g}-x))}{\sin(kL_\mathrm{g})} \tag{2.13}$$

and the channel impedance is found to be

$$\begin{aligned} Z_\mathrm{g,GS} = \left.\frac{V_{1,\mathrm{GS}}(x)}{j_{1,\mathrm{GS}}(x)W}\right|_{x=0} &= \frac{iks^2m}{\omega q^2 n_0 W}\cot(kL_\mathrm{g}) \\ &= \frac{ikn_0}{\omega W}\frac{\partial n}{\partial \phi}\cot(kL_\mathrm{g}) \end{aligned} \tag{2.14}$$

The channel impedance is a crucial design parameter for TeraFET detectors. In a real device with attached antenna and possible parasitic circuit elements, the amount of power of the incoming radiation which is available for the actual plasmonic detection mechanism is distributed over the device elements depending on their relative high frequency impedances according to a simple voltage divider picture (see Chapter 5). In particular, significant amounts of the incoming power can be “lost” to ungated access regions of the transistor.

[8]Note again that the expressions for gate-to-channel voltage, carrier velocity and channel impedance apply only for the case of AC source-gate shunting and full oscillation at the drain side of the channel. They take slightly different forms for other coupling schemes (see Appendix A.2.1). For a more detailed overview see, e.g., Ref. [43, ch. 3]

2.3.2 THz response

Second order analysis of the fluid-dynamic model yields the DC induced detector response to an applied high frequency signal with angular frequency ω. Non-linear mixing of induced plasma waves in the channel leads to rectification of the signal, which is the basis for the plasmonic mixing principle. The FET's DC voltage response is found by integration of the differential transport equations Eqs. (2.1) and (2.2) over the active gated channel length L_g retaining all oscillatory terms up to the second order in ω, which produce a stationary response to the applied external signal. The induced detector signal V_det can then be derived as (see Appendix A.2)

$$V_\mathrm{det} = V(x = L_\mathrm{g}) - V(x = 0) = \frac{q}{m}\frac{V_\mathrm{a}^2}{4s^2} f(\omega). \tag{2.15}$$

the product of a quasi-stationary response and a frequency-dependent *enhancement* or *efficiency factor* $f(\omega)$, whose exact form again depends on the applied boundary conditions. Note that the detection signal can also be read out as current signal where the relation

$$I_\mathrm{det} = \frac{V_\mathrm{det}}{R_\mathrm{DC}} \tag{2.16}$$

with the FET's DC drain-source resistance R_DC holds.

For the drain coupling, AC gate-source shunting boundary conditions defined in Eq. (2.7) the enhancement factor takes the form [42], [43]

$$\begin{aligned} f_\mathrm{D}(\omega) &= 1 + \beta \frac{\sinh^2(k_\mathrm{i} L_\mathrm{g}) - \sin^2(k_\mathrm{r} L_\mathrm{g})}{\cosh^2(k_\mathrm{i} L_\mathrm{g}) - \cos^2(k_\mathrm{r} L_\mathrm{g})} \\ \beta &= \frac{2}{\sqrt{1 + \left(\frac{1}{\omega \tau_\mathrm{p}}\right)^2}} \end{aligned} \tag{2.17}$$

where k_r and k_i are the real and imaginary parts of the wavevector $k = k_\mathrm{r} - ik_\mathrm{i}$ from Eq. (2.5). For coupling of the high frequency signal between gate and source and open drain terminal, the efficiency factor is calculated as [18], [43]

$$f_\mathrm{GS}(\omega) = 1 + \beta - \frac{1 + \beta \cos(2k_\mathrm{r} L_\mathrm{g})}{\sinh^2(k_\mathrm{i} L_\mathrm{g}) + \cos^2(k_\mathrm{r} L)} \tag{2.18}$$

A simplified factor can be defined for the broadband, long-channel case where no significant reflections at the channel ends occur. In this regime, the oscillatory terms in both equations Eqs. (2.17) or (2.18) reduce to unity for $kL_\mathrm{g} \gg 1$ and

$$f_\mathrm{s}(\omega) = 1 + \beta = 1 + \frac{2}{\sqrt{1 + \left(\frac{1}{\omega \tau_\mathrm{p}}\right)^2}} \tag{2.19}$$

The simplified efficiency factor asymptotically approaches a maximum value of three for large ω [18], [43]. Further discussion of the enhancement factor is given in Section 2.4.3.

The quasi-static voltage response can be shown to take the same form as the

pre-factor in Eq. (2.15) (see Appendix A.2.1) and with the definition of plasma velocity Eq. (2.4) we find

$$\begin{aligned} V_{\mathrm{QS}} &= \frac{q}{m}\frac{V_{\mathrm{a}}^2}{4s^2} \\ &= \frac{V_{\mathrm{a}}^2}{4}\frac{1}{n_0}\frac{\partial n}{\partial \phi} \\ &= \frac{V_{\mathrm{a}}^2}{4}\frac{1}{\sigma}\frac{\partial \sigma}{\partial \phi} \end{aligned} \tag{2.20}$$

where we introduced the DC channel conductivity

$$\sigma = q n_0 \mu \tag{2.21}$$

This remarkable result implies that the quasi-static voltage response of a TeraFET can be predicted from its DC channel conductance $G(V_G) = \sigma W/L_{\mathrm{g}}$, which is accessible via conventional DC I-V measurements. However, a few remarks should be made concerning this observation.

First, a similar result was obtained by neglecting all but the field-dependent term in Eq. (2.1) corresponding to $j = -\sigma\partial_x\phi$ [74]. The approach reveals that in the quasi-static analysis, plasma wave phenomena are not considered and the prediction of the detector response after Eq.(2.20) is based purely on resistive mixing (see below). While this can be justified for low-frequency application, the inconsiderate use of the formula in the discussion of THz detection experiments is highly questionable though unfortunately often found in TeraFET literature. Plasmonic enhancement of the quasi-static response is accounted for in the full detector response Eq. (2.15) by the frequency-dependent enhancement factor $f(\omega)$ (for further discussion, see Section 2.4.3).

Second, besides plasmonic enhancement, the THz response of a real TeraFET is strongly influenced by the HF behavior of the channel impedance Z_{g} (Eq. (2.10)), frequency-dependent impedance matching of integrated antenna structures, HF power distribution over the gated and ungated channel regions, and influences of other parasitic device elements. It can therefore not be expected that a simple analysis of DC device parameters is sufficient to predict HF detection characteristics. The quasi-static response must therefore be embedded in a more comprehensive formalism accounting for the above phenomena, as was suggested, e.g., in Ref. [42]. Lastly, it will be shown in this thesis that other physical mechanism of THz rectification may take place in TeraFETs, which are naturally not covered by the presented analysis of plasma wave mixing.

In conclusion, the quasi-static TeraFET response after Eq. (2.20) should be applied only as a rule-of-thumb and has shown to yield remarkably good approximations to measured THz detection signals in some situations. It must however be emphasized that this can be misleading since important HF phenomena are not considered and deviations from real THz detection signals are often substantial. Another important aspect here is that the amplitude of the oscillating signal at the gated channel region V_{a} is commonly not an accessible parameter in real detection experiments. In general, a normalization of equation EQ (2.20) is therefore necessary, which can mask significant deviations between measured and predicted THz responses. This underlines the need for the implementation of the intrinsic plasma wave detection

Table 2.1: Detection regimes of TeraFETs (in reference to Table 3 in [43])

Wavelength \ Frequency	$\omega\tau_{\mathrm{p}} < 1$ *strong damping*	$\omega\tau_{\mathrm{p}} > 1$ *weak damping*
$\mathrm{Re}\{kL_{\mathrm{g}}\} < 1$ *short channel*	Classical resistive mixing	Resonant plasmonic mixing
$\mathrm{Re}\{kL_{\mathrm{g}}\} > 1$ *long channel*	Distributed resistive mixing	Non − resonant plasmonic mixing

mechanism in a full device model accounting for extrinsic influences on TeraFET detection signals.

2.4 Detection regimes

The above plasma wave model naturally leads to various detection regimes in which the detector can be operated. Depending on the frequency of the applied radiation, the detection principle is *classical resistive mixing* by modulation of the channel conductance, or *distributed resistive mixing* or *plasmonic mixing* by non-linear self-mixing properties of induced charge density waves. From an equivalent circuit point of view, when the wavelength of the induced plasma oscillations is much longer than the channel length, the transistor's 2DEG channel can be represented by a single lumped RC element and the wave picture can be neglected. On the other hand, for higher frequencies where the plasma wavelength becomes comparable to or shorter than the channel length, the lumped element picture loses its validity. The local modulation of carrier density and velocity in the channel by the applied signal become important and require a distributed element description [19]. The transistor's gated channel region must then be treated as a transmission line composed of RLC unit cells [44], [46], [48]. As is known from basic transmission line theory (e.g., [75], [76]), a wave-based description identical to the solutions of the fluid-dynamic model Eqs. (2.1) and (2.2) is then suitable to solve the fundamental set of differential equations for channel voltage and current – the *telegrapher's equations* (see Section 2.6).

Dyakonov and Shur discussed the possibility of rectification of HF signals in FETs from a charge carrier transport point-of-view [18] rather than a transmission line approach. While their formulation of the detection model was based on fluid dynamic differential equations for carrier density n and drift velocity v, both sets of equations are equally valid for the description of the underlying physical detection processes – one stemming from a more physics-based viewpoint, the other from an electrical engineering approach.

The plasma wavevector in Eq. (2.5) is a complex quantity and hence describes propagation and attenuation of the waves. A characterization of detector operation regimes is commonly based on the capability of the induced plasma waves to propagate along the channel. Two criteria can be formulated for this purpose.

A transition point from strong to weak damping can be loosely defined at the

frequency where the product of frequency and momentum relaxation time $\omega\tau_\mathrm{p}$ becomes unity. For low frequencies $\omega\tau_\mathrm{p} \ll 1$ the imaginary part in Eq. (2.5) is large, the waves are strongly damped or even overdamped, and no full oscillation cycle can develop before the wave is attenuated. On the other hand, when the excitation frequency is large and $\omega\tau_\mathrm{p} \gg 1$, the waves are only weakly damped and can survive multiple oscillations before decaying.

A second criterion is the length of the (gated) channel L_g compared to the plasma wavevector. In a comparably short channel, the waves can propagate along the channel, reach its end, and be reflected off the boundary[9] before they are significantly attenuated. The channel then acts as a cavity for standing waves where superposition of waves and resonance features can evolve. With the help of the plasma wavevector k a transition from the so-called *short channel* ($\mathrm{Re}\{kL_\mathrm{g}\} \ll 1$) to the *long channel* ($\mathrm{Re}\{kL_\mathrm{g}\} \gg 1$) regime can be formulated.

In conclusion, the four regimes of detector operation shown in Table 2.1 can be distinguished. The transition between regimes is a smooth one rather than exactly fixed by the wavelength/ frequency criteria [18], [42].

2.4.1 Classical resistive mixing

We mentioned before that for low frequencies, the transistor channel can be described by a simple lumped RC circuit model. In general, the drain-source current of an FET can be described by the basic relation [77][78, ch. 7]

$$I_\mathrm{ds} = V_\mathrm{ds} G_\mathrm{ds} \propto \left[(V_\mathrm{gs} - V_\mathrm{th}) - \frac{V_\mathrm{ds}}{2} \right] V_\mathrm{ds} \tag{2.22}$$

where the channel conductance $G_\mathrm{ds}(V_\mathrm{gs}) = 1/R_\mathrm{ds}(V_{gs})$ is controlled by the gate-to-channel voltage V_gs.[10] V_th is the FET's threshold voltage. Let us assume now that in addition to a DC bias, the gate and drain voltage are simultaneously modulated by a (small) oscillating radiation signal with angular frequency ω and amplitude V_a

$$\begin{aligned} V_\mathrm{ds} &= V_\mathrm{D} + V_\mathrm{a}\cos(\omega t) \\ V_\mathrm{gs} &= V_\mathrm{G} + V_\mathrm{a}\cos(\omega t) \end{aligned} \tag{2.23}$$

Here, V_D and V_G are externally applied gate and drain bias voltages. The resulting drain current is proportional to $\cos^2(\omega t)$ and via non-linear frequency mixing gives rise to a time averaged DC drain-source current response of the detector

$$I_\mathrm{det} = \langle I_\mathrm{ds} \rangle \propto \frac{V_\mathrm{a}^2}{4} \tag{2.24}$$

[9] The ends of the intrinsic FET channel region, i.e., the transition regions from gated to ungated channel regions or contacts, are in general no abrupt boundaries and propagating waves may be partly reflected and partly transmitted. This is so far not considered in the model implementation presented in this thesis and can lead to a possible overestimation of plasmonic effects in the device simulations (see Chapter 7)

[10] We assume for all discussions that the source terminal is on AC and DC ground and use the subscript "gs" to denote the gate-to-channel voltage. The subscript "ds" denotes the drain-source voltage.

This is the so-called principle of classical *resistive mixing*. Since the rectified signal is proportional to the squared amplitude of the applied oscillating signal, this is sometimes referred to as *square (power) law detection*. The classical resistive mixing regime is contained as a low frequency limiting case in the (distributed) fluid dynamic model Eqs. (2.1) and (2.2) and can be derived by neglecting time derivatives and the convective term [79]. As a noticeable consequence, the continuity equation states that the modulation of charge density in the channel is spatially uniform at any point in time and the channel conductance is modulated uniformly along the channel. The channel impedance Eq. (2.10) reduces to a simple real-valued drain-source DC resistance

$$R_{DC} = \frac{1}{qn_0\mu}\frac{L}{W} = \frac{1}{\sigma}\frac{L}{W} \tag{2.25}$$

with

$$\mu = \frac{q\tau_{\mathrm{p}}}{m} \tag{2.26}$$

the common definition of carrier mobility.

2.4.2 Distributed resistive mixing

In the regime of distributed resistive mixing ($\omega\tau_p < 1$), the transistor channel can be modeled by a simple transmission line of distributed RC unit cells. This is the case when the first two terms in Eq. (2.1) and (2.2) can be neglected [19], [42], [46]. The wave-like nature of the excitation of charge carrier density and velocity in the channel already becomes evident in this regime and a non-quasi-static treatment of detection must be applied. The charge density waves in this frequency regime are strongly overdamped and no resonances can form. The actual rectification mechanism is due to the second term in Eq. (2.2), i.e., a simultaneous local modulation of charge density and velocity with frequency ω of the applied oscillation signal. Again, the product of the two oscillating quantities leads to non-linear frequency mixing and yields a DC current or voltage response as was discussed in Section 2.3. Some mathematical details are given in Appendix A. Extended discussion of the concept of distributed mixing in TeraFETs can, e.g., be found in [19].

Two important remarks should be made here. First, it can be shown that the detector's voltage or current response takes the same form as in the limiting quasi-static case [79] for long channels ($\mathrm{Re}\{kL_{\mathrm{g}}\} < 1$) and is independent of the channel length – although the local modulation of carrier density and velocity could suggest otherwise. The reason is that the actual rectification happens only on the scale of a decay length of the overdamped plasma oscillation before their amplitude decreases by a factor $1/e$. The remaining channel parts merely act as parasitic resistance and shunting capacitance [19], [48], which can, however, have significant influence on the actual performance of the detector.

A second important aspect is that while classical mixing is limited by the transistor's conventional cut-off frequencies ,[11] the plasma wave mixing principle does not

[11] Typical cut-off frequencies for common FETs lie in the range of some tens up to a few hundreds of GHz, although transistors witch much higher cut-off frequencies have been reported.

rely on classical single carrier transition times [80] and can in principle extend far into the THz spectral regions [7], [69], [71].

2.4.3 Plasmonic mixing

As the applied frequencies are further increased and $\omega\tau_p \gg 1$, the transport model Eqs. (2.1) and (2.2) must be employed in their full form. The additional time and spatial dependence of the carrier velocity becomes significant and the only weakly damped charge density waves can propagate along the channel with multiple oscillations before they decay. A full plasmonic picture following the derivations in Section 2.3 applies. In the transmission line picture (see Section 2.6), the finite inertia of charge carriers must be accounted for by introducing a kinetic inductance L in the distributed equivalent circuit, now represented by a transmission line of RCL unit cells [11], [43], [44], [46], [48]. Two physical situations from Table 2.1 can be distinguished in this detection regime:

For short channels ($\mathrm{Re}\{kL_\mathrm{g}\} \ll 1$), the plasma waves can be reflected off the boundary at the end of the channel and resonant standing waves can evolve in the channel. This operation regime is therefore termed the regime of *resonant detection*. The exact form of resonant behavior strongly depends on the specific boundary conditions at the ends of the transistor channel (see below).

For long channels ($\mathrm{Re}\{kL_\mathrm{g}\} \gg 1$), the plasma waves can propagate along the channel but they decay before a significant reflection at the boundaries can occur. In this case, just like for the distributed resistive mixing, the rectification mechanism is self-mixing of plasma waves within their decay length. However, a plasmonic enhancement of detection efficiency compared to the quasi-static limit may be present even without the formation of resonances (cp. Eq. (2.19)). Since the detection is not limited to a resonance condition, the operation regime is commonly denoted as *non-resonant* or *broadband*. The actual bandwidth of a real TeraFET, however, is usually determined rather by the effective bandwidth of the radiation coupling antenna than the intrinsic principle of rectification. The TeraFETs which were fabricated over the course of this work were designed as broadband detectors and most of the following discussions in this thesis are focused on non-resonant THz detection with FETs.

The detection mechanism in the plasmonic regime can be considered an "enhancement"[12] of quasi-static distributed resistive mixing. A dimensionless, frequency-dependent efficiency factor $f(\omega)$ can be introduced to account for the plasmonic enhancement

$$V_\mathrm{det}(\omega) = V_\mathrm{QS} \cdot f(\omega) \tag{2.27}$$

of the quasi-static voltage response V_QS of the detector. Derivation of analytical expressions for the enhancement factor was presented in Section 2.3 for two distinct types of boundary conditions associated with the coupling schemes shown in Fig. 2.2.

Figure 2.3 shows plots of the three variants of $f(\omega)$ after Eqs. (2.17), (2.18), and (2.19) versus radiation frequency for the intrinsic channel region of an AlGaN/GaN

[12]Note that the efficiency can under certain conditions be reduced instead of enhanced, see discussion below.

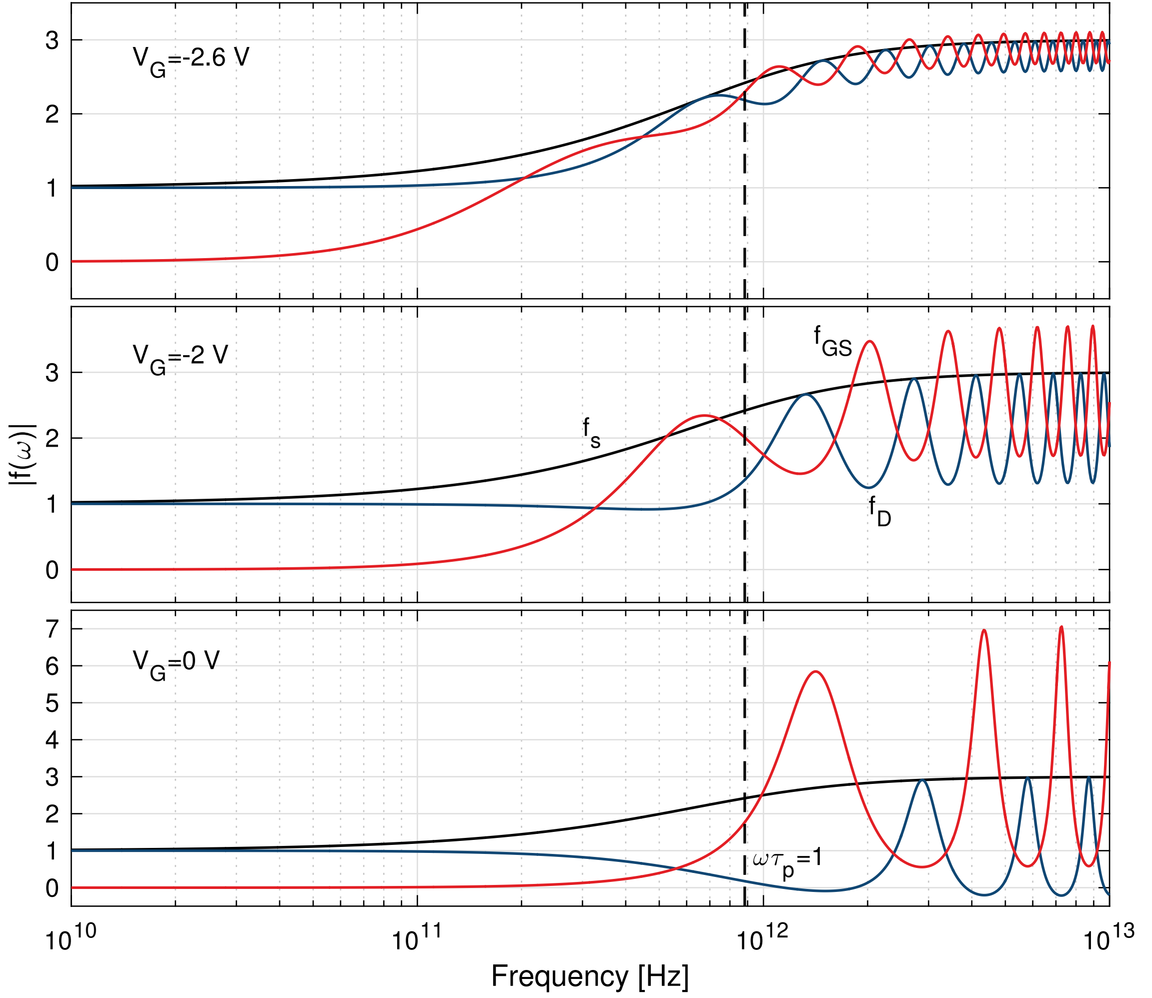

Fig. 2.3: Plasmonic enhancement factors versus radiation frequency of an AlGaN/GaN TeraFET investigated in Chapter 6. The plot displays the enhancement factors for drain coupling (f_{D}), gate-source coupling (f_{GS}) and the long-channel case (f_{s}) for three different gate bias voltages V_{G}. The quasi-static (distributive resistive mixing, Eq. (2.20)) limit is set by unity for drain-coupling and zero for gate-source coupling (cp. [42]).

device, which will be characterized in more detail later. The gate bias voltages for the three plots V_{G} were chosen as roughly 0.2 V below the threshold voltage (V_{th} =-2.46 V), 0.4 V above the threshold, and far above the threshold at 0 V gate bias, respectively. We find that the evolution of resonances – setting in roughly at frequencies where $\omega\tau_{\mathrm{p}} = 1$ and the plasmonic regime is reached – is of opposite nature, constructive or destructive, for the two coupling schemes. For the drain coupling situation (f_{D}, blue line), the long-channel approximation (f_{s}, black line) presents a limiting case with a maximum enhancement up to a factor of three for $\omega\tau_{\mathrm{p}} > 1$ and destructive resonances merely lead to a decrease of plasmonic efficiency. On the other hand, for gate-source coupling (f_{GS}, red line) this limit is exceeded due to constructive resonances at the same frequencies. Note that for operation far above the threshold ($V_{\mathrm{G}} = 0$ V, bottom plot) the efficiency can even decreases below unity at the destructive resonances of f_{D} and lead to an actual reduction of the detector response compared to the distributed resistive mixing regime. The frequency of the

multiple resonances can be shown to be located close to multiples of the fundamental plasma resonance frequency [18]

$$\omega = \frac{\pi s}{2L_{\mathrm{g}}} \tag{2.28}$$

The presented analysis of plasmonic enhancement of classical distributed mixing could tempt a device designer to aim for a realization of the strong resonant enhancement situation of f_{GS}at the desired operation frequency. In fact, it was proposed in the original works by Dyakonov and Shur [18] that exploitation of plasmonic resonances could lead to a new form of extremely sensitive THz detectors with several orders of magnitude of enhancement of efficiency. However, we are going to show in numerical simulations performed with the implemented TeraFET model (Chapter 5), that the enhancement is mostly of theoretical value since it is merely a feature of the direct response of a real TeraFET device. The important figures of merit describing the efficiency of a detector, on the other hand, are its responsivity and sensitivity (see Section 6.1), which are both related to the input radiation power available to the intrinsic, rectifying detector part. We will show that these quantities do not exhibit a strong enhancement above the long-channel limiting case of $f_{\mathrm{s}}(\omega)$.

2.5 Asymmetric boundary conditions

A crucial assumption in the above discussion and derivations have been the boundary conditions, e.g., in the manifestation of Eq. (2.7). Effectively, these conditions represent a situation in which one end (drain) of the channel is subject to the full potential oscillation, while the other (source) end is pinned to AC ground . An inherent spatial asymmetry in the oscillating gate-to-channel potential (and voltage, respectively) exists. From simple symmetry arguments it is evident that no measurable rectified voltage or current could build up between the undistinguishable transistor drain and source contacts for an electrically balanced device [48]. In the plasma wave picture, waves would be excited from both ends of the channel inducing rectified signals of opposite sign which would add up to zero.

A demonstration of the principle with AlGaN/GaN HEMT TeraFETs fabricated in the course of this work can be found in Ref. [2]. Three detector designs were realized where the wings of integrated bow-tie antennas were coupled to the transistor with different levels of asymmetry as depicted in Fig. 2.4 on the left. The detectors were scanned across a THz beam with Gaussian beam profile and magnitude and relative phase of the rectified signal were measured with a lock-in amplifier (Fig. 2.4 on the right). In the fully symmetric transistor layout A, plasma wave mixing signals of equal magnitude but opposite sign are induced from both transistor ends under homogenous illumination of both antenna wings – correspondingly, the measurements shows zero signal at the center of the THz beam. Design B introduces a partial asymmetry by varying the length of the ungated access regions on source and drain side – waves are still launched from both ends but with different amplitudes. The point of zero detection signal therefore shifts in the measurement to the location where the inhomogeneous illumination of both antenna wings matches the difference in signal magnitude. Finally, a fully asymmetric coupling situation is realized in Design C by the implementation of capacitive coupling between gate and drain (Metal-

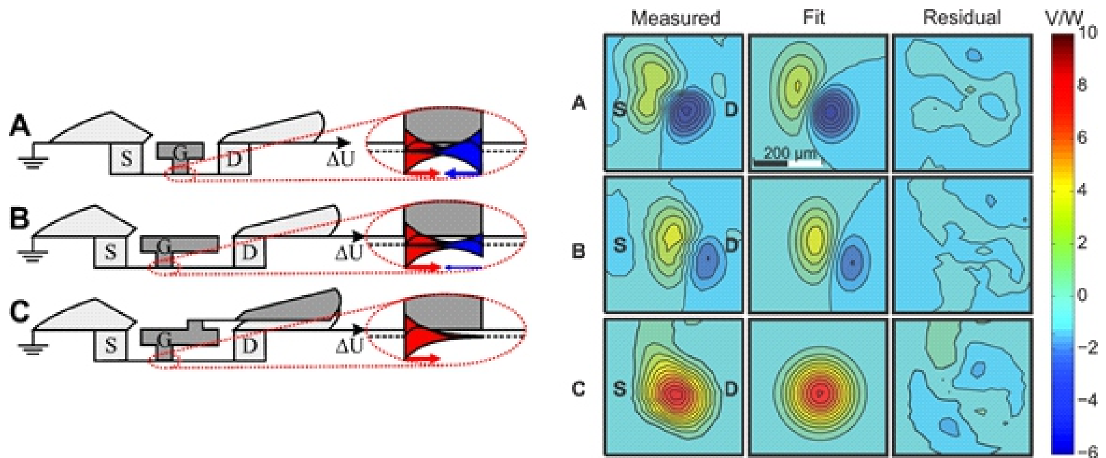

Fig. 2.4: Left: Schematic of different detector layouts. The radiation coupling is varied from fully symmetric (A) over partly asymmetric (B) to fully asymmetric (C) coupling. Right: THz beam profile scans performed with the three detectors. The color coding (red or blue) represents magnitude and phase of the measured signal. Efficient detection occurs only for fully asymmetric coupling (C) whereas the signal nearly vanishes for designs A and B under homogenous illumnination. Figures taken from Ref. [2].

insulator-metal, MIM capacitance). The channel potential is pinned to AC ground on this end and the signal exhibits full asymmetry for homogeneous illumination, hence, the measured signal shows maximum magnitude at the center of the THz beam. This experiment illustrates the requirement of asymmetric boundary conditions in the high frequency modulated channel potential for efficient TeraFETs.

The asymmetry in the channel potential can be achieved in different ways. It could be built in the transistor layout itself or be realized by appropriate coupling of the incoming radiation to the transistor terminals.[13] The latter can be implemented by the use of a suitable design of integrated antenna feeding the incoming signal to one terminal only (see design of detectors in Chapter 6). The introduction of capacitive coupling between the gate and the other terminal of the transistor implements an AC shunt remains open. A gate-to-channel potential is created on one side only while the other side remains pinned to AC ground. Over the time of this work it became evident, that the implementation of drain coupling boundary conditions by implementation of an additional shunting capacitance yielded highly efficient TeraFETs in both investigated material systems [5], [13].

Besides being a requirement for efficient exploitation of resistive mixing in an FET, the asymmetry in the channel potential can have profound consequences on the nature of the detection mechanisms taking place in the device (see Chapter 7) [12], [30], [32]. A non-uniform gate-to-channel potential in turn leads to a non-uniform spatial distribution of the energy of the incident electromagnetic wave to the charge

[13]It should be mentioned that an asymmetric situation can also be achieved by drawing of a drain-source current. However, in this case the noise characteristic of the transistor would change from purely thermal noise (see Section 6.1.1) to additional shot noise contributions, which makes zero drain bias operation favorable for detector operation. The unbiased operation is one of the major advantages of TeraFETs over Schottky diode-based rectifiers.

carrier system which can gives rise to diffusive carrier transport, in particular a hot carrier thermoelectric effect. When carrier-carrier scattering in the electronic system is significantly faster than phonon or impurity scattering with the lattice, the excess energy is distributed via multiple collision events within the carrier ensemble leading to an increased temperature of carriers with respect to carriers in thermal equilibrium with the lattice. This establishment of an elevated temperature of the ensemble of charge carriers is known as the *hot-carrier effect* and has been discussed extensively in the literature (see, e.g., Refs. [23], [26], [81], [82]). Since the heating of carriers is asymmetric over the device, a thermal gradient in carrier temperature can induce a diffusion current of charge carriers - known as the *hot-carrier thermoelectric effect* - which can generate a measurable DC current (see, e.g., Refs. [26], [28], [83]–[85]).

Simultaneously, as a direct consequence of the carrier density-controlling function of the gate in an FET, a local variation of the gate-to-channel potential can as well generate a gradient in charge carrier density along the channel. This leads again to a diffusion of carriers in order to equalize the carrier density over the channel. In a thermodynamic picture, the product of particle density n and their temperature T_C represents a hydrodynamic pressure via the well-known relation

$$P = n k_\mathrm{B} T_\mathrm{C} \tag{2.29}$$

In conclusion, when a pressure gradient in the electronic system of the 2DEG gas in an FET is induced by asymmetric coupling of the incoming electromagnetic radiation, a diffusive DC can be the result, in addition to the DC current generated by the plasma wave-based mixing mechanism. Recent experimental observations indicate that these effects cannot be neglected even at room temperatures and must be included in a comprehensive device model. In particular in carbon-based low-dimensional systems such as graphene and carbon nanotubes, where the decoupling of the carrier ensemble from the crystal lattice is strong [27], [86], experiments show that the thermoelectric signals can even be of roughly the same order of magnitude as the plasma wave mixing signal. We will see in the following that while the fluid-dynamic model employed by Dyakonov and Shur does not account for the above diffusive effects, they can be added by including the pressure gradient in the model.

We find that the contribution of the density gradient diffusive effect is negligible in the fabricated devices and could not be investigated separately. On the other hand, significant thermoelectric signals were observed in all devices, which were charaterized in the course of this work. The experimental evidences and further discussion is given in Chapter 7.

2.6 Transmission line equivalent circuit description

The fluid dynamic transport model described by Eqs. (2.1) and (2.2) can be translated into an equivalent circuit description with a set of differential equations describing the AC voltage and current in an RCL distributed transmission line. The use of such an equivalent circuit model has been proposed before in the literature, e.g., in Refs. [19], [44], [46], [48], [87]. An in-depth discussion of the application of a transmission

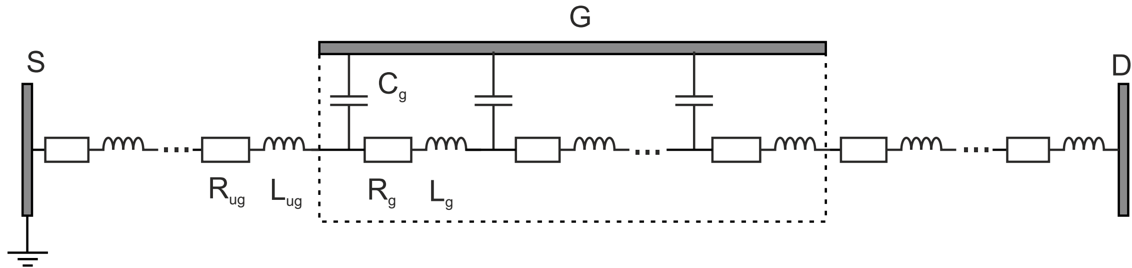

Fig. 2.5: Distributed transmission line equivalent circuit representation of a TeraFET.

line model to plasma excitations in 2DEGs far beyond the scope of this thesis can be found, e.g., in the work of Aizin and Dyer [87].

Both modeling approaches are equivalent and an appropriate implementation and HF analysis of the transmission line model in a numerical circuit simulation should yield the same results - in particular, the same plasmonic mixing efficiency $f(\omega)$ - as derived before from the fluid-dynamic transport model. It is a major advantage of an equivalent circuit implementation that the intrinsic gated channel element can be embedded in an extended device model including extrinsic detector components, such as, ungated channel regions, parasitic contact and access resistances or capacitances, S-Parameters from antenna simulations, etc. Another important aspect is that the derived analytic equations for the intrinsic plasma wave mixing mechanism relied on precisely defined boundary conditions of asymmetric radiation coupling to the transistor. In a real device, the coupling situation can in general not be assumed to be ideal and the analytical expressions - in particular the ones for the AC impedance of the gated channel part and the efficiency factor $f(\omega)$ - may lose their validity. A numerical circuit simulation can account for such deviations, e.g., when antenna port S-Paramter data are included in the circuit model, since a self-consistent solution of device currents and voltages is calculated.

Figure 2.5 shows an schematic illustration of a transmission line equivalent circuit of an FET. From basic transmission line theory, a set of differential equations governing the AC voltage and current in a transmission line can be formulated, the so-called *telegrapher's equations*[14] [75, ch. 2]

$$\partial_x V(x,t) = -R_{\mathrm{g}} \cdot I(x,t) - L_{\mathrm{g}} \cdot \partial_t I(x,t) \tag{2.30}$$

$$\partial_x I(x,t) = -C_{\mathrm{g}} \cdot \partial_t V(x,t) \tag{2.31}$$

Mathematically, the above equation are equivalent to the fluid-dynamic transport equations used for the description of the plasma wave mixing mechanism. Using the identity of Eqs. (2.1) and (2.2) and Eqs. (2.30) and (2.31) the electrical quantities

[14]Note that we have implicitly assumed here a vanishing gate-to-channel conductance for a non-leaking gate. When significant gate leakage currents are present in the device, an additional term $-G \cdot V(x,t)$ should be included in Eq. 2.30. Note , however, that this would induce significant noise contribution to the detector's thermal noise.

are easily associated with physical device parameters as

$$R_{\mathrm{g}} = \frac{m}{q^2 n_0 \tau_{\mathrm{p}}} \cdot \frac{1}{W} = \frac{1}{q n_0 \mu} \cdot \frac{1}{W} = \frac{1}{\sigma} \cdot \frac{1}{W} \tag{2.32}$$

$$L_{\mathrm{g}} = R_{\mathrm{g}} \tau_{\mathrm{p}} \tag{2.33}$$

$$C_{\mathrm{g}} = \frac{\varepsilon_0 \varepsilon}{d} W = q \frac{\partial n}{\partial V_{\mathrm{gs}}} W \tag{2.34}$$

with R_{g} being the resistance, L_{g} the inductance and C_{g} the capacitance per unit length of the distributed transmission line. Note that R_{g} takes the same form as in the quasi static limit Eq. (2.25). Note also that L_{g} can be neglected in a reduced RC model of the distributed resistive mixing regime (cp. Section 2.4.2) but must be included in a general description of the plasmonic mixing mechanism and accounts for the final inertia of charge carriers [44], [88] – it is therefore commonly referred to as *kinetic inductance*. In a similar manner as presented before for the fluid-dynamic model equations, Eqs. (2.30) and (2.31) can be transformed into a wave equation and the solutions again are propagating waves with a complex propagation constants [75, ch. 2]. A characteristic high frequency impedance of the transmission line can then be defined as

$$Z_{\mathrm{g}} = \sqrt{\frac{R_{\mathrm{g}} + i\omega L_{\mathrm{g}}}{i\omega C_{\mathrm{g}}}} \tag{2.35}$$

The ungated channel regions can be treated in the exact same manner as the gated regions with simply the gate capacitance omitted [46]. For our implementation of the TeraFET circuit model, the ungated resistance R_{ug} is obtained as a fit parameter from measurements of the detector's DC drain-source resistance (see Section 4.2.2). Note that the question whether a distributed or lumped circuit approach for the access regions should be employed is still the subject of ongoing research. It was pointed out that ungated plasmons can exist in the ungated channel parts, and interaction with gated plasmons under the FET's gate must be considered [11], [73], [89], [90]. The matter is not treated any further in this thesis.

One final remark should be made about the application of standard transmission line theory to describe the detection mechanism in TeraFET detectors. A crucial quantity for the efficiency of the detection with TeraFETs is the power, which is delivered to the intrinsic “active” detector region, i.e., the gated region of the channel where the non-linear plasma wave mixing takes place. In an ideal design, all power is dissipated in this gated region and the transmission line must be treated as lossy. This is a somewhat different situation than in the common textbook treatment of power distribution in transmission lines in most literature and should be paid special attention [43].

The transmission line equations of this section can be implemented in equivalent circuit simulation tools in order to analyze the high frequency behavior of the characteristic impedances, the power distribution in the device and eventually the detector response. The implementation is presented after the formulation of a comprehensive hydrodynamic transport model in Chapter 4.

Chapter 3

Hydrodynamic model

The fundamental equation governing transport phenomena in non-equilibrium thermodynamics is the *Boltzmann transport equation* (BTE). It describes the state of each particle in a thermodynamic ensemble in a six-dimensional phase space. Such an ensemble may well be the system of charge carriers in a semiconductor, hence, the BTE forms a basis for electronic transport models employed to describe charge carrier dynamics in electronic devices. The same fundamental BTE has long been known to form the basis of the description of fluid dynamic systems. Because of this analogy, the carrier transport in semiconductors can in many situation be treated by fluid dynamic equations, e.g., *Euler's equation* Eq. (2.1) introduced in Chapter 2. This section outlines the procedure to obtain a comprehensive formulation of a hydrodynamic transport model from the fundamental BTE by the so-called *method of moments*. Some details on the respective calculations discussed in this chapter are given in Appendix B.

3.1 The Boltzmann transport equation

Considering only classical mechanics and neglecting quantization effects, the BTE is merely another formulation of Newton's laws of motion to be fulfilled for every particle in the ensemble under investigation. The state of a particle can be altered by an external force field $F(\boldsymbol{r}, t)$ or by random scattering events. For the case of charge carriers in semiconductors and in the context of this thesis, the acting external force is the electric Coulomb force

$$\boldsymbol{F}(\boldsymbol{r}, t) = -q\boldsymbol{\mathcal{E}}(\boldsymbol{r}, t) \tag{3.1}$$

exerted on a charge carrier with elementary charge q by an externally applied electric field $E(\boldsymbol{r}, t)$. Various scattering mechanisms can in general be present, the most important ones are carrier-phonon scattering, carrier-carrier scattering and ionized impurity scattering. Rigorous treatment and discussion of scattering processes is far beyond the scope of this thesis, but can be found in the literature, e.g. in an elaborate discussion in Ref. [55] or in Refs. [54], [91].

In most realistic physical situations, the thermodynamic ensemble is usually formed by an enormous number of particles (e.g. the number of charge carriers in

a conventional semiconductor device > 10^{11} cm^{-1}) and it is often not practical to solve Newton's equations for each individual particle (although a variety of numerical methods exist today, to implement such calculations). Instead, one rather chooses a statistical approach for the problem: A distribution function $f(\boldsymbol{r}, \boldsymbol{p}, t)$ describing the probability density of finding a particle with momentum $\boldsymbol{p}$ at a given position $\boldsymbol{r}$ and at time t. Formulation and solution of the BTE then yields this distribution function.

The fundamental BTE for a particle ensemble in six-dimensional position-momentum $(\boldsymbol{r} - \boldsymbol{p})$ phase space[15] reads

$$\partial_t f + \boldsymbol{v} \cdot \nabla_{\boldsymbol{r}} f + \boldsymbol{F} \cdot \nabla_{\boldsymbol{p}} f = C\,[f] = -\frac{f - f_0}{\tau} \tag{3.2}$$

Here, $\boldsymbol{v}$ is the velocity and $C\,[f]$ is the so-called *collision operator*. In general this operator can take an extremely complex form accounting for the various types of scattering processes in the system. We limit ourselves in this work without proof to the so-called *relaxation time approximation*, where the operator simply describes a characteristic time τ it takes for an excited system with non-equilibrium distribution f to relax back to its equilibrium state f_0 by random collision events. Much deeper discussions on the collision operator, the relaxation time approximation and the mathematical properties of the BTE can be found in the literature (e.g., Refs. [54], [55]).

There are multiple ways of obtaining the BTE from basic considerations and a great count of literature on the topic exists – an incomplete list of valuable examples are Refs. [54], [55], [91]–[94]. Two intuitive ways which provide some insight into the meaning of the BTE are the derivations via unique phase space trajectories, or by formulating a balance equation for the conservation of the number of particles in a given phase space volume [55, ch. 2.3].

Note that while the BTE is a microscopic equation, one is commonly interested in the behavior of the entire ensemble rather than individual particles. The distribution function will thus serve to derive equations for averaged macroscopic physical quantities, e.g., particle density and particle current density. Since in this work we are concerned with the description of semiconductor FETs, in the following discussions the particles forming the ensemble will be charge carriers (electrons or holes), the force will be the Coulomb force according to Eq. (3.1), the particle density will be a two-dimensional charge carrier density n, and the particle current density will be the electric current density

$$\boldsymbol{j} = -qn\boldsymbol{v}_{\mathrm{d}} \tag{3.3}$$

with v_d the average drift component of the carrier velocity. In addition, we consider

[15] Note that in a more generalized form, a particle generation and recombination term can also be included on the RHS of the BTE.

a semi-classical parabolic band approximation[16] for the energy of the carriers

$$E(\boldsymbol{r}, \boldsymbol{k}) = \frac{\hbar^2 k^2}{2m} + E_\mathrm{c}(\boldsymbol{r}) \tag{3.4}$$

with m the effective mass of charge carriers and E_c the energy of the conduction band edge. The BTE can also be expressed in terms of the quasi-wavevector in $\boldsymbol{k}$-space ($\boldsymbol{k} = \boldsymbol{p}/\hbar$) and then reads

$$\frac{\partial f}{\partial t} + \boldsymbol{v} \cdot \nabla_{\boldsymbol{r}} f + \frac{\boldsymbol{F}}{\hbar} \cdot \nabla_{\boldsymbol{k}} f = -\frac{f - f_0}{\tau} \tag{3.5}$$

3.1.1 The distribution function

The distribution function $f(\boldsymbol{x}, \boldsymbol{k})$ in the BTE describes the probability density of finding a particle with quasi-wavevector $\boldsymbol{k}$ at position $\boldsymbol{r}$. Without giving a detailed derivation (see, e.g., [54]), from statistical considerations one finds that for fermionic particles, the equilibrium[17] distribution function takes the general form of a *Fermi-Dirac distribution*

$$f_0(\boldsymbol{r}, \boldsymbol{k}) = \frac{1}{e^{\frac{E(\boldsymbol{r},\boldsymbol{k}) - E_\mathrm{F}}{k_\mathrm{B} T_\mathrm{C}}} + 1} \tag{3.6}$$

Here, k_B is Boltzmann's constant, T_C is temperature, and E_F the Fermi energy. The energy $E(\boldsymbol{r}, \boldsymbol{k})$ is the carrier's energy after Eq.(3.4) divided into potential and kinetic energy. For energies larger than $E - E_\mathrm{F} \gg 3k_\mathrm{B}T_\mathrm{C}$ the Fermi-Dirac distribution can be approximated by a *Maxwell-Boltzmann* distribution (sometimes referred to as *Maxwellian*)

$$f_0(\boldsymbol{r}, \boldsymbol{k}) \approx \frac{1}{e^{\frac{E(\boldsymbol{r},\boldsymbol{k}) - E_\mathrm{F}}{k_\mathrm{B} T_\mathrm{C}}}} \tag{3.7}$$

Semiconductors with a carrier distribution described by Eq. (3.6) are called *degenerate*, while semiconductors described by Eq. (3.7) are called *non-degenerate*. For the FETs investigated in this thesis, the approximation applies only for a restricted regime of applied gate voltages close to and below the transistor's threshold. In the following derivations we therefore apply the full Fermi-Dirac statistic.

Since the energy in Eqs. (3.6) is $E \propto k^2$ the distribution function is symmetric about $\boldsymbol{k} = 0$ in equilibrium – the mean momentum or velocity of the carrier ensemble is thus zero. Application of an external force can drive the ensemble out of equilibrium. When the magnitude of the force is not too strong, the non-equilibrium distribution function can be approximated by a small perturbation of f_0. An often applied ansatz is to describe the perturbation as a small shift of f_0 in $\boldsymbol{k}$-space by a drift component so that $E(\boldsymbol{k}) \propto |\boldsymbol{k} - \boldsymbol{k}_\mathrm{d}|^2$ and

$$f = f_0 + f_1 = f_0 + \frac{\partial f_0}{\partial E} \boldsymbol{v}_\mathrm{d} \tag{3.8}$$

[16] The parabolic band approximation certainly does not apply to graphene as a truly two-dimensional material with linear energy dispersion relation $E(\boldsymbol{k}) = \hbar k v_\mathrm{F}$. Some implications for a device model are discussed in Chpater 7.

[17] i.e., no net current flow

with $\boldsymbol{v}_\mathrm{d} = \hbar \boldsymbol{k}_\mathrm{d}/m$ the drift velocity as in Eq. (3.3). The distribution function is then transformed into a so-called *displaced* Fermi-Dirac distribution

$$f(\boldsymbol{r}, \boldsymbol{k}) = \frac{1}{e^{\frac{\frac{\hbar^2 |\boldsymbol{k}-\boldsymbol{k}_\mathrm{d}|^2}{2m} + E_\mathrm{c}(\boldsymbol{r}) - E_\mathrm{F}}{k_\mathrm{B} T_\mathrm{C}}} + 1} \tag{3.9}$$

For reasons of simplified notation we introduce a scaled Fermi energy as $\epsilon_\mathrm{F} = (E_\mathrm{F} - E_\mathrm{c})/(k_B T_\mathrm{C})$ and in the following write the Fermi-Dirac distribution function as

$$f(\boldsymbol{r}, \boldsymbol{k}) = \frac{1}{e^{\frac{\hbar^2 |\boldsymbol{k}-\boldsymbol{k}_\mathrm{d}|^2}{2m k_B T_\mathrm{C}} - \epsilon_\mathrm{F}} + 1} \tag{3.10}$$

We conclude by showing that the parameter τ in Eq. (3.5) indeed has the meaning of a relaxation time constant. Considering only the temporal dependence of the distribution function, the BTE reduces to the ordinary differential equation

$$\partial_t f(t) = -\frac{f(t) - f_0}{\tau} \tag{3.11}$$

with solution

$$f(t) - f_0 = C e^{-\frac{t}{\tau}} \tag{3.12}$$

where the constant $C = f(0) - f_0$. The parameter τ therefore is a measure for the time it takes for a displaced distribution function $f = f_0 + f_1$, which has been shifted out of equilibrium by an external force, to relax back to the equilibrium f_0 by random scattering events.

3.1.2 The method of moments

The microscopic BTE Eq. (3.5) can be used to derive various macroscopic charge carrier transport models. A hierarchical classification of transport models can be found in Ref. [54]. Two model classes can be emphasized, i.e., diffusive and hydrodynamic models. These two classes are based on the assumption that scattering processes, in particular carrier-carrier collisions, become relevant. The carrier transport then exhibits collective behavior and the transport models are to a large extent analogous to fluid dynamic models.

Several methods exist to derive macroscopic transport models from the microscopic BTE [95], [96]. In this section we will introduce the probably most prominent method, the *method of moments*. To derive averaged quantities of interest from the distribution function, the latter is multiplied by appropriate weighting functions

$\Phi(\boldsymbol{k})$ and integrated over all possible states[18,19] k [95]

$$\langle \Phi(\boldsymbol{k}) \rangle = \frac{1}{2\pi^2} \int \Phi(\boldsymbol{k}) f(\boldsymbol{r}, \boldsymbol{k}) \,\mathrm{d}^2k \tag{3.13}$$

with the notation $\langle \cdot \rangle$ for averaged quantities.

Recall for the simplest case the basic meaning of the distribution function – it describes the probability of finding a particle with momentum $\boldsymbol{k}$ at a given position $\boldsymbol{r}$. Thus, integration over the probabilities for all possible states yields simply the carrier density

$$n = \frac{1}{2\pi^2} \int f \,\mathrm{d}^2k = \langle 1 \rangle \tag{3.14}$$

With this "definition", further meaningful averages can be evaluated, for example

$$v_\mathrm{d} = \frac{1}{n} \frac{1}{2\pi^2} \int \boldsymbol{v} f \,\mathrm{d}^2k = \frac{1}{n} \langle \boldsymbol{v} \rangle \tag{3.15}$$

$$nw = n \frac{1}{2\pi^2} \int \frac{\boldsymbol{p}\boldsymbol{v}}{2} f \,\mathrm{d}^2k = \left\langle \frac{\boldsymbol{p}\boldsymbol{v}}{2} \right\rangle = \langle E \rangle \tag{3.16}$$

the average (drift) velocity $\boldsymbol{v}_\mathrm{d}$ and the energy density nw. Rewriting in terms of quasi-wavevector with (3.4) we can rewrite to

$$n = \langle 1 \rangle = \left\langle \boldsymbol{k}^0 \right\rangle \tag{3.17}$$

$$v_\mathrm{d} = \frac{\hbar}{nm} \left\langle \boldsymbol{k}^1 \right\rangle \tag{3.18}$$

$$nw = n \frac{\hbar^2}{2m} \left\langle \boldsymbol{k}^2 \right\rangle \tag{3.19}$$

$$\tag{3.20}$$

Because of their order in quasi-wavevector (or momentum), Eqs. (3.17), (3.18), and (3.19) are called the *zeroth, first, and second moment* of f. In Appendix B.1, an explicit evaluation of some of the above quantities is given. Note that by multiplication of Eq. (3.18) with $-qn$ we also obtain a "density", namely a density of velocity, which is the definition for the electric current density $\boldsymbol{j} = -qn\boldsymbol{v}_\mathrm{d}$.

3.1.3 Balance equations

The underlying idea of the method of moments approach is to simplify the full BTE by considering only a limited number of moments to derive evolution (or balance) equations for the macroscopic quantities. The method of obtaining generalized balance

[18] Equation (3.13) in general must be formulated in three dimensions, however, since we discuss in this thesis the transport properties of 2DEGs in FETs, we limit our derivation to the two-dimensional case.

[19] The normalization factor in front of the integral is the number of possible states in a two-dimensional volume $\mathrm{vol}_\mathrm{2d} = 1/(2\pi)^2$in $\boldsymbol{k}$-space multiplied by factors $g_\mathrm{s} = 2$ and $g_\mathrm{v} = 1$, the spin and valley degeneracy for Wurtzite GaN. Note that for single-layer graphene $g_\mathrm{s} = g_\mathrm{v} = 2$.

equations from the BTE is explained in great detail in Ref. [55, ch. 5]. This section is loosely based on the same reference together with Refs. [54], [94], although following a slightly different sequence of derivation.

We discussed before that the description of carrier transport in our TeraFETs can be reduced to a one-dimensional treatment (see Section 2.2). Therefore, the spatial gradient in the BTE is replaced by a simple derivative with respect to the x-direction. The BTE Eq. (3.5) is multiplied by appropriate weighting functions $\Phi(\boldsymbol{k})$ as introduced before and then integrated over $\boldsymbol{k}$-space to yield the general form[20]

$$\frac{1}{2\pi^2}\int_0^\infty \Phi(k)\partial_t f\,\mathrm{d}^2k + \frac{1}{2\pi^2}\int_0^\infty \Phi(k)(v\partial_x f)\,\mathrm{d}^2k + \frac{1}{2\pi^2}\int_0^\infty \Phi(k)(\frac{F}{\hbar}\partial_{\boldsymbol{k}} f)\,\mathrm{d}^2k = -\frac{1}{2\pi^2}\int_0^\infty \Phi(k)\frac{f-f_0}{\tau_\Phi}\,\mathrm{d}^2k \tag{3.21}$$

Note that the integration still has to be performed over two-dimensions in $\boldsymbol{k}$-space, since we are considering 2DEGs in FETs. The explicit calculations of some of the above terms is shown in Appendix B.1. A thorough mathematical discussion is far beyond the scope of this work but can be found in the respective literature, e.g., in Refs. [54], [55], [84], [94]. Note also that we have introduced here the subscript τ_Φ for the relaxation time, since scattering in each individual balance equation is determined by the respective scattering mechanism corresponding to the applied moment - e.g., momentum scattering τ_p for $\Phi = \boldsymbol{p}$ and energy scattering τ_e for $\Phi = E$.

3.2 Transport models

We discussed above the procedure to obtain balance equations for avaraged quantities from the BTE. A generalized balance equation Eq. (3.21) was formulated. We now show the deduction of a hydrodynamic model following the method of moments. For reasons of completeness, we will first show the derivation of the so-called *drift-diffusion model*, which is, however, not sufficient for our purpose of describing the detection mechanisms in TeraFET detectors. We will thus discuss the respective limitations and motivate the extension of the diffusive model to a *hydrodynamic transport model*.

3.2.1 Charge continuity equation

The most simple balance equation is obtained by employing the zeroth order moment $\Phi = 1$ in Eq. (3.21). Following the evaluation of the individual terms in Eq. (3.21) presented in Appendix B.2.1, the *charge continuity equation* is derived

$$q\partial_t n = \partial_x j \tag{3.22}$$

[20]Note that the integration in principle has to be over the Brillouin zone as in the previous sections. Since the magnitude of the distribution function decreases rapidly for higher momentum $f \propto \exp(-k^2)$, the integration can be extended to infinity [55].

which can alternatively be deduced from Maxwell's equations directly [94]. The continuity equation alone, however, does not constitute a model for charge transport but merely reflects conservation of charge when no carrier generation or recombination is allowed. To derive a full transport model, weight functions at least up to the first order in k must be applied to the BTE.

3.2.2 The drift-diffusion model

The *drift-diffusion* model is the simplest charge carrier transport model that can be obtained from the BTE [95]. In order to derive the drift-diffusion equation in its established form, the weighting function $\Phi = \boldsymbol{p}$ is employed in Eq. (3.21). The result is an equation for the density of carrier flux, i.e., the current density. For the calculation, a steady-state situation is assumed [55, ch. 5], where the time derivative of f vanishes. A list of further assumptions can be found in Ref. [94, ch. 2.3]. Again, evaluation of the individual terms is given in Appendix B.2.2. The drift-diffusion equation for the current density is derived as

$$j = qn\mu\mathcal{E} + \mu k_{\mathrm{B}}\partial_x \left(nT_{\mathrm{C}}\right) \tag{3.23}$$

In its original form, the model was first proposed by v. Roosbroeck in 1950 [97]. In the same work, the two main assumptions for the validity of the model are summarized. On one hand, it is assumed that frequent collisions of carriers lead to a time independence of the drift current on a timescale of the relaxation time – hence, the steady-state assumption. Second, "high fields [...] for which the carriers are not substantially in thermal equilibrium with the lattice are ruled out" [97, p. 569]. The latter assumption in particular states, that the temperature in Eq. (3.6) is equal to the lattice temperature and $T_{\mathrm{C}} = T_{\mathrm{L}}$ [81]. Evaluation of the average carrier energy in two dimensions (see Appendix B.1.3) leads to the well-known result from the equipartition theorem[21]

$$\langle E\rangle = nw = nk_{\mathrm{B}}T_{\mathrm{L}} \tag{3.24}$$

for a Fermi-Dirac distribution function, where the drift component of the energy density is commonly neglected in the drift-diffusion formalism [55], [95]. Equation Eq. (3.23) can then be expressed in the form commonly found in the literature

$$j = qn\mu\mathcal{E} + qD\partial_x n \tag{3.25}$$

The two introduced quantities $\mu = q\tau_{\mathrm{p}}/m$ and $D = \mu k_{\mathrm{B}}T_{\mathrm{L}}/q$ are called the *carrier mobility* (cp. Eq. (2.26))) and *carrier diffusivity*, respectively. In this original form, the basis of the drift-diffusion model becomes apparent - the current density is the sum of a drift component due to an electric force term and a diffusion component associated with a gradient in charge carrier density. The model is completed by the charge continuity equation as well as Poisson's equation for the electrostatic potential [94].

A number of rather stringent assumptions were made during the derivation of the drift-diffusion equation [94, ch. 2.3]. Formally it can be shown that the model

[21] in two dimensions

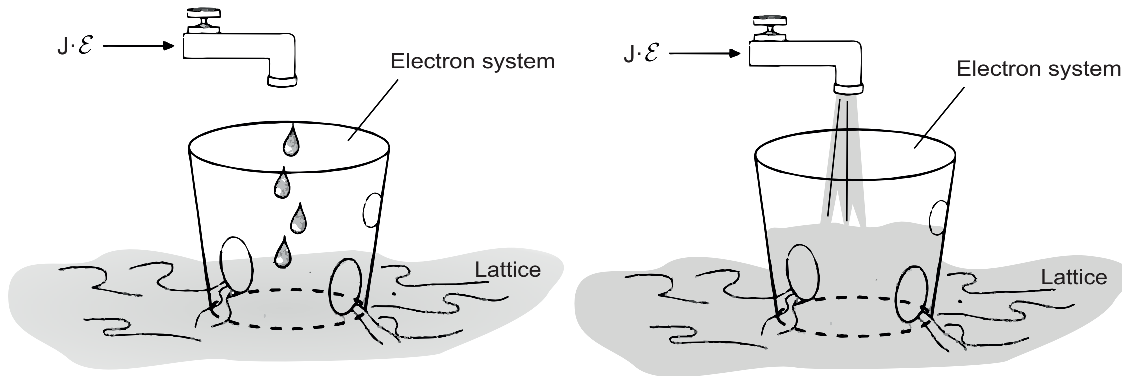

Fig. 3.1: Bucket analogy for hot carriers, from Ref. [55, p. 284].

is valid in situations where a characteristic device length (e.g., the dimensions of a semiconductor) is much larger than the mean free path a particle can travel on average before undergoing a scattering event. Also, in particular the relaxation time approximation is based on a low-field assumption, i.e., small applied voltages. For typical semiconductors, the constraints are device dimensions of roughly 1 µm and voltages smaller than 1 V. Nevertheless, the model has long been successfully applied for the simulation of real electronic devices, even in situations not strictly satisfying the approximations [54], [95]. Several empirical extensions of the drift-diffusion equation as well as in-depth discussions can be found in the literature – some overview of references is given in Ref. [54, ch. 5.1].

3.2.3 Hot carriers

In the context of this work, probably the most profound restriction of the drift-diffusion model in the form of Eq. (3.25) is the assumption that the charge carrier system is in thermal equilibrium with the crystal lattice and the diffusion component is determined solely by a spatial gradient of the carrier density. This is commonly termed a *low-field* situation [55]. In this case the average kinetic energy is given by Eq. (3.24). However, under conditions of high fields and/ or where the exchange of energy between the carrier ensemble and the lattice is too slow to follow the excitations of an externally applied field, the carrier temperature can be significantly elevated above the constant lattice temperature. In more detail: “An effective temperature T_C is always established in an electronic ensemble [...] when the electron-electron [...] interaction dominates over both phonon and impurity scattering” [82, p. 387]. The carrier temperature then depends on the electric field $\mathcal{E}$ from which the carriers gain their additional energy and the average kinetic energy becomes

$$\langle E \rangle = n k_\mathrm{B} T_\mathrm{C}(\mathcal{E}) \tag{3.26}$$

This effect of an elevated temperature of the carrier ensemble with respect to the temperature of the crystal lattice is referred to as the *hot carrier effect* [81].

A nice illustration of the build-up of a heated carrier distribution is the *leaking water bucket analogy* from Ref. [55], which is depicted in Fig. 3.1. The electronic

system is represented by the water inside the bucket and the average energy $k_B T_C$ of carriers is reflected by the water level. The water puddle outside the bucket at ground level represents the crystal lattice at temperature T_L. The electric field strength in the analogy correlates to the amount of water flowing out the faucet and the size of the holes in the bucket correlates to the ratio of relaxation times τ_p/τ_e. In the low field - i.e., dripping faucet - situation on the left, carriers gain only limited energy, which on average relaxes to the lattice temperature before a significant electronic temperature above T_L can establish. Water flows out of the bucket as fast as it flows in and the bucket remains, on average, empty. On the other hand, when the size of the openings in the bucket is small and the water jet is strong - analogous to small τ_p and high fields - water cannot flow out of the bucket fast enough and rises to a certain level inside the bucket until a steady-state situation of no net energy flow is reached. Energy is distributed amongst carriers rather than exchanged with the lattice and an electronic temperature $T_C > T_L$ establishes.

A closer look on Eq. (3.23) reveals that is it the gradient in average kinetic energy density w, which can lead to carrier diffusion [55]. In general, the spatial energy density variation can be due to a local variations of the carrier density and a of carrier temperature, respectively, when $T_C \neq T_L$ in Eq. (3.6)[22] and (3.24). Equation (3.23) in the general case then reads

$$j = qn\mu\mathcal{E} + qD\partial_x n + qnD_T\partial_x T_C \tag{3.27}$$

where a *thermal diffusivity* $D_T = \mu k_B/q$ is introduced. A similar result (see Appendix B.3 was obtained by Stratton in a more detailed analysis[98].

It remains to find a way to explicitly calculate the local carrier temperature T_C to be inserted into Eq. (3.27). Extensions of the drift-diffusion formalism are, e.g., empirical extension by allowing the mobility and diffusion coefficient to be dependent on the local fields [81], [99] or the formulation of a *local energy balance equation* [95]. Energy transsport models can be derived by including the next higher order moment of the BTE [54, ch. 6]. Recall that another strong approximation in the above derivation was the assumption of a steady-state situation for the current density ignoring transient effects and convective currents are not included in the drift-diffusion model. A more generalized set of macroscopic balance equations can be derived from the BTE by taking the next higher order weighting function for the carrier kinetic energy into account $\Phi = E = \boldsymbol{pv}/2$ and retaining transient and convective currents. The resulting model is then called a *hydrodynamic transport model* [54] and will be discussed in the next section.[23]

[22] The respective distribution function with carrier temperature $T_C \neq T_L$ is accordingly called a heated Fermi-Dirac distribution, which is - loosely speaking - a smeared out variant of the Fermi-Dirac distribution with $T_C = T_L$ (see, e.g., [55, ch. 5]).

[23] Precisely, the „class“ of transport models – diffusive or hydrodynamic – is determined by scaling of the initial BTE, e.g., with the so-called Knudsen number. The choice of scaling depends on the detailed form of the collision operators in equilibrium [54, ch. 2.1]. An in-depth discussion is beyond the scope of this work.

3.2.4 The hydrodynamic transport model

In Chapter 2, a theory for the mechanism of plasmonic rectification of HF signals in FETs was presented. The discussion was based on a reduced hydrodynamic transport model describing the charge carrier transport in the transistor. The model is reduced in the sense that diffusive currents induced by local variations of the carrier kinetic energy density - due to variations in carrier density or carrier temperature, as discussed above - are neglected and $\partial_x(nT_\mathrm{C}) = 0$. Such models are sometimes referred to as *isothermal* [54, p. 202]. Recent experiments, however, indicate that diffusion must in general be accounted for in the description of THz detection with TeraFETs (see Chapter 7 and Refs. [30], [32]).

A full hydrodynamic transport model extends the drift-diffusion approach by accounting for three major aspects – the non-stationary behavior of the current density, a flux equation for the energy densisty, and a convective current contribution. Two popular approaches of derivation of higher order transport equations were performed by Stratton [81] and by Bløtekjær [100] leading to almost comparable models although based on different assumptions. An evaluation of the two models cannot be given easily, since in practice, both models are used for device simulation and can yield accurate results depending on the exact situation under consideration. The fact that the carrier mobility as well as the relaxation times show up as material parameters can “cloud” the underlying differences of the models [55] and must be investigated in detailed analysis – a deeper discussion of the validity of the various transport models in bulk semiconductor or real device situations can be found in the literature, in particular in Refs. [54], [55], [84]. In this work, we limit ourselves to the derivation of the transport equations following Bløtekjær’s approach [100].

The general procedure of obtaining balance equations from the BTE has been demonstrated in the previous section. To formulate an extended transport model including a balance equation for the local energy density, the method of moments is applied to the BTE with weighting functions $\Phi = 1$, $\Phi = \boldsymbol{p}$, and $\Phi = E$. An individual macroscopic relaxation time in the relaxation time approximation is associated with each moment equation. Again, the zeroth order weighting function yields the standard continuity equation for charge carriers Eq. (3.22).

The weighting function $\Phi = \boldsymbol{p}$ is applied following the procedure in Section 3.1.3. In contrast to the drift-diffusion approach, the time-dependent term is not neglected, therefore, the restriction of a slowly varying current with respect to the relaxation time is dropped. Also, the kinetic energy density is more generally expressed as [55], [101]

$$\langle E \rangle = nw = \frac{1}{2} mnv_\mathrm{d}^2 + nk_\mathrm{B}T_\mathrm{C} \tag{3.28}$$

i.e, as the sum of an average drift component as well as random *thermal* motion as derived in Appendix B.1.3.[24]

Finally, the second order weighting function $\Phi = \hbar^2 k^2/2m$ is applied to the BTE to yield a continuity equation for the kinetic energy density. The procedure is outlined in Appendix B.2.3. The resulting set of balance equations then forms the

[24]Recall that the drift component of the energy density was neglected in the derivation of the drift-diffusion model.

so-called *hydrodynamic transport model*, which can be formulated in terms of the current density as [54, p. 201]

$$\partial_t n = \frac{1}{q}\partial_x j \tag{3.29}$$

$$j = qn\mu\mathcal{E} + \frac{\tau_\mathrm{p}}{q}\partial_x\left(\frac{j^2}{n}\right) + \mu k_\mathrm{B}\partial_x(nT_\mathrm{C}) - \tau_\mathrm{p}\partial_t j \tag{3.30}$$

$$\partial_t(nw) = \frac{1}{q}\partial_x\left[j\left(w + k_\mathrm{B}T_\mathrm{C}\right)\right] + j\mathcal{E} - \frac{n(w - k_\mathrm{B}T_\mathrm{L})}{\tau_\mathrm{e}} \tag{3.31}$$

together with the kinetic energy

$$w = \frac{m}{2q^2}\frac{j^2}{n^2} + k_\mathrm{B}T_\mathrm{C} = \frac{1}{2}mv_\mathrm{d}^2 + k_\mathrm{B}T_\mathrm{C} \tag{3.32}$$

Note that we have omitted here the Fermi integrals, which were obtained during the derivation of the model employing a Fermi-Dirac distribution function. For the operation of semiconductor TeraFETs close to the threshold, where usually the highest detection sensitivity is observed, the assumption of non-degeneracy commonly holds and a Maxwell-Boltzmann distribution function applies. It should be kept in mind, however, that operation at gate bias voltages high above the threshold may require Fermi-Dirac statistics. The thermal energy terms in Eqs. (3.29)-(3.32) must then be replaced by

$$k_\mathrm{B}T_\mathrm{C} \rightarrow k_B T_\mathrm{C}\frac{\mathcal{F}_1(\epsilon_\mathrm{F})}{\mathcal{F}_0(\epsilon_\mathrm{F})} \tag{3.33}$$

This is up until this stage not implemented in the device model presented in the next chapter.

The presented derivation of the hydrodynamic transport model was based on a rather "ruthless" application of the method of moments to the BTE. At various stages, implicit assumptions or simplifications on mathematical or argumentative procedures were employed to keep the presentation on a comprehensible level. There exists a multitude of literature on the topic going into details far beyond the scope of this work. In particular, note that the method of moments produces equations which themselves depend on the respective next higher moment, thus, the system of equations is always underdetermined and has to be complemented by appropriate *closure relations*. The validity of commonly applied closure relations is still subject to ongoing research and discussions [54], [102], especially with regard to increasing complexity and decreasing dimensions of today's semiconductor devices. A valuable starting point for a list of further in-depth literature on the topic of transport models in general and their formal derivation are Refs. [54], [55], [84], [94], [95].

3.3 Comparison of the Dyakonov-Shur and the hydrodynamic transport model

The hydrodynamic transport model in it's current density formulation helps to elucidate the individual contributions to the total current density in the transport

Eq. (3.30), which can be understood as the sum of a drift, convection and diffusion current density

$$j = \underbrace{qn\mu\mathcal{E}}_{j_{\text{drift}}} + \underbrace{\frac{\tau_{\text{p}}}{q}\partial_x\left(\frac{j^2}{n}\right) - \tau_{\text{p}}\partial_t j}_{j_{\text{conv}}} + \underbrace{\mu k_{\text{B}}\partial_x(nT_{\text{C}})}_{j_{\text{diff}}} \tag{3.34}$$

In order to confirm that the hydrodynamic equations indeed present an extension of the fluid dynamic transport model by diffusive (pressure) terms, we compare the above current density formulation of the transport equation to the velocity formulation from Eqs. (2.1) and (2.2). A listing of the individual terms is given in Table 3.1.

Table 3.1: Comparison of constituent current densities in fluid-dynamic transport model in velocity formulation and hydrodynamic model in current density formulation.

Term	HTM	DS	Transformation
Drift current density	$j_{\text{drift}} = qn\mu\mathcal{E}$	$-\frac{q}{m}\partial_x\phi + \frac{v}{\tau_{\text{p}}}$	$\mathcal{E} = -\partial_x\phi, j = -qnv$
Convection current density	$j_{\text{conv}} = \frac{\tau_{\text{p}}}{q}\partial_x\left(\frac{j^2}{n}\right) - \tau_{\text{p}}\partial_t j$	$\partial_t v + v\partial_x v$	$j = -qnv, \cdot\frac{-1}{qn\tau_{\text{p}}},$ $\partial_t n = -\partial_x(nv)$
Diffusion current density	$j_{\text{diff}} = \mu k_{\text{B}}\partial_x(nT_{\text{C}})$	$\left(\frac{k_{\text{B}}}{mn}\partial_x(nT_{\text{C}})\right)$	$\mu = \frac{q\tau_{\text{p}}}{m}, \cdot\frac{-1}{qn\tau_{\text{p}}}$

The continuity equation Eq. (2.2) is readily transformed into Eq. (3.29) via multiplication by $-q$. The current density equation Eq. (3.30) is translated into Euler's equation Eq. (2.1) by expanding partial derivatives with the help of the product rule, replacing the current density $j = -qnv$, using the definition of carrier mobility Eq. (2.26) and electrostatic potential $\mathcal{E} = -\partial_x\phi$, and by application of the continuity equation Eq. (3.29). The formulation of the hydrodynamic transport model in terms of carrier velocity is given in Appendix B.2.3 and indeed shows that the difference between the two transport models - the fluid-dynamic and the hydrodynamic model - is an additive term $(k_{\text{B}}/mn)\partial_x(nT_{\text{C}})$ accounting for the gradient in carrier density and temperature, the latter giving rise to the thermoelectric signal contributions observed in recent TeraFET detection experiments.

The current formulation of the model can directly by implemented in a circuit simulation software, which is commonly set up to deal with nodal voltages and currents rather than carrier density and velocity. The current $I = I_{\text{drift}} + I_{\text{diff}} + I_{\text{conv}}$ through the device is analogously calculated as the sum of drift, diffusion, and convection current and multiplication of the individual current densities in Eq. (3.34)

by the channel width W. A respective device model was implemented in the course of this work to allow for a simulation of the THz with TeraFETs on a device level. The next chapter presents some specific details about the implementation of the detector model in the circuit simulation software.

Chapter 4

Circuit model implementation

The hydrodynamic model, which was developed in the previous chapter, was presented in a current density formalism. The model equations can therefore directly be implemented in a circuit simulation environment. We chose the commercial simulation tool Keysight Advanced Design System (ADS), since it offers the possibility to implement user defined non-linear circuit elements via the definition of port equations for current and voltage. The detector model was implemented in the distributed transmission line approach as introduced in Section 2.6.

DC simulations are performed to obtain static device drain-source resistances. Internally, the circuit solves forms a set of algebraic differential model equations, which are solved under certain assumptions, in particular, neglecting of time derivatives, replacing complex impedances by real conductances and treating capacitances and inductances as open and short circuits, respectively [51].

Simulation of the high frequency response of the TeraFET equivalent circuits is performed as so-called *harmonic balance analysis*. The solver calculates input and output currents and voltages of linear circuit elements in the frequency domain, while nonlinear elements are sampled in time domain and then transformed to frequency domain by Fourier analysis. Solution of the algebraic equations is based on the assumption that a steady-state solution exists, which can be approximated by truncated Fourier series. Hence, the solution does not represent transient-behavior of the circuit [51]. In our simulations, calculations were performed for a single fundamental tone of the excitation signal at ω as higher harmonics were found to be negligible. The TeraFET detector signal is read out as DC current or voltage from the simulation.

This chapter presents some of the details of the implementation of the hydrodynamic model for the intrinsic (gated) and ungated channel region. Simulations results are verified by comparison to analytic calculations based on equations presented in Chapter 2. For real TeraFET device analysis, the subsequent chapter presents simulations results for a full device model, where the intrinsic channel is then embedded in an equivalent circuit including ungated access regions as well as extrinsic components such as port S-Parameters of the integrated antennas.

4.1 The intrinsic distributed channel

A hydrodynamic description applies for the carrier dynamics in the channel of an FET when the mean free path of carriers with respect to carrier-carrier collisions is significantly smaller than the channel length. Carriers then experience multiple collisions in the device and excess energy is distributed within the electronic subsystem – the carrier ensemble exhibits collective behavior. This is the basis for the fluid-dynamic description of the underlying transport mechanisms in TeraFETs. It was discussed above, that such transport models can be described analogously by a distributed equivalent circuit model, namely a transmission line of RCL unit cells described by the telegrapher's equations Eqs. (2.30) and (2.31). For the intrinsic channel, results from numerical simulations can directly be compared to the analytic expressions discussed in Chapter 2, in particular, the plasmonic enhancement factor $f(\omega)$ described in Section 2.4.3 is reproduced to validate the equivalent circuit implementation of the plasmonic mixing mechanism.

In the circuit simulation software ADS, we choose so-called *Symbolically Defined Devices* (SDDs), which allow to explicitly state symbolic non-linear equations for either current or voltage to represent the resistance, inductance, and capacitance per unit length according to Eqs. (2.32), (2.33), and(2.34), respectively. SDDs can be defined with multiple ports allowing for multiple current branches for multi-terminal devices, e.g., for a three-terminal FET. In particular, unconnected open ports can be used to calculate auxiliary quantities by defining pseudo-voltages – not necessarily representing actual voltages in terms of physical units - which can then be referenced in the "real" port equations. We make use of this "workaround", e.g., in the calculation of the local electronic temperature depending on the gate-to-channel potential in each SDD element.

Figure 4.1 at the top shows an equivalent circuit representation of two RCL unit cells of the transmission line model of the gated FET's gated channel region. In the same figure at the bottom, the corresponding schematic of the implementation of the transmission line model by SDD elements is depicted. The internal resistance, capacitance and inductance of the i'th RCL unit cell are denoted by R_i, C_i, and L_i, respectively. The internal currents I_1 and I_2 and internal voltages V_1 and V_2 of the unit cell are defined by the respective port current equations in the simulation environment, where the polarity is denoted by the "+" and "-" signs in the schematics. The equations presented in this section for the intrinsic gated channel region are easily modified for the ungated access regions on the source and drain side of the channel. For the ungated regions of the channel, the gate contact is simply removed and the same distributed SDD element implementation can be used with $I_2 = 0$.

4.1.1 Gate capacitance

The SDD port 2 represents the charge density controlling functionality of the FET's gate metal layer. The local capacitance per unit length is given by the time derivative of the local total charge Q in the FET's inversion layer

$$Q = qnW\Delta x \tag{4.1}$$

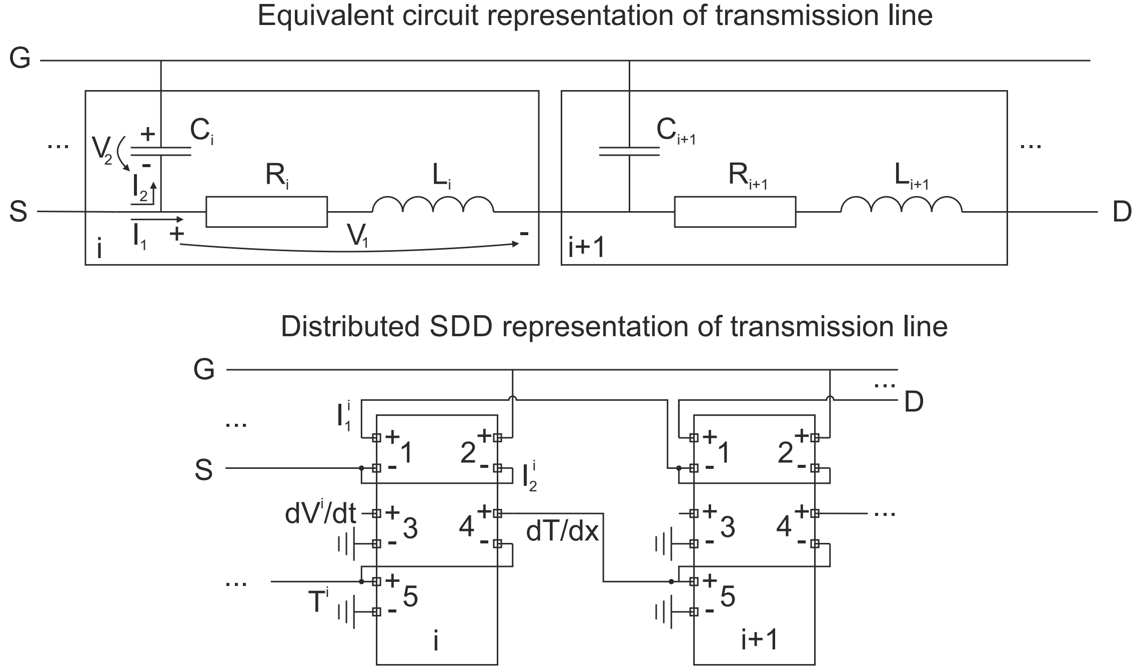

Fig. 4.1: Top: Extract from equivalent circuit representation of the FET's gated channel region. The subscripts of the internal currents and voltages represent the port numbers of the respective SDD element. Bottom: Extract from SDD representation of the transmission line model.

Here, $\Delta x = L_\mathrm{g}/N$ is the length interval separating the total gated channel length L_g into N unit cells. The charge carrier density is a function of the local gate-to-channel voltage

$$n = n(V_2(t)) \tag{4.2}$$

where the gate-to-channel voltage itself is modulated with the frequency of the incoming radiation at the gate terminal. Explicit calculation of n is based on a unified charge control model (UCCM [103]) modified by a voltage dependent non-ideality factor. For further discussion, see Section 4.2.2 on device parameter extraction. In total, the port equation for SDD port 2 therefore becomes

$$\begin{aligned} I_2 = \partial_t Q &= qW\Delta x \partial_t n \\ &= qW\Delta x \frac{\partial n}{\partial V_2} \partial_t V_2 \end{aligned} \tag{4.3}$$

A grounded "dummy" port (here no. 3) is used to define an internal "voltage" $V_3 = \partial_t V_2$, which can be referenced in the current equations of the other ports. Time derivatives of internal currents or voltages are already implemented in the ADS circuit simulation environment when using harmonic balance analysis. They can directly be employed in the symbolic equations of SDD circuit elements and are internally calculated in frequency domain via weighting of nodal currents or voltages by a factor $i\omega$. The local derivative $\partial n/\partial V_2$ can be derived in analytical form from Eq. (4.2).

4.1.2 Drift current

The current I_1 of SDD port 1 represents the current flowing in the channel from source to drain contact. The total current can be split into the individual current contributions as discussed above (comp. Eq. (3.34) and Table 3.1):

$$I_1 = I_{\text{drift}} + I_{\text{conv}} + I_{\text{diff}} \tag{4.4}$$

The drift current contribution is represented by the ohmic resistance R_i in the RCL equivalent circuit (Fig. 4.1). In the current density formulation it is given by

$$I_{\text{drift}} = j_{\text{drift}} W = qn\mu\mathcal{E}W \tag{4.5}$$

The carrier density $n(V_2)$ is calculated according to Eq. (4.2) (explicit form given in Section 4.2.2) and the local longitudinal electric field $\mathcal{E}$ in the channel is given as the negative spatial gradient of the local gate-to-channel potential ϕ. In the distributed SDD circuit, the latter is calculated from the intrinsic SDD voltage V_1 at port 1 divided by the spatial interval Δx

$$\mathcal{E} = -\partial_x \phi \approx \frac{-\Delta V_2}{\Delta x} = -\frac{V_1}{\Delta x} \tag{4.6}$$

where N is again the total number of unit cells employed in the discretization of the channel. Note that we use here that the internal voltage V_1^i of the i'th SDD element already represents a local differential voltage $\Delta V_2 = V_2^{i+1} - V_2^i$ of the gate-to-channel voltage of two successive SDD elements i and $i+1$. For infinitesimal Δx as the number of distributed elements is increased, the difference quotient in Eq. (4.6) approximates a spatial derivative.

4.1.3 Convection current

Convective current contributions become important for increasing frequencies as $\omega\tau_{\text{p}} \gg 1$ as discussed in Section 2.4.3. A full plasmonic description of the channel requires the introduction of a kinetic inductance L_i in the transmission line's unit cells [44]. In the hydrodynamic transport picture, the time and spatial derivative of current density in Eq. (3.30), or of drift velocity in the fluid dynamic description Eq. (2.1), respectively, must be accounted for in the distributed equivalent circuit representation. The convective current is given by ((comp. Eq. (3.34) and Table 3.1):

$$\begin{aligned} I_{\text{conv}} = j_{\text{conv}} W &= \left[\frac{\tau_{\text{p}}}{q} \partial_x \left(\frac{j^2}{n} \right) - \tau_{\text{p}} \partial_t j \right] W \\ &= 2W \frac{\tau_{\text{p}}}{q} \frac{j}{n} \partial_x j - W \frac{\tau_{\text{p}}}{q} \frac{j^2}{n^2} \partial_x n - \tau_{\text{p}} W \partial_t j \end{aligned} \tag{4.7}$$

Application of the charge continuity equation Eq. (55) to the first term on the RHS yields

$$\begin{aligned} 2W \frac{\tau_{\text{p}}}{q} \frac{j}{n} \partial_x j &= 2W \tau_{\text{p}} \frac{j}{n} \partial_t n \\ &= 2W \tau_{\text{p}} \frac{j}{n} \frac{\partial n}{\partial V_2} \partial_t V_2 \end{aligned} \tag{4.8}$$

Again, $\partial n / \partial V_2$ is evaluated in analytic form and the time derivative is calculated by direct implementation in the circuit solver.

In the second term on the RHS of Eq. (4.7) we expand the spatial derivative of n to find

$$\begin{aligned} W \frac{\tau_\mathrm{p}}{q} \frac{j^2}{n^2} \partial_x n &= W \frac{\tau_\mathrm{p}}{q} \frac{j^2}{n^2} \frac{\partial n}{\partial V_2} \partial_x V_2 \\ &= -W \frac{\tau_\mathrm{p}}{q} \frac{j^2}{n^2} \frac{\partial n}{\partial V_2} \mathcal{E} \end{aligned} \tag{4.9}$$

where we have used the definition of the longitudinal electric field Eq. (4.6).

4.1.4 Diffusion current

A comprehensive hydrodynamic model includes diffusive currents due to gradients in the local pressure (nT_C) of the 2DEG. The diffusive currents can again be separated into two contributions accounting for variations in the local carrier density n and the temperature of the carrier ensemble T_C, respectively:

$$\begin{aligned} I_\mathrm{diff} = j_\mathrm{diff} W &= \mu k_\mathrm{B} W \partial_x \left(n T_\mathrm{C} \right) \\ &= \left(\mu k_\mathrm{B} n \partial_x T_\mathrm{C} + \mu k_\mathrm{B} T_\mathrm{C} \partial_x n \right) W \\ &= (\mu k_\mathrm{B} n \partial_x T_\mathrm{C} + \mu k_\mathrm{B} T_\mathrm{C} \frac{\partial n}{\partial V_2} \mathcal{E}) W \end{aligned} \tag{4.10}$$

The spatial derivative in the second term on the RHS is expanded as before in Eq. (4.9) and is thus proportional to the local electric field $\mathcal{E}$ in the channel. The spatial gradient of the carrier temperature T_C is obtained by recursively feeding T_C^{i+1} back to element i, which is realized by the interconnect of ports (here: 5 and 4) of two successive SDD elements as shown in the bottom scheme in Fig. 4.1.

4.1.5 Carrier temperature

As discussed in Section 3.2.3, when carriers are excited by an external electric field and their excess energy is distributed by carrier carrier scattering within the electronic system instead of dissipated by electron phonon scattering to the crystal lattice, an elevated electronic temperature $T_\mathrm{C} > T_\mathrm{L}$ can establish. Time and spatial evolution of the energy density is in principle described by the energy density balance equation Eq. (3.31) in the hydrodynamic transport model. For our implementation we apply a number of simplifications, which are commonly used for the equation, to implement a carrier temperature in the circuit model.

We assume so-called *diffusive scaling* [54, ch. 2.1] of the energy equation Eq. (3.31) and neglect time evolution of the average carrier energy density nw considering only a steady-state situation. Furthermore, the the drift velocity component of the carrier energy Eq. (3.32) is assumed to be small against the thermal energy and $w = k_\mathrm{B} T_\mathrm{C}$ so that [95]

$$w \approx k_\mathrm{B} T_\mathrm{C} \tag{4.11}$$

In total, the energy density equation Eq. (3.31) is reduced to

$$j \mathcal{E} = \frac{n k_\mathrm{B}}{\tau_\mathrm{e}} \left(T_\mathrm{C} - T_\mathrm{L} \right) \tag{4.12}$$

Replacing the electric field via $j = \sigma\mathcal{E}$ with the static conductivity $\sigma = qn\mu = q^2 n\tau_\mathrm{p}/m$ we calculate from Eq. (4.12) the local carrier temperature is as

$$T_\mathrm{C} = \frac{mj^2}{q^2 n^2 k_\mathrm{B}} \frac{\tau_\mathrm{e}}{\tau_\mathrm{p}} + T_\mathrm{L} = \frac{\tau_\mathrm{e}\tau_\mathrm{p} q^2 \mathcal{E}^2}{m k_\mathrm{B}} + T_\mathrm{L} \tag{4.13}$$

The derived expression for carrier temperature T_C - as expected - contains the ratio of energy and momentum scattering time, reflecting the efficiency of carrier heating. The second representation elucidates the dependence of T_C on electric field energy. A hydrodynamic model with this simplified approach for the energy density equation is sometimes referred to as *energy transport model* [54]. Notice, however, that our model implementation contains convective currents, which are commonly neglected in energy transport models[95], and we apply the diffusive scaling only to the energy density equation.

4.2 Verification of the model implementation

Before extending the circuit model to a real device situation including extrinsic detector parts we cross-verified simulation results with analytical calculation based on the fluid dynamic model presented in Chapter 2. In particular, we compare calculations of the intrinsic[25] DC resistance, high frequency impedance and the plasmonic enhancement factor $f(\omega)$. The implemented transmission line circuit model depends on a number of device parameters which can be extracted from measurements of the TeraFETs DC drain-source resistance. These parameters are then used in analytic calculations and numerical simulations with the circuit implementation of the TeraFET model. Some details on the experimental acquisition of the DC data are presented in Section 6.2.1. As a test bed for the verification, we choose device parameters of one particular AlGaN/GaN HEMT which was fabricated in the course of this work - more details on the respective device are given in Section 6.3.2.

4.2.1 Charge control model

The most important feature of an FET is the control of the channel conductance by modulation of the carrier concentration of its inversion layer by an applied gate-to-channel potential or voltage. In Appendix B.1.1 we calculated an explicit form for the carrier density in the 2DEG of a semiconductor FET (comp. Eq. (B.10) in Appendix B.1.1) and found the functional dependence

$$n(E_\mathrm{F}) = \frac{m k_B T}{\pi \hbar^2} \ln\left(1 + e^{\frac{E_\mathrm{F} - E_\mathrm{c}}{k_B T}}\right) \tag{4.14}$$

on the Fermi energy. On the other hand, the carrier density is controlled by an applied gate voltage with respect to the transistors threshold voltage $V_\mathrm{G} - V_\mathrm{th}$. To formulate a charge control model, the precise relation of $V_\mathrm{G} - V_\mathrm{th}$ and $E_\mathrm{F} - E_\mathrm{c}/(k_B T)$ would

[25] "intrinsic" in the same sense as introduced before, i.e., implementing only the gated region of the FET's channel in the circuit model.

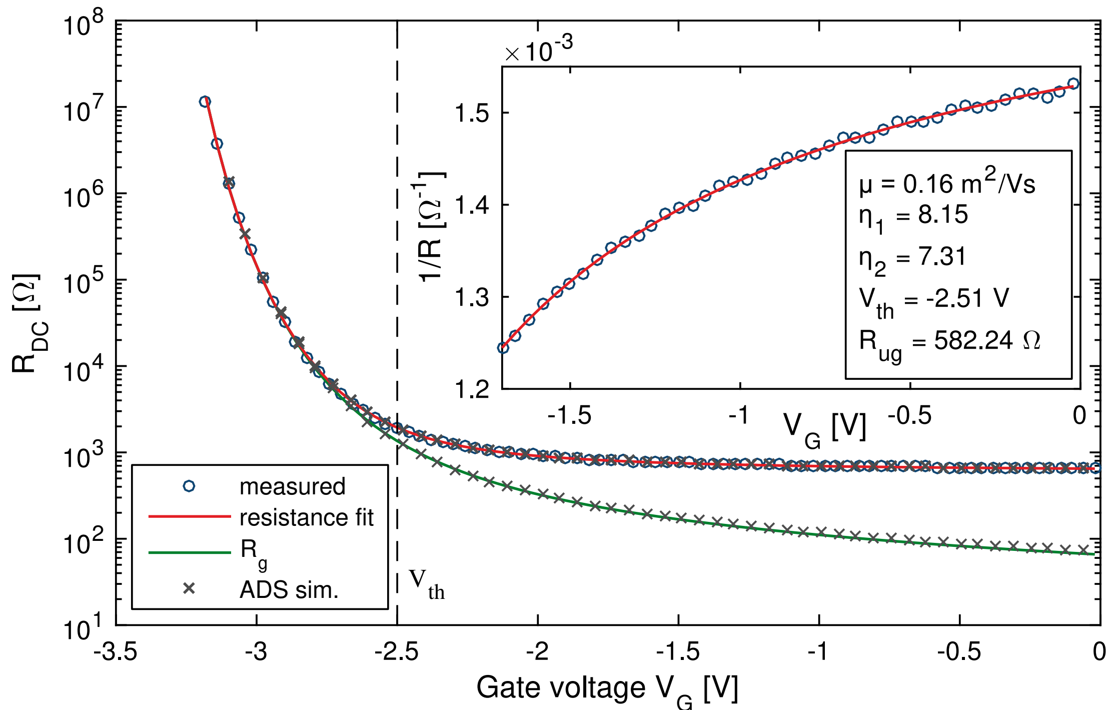

Fig. 4.2: Fit for device parameter extraction of a measured DC drain-source resistance of an AlGaN/GaN HEMT (for device details see Section 6.3.2). The measured DC resistance data is plotted as open circles while the fit is plotted as red solid line. The inset shows the first stage of the fit routine for extraction of ungated resistance R_{ug} and threshold voltage V_{th} from strong inversion regime. The solid green line corresponds to the resistance of only the gated channel region. Black crosses are simulated data from the transmission line equivalent circuit model implementation.

be required. It is in general not easy to find an exact expression for this relation. Different charge control models exist for different types of transistors and a universal formula cannot be given. Nevertheless, it is possible to use interpolation approaches which allow the description of the I-V characteristics of semiconductor FETs by a number of fit parameters. For Si MOSFETs, it was shown that the introduction of a fit parameter η can be used to describe the approximate relation between charge control by gate voltage and by Fermi energy. The factor η is often denoted as the transistor's *non-ideality factor*. With this assumption, a *unified charge control model* (UCCM) can be formulated to describe device operation in both below and above threshold regimes [103]

$$n(V_{\mathrm{G}}) = \frac{C\eta V_{\mathrm{T}}}{q} \ln\left[1 + \frac{1}{2} e^{\frac{V_{\mathrm{G}} - V_{\mathrm{th}}}{\eta V_{\mathrm{T}}}}\right] \tag{4.15}$$

In the model, the capacitance C is the same gate-to-channel capacitance per unit length as defined earlier in Eq. (2.34), $V_{\mathrm{T}} = k_{\mathrm{B}}T/q$ is the so-called *thermal voltage* and η is the non-ideality factor originally introduced to describe the slope in the sub-threshold operation regime. The UCCM has the same functional dependence as $n(E_{\mathrm{F}})$ in Eq. (4.14).

While good fit results can be obtained for Si CMOS devices with the non-ideality factor being a constant, we found that a modification is necessary to properly fit

measurements of the DC drain-source resistance of our AlGaN/GaN TeraFETs and also FETs in various other materials (data not shown here). We therefore introduced an additional gate voltage dependence in the non-ideality factor

$$\eta(V_\mathrm{G}) = 1 + \ln\left[1 + e^{\eta_1(V_\mathrm{G}-V_\mathrm{th})+\eta_2}\right] \tag{4.16}$$

with two constants η_1 and η_2. The functional dependence Eq. (4.16) is an empirical one, which ensures that for the deep sub-threshold regime the non-ideality factor has unity as lower boundary. Other approaches exist to formulate charge control models for AlGaN/GaN HEMTs [104], [105], however, they employ approximately the same number of fit parameters and show less resemblance with the fundamental expression for carrier density Eq. (4.14). A more detailed investigation of this matter is beyond the scope of this thesis and here we continue with Eq. (4.15) together with Eq. (4.16), which yields excellent fit results and sensible values for the physical fit parameters for the investigated devices.

4.2.2 Parameter extraction from DC resistance

Figure 4.2 shows an exemplary fit of a DC-measured drain-source resistance R_DC of an AlGaN/GaN TeraFET with a gate length of $L_\mathrm{g} = 250$ nm and width of $W = 3$ µm (more details on the device are given in Section 6.3.2). Since the measurement was performed on a real device, R_DC is naturally the sum of the voltage-controlled resistance of the gated channel region R_g and voltage-independent series resistance R_ug. The series resistance contains contributions from channel access regions (with length $L_\mathrm{ug} = 350$ nm on drain and source side in this example), contact resistances and possible other parasitic series resistances in the DC measurement path. The total measured resistance is therefore fitted as

$$R_\mathrm{DC}(V_\mathrm{G}) = R_\mathrm{g}(V_\mathrm{G}) + R_\mathrm{ug} \tag{4.17}$$

Here, the DC resistance can be considered as the quasi-static limiting case of Eq. (2.10) where $\tan(kL_\mathrm{g}) \approx L_\mathrm{g}$ and $k \approx s^{-1}\sqrt{-i\omega/\tau_\mathrm{p}}$ and therefore [42], [103]

$$\begin{aligned} R_\mathrm{g} &= \frac{1}{\sigma}\frac{L_\mathrm{g}}{W} \\ &= \frac{1}{n}\frac{L_\mathrm{g}}{q\mu W} \end{aligned} \tag{4.18}$$

with the charge density defined after Eq. (4.15).

We employ a two-stage fit routine where first, the ungated resistance R_ug and the threshold voltage are determined by fit the measured data far above the threshold in the so-called strong inversion regime. For large V_G above threshold, the charge density Eq. (4.15) in the channel can be approximated by the well known gradual channel approximation relation

$$n \approx \frac{C(V_\mathrm{G} - V_\mathrm{th})}{q} \tag{4.19}$$

The charge control is therefore linear in V_G in this region. In the first stage of the fit routine, we fit the inverse of the channel resistance, i.e., the channel conductance,

which for the gated part after Eq. (4.18) is directly proportional to the carrier density n. Thus

$$R_{\mathrm{DC}} = \frac{1}{G_{\mathrm{DC}}} = \frac{1}{G_{\mathrm{g}}} + R_{\mathrm{ug}} \tag{4.20}$$

where the conductance of the gated region is represented by a linear fit function $G_{\mathrm{g}} = Ax + B$. From Eq. (4.19) we determine the two fit parameters $A = C/q$ and $B = -(C/q)V_{\mathrm{th}}$. The employed fit function for the DC drain-source conductance in the strong inversion regime is then given as

$$G_{\mathrm{DC}} = \frac{1}{R_{\mathrm{DC}}} = \frac{Ax + B}{1 + R_{\mathrm{ug}}(Ax + B)} \tag{4.21}$$

with fit parameters A, B, and R_{ug}. The threshold voltage is calculated from the fit parameters as $V_{\mathrm{th}} = -B/A$.

In the second fit stage, the full DC resistance measurement data is fitted using Eq. (4.15) with fit parameters μ, η_1, and η_2 and device parameters R_{ug} and V_{th} from fit stage 1. The complete set of device parameters obtained from the fit routine is displayed in the inset box in Fig. 4.2. Lastly, the figure also shows the DC resistance of only the gated channel region R_{g} as solid green line, which was calculated from the extracted device parameters after Eq. (4.18).

Recall again that the fit procedure in this section was presented for AlGaN/GaN-based TeraFETs. Several adaptions may be necessary for measurements in different material systems, in particular graphene with ambipolarity of charge transport. As a final remark, note again that the ungated resistance R_{ug} in general does not simply represent the resistance of the ungated access regions of the FET channel. It can contain several other parasitic serial resistances in the DC measurement path, e.g., ohmic resistances of the drain and source metal contacts, which cannot easily be discriminated from the resistance of the ungated regions. In particular, for the investigated AlGaN/GaN TeraFETs, the sheet resistance of the ungated channel regions amounted to only ~ 20 % of the total ungated resistance. Since the contact resistances can exhibit strong frequency dependency, further detailed investigation of influences on HF behavior is required. A deeper analysis is beyond the scope of this work and each access region for simplification was attributed a resistance of $R_{\mathrm{ug}}/2$ in the presented simulations for symmetric device geometries. We discuss a possible effect on the frequency dependence of the TeraFET's HF impedance in Chapter 7.

4.2.3 Comparison of analytic calculations and numerical circuit simulations

The main plot in Fig. 4.2, besides the measured DC resistance and the fitted curve for device parameter extraction, also shows results of a DC simulation performed with the circuit model implementation in the circuit solver as black cross symbols. A screenshot of the equivalent circuit for the DC simulation is depicted in Fig. 4.3. The gated and ungated transistor region for the DC simulation each consisted of

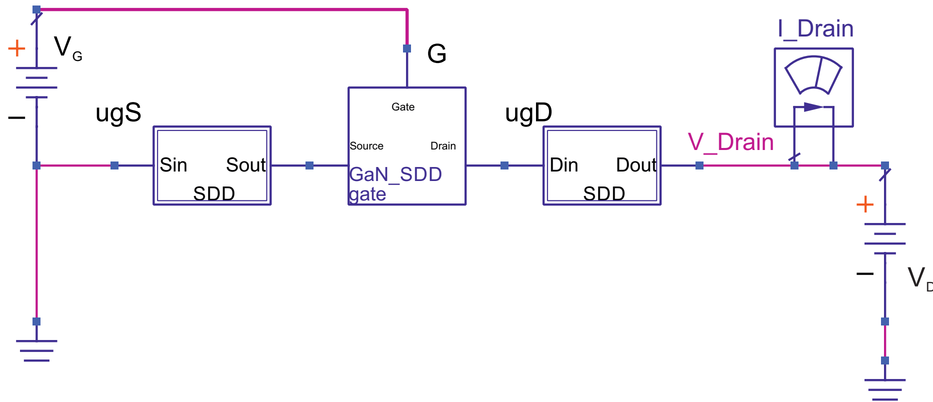

Fig. 4.3: Circuit model for DC resistance simulation with the circuit solver. The simulation is performed for low $V_{\mathrm{D}} = 0.01$ V and the resistance is calculated from simulation results as the ratio $V_{\mathrm{Drain}}/I_{\mathrm{Drain}}$. Exemplary simulation results for an AlGaN/GaN TeraFET are plotted as black cross symbols in Fig. 4.2.

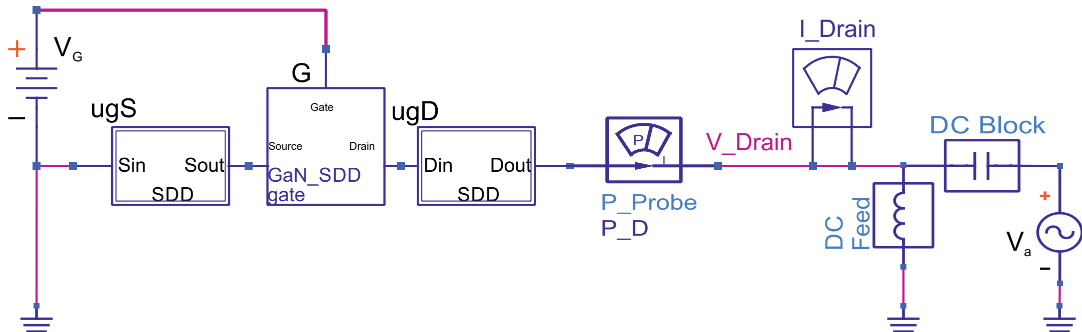

Fig. 4.4: Drain coupling implementation of TeraFET equivalent circuit model for the HF harmonic balance simulations. For simulation of the intrinsic detection mechanisms, a fixed voltage amplitude at the transistor drain is used as signal source, in particular, no antenna impedance is included. The source and drain side SDD circuits are RL transmission line representations with 20 elements each. The gated region is composed of a variable number of discrete RCL elements, for simulations in this work we chose N=720 elements (see discussion below).

20 discrete RCL transmission line elements.[26] Two simulations were performed with the ungated access regions activated and shunted, respectively. For both situations, the analytic calculations and numerical simulations compared in Fig. 4.2 show an excellent agreement, which verifies that the circuit model yields a correct device DC resistance from device parameters extracted with the above fit routine.

We now cross-verify the TeraFET's intrinsic high frequency channel impedance obtained from harmonic balance simulations with the circuit solver software. The circuit implementation of drain coupling boundary conditions is illustrated in Fig. 4.4. For the results in this section, the ungated channel parts were shunted and a fixed voltage oscillation $V_{\mathrm{a}} \cos(\omega t)$ was applied at the drain end of the channel by a

[26]Recall, however, that a distributed approach is not required for DC simulations and the transistor could have well been reduced to a lumped RC equivalent circuit.

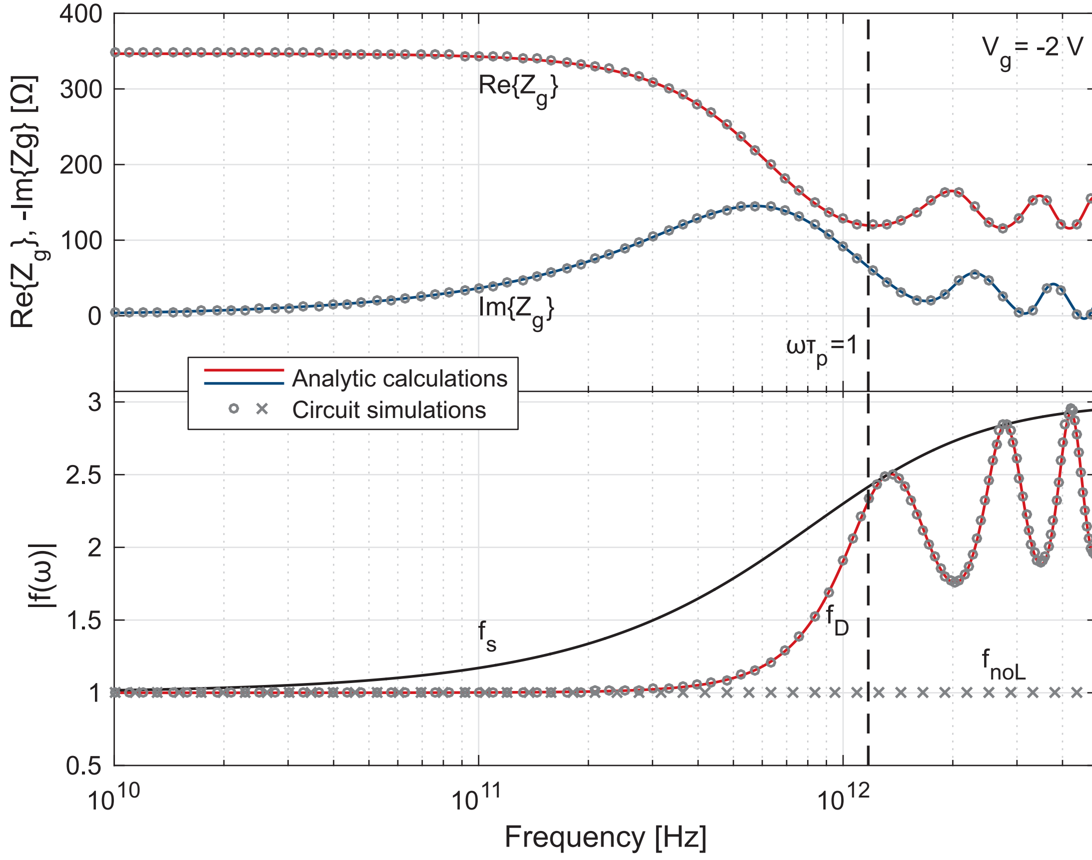

Fig. 4.5: Real and Imaginary parts of the complex channel impedance Z_{g} (top graph) and plasmonic enhancement factor f_{D} (bottom graph) for drain-coupling scheme. Solid lines are from analytic calculations, black symbols are circuit simulation results. The black solid line represents the long-channel case. In the bottom graph, circuit simulation results are included with convective current contributions switched off, where no enhancement of resistive mixing exisits and $f_{\mathrm{noL}} = 1$.

single tone high frequency source.

Fig. 4.5 shows calculations of the real and imaginary parts of the complex high frequency channel impedance Z_{g} after Eq. (2.10) as well as the plasmonic enhancement factor $f_{\mathrm{D}}(\omega)$ after Eq. (2.17) as solid lines. The real part of Z_{g} for $\omega\tau_{\mathrm{p}} > 1$ exhibits resonances close to the plasma resonance frequencies (comp. (2.28)) in the enhancement factors f_{D} and f_{DS} discussed in Section 2.4.3 and is shown in the bottom graph of the figure. The plotted curves were calculated for the same AlGaN/GaN test device as above and again for a gate bias voltage of $V_{\mathrm{g}} = -2$ V.

The analytic results are compared to numerical calculations for the same (drain-coupling, comp. Fig. 2.2 and Fig. 4.4) boundary conditions, represented as black symbols. The high frequency impedance can directly be calculated as ratio of complex drain voltage and current $V_{\mathrm{Drain}}(\omega)/I_{\mathrm{Drain}}(\omega)$ at the fundamental excitation frequency of the harmonic balance solver. For this purpose, voltage and current can be obtained from the simulation by placing respective probe components, denoted in Fig. 4.4 as “V_Drain” and “I_Drain”.

On the other hand, the enhancement factor is obtained as ratio of the frequency-

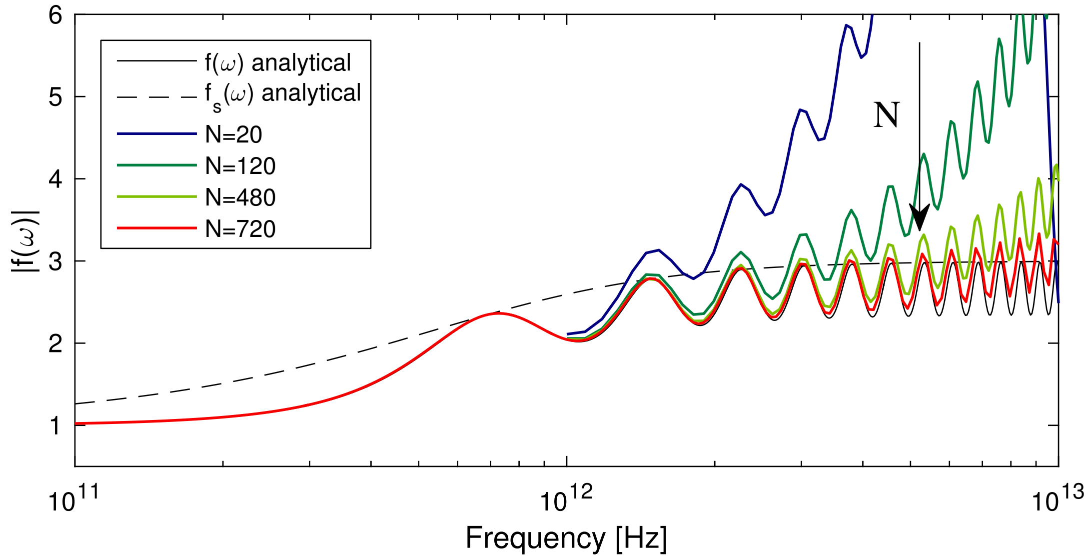

Fig. 4.6: Effect of level of discretization on accuracy of the circuit simulation. Simulation of $f(\omega)$ performed for different number N of discrete elements. Light gray lines correspond to the analytical calculation.

dependent DC current response of the detector measured at the drain output $I_{\text{det}}(\omega)$ and the same response signal in the quasi-static limit I_{QS} when low frequency radiation is applied (taken as 1 kHz in the simulation)

$$f(\omega) = I_{\text{det}}(\omega)/I_{\text{QS}} \tag{4.22}$$

The current responses are obtained as the DC components of the current probe signal "I_Drain" (see Fig. 4.4). For both the enhancement factor and the channel impedance, results from numerical simulations with the circuit implementation match the corresponding analytical calculations in the investigated frequency regime.

The implementation of the transport model as a distributed transmission line equivalent circuit is based on the concept that for high applied frequencies a transition from classical resistive mixing to distributed resistive mixing occurs [19] and the rectifying channel must be treated as a distributed transmission line rather than a lumped RC element (comp. Chapter 2). For further increasing frequencies, an enhancement of the distributed resistive mixing by non-linear self-mixing properties of the induced plasma waves sets in. In the hydrodynamic equations, the self-mixing is represented by the convective terms (comp. Eq. (3.34) or Table 3.1). To verify this assumption and the correct implementation of the circuit model, the bottom graph in Fig. 4.5 also shows results from a circuit simulation where the convective current contribution has been switched off ($f_{\text{noL}}(\omega)$). As expected, the mixing efficiency remains unity for all frequencies in this case and no plasmonic enhancement over distributed resistive mixing is obtained.

It must be mentioned here that for increasing radiation frequency numerical instabilities in the simulation can occur. This in an effect of the discretization length Δx of the distributed transmission line model for the channel, i.e., the deviations depend on the number of discrete SDD elements used for the simulation. Figure 4.6 shows the factor $f_{\text{D}}(\omega)$ calculated using different numbers N of discrete elements in

the circuit simulation. It can be seen that the results from the numerical simulation converge towards the analytic result for increasing N. For the simulations in Fig. 4.5 we chose a number of $N = 720$ discrete elements[27] – corresponding to a size of the unit cells of 0.5 nm - which yields accurate simulation results in the frequency regime of interest up to roughly 5 THz. A thorough analysis of this effect is still subject to further investigation.

[27]The ungated channel regions are modeled with $N_{\mathrm{ug}} = 20$ unit cells each. There, the influence of discretization proved to be negligible.

Chapter 5

Simulations

In Chapter 4 we presented the implementation and verification of the hydrodynamic transport model in a circuit solver. This chapter presents simulation results concerning the plasma wave mixing mechanism in TeraFETs which were performed with the numerical model. We first show simulations of the intrinsic mixing in a gate-source coupling situation and discuss the influence of plasma resonances as predicted by Dyakonov and Shur [18]. A major drive in the research of TeraFETs and their fabrication in different materials with high carrier mobilities was the prospect of a strong enhancement of plasmonic rectification in the resonant detection regime (see Section 2.4), where strong resonances in the plasmonic efficiency factor $f(\omega)$ were predicted. We reproduced in analytical calculations and the simulations performed in the previous chapter that such resonant behavior can indeed be observed. However, the performance of radiation detector is not characterized by the efficiency of its intrinsic detection mechanism only, but power coupling to the rectifying element must be taken into account. We address this issue in the following section. The subsequent section then shows the influence of ungated channel regions on the spatial power distribution over the TeraFET's transistor.

5.1 Detection sensitivity in the resonant plasmonic mixing regime

It was proposed in the original theoretical work on FETs for THz detection by Dyakonv and Shur [18] that a strong enhancement in detection efficiency could be achieved when the detectors are operated in the resonant plasmonic detection regime (see Section 2.4). As discussed earlier with the help of the analytic, fluid-dynamic device model, constructive resonant enhancement can indeed be present in the plasmonic efficiency factor $f(\omega)$ when gate-source coupling boundary conditions are employed (cp. Fig. 2.3). However, this observation has led to a questionable premise in research dedicated to FET-based THz detectors, namely, that ultra sensitive devices can be expected from resonant plasmonic detector operation. In this section, however, we present a number of simulation results, which indicate that no significant enhancement of detection sensitivity can be expected in this regime of TeraFET operation. The reason is inefficient power coupling to the intrinsic channel region at

close to the plasma wave resonant frequencies.

The important figure of merit to describe the performance of a detector is not the efficiency of intrinsic detection mechanism, but rather its responsivity and sensitivity - the latter often measured as noise equivalent power (NEP). The responsivity (denoted here by the German type Fraktur letter $\mathfrak{R}$) relates the detector's radiation respones to to the available power of the incoming signal. The NEP, in turn, relates the responsivtiy to the detector's inherent noise signals. The two quantities are commonly defined as[28]

$$\mathfrak{R}_I = \frac{I_{\text{det}}}{P_{\text{in}}} \tag{5.1}$$

$$\text{NEP} = \frac{I_{\text{N}}}{\mathfrak{R}_I} = \sqrt{\frac{4k_{\text{B}}T}{R_{\text{DC}}}}\frac{1}{\mathfrak{R}_I} \tag{5.2}$$

where P_{in} is the power of the coupled radiation, I_{N} is the detector's current noise spectral density, k_{B} is Boltzmann's constant and T, in our case, is room temperature. We have assumed here already that the dominating noise source in zero drain bias-operated TeraFETs is thermal noise exhibited by the detector's DC drain-source resistance R_{DC}. Experimental proof of this assumption is given in Chapter 6. More details on the definition of responsivity and NEP, in particular with respect of the precise definition of the input power P_{in}, will be given in the same chapter dealing with the experimental characterization of TeraFETs.

Figure 5.1 shows simulation results obtained for the plasmonic response of the intrinsic FET region under gate-source coupling conditions (cp. Fig. 2.2 on the right). Ungated channel regions as well as diffusive transport contributions were not included in the simulation. It therefore represents the situation as described by Dyakonov and Shur [18].[29]

The simulations were carried out for the same set of device parameters of an AlGaN/GaN TeraFET as presented in Section 4.2.2 and at the same gate bias voltages $V_{\text{G}} = -2.6$ V, -2 V, and 0 V, as investigated before (see Section 2.4.3). These points correspond to gate bias of highest device sensitivity (see below Section 6.3.2), operation slightly above threshold ($V_{\text{th}} = -2.51$ V), and operation in the strong inversion regime, respectively. The plasmonic enhancement factors $f_{\text{GS}}(\omega)$ shown here as solid black lines in the left plots on the right axes are identical to the ones obtained earlier from analytic calculations after Eq. (2.18). The long-channel approximation is plotted as dashed line. We now compare the relative enhancement in detection sensitivity in terms of NEP to the enhancement of plasmonic mixing predicted by $f_{\text{GS}}(\omega)$.[30]

The applied HF signal in the simulations had a fixed voltage amplitude of $V_{\text{a}} = 1$ mV for all frequencies and bias voltages. For an ideal power source without

[28] Note that equivalent expressions can be formulated for voltage responsivity and voltage noise spectral density using the simple relation $I_{\text{det}} = V_{\text{det}}/R_{\text{DC}}$.

[29] The gray symbols in the figure represent simulated data points, the solid lines are plots of the same data for better visibility only.

[30] Note for that matter that lower NEP corresponds to higher sensitivity.

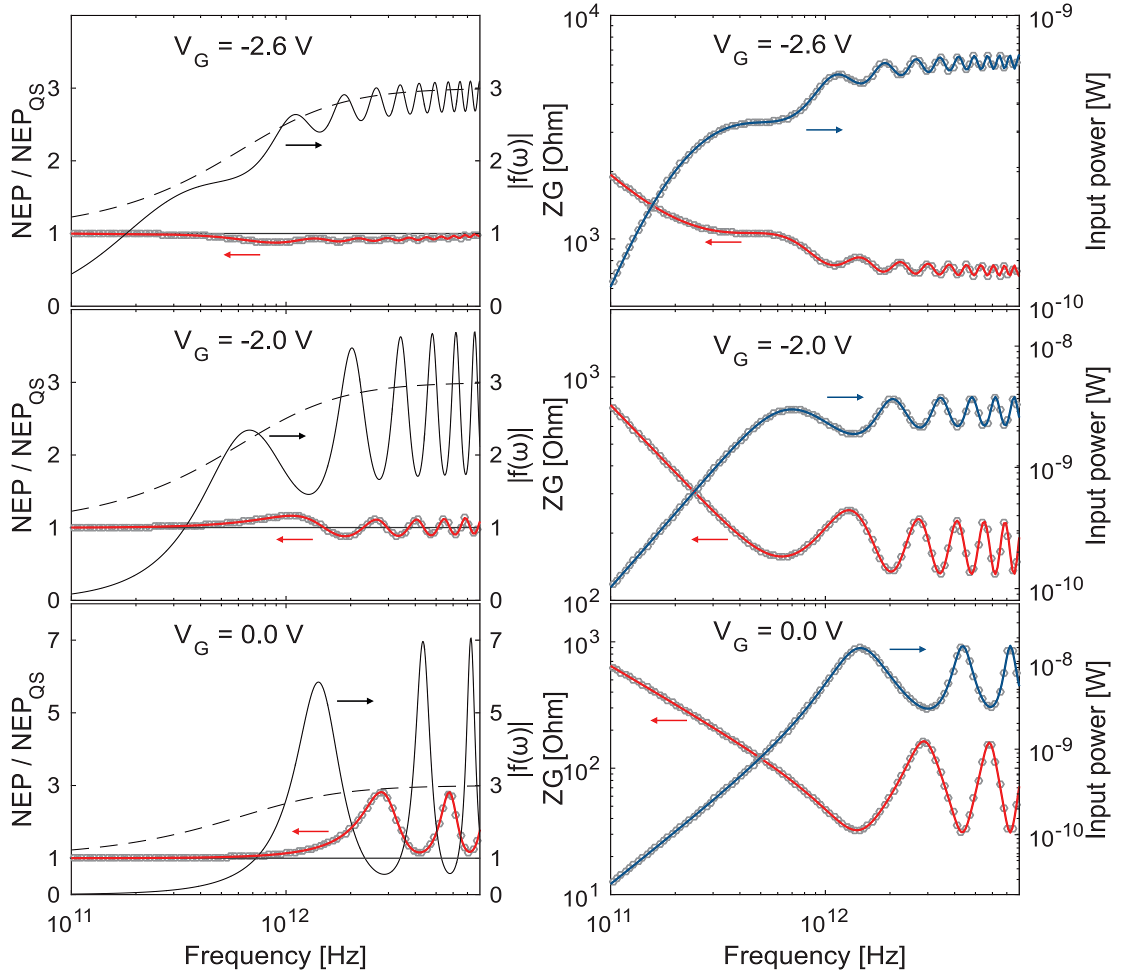

Fig. 5.1: Simulation of the intrinsic NEP (left plots, left axes), gate impedance (right plots, left axes), and input power (right plots, right axes) for gate coupling boundary conditions and different gate bias voltages. The NEP is plotted relative to the quasi-static value. for increasing gate voltage above threshold (top to bottom) the enhancement of the device NEP decreases with increasing strength of resonances. The reason is a an increased power coupling at these frequencies.

additional internal impedance, the power delivered to the load - in this case the FET channel impedance Z_g - is therefore given as

$$P_{in} = \frac{V_a^2}{2} \frac{Re\{Z_g\}}{|Z_g|^2} \tag{5.3}$$

which is reproduced by the circuit simulation. The input power P_{in} is plotted as blue line on the right axes in the right plots. We find that the input power shows pronounced resonances close to the resonant plasma frequencies. This behavior is caused by according resonances in the complex channel impedance plotted in the same graphs as red lines on the left axes. Because $P_{in} \propto 1/Z_g$ maximum power is delivered to the device at the frequencies of resonant enhancement in the efficiency factor $f_{GS}(\omega)$. A a consequence, no efficient detection is found at these frequencies,

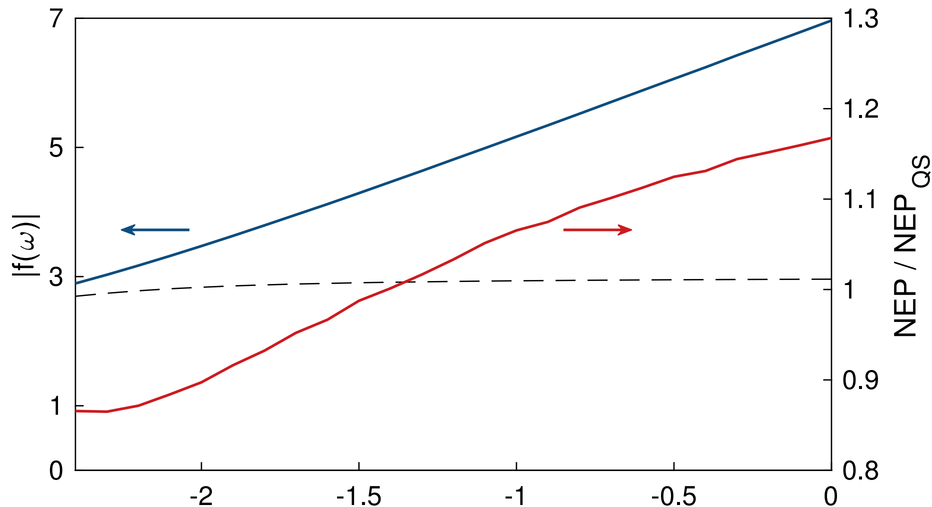

Fig. 5.2: Comparison of improvement in intrinsic detector NEP depending on plasmonic enhancement factor versus gate voltage. The blue curve on the left axis represents the enhancement in $f(\omega)$ at the second (fully developed) plasma wave resonance (depending on the applied gate bias V_G, comp. Fig. 5.1). The red curve on the right axis shows the according enhancement in NEP compared to the quasi-static NEP_{QS} at the respective frequencies for each V_G. An enhancement in sensitivity is only present at gate voltages close to the transistor's threshold, where no significant plasmonic resonances are observed.

with respect to device responsivity (cp. Eq. (5.1)). This is clearly reproduced in the plot of the sensitivity in terms of NEP relative to the NEP at quasi-static device operation after Eq. (2.20). Note that the noise determined by the DC resistance is constant over frequency. A slight improvement of NEP can be observed, however this reversly corresponds to the strength of plamonic enhancement in the efficiency factor.

To emphasize this observation, Fig. 5.2 shows the dependence of improvement in NEP on the strength of resonances in $f_{GS}(\omega)$. On the left axis, the values of the enhancement factor for the second (full) plasma resonance (cp. Eq. (2.28)) are plotted, for example, around 2 THz for $V_G = -2V$. The dashed line again represents the long-channel limit in $f(\omega)$. It becomes evident here that the NEP degrades (grows larger) when the enhancement in f becomes larger. At low bias voltages, where almost no resonant enhancement above the long-channel limit remains, the NEP is lowest.

To summarize this remarkable observation, we found that a strong enhancement in the efficiency factor as calculated by the theory of plasma wave mixing in FETs does not implicate an improvement in device sensitivity. This result constitutes a far-reaching contrast to previous predictions in TeraFET literature, where the prospect of strongly enhanced THz detection was promoted based on the considerations of the efficiency factor alone. We come to the conclusion that in order to fabricate efficient TeraFETs, avoiding of resonances is favorable and device design should always be dedicated to reaching a situation as close as possible to the long-channel limit. Note finally, that the above calculations were performed for the intrinsic FET only. In the next section, inclusion of additional ungated channel regions will be discusse, which poses a great challenge on device designers to actually achieve this favorable situation.

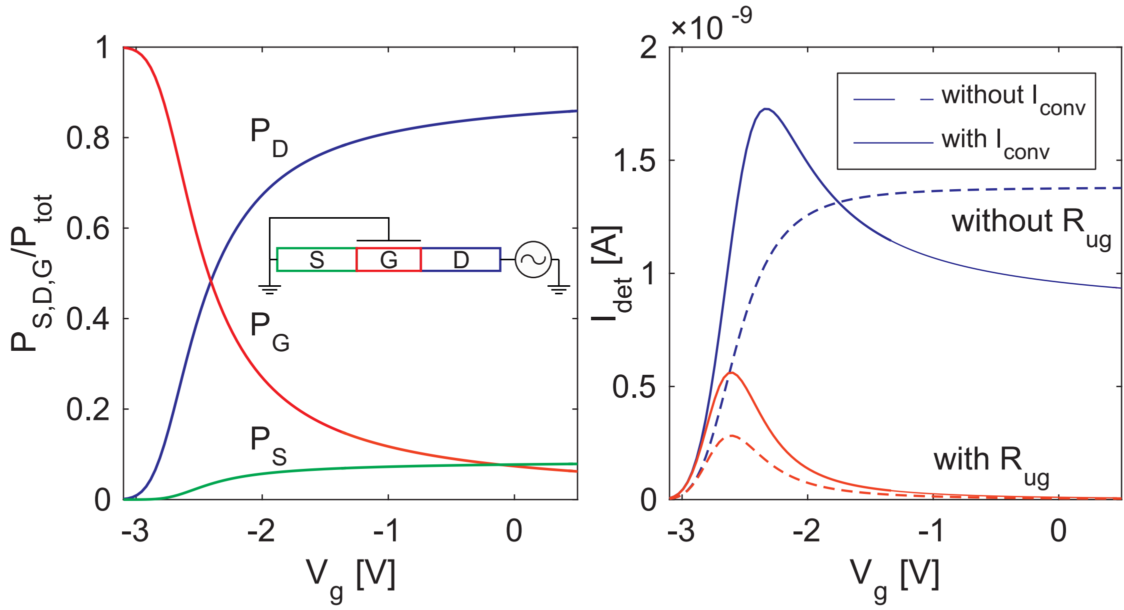

Fig. 5.3: Left: Power distribution over FET channel regions relative to input power versus applied gate bias V_g The channel regions are labelled P_S for the power dissipated in the source-side access region, P_D for the drain-side access region, and P_G for the power dissipated in the gated channel region responsible for the rectification. Simulations were performed at 0.6 THz.

5.2 Circuit simulations with ungated access regions

5.2.1 Power distribution

In many FET technologies, the transistor channel is only partially gated and embedded in ungated access regions as shown in the simplified FET schematic in Fig. 2.1. The carrier density-controlling function of the gate metal has no impact on these regions where a fixed carrier density exists. The ungated channel regions therefore constitute a gate voltage-independent series resistance to the total drain-source resistance of the device (cp. Section 4.2.2). They do not contribute directly to the plasma wave-based detection mechanism. As mentioned before, it has been discussed, however, that the formation of ungated plasmons and their interaction with the gated plasmons of the intrinsic detector element can have an influence on the detection mechanism, which must be considered. For more discussion on this topic see, e.g., Refs. [11], [73], [89], [90].

Recall that in Chapter 4 we have assumed a constant voltage amplitude reaching the intrinsic detector region at each frequency and have ignored variations in reactance and resistance with frequency. Consider now, that the incident power in general is distributed over the intrinsic (Z_g) and extrinsic (R_{ug}) regions of the FET channel. The distribution follows a simple voltage divider rule as the ratio of impedances of the individual circuit elements of the individual channel regions. More power is delivered to regions with higher impedance. On the other hand, only the fraction of

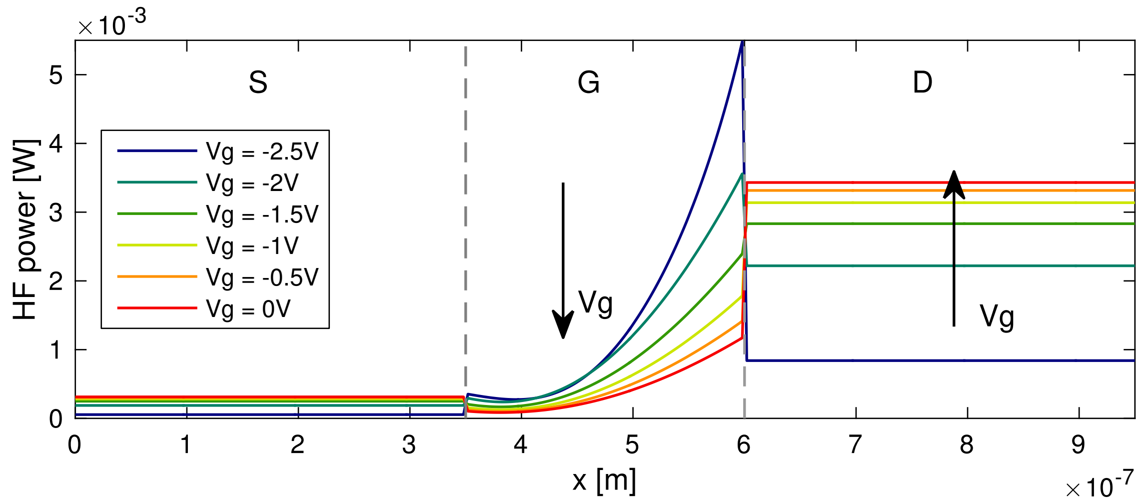

Fig. 5.4: Spatial power distribution over the channel of a TeraFET in drain coupling scheme at 0.6 THz. The dashed lines mark the boundaries of the channel regions for the source-side ungated (S), gated (G) and drain-side ungated (D) parts. The arrows indicate the change of power in the gated and drain-side ungated regions with increasing gate bias voltage above threshold

the total power reaching the gated channel region is available to the plasma wave mixing mechanism.

The power distributed to each of the FET channel regions can be read out from the circuit solver by placing AC power probes at the respective channel positions. Fig. 5.3 in the left graph shows a simulation of the distribution of the total input power P_{tot} in a TeraFET with similar device parameters as in Section 4.2 when ungated parts are added and for drain-coupling (cp. Fig. 4.4). The power dissipated in the source-side ungated region, the gate region, and the drain-side ungated region are denoted as P_{S}, P_{G}, and P_{D}, respectively. With increasing gate voltage, an increasing amount of power is delivered to the drains-side ungated channel region due to a decrease of the impedance of the gated channel. This power is not available for the actual rectification mechanism, hence, the current response decreases as plotted in the right graph in Fig. 5.3. The graph shows the detector's current response for two situations with the ungated channel parts included (red curves) in the simulation or shunted (blue curves). The signals of the simulation with ungated parts show a pronounced peak and then rapidly decrease to zero, while the current responses reach a plateau when the ungated parts are shunted. This behavior reflects the relative amount of power coupled to the rectifying gated channel region. For shunted ungated parts, all the input power P_{tot} is available for mixing in the gated region and the exact shape of the response curve merely reflects the plasmonic mixing efficiency, i.e., the shape of the enhancement factor $f(\omega, V_{\text{g}})$. For comparison, the intrinsic, purely distributed resistive mixing response without the factor is plotted as dashed blue line. It simply rises monotonically to a constant value.

The implementation of the detector channel as distributed transmission line allows visualization of the spatial distribution of the input power over the individual SDD unit cell. The local power distributed on each transmission line element versus

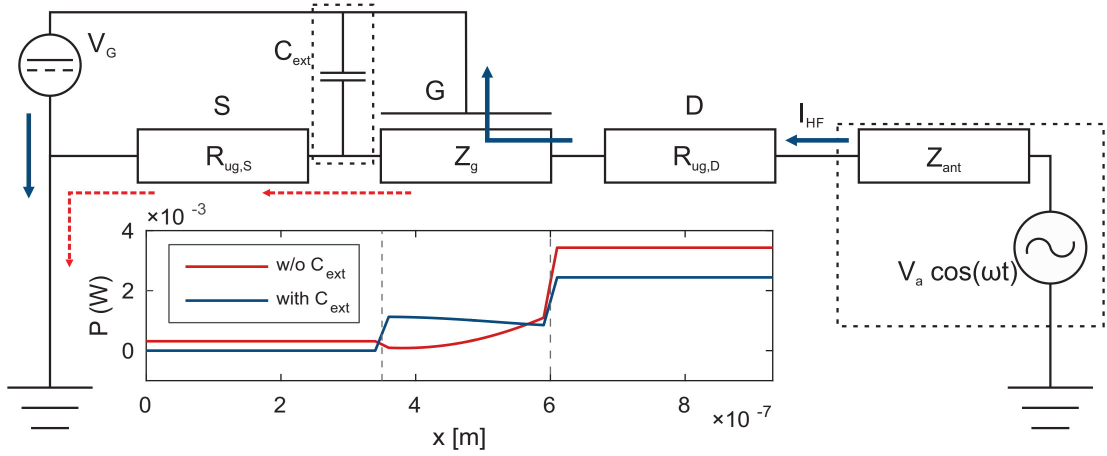

Fig. 5.5: HF current paths for a TeraFET equivalent circuits. Blue arrows show the flow of AC current in the case of ideal drain coupling and gate source shunting. Dashed red arrows indicate parasitic currents in source-side ungated channel region when gate-sou rce shunting by the gate capacitance is insufficient. Implementation of an external gate-source shunting capacitance C_{ext} pins the gate the source side of the gated channel to AC ground to prevent current flow through the source. The inset plot shows simulations of THz power dissipated in the different transistor regions for situations with (blue) and without (red) C_{ext} for gate bias $V_{\text{g}} = 0$ V and a frequency of 0.6 THz.

distance is plotted in Fig. 5.4 for a number of gate voltages and for 0.6 THz radiation. As expected, for gate biases close to and below the threshold voltage $V_{\text{th}} = -2.46$ V, the major amount of power is concentrated in the gate region where the impedance grows exponentially and far exceeds the impedance of the ungated parts. As the gate voltage rises above threshold, the power is more evenly distributed over the device as discussed above until the situation is reversed and the largest amount of the input power is dissipated in the ungated region on the drain-side of the device. The inverse trend is illustrated by the arrows in the respective channel regions in Fig. 5.4. Less power is therefore available for rectification in the device and the THz response decreases to zero for gate voltages high above the threshold, as indicated already before in the right graph of Fig. 5.3.

A number of peculiarities of the simulation results for the particular AlGaN/GaN device parameters should be discussed here: First, the source part of the channel shows a behavior similar to the drain part. The power delivered to the source-side ungated region increases for voltages above threshold. A crossover of the power of gated and source-side channel region can be seen in the graph in Fig. 5.3 close to zero gate bias. For idealized drain coupling boundary conditions, however, the gate should lie on AC ground and as a result, no AC current should flow through the ungated resistance on the source-side. The situation is illustrated in Fig. 5.5 where the blue arrows indicate the AC current path for the idealized coupling scheme. The transistor HF impedance “seen” by the receiving integrated antenna is only the sum of the drain-side ungated impedance and the intrinsic impedance Z_{g} (cp. Section 6.1.2). Furthermore, it was mentioned in Section 2.4.2 that the self-mixing of plasma waves takes place in the gated region within an effective detection length, which is shorter than the gated region for the present set of parameters. The remaining gated

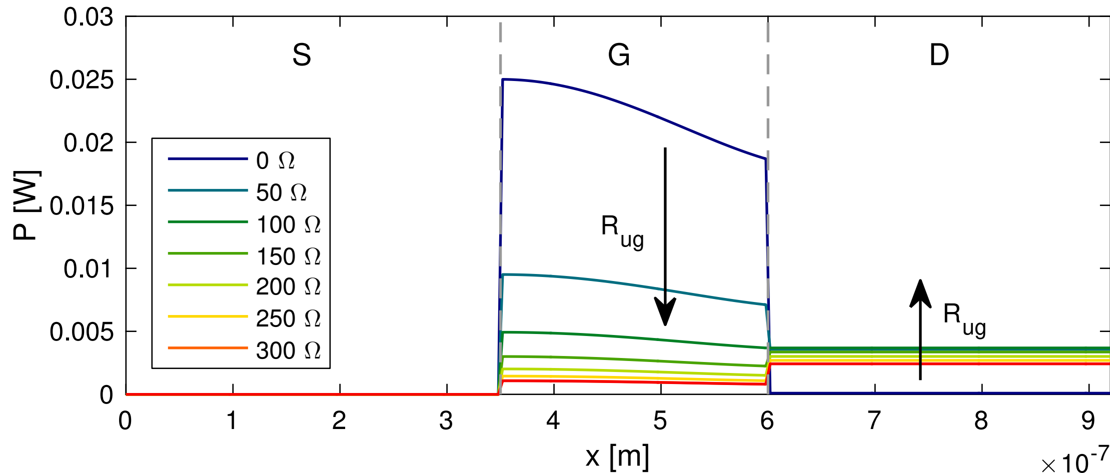

Fig. 5.6: Power distribution over TeraFET channel for varying resistance values R_{ug}. Simulations were performed with external gate-source shunting capacitance C_{ext}.

channel part acts as AC shunting capacitance to the gate contact to establish drain coupling, gate-source shunting boundary conditions. However, when the remaining gated region is to short so that shunting is insufficient, the gate is not fully AC grounded and a fraction of the AC current will flow through the ungated resistance $R_{\mathrm{ug,S}}$. Consequently, some fraction of the input power is "lost" to the source-side ungated region as was the case for the simulation in Fig. 5.4. A more profound consequence is the possible excitation of a reverse plasma wave counteracting the wave entering the channel from the drain side and reducing the efficiency of the plasmonic rectification. A quantitative analysis of this influence was not performed in this work.

When the length of the gated channel is increased, capacitive coupling is increased and the losses are reduced.[31] Another option is to implement an additional external AC shunting capacitance C_{ext} between gate and source to force the gate on AC ground. The inset plot in Fig. 5.5 shows a direct comparison of circuit simulation results for the power distribution at $V_{\mathrm{g}} = 0$ V and radiation frequency of 600 GHz obtained without and with C_{ext}. In the latter case, the power dropping over $R_{\mathrm{ug,S}}$ is indeed zero and all power is distributed between the gate and drain parts. It should therefore be the aim during device design to realize optimal gate-source shunting boundary conditions to prevent power loss to the source-side ungated channel region.

Second, it can be formulated in general, that reduction of ungated access resistances should increase the efficiency of plasma wave rectification in TeraFETs. The plot in Fig. 5.6 compares power distribution situations for several values of the ungated resistance R_{ug} in Eq. (4.17). All power is delivered to the gate when no ungated series resistances are present. For increasing R_{ug} the relative amount of power under the gate decreases and is shared with the drain-side access region.

As a conclusion from the above observations, a crucial task in TeraFET design is to ensure that the desired boundary conditions for radiation coupling are met as close

[31] The length of the gated channel region, however, is often a fixed device parameter inherent to the employed semiconductor technology node and cannot be varied arbitrarily.

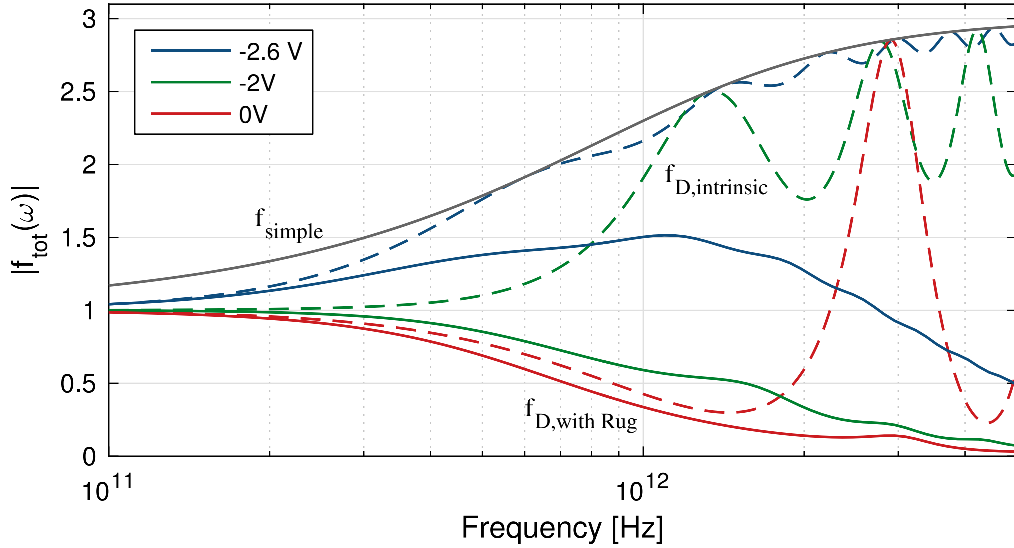

Fig. 5.7: Plasmonic enhancement factor $f(\omega)$ for a TeraFET with drain-coupling scheme including ungated channel regions for different gate voltages (solid lines). The enhancement factor is in all cases reduced compared to the intrinsic case (dashed lines), since power is dissipated in the ungated regions.

as possible and the incident high frequency power is efficiently coupled to the active detector region. The simulations were performed for a fixed frequency of 0.6 THz. The influence of ungated series resistances, however, can exhibit a strong dependency on frequency. While the resistance of the ungated channel region is nearly constant, in particular the contact resistances change with increasing frequency. Such effects are not considered in this work and a fixed R_{ug} is used for all frequencies in the circuit simulation. Further investigations on the issue should be carried out in the future, as the influence of extrinsic resistances on the power distribution in the device is essential in the understanding of the detector performance.

5.2.2 Influence on plasmonic mixing efficiency

In Chapter 2 some fundamentals of plasma wave mixing at frequencies above $\omega\tau_p \gg 1$ were discussed. An efficiency factor $f(\omega)$ was introduced to account for plasmonic enhancement of distributed resistive mixing. In Section 5.1 we presented simulations of the enhancement factor in the case of gate-source mixing. Both these earlier discussions were based on precisely defined drain-coupling boundary conditions, which were employed to derive the analytic forms of $f(\omega)$ in Eqs. (2.17) and (2.18). Moreover, it was assumed that all available radiation power was coupled to the intrinsic gated region of the FET and therefore available for the mixing mechanism. Results in the previous section, on the other hand, showed that when ungated detector elements are included, the exact satisfaction of boundary conditions may not be valid anymore depending on the extrinsic device architecture. In such cases, analytic solutions for the enhancement factor $f(\omega)$ in general may not exist. We also showed that significant amounts of power can be lost to the ungated resistances. It is one of the most important advantages of the implementation of the TeraFET transport

model in in a numerical circuit solver that simulations of real device situations can be performed.

The influences of extrinsic detector elements on the exact radiation coupling and power distribution is naturally included in simulation results from the circuit solver when such elements are added to the circuit model. In Section 4.2.3 it was shown that the intrinsic efficiency factor $f(\omega)$ could be retrieved from circuit simulations as the ratio of quasi-static and high frequency current response (cp. Eq. (4.22)). Accordingly, a total efficiency factor $f_{\mathrm{tot}}(\omega)$ can be extracted from simulations, which then not only reflects plasmonic mixing efficiency but also extrinsic influences on the overall detection process.

Figure 5.7 shows simulations of $f_{\mathrm{tot}}(\omega)$ for the drain-coupling scheme displayed in Fig. 4.4 with the ungated parts activated (in contrast to Fig. 4.5) and for different applied gate bias voltages. As expected already from the discussion in the previous section, for all gate biases the mixing efficiency is always reduced compared to the intrinsic case – indicated as dashed lines in the figure - due to partial distribution of incident power to the ungated channel parts. Note that the efficiency decreases towards higher gate voltages above the threshold towards $V_{\mathrm{G}} = 0$ V, which reflects the rising influence of the drain-side ungated part and decreasing impedance of the gated region according to the overall power distribution shown before in Fig. 5.3. Again, the message here is that reduction of the ungated regions should be aimed for during device design in order to prevent negative influence on the plasmonic detection efficiency of TeraFETs.

Chapter 6

TeraFET characterization

TeraFET have up until today been successfully implemented in various material systems and high sensitivity THz detection capability has been demonstrated. After a number of initial, pioneering works [106]–[108] the first thorough detection experiments were performed in the early to mid-2000's using commercial GaAs/AlGaAs and GaN/AlGaN HEMTs [67], and Si MOSFETs [109], [110] for the non-resonant detection of THz radiation. In some studies, the observation of resonant plasmonic detection under non-zero drain-bias conditions was claimed [65], [66], [111]. The first devices employed for proof-of-principle experiments, however, were not intentionally fabricated for the purpose of THz detection, and in particular, the radiation coupling situation was mostly undefined. It was supposed in most of these works that bonding wires, contact pads for electrical contacting of the transistors, and other electrical leads or wires served as largely unspecified "antennas". Nevertheless, the plasma wave detection principle proposed by Dyakonov and Shur [18] was successfully demonstrated and investigated in some detail in these early works.

In the succeeding years, design and fabrication of specialized TeraFET devices intended for THz detection, and particularly the integration of efficient antenna structures – resonant and broadband designs - has led to a tremendous improvement of TeraFET performances in terms of responsivity and sensitivity. Eventually, recently fabricated TeraFETs exhibit sensitivities well comparable to other state-of-the-art THz detector technologies, foremost Schottky diode-based receivers for the lower THz regions [20], [21], [43], [71]. The most sensitive (resonant antenna) devices have so far been realized in Si MOSFET technology, which is mainly due to the maturity and commercial availability of this semiconductor technology. A wide range of literature on the above experimental works exists and cannot be presented extensively in the scope of this thesis. Some review-type publications are, e.g., Refs. [20]–[22], [71].

In the course of this work, a number of TeraFETs with integrated broadband antennas were designed and fabricated in different materials with two main intensions: (a) to optimize the detection performance by careful design and modeling of the TeraFETs, and (b) to further investigate the underlying physical detection mechanisms in the devices. The selected material systems were AlGaN/GaN HEMTs and graphene FETs with integrated broadband antennas. During the characterization experiments, additional physical detection mechanisms became evident, which cannot not be explained by the intrinsic plasma wave mixing principle [18], [19],

[30], [34], [41], [42], [47], [48], [74], [90] alone. We argued before that these signals are thermoelectric signals due to local heating of charge carriers in the transistor channel.

This chapter presents results from THz detection experiments of the fabricated AlGaN/GaN and graphene TeraFETs in terms sensitivity of THz detection. Details of detector design and fabrication, the evaluation procedures of DC and THz measurements, and important critical issues therein are discussed. The focus of this chapter lies on the achievements in record detection sensitivity for both technologies, which could be reached by careful design based on the theoretical considerations of the previous chapters. The subsequent chapter then discusses in particular the observation of the thermoelectric signal contributions, which are compared to predictions from the implemented device model.

6.1 TeraFET figures of merit

When characterizing and evaluating the performance of radiation detectors, two important figures of merit should be considered. On one hand, the *responsivity* describes the detectors radiation response signal relative to the amount of available radiation power - it is thus a quantity reflecting the efficiency of the underlying detection mechanism in the device. On the other hand the *noise equivalent power* (NEP) relates the detector's responsivity to it's inherent noise level, the NEP is thus understood as a measure of the detector's sensitivity.

We discussed before that the rectifying detection mechanisms in TeraFETs produces a measurable DC current $I_{\mathrm{det}}(\omega)$ or voltage $V(\omega)$ response to an incident high frequency radiation signal (cp. Chapter 2). Both quantities are related to each other following Ohm's law by the detector's DC drain-source resistance

$$V_{\mathrm{det}} = I_{\mathrm{det}} \cdot R_{\mathrm{DC}} \tag{6.1}$$

The magnitude of the measured responses depends on the available power of incident radiation, hence, in order to compare the performance of multiple detectors, the *current responsivity* and *voltage responsivity* $\mathfrak{R}_I$ and $\mathfrak{R}_V$ are defined as

$$\begin{aligned} \mathfrak{R}_I &= \frac{I_{\mathrm{det}}}{P_{\mathrm{in}}} \\ \mathfrak{R}_V &= \frac{V_{\mathrm{det}}}{P_{\mathrm{in}}} = \frac{I_{\mathrm{det}}}{P_{\mathrm{in}}} \cdot R_{\mathrm{DC}} \end{aligned} \tag{6.2}$$

The responsivity relates a measured THz response signal to the THz power available to the detector. Therefore, it is a measure for the efficiency of detection. Note that saturation effects may occur for very high radiation power levels and the dependence of responsivity on the incident power may no longer be linear in such cases. Also, it cannot be stressed enough here that a fundamental aspect in the concept of responsivity is the definition of the incidenct power P_{in} and the exact meaning of the term "available power". A detailed discussion on the topic follows in Section 6.1.2.

6.1.1 NEP and thermal noise of zero-biased TeraFETs

While the responsivity considers only the measured TeraFET response with respect to input power, for the characterization of the detector's *sensitivity* noise contributions to the detection signal must be taken into account. An according figure of merit is the NEP, which is defined as the ratio of the detector's current or voltage noise spectral density (I_N or V_N) in 1 Hz bandwidth and the current responsivity or voltage responsivity, respectively

$$\begin{aligned}\mathrm{NEP}_I &= \frac{I_\mathrm{N}}{\mathfrak{R}_I}\\ \mathrm{NEP}_V &= \frac{V_\mathrm{N}}{\mathfrak{R}_V}\end{aligned} \tag{6.3}$$

Hence, the NEP can be understood to yield a signal-to-noise ratio of unity for an input power at noise level. The unit of NEP is $\mathrm{W}/\sqrt{\mathrm{Hz}}$. The exact form of the noise spectral density depends on the device under investigation. We confirmed in a number of experiments that the dominating noise source in TeraFETs can be assumed to be thermal noise.[32]

Any electronic detector exhibits noise signals at the output depending on the mode of operation and intrinsic and parasitic circuit elements in the detection circuit. It manifests as a measureable *rms* noise current or voltage. The most basic form of electronic noise is the so-called *thermal* or *Johnson-Nyquist* noise of a simple resistor and was first described in detail by Schottky, Johnson, and Nyquist [112]–[114]. Its origin is the statistical, thermal motion of carriers within an ohmic resistance inducing a noise current or voltage, respectively, proportional to the square root of temperature and resistance [75, ch. 10]

$$\begin{aligned}V_\mathrm{N} &= \sqrt{4k_\mathrm{B}TR\Delta f}\\ I_\mathrm{N} &= \frac{V_\mathrm{N}}{R} = \sqrt{\frac{4k_\mathrm{b}T\Delta f}{R}}\end{aligned} \tag{6.4}$$

with Δf the noise bandwidth. Assuming an ideal *cold* (zero drain-biased) FET as before in Section 2.6 with negligible gate-to-channel conductance, we expect that the dominating noise source is indeed the thermal noise of the total drain-source resistance R_DC. This assumption is frequently made for TeraFET detectors [15], [48], [69], [110], [115], [116].

In order to verify the premise, we performed precise noise measurements for a number of TeraFETs realized in different material systems, namely a Si-MOSFET, an AlGaN/GaN HEMT and a graphene FET. Figure 6.1 shows the respective experimental data, which have in parts been published before. In the top left graph, the measured noise current of a 90 nm Si-CMOS TeraFET with resonant patch antenna is plotted against the theoretical thermal noise after Eq. (6.4) expected from measurements of its DC resistance [7]. The noise current lies well above the noise floor of an employed current amplifier and good agreement with the theoretical

[32] While this seems natural for an ideal transistor and is commonly claimed in TeraFET literature, experimental proof has - to the author's knowledge - not been published before.

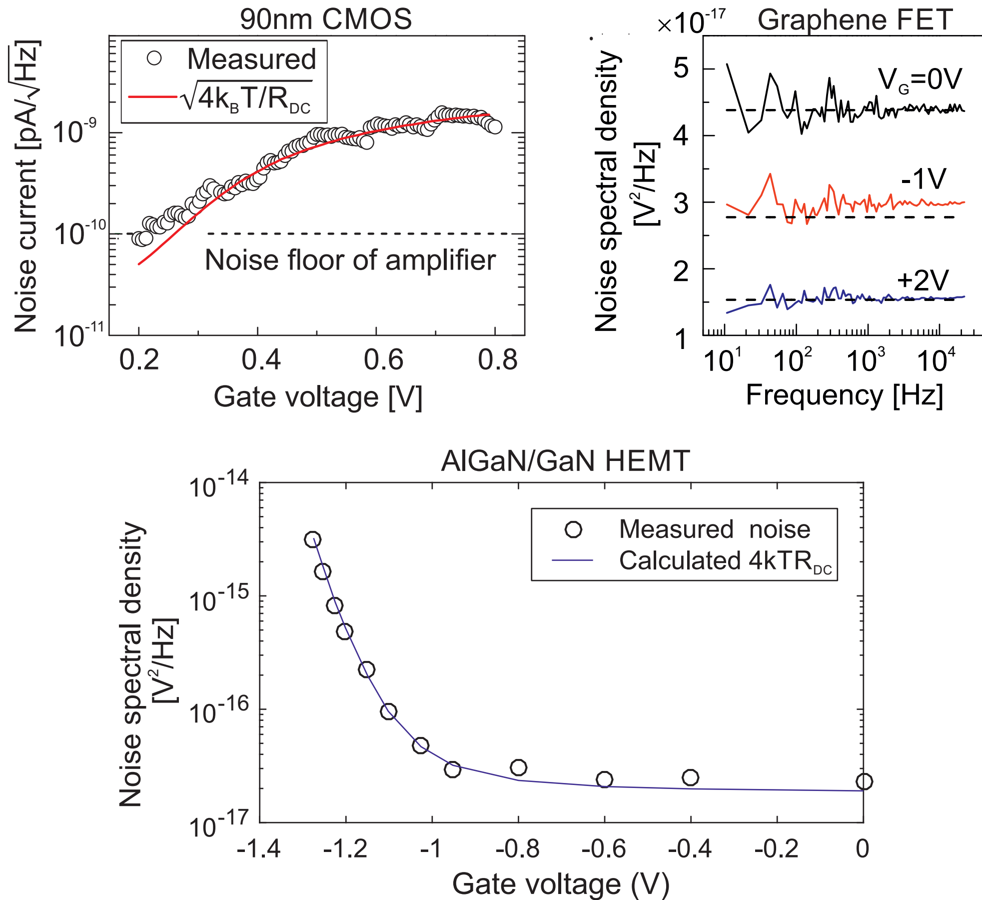

Fig. 6.1: Noise measurements for verification of thermal noise assumption in TeraFETs in various materials. Top left: 90 nm CMOS TeraFET with integrated resonant patch antenna[7]. Top right: Graphene FET with broadband bow-tie antenna (device details see Section 6.4, [5]). Bottom: AlGaN/GaN TeraFET with 100 nm and integrated broadband bow-tie antenna (device details see Section 6.3.3). Small deviations from the expected thermal noise, in particular in graphene and GaN, are most likely due to unwanted charging effects.

values is observed. The top right graph in the figure shows the noise spectral density of a CVD-grown graphene TeraFET (for device details see Section 6.4 and Ref. [5]) at three distinct gate bias voltages versus modulation frequency [5]. Except from a slight offset at $V_{\mathrm{G}} = -1$ V the measured noise again fits well to the theoretical thermal noise at the same bias points indicated as dashed horizontal lines for sufficiently high modulation frequencies [43]. It is assumed that the deviations for $V_G = -1$ V were caused by charging effects since the gate bias was applied over a relatively long time of several minutes. We discuss some of these issues in Ref. [10] and further investigation of charging effects in graphene can be found in Ref. [117]. Finally, the bottom graph shows the noise spectral density versus gate bias voltage of a recently measured AlGaN/GaN-based TeraFET (device details given in Section 6.3.3). Again, fairly good agreement with the expected curve after Eq. (6.4) is found.

In conclusion, from the above measurement results, thermal Johnson-Nyquist noise has been confirmed as the main noise source of the investigated TeraFETs. The

according NEP for TeraFETs therefore takes the form

$$\mathrm{NEP}_V = \frac{\sqrt{4k_\mathrm{B}TR_\mathrm{DC}}}{\mathfrak{R}_V} = \mathrm{NEP}_I = \frac{\sqrt{4k_\mathrm{B}T/R_\mathrm{DC}}}{\mathfrak{R}_I} \tag{6.5}$$

Note that other noise sources may be present in TeraFETs under non-ideal operation conditions. Deviations from the expected thermal noise can, e.g., be due to charging effects of defect states (in particular in AlGaN/GaN and graphene devices), unwanted gate leakage currents under high gate bias operation or $1/f$ noise contributions for low modulation frequencies. It is in particular the measurement of the DC drain-source resistance as basis for the calculation of thermal noise after Eq. (6.4), which must be carried out with great care. A more detailed treatment of this aspect is beyond the scope of this thesis and subject to ongoing research, but some further remarks on the problematic of precise measurement of the DC resistance and noise figures of TeraFETs have been made in Ref. [10]. Further theoretical insight can be found in literature dedicated to noise phenomena in semiconductor materials, a good introduction is, e.g., Ref. [118].

Whenever an exact quantification of the responsivity cannot be given - e.g., when the incident power cannot be determined - the sensitivity can be expressed in terms of a dimensionless *signal-to-noise ratio* (SNR)

$$\mathrm{SNR_V} = P_\mathrm{meas}/P_\mathrm{noise} \tag{6.6}$$

of measured signal power and measured noise power. In some of the performed characterization experiments presented below, the available THz power was to low for a quantitative measurement with available calibrated powermeters. Therefore, the SNR of the TeraFET under investigation was compared to the SNR of other detectors in order to evaluate its performance. The SNR is often expressed in dezibel (dB) when the dynamic range of the measured signals is large.

6.1.2 Optical versus electrical responsivity and NEP

It was mentioned above that a crucial parameter for the determination of responsivity and consequently NEP of TeraFETs is the precise definition of the input power P_in to which the measured detector signals are related. Here, a number of effects must be accounted for - the efficiency and effective area of the integrated receiving antenna, antenna matching to the intrinsic channel region, optical losses due to beam-shaping elements such as substrate lenses, and possible additional extrinsic parasitic losses. Details on the matter cannot be discussed in the scope of this thesis and we just give a short summary of the most important factors, which influence the power reaching the active detector.

First, free-space radiation is coupled to the active detector elements via integrated antenna structures with finite radiation *efficiency*. Power may be lost due to ohmic losses in the antenna, which is accounted for by an antenna efficiency factor. At the same time, any antenna exhibits a *directivity* depending on the characteristic radiation pattern of the specific type of antenna. Free-space power is effectively coupled only in certain directions and an *antenna gain* can be defined as the product

of antenna efficiency and directivity. The for aperture antennas can be expressed in terms of an antenna *effective area* [75] related to the geometric dimensions of the antenna structure. The effective area is “the ratio of the available power at the terminals of a receiving antenna to the power flux density of a plane wave incident on the antenna” [119, p. 83]. Loosely speaking the effective area is a measure of how effectively the antenna accepts power from an incident plane wave electric field. Without going into much further details here, it can be shown from basic antenna theory that the maximum effective area relates to the antenna gain as [119, ch. 2]

$$A_{\text{eff}} = \frac{G\lambda^2}{4\pi} \tag{6.7}$$

This approach is often applied in the literature to estimate the power for the calculation of the TeraFETs responsivity.

Second, the above equation implicitly assumed perfect conjugate matching of antenna and load impedance. Although it is the designers task to fulfill this condition best possible, in general, the antenna impedance Z_{ant} may not be exactly matched to the load for all operation frequencies, i.e., in the case of a TeraFET detector, the impedance of the intrinsic channel region Z_{t}. An *antenna matching factor* can be defined as the ratio of the power delivered to the antenna load P_{L} and the maximum available power from the antenna P_{max}. From basic transmission line theory [75, ch. 2][76, ch. 9] the antenna matching factor can be derived to be [43]

$$M(Z_{\text{ant}}, Z_{\text{t}}) = \frac{P_{\text{L}}}{P_{\text{max}}} = \frac{4\text{Re}\left\{Z_{\text{ant}}\right\}\text{Re}\left\{Z_{\text{ug}} + Z_{\text{g}}\right\}}{\left|Z_{\text{ant}} + Z_{\text{ug}} + Z_{\text{g}}\right|^2} \tag{6.8}$$

where we have already used that the HF impedance of the transistor “seen” by the antenna for ideal drain coupling as illustrated in Fig. 5.5 is $Z_{\text{t}} = Z_{\text{ug}} + Z_{\text{g}}$.

Third, optical losses in the experimental system may be present, e.g., at interfaces of optical components such as substrate lenses. Internal reflections in the optical components may be present under non-ideal Gaussian beam coupling conditions [120], [121]. An aplanatic optical configuration minimizes these influences and was employd in our experiments (see below).

As a further aspect, recall from Chapter 5 that power incident on the TeraFET device is distributed over the detector related to the HF impedances of intrinsic and extrinsic circuit elements. It was discussed that only the fraction of incident power reaching the gated channel region is available for the plasma wave detection mechanism. Including optical losses, antenna factors and power distribution to the intrinsic detector part, the (current) responsivity and NEP after Eqs. (6.3) and (6.5) of the TeraFET should ideally be given with respect to this power actually reaching the transistor channel as

$$\mathfrak{R}_I^{\text{el}} = \frac{I_{\text{det}}}{P_{\text{in}}^{\text{el}}}, \quad \mathfrak{R}_V^{\text{el}} = \frac{V_{\text{det}}}{P_{\text{in}}^{\text{el}}} \tag{6.9}$$

$$\text{NEP}^{\text{el}} = \frac{\sqrt{4k_{\text{B}}T/R_{\text{DC}}}}{\mathfrak{R}_I^{\text{el}}} = \frac{\sqrt{4k_{\text{B}}TR_{\text{DC}}}}{\mathfrak{R}_V^{\text{el}}} \tag{6.10}$$

We term the respective quantites *electrical* responsivity, NEP and power denoted by the superscript “el”.

In real detection experiments of free-space THz radiation with TeraFETs it is in general not easily possible to determine the power $P_{\mathrm{in}}^{\mathrm{el}}$ reaching the transistor channel and probing the electric field in the channel experimentally is hardly feasible. Therefore, determination of the TeraFET's electrical responsivity and NEP is commonly based on reasonable assumptions on optical, antenna, and parasitic losses [20]. It is convenient to define a responsivity and NEP of a TeraFET related to the total available power in the THz beam at the detector's position. We term the quantities *optical* responsivity and NEP denoted by the superscript "opt"

$$\mathfrak{R}_I^{\mathrm{opt}} = \frac{I_{\mathrm{det}}}{P_{\mathrm{in}}^{\mathrm{opt}}}, \quad \mathfrak{R}_V^{\mathrm{opt}} = \frac{V_{\mathrm{det}}}{P_{\mathrm{in}}^{\mathrm{opt}}} \tag{6.11}$$

$$\mathrm{NEP}^{\mathrm{opt}} = \frac{\sqrt{4k_{\mathrm{B}}T/R_{\mathrm{DC}}}}{\mathfrak{R}_I^{\mathrm{opt}}} = \frac{\sqrt{4k_{\mathrm{B}}TR_{\mathrm{DC}}}}{\mathfrak{R}_V^{\mathrm{opt}}} \tag{6.12}$$

Naturally, the optical values represent the performance of the system "antenna + detector" and can be viewed as conservative lower and upper limits for the the electrical responsivity and NEP, respectively, of the de-embedded active TeraFET transistor.

Unfortunately, in literature on experimental determination of TeraFET detector performances it is not always clearly pointed out how presented values were obtained from measurement data. We stress here again, that a meaningful comparison of detectors is only possible when the above considerations are met with particular care. It is essential that underlying assumptions on, e.g., optical reflection losses, antenna efficiency, etc. are precisely stated.

6.2 Experimental setups

This section describes the general experimental setup, which was employed to characterize fabricated TeraFETs in THz detection experiments. Some specific modifications are addressed in the respective sections for the individual devices under test.

6.2.1 DC measurements

Measurements of the DC drain-source resistance of the fabricated TeraFETs were performed to allow for the extraction of physical device parameters, which form the basis for analytic and numerical calculation with the TeraFET models presented in the previous chapters. A two-stage fit routine for parameter extraction from the measured DC resistance of AlGaN/GaN TeraFETs was discussed in Chapter 4. In Section 6.1.1 we pointed out that precise measurements of the DC resistance are essential for an accurate calculation of the thermal noise in TeraFETs when evaluating the detector's sensitivity in terms of NEP after Eq. (6.5).

For our experiments we employed a high-precision semiconductor analyzer SMU (*source-measure-unit*) to obtain the DC drain-source conductance $G_{\mathrm{DC}} = I_{\mathrm{D}}/V_{\mathrm{D}}$ from measurement of the drain current $I_{\mathrm{D}}(V_{\mathrm{G}}, V_{\mathrm{D}})$ versus applied gate voltage V_{G}. The measurement setup is illustrated in Fig. 6.2. The source terminal in our devices is always defined to lie on common DC ground set as $V_{\mathrm{S}} = 0$ V reference. We used

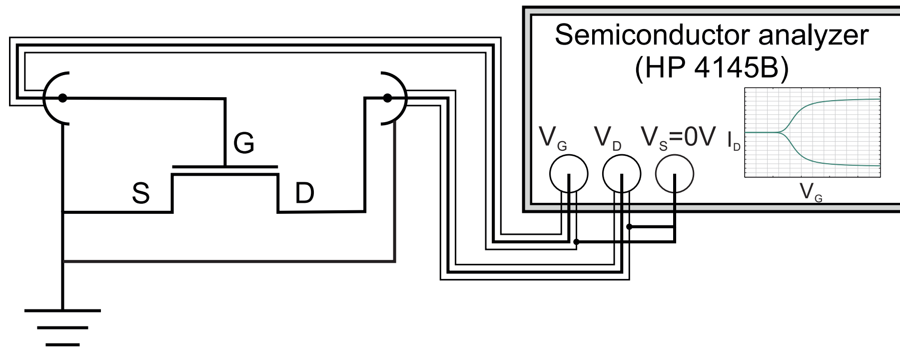

Fig. 6.2: Setup for the measurement of the TeraFET's DC drain-source resistance R_{DC}.

shielded BNC cables for connection of the TeraFETs where the shielding for both gate and drain were connected to the same DC ground of the voltage source. A small drain voltage of $V_{\mathrm{D}} = \pm 0.01$ V was applied in forward and backward direction to bias the device and the DC drain-source resistance $R_{\mathrm{DC}} = V_{\mathrm{D}}/G_{\mathrm{DC}}$ was obtained as an the average of the two measurements. It is expected that minor fluctuations of the channel resistance can to some extent be averaged out. Note however, in particular when strong hysteresis behavior is present in the device, e.g., due to charging of defect states in the employed materials, an averaging is not advisable and device characterization should be performed independently for forward and backward biasing and a full hysteresis analysis should be included.

6.2.2 THz sources

The measurements presented in this work were performed with two different sources for THz radiation, namely a frequency tunable all-electronic source working in the range of 490 to 650 GHz and a fiber laser-based optoelectronic source working in a much wider frequency range of 50 GHz up to 1.2 THz.

All-electronic THz source

Since direct electronic generation of radiation in the THz frequency regime is highly challenging,[33] a widely employed approach is the electronic generation of lower frequency continuous-wave (CW) in the GHz region and frequency upconversion to the THz by nonlinear mixing in, e.g., diode-based multipliers. Such systems are frequently named *all-electronic* sources and common frequencies lie in the range of some tens of GHz up to roughly 2 THz. Examples of electronic oscillators for the generation of the fundamental frequencies are Gunn diodes and high frequency transistors [43], [126]. Multiplication of the fundamental frequency then happens in a fine-tuned chain of waveguide-based amplifiers and frequency multipliers to achieve the desired output frequency range and power levels, where as a general rule, wider tunable output ranges yield lower maximum achievable output powers and vice versa.

[33] Examples are backward wave oscillators (BWOs), traveling-wave tubes (TWTs) and other vacuum electronic devices [122], semiconductor-based technologies like resonant tunnelling diodes [123]–[125], and even accelerator-based sources like the free electron laser (FEL)[122].

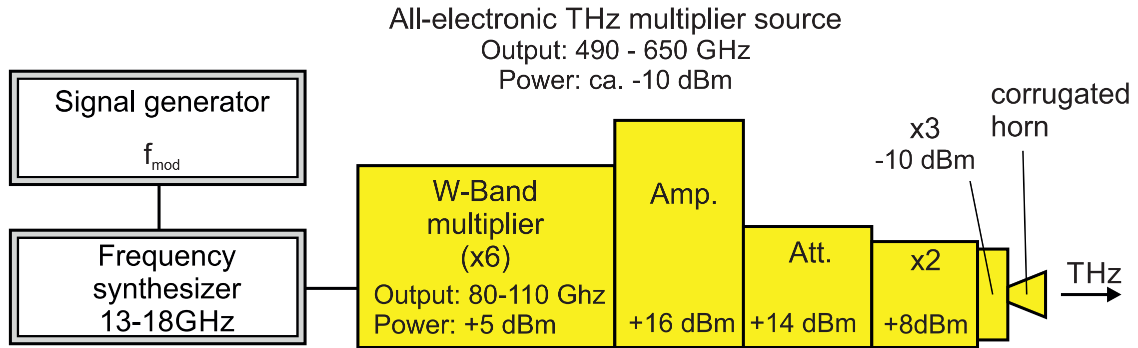

Fig. 6.3: Schematic of the employed all-electronic, multiplier chain-based THz source. The output frequency was tunable in the range of 490 to 650 GHz with an output power of roughly -10 dBm. A synthesizer with output frequency between 13 and 18 GHz was used to drive the source. The output was electronically chopped with a rectangular modulation signal f_{mod} in the range of 300 Hz up to 3 kHz.

Typical output powers for all-electronic multiplier chain-based THz sources lie in the range of several ten microwatts up to a few milliwatts depending on the exact configuration and maximum frequency.

Figure 6.3 shows a schematic drawing of the commercial[34] all-electronic source, which was used for calibrated THz measurements presented in this work. The source was tunable in the range of 490 to 650 GHz with the fundamental oscillation frequency around 13 to 18 GHz being provided by an external electronic frequency synthesizer (HP 8341A). The figure gives rough power levels of the individual stages of the waveguide-based multiplier chain while a detailed swept measurement of the output power of each stage acquired with an photoacoustic powermeter (see below) is plotted in Fig. 6.4. After initial multiplication of the input signal to the W-Band, the output is amplified by an MPA amplifier and flattened over the available frequency range. A subsequent variable attenuater was used to adjust to the maximum input power level of the following active frequency doubler. Finally, a passive frequency tripler multiplies the signal to the 490 to 650 GHz region. The THz frequencies are then irradiated by a corrugated horn antenna.

The main advantage of todays electronic THz sources are relatively high output powers compared to other, e.g., optoelectronic systems. The output power of the employed source allowed calibrated power measurements with a large-area, photoacoustic powermeter[35] with a typical NEP of 5 $\mu\text{W}/\sqrt{\text{Hz}}$. Calibrated measurements of the available THz power are essential in TeraFET characterization experiments for a reasonable evaluation of absolute detector performances (comp. previous section). The detection principle of the photoacoustic powermeter is based on ohmic heating of a thin metal film inside a large-area, gas-filled cavity by the incident radiation. The pressure change is transformed into an ouput voltage signal of the device. Since the working principle is radiative absorption in the metal film, the powermeter is extremely broadband and specified for "30 Hz to 3 THz and beyond" [128]. As a

[34] Custom built by RPG Radiometer Physics GmbH [127]

[35] Thomas Keating Ltd. Absolute Terahertz Powermeter [128]

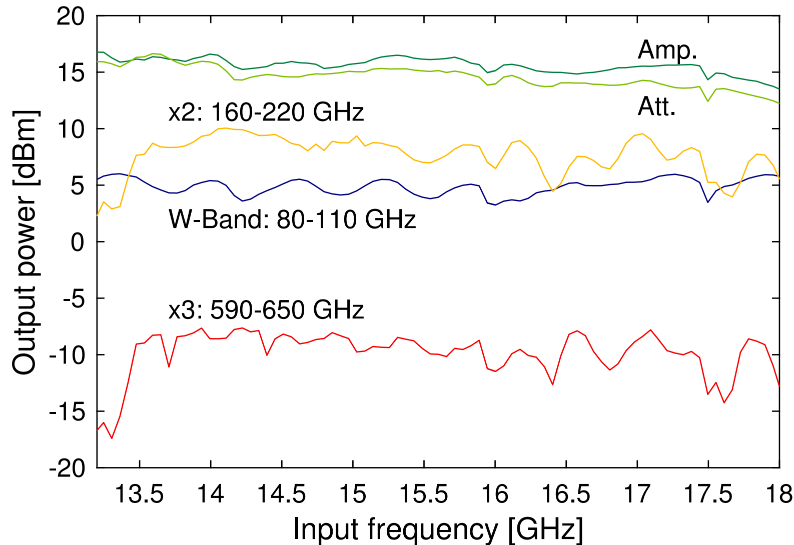

Fig. 6.4: Ouput powers of the individual stages of the multiplier chain of the all-electronic THz source employed for TeraFET characterization.

downside of the thermal heating principle, the response time is comparably slow and the modulation frequency was limited to 30 Hz.

Photomixer THz source

For broadband characterization of our TeraFETs we used a second THz source, namely a CW optoelectronic, two-color fiber laser-based photomixer system.[36] THz radiation is generated by coherent superposition of two laser beams with defined detuning so that the difference frequency $\Delta f_{\mathrm{THz}} = f_2 - f_1$ of intensity modulation of the resulting beating signal lies in the THz region [131]. The combined laser beam is focused onto a narrow gap of a microscopic metal-semiconductor-metal structure periodically generating free charge carriers which are accelerated in an applied DC bias field. The coherent superposition of the individual motion of charge carriers induces an oscillating photocurrent, which is fed to an integrated planar antenna for broadband emission of the electric THz field. Some more details on the process of THz generation by photomixing in semiconductors can be found, e.g., in Ref. [126], [131]. The photomixer system employed in our characterization experiments was based on InGaAs/InP semiconductor material and emitted a linear polarized beam from an integrated bow-tie antenna. An illustration of the system is shown in Fig. 6.5. Photomixer-based THz sources offer a wide range of tunability by altering the difference frequency of the applied lasers. The described system used two *distributed feedback* (DFB) lasers, whose frequencies could be tuned by thermal controlling of the internal grating structures and/ or controlling of the laser currents. In total, the system offered broadband tunability over a bandwidth from 0.1 GHz to 1.2 THz.[37] The photomixer source yielded output powers of roughly 48 µW at 100 GHz,

[36] TOPTICA TeraScan 1550 [129], [130]

[37] Replacing one of the laser modules enabled additional laser combinations and allowed an enhancement of the output frequency range up to 2.7 THz [130]

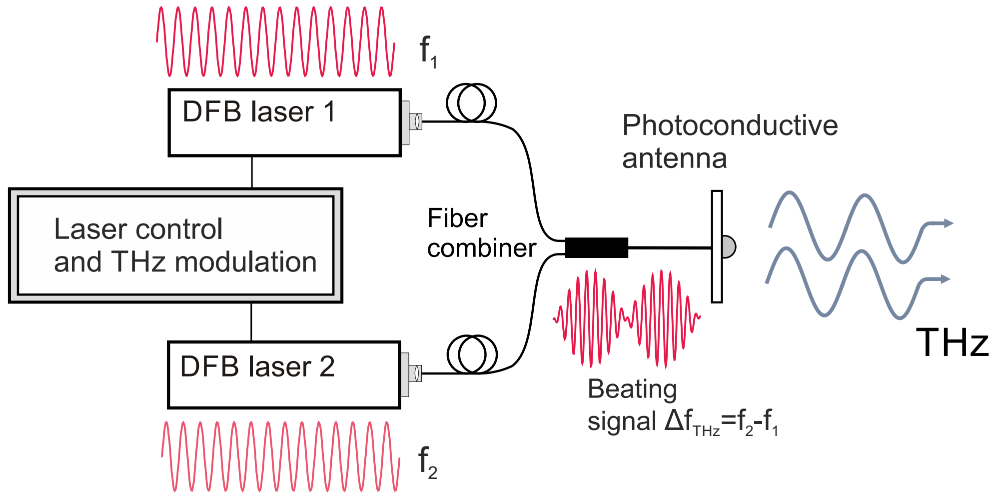

Fig. 6.5: Schematic of the photomixer-based THz source (Toptica TeraScan 1550[129]) in a spectroscopy configuration setup. The beating signal of two temperature and current-adjustable distributed feedback (DFB) lasers around 1550 nm is focused onto a photoconductive antenna fabricated in InGaAs. Application of a modulated AC bias generates an oscillating photocurrent, which induces the irradiation of continuous-wave THz waves via the integrated broadband bow-tie antenna. The same principle can be applied for coherent detection (Rx) of the transmitted (Tx) signal. The output frequency of the employed source was from 0.1 to 1.2 THz.

exponentially decreasing down to 4 µW at 500 GHz and 0.4 µW at 1 THz [13], [130].

In contrast to the all-electronic source, the comparably low output power levels of the photomixer THz system did not allow for a power measurement with the calibrated photoacoustic powermeter. Nevertheless, we employed the source in TeraFET characterization experiments to investigate the broadband behavior of our devices. Measurement results were compared to the TeraFET performance in terms of detector SNR (comp. Section 6.1.1) with two reference detectors. First, a second photoconductive antenna similar to the one for transmission of the generated THz radiation could be employed for coherent detection of the THz signal. As a second reference we used a Golay cell with an estimated, flat response over the investigated frequency range. Although the Golay cell offered a higher sensitivity than the photoacoustic powermeter, no absolute power calibration was available for an accurate determination of the output power of the broadband photomixer system.

It should be noted that the photomixer system for both, the transmitter and receiver module, employs planar bow-tie antennas with certain frequency-dependency of directivity. We observed a slight movement of the THz beam with respect to the optical axis of our setup. The variations, however, were small and we neglected the influence on optimal detector alignment when performing frequency sweep measurements. A possible improvement could be the automation of precise detector alignment with electrical actuators, however, this could drastically increase the measurement time and was not implemented at the time of TeraFET characterization.

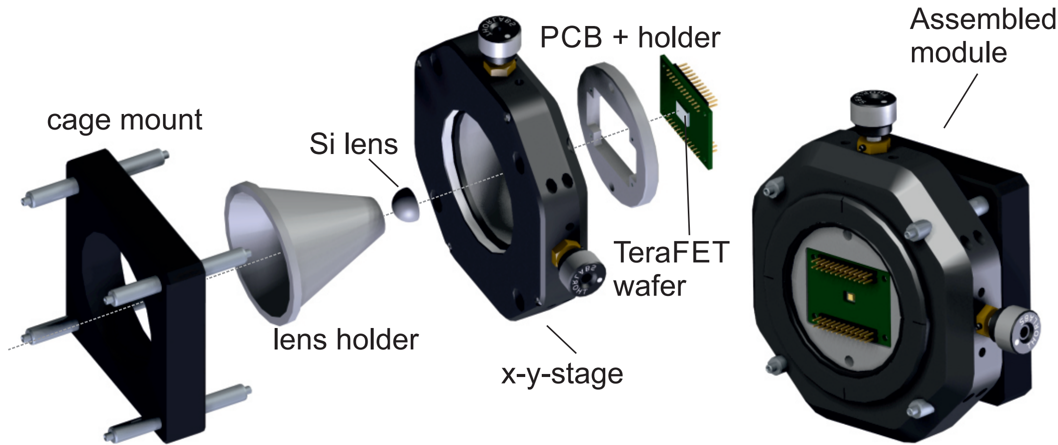

Fig. 6.6: TeraFET detector module. The semiconductor die containing the actual TeraFETs with integrated antennas is placed on a Si carrier wafer and then glued and wire-bonded to a PCB board for electrical contacting. A hyper-hemispherical Si lens in fixed on the setup's optical axis by a lens holder. The PCB with the TeraFET die is mounted in a x-y translation stage for selection of individual detectors and for precise alignment with respect to the fixed substrate lens.

6.2.3 Detector module

The fabricated semiconductor dies containing several TeraFETs were integrated in a compact detector module mainly for experimental reasons. On one hand, the usual chip size of the semiconductor dies is very small (a few square millimeters) and electrical contacting must be realized via wire bonding or needle probing of integrated contact pads. In particular during the experimental phase of characterization of newly fabricated devices, the possibility of easy switching between detectors on the same die without having to disassemble the experimental setup is desirable. On the other hand, the main direction of directivity is perpendicular to the surface into the direction of the substrate for planar antenna structures. Therefore, including a silicon substrate lens on the backside of the silicon wafer can eliminate power loss due to unwanted substrate modes[121]. For these purposes we developed detector modules incorporating the above experimental requirements.

Figure 6.6 shows a technical drawing of a TeraFET module. The semiconductor die containing the TeraFETs was glued with the substrate side to a piece of high resistivity silicon wafer as a sample holder. The wafer in turn was then glued to a printed circuit board (PCB) containing contact pads and pin connectors in a standard layout for all individual TeraFETs on a single detector die. Contacting of the detectors was realized via gold wire bonding. The PCB was attached to an x-y translation stage mountable on a standardized cage system for easy positioning of the module on the optical axis of the THz setup. Electrical connection of the individual TeraFETs was via the accessible pin connectors on the backside of the module. A Si substrate lens was held in place on the optical axis by a conically tapered holder (see drawing). With this combination of fixed substrate lens and adjustable sample holder, alignment of the TeraFET under test as well as switching between devices without altering the optical system was possible.

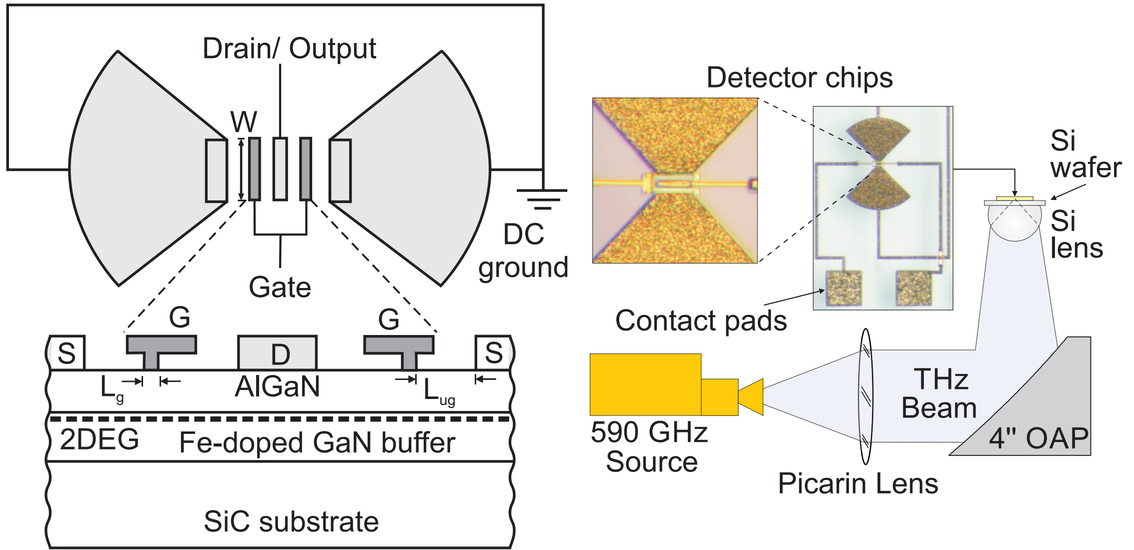

Fig. 6.7: Left: TeraFET design and technology schematic of differential AlGaN/GaN HEMT transistors with integrated broadband bow-tie antenna. Device parameters are $L_{\mathrm{g}} = 250$ nm, $L_{\mathrm{ug}} = 500$ nm and varying widths of $W = 3$, 5, 10, 20, and 50 µm. Right: Experimental setup for detector characterization. Figure reproduced from [15].

In our setups, we employed a hyper-hemispherical Si substrate lens for optimal Gaussian beam coupling. The lens had a diameter of 12 mm and a total thickness of 6.8 mm. Together with the carrier wafer ($\sim$ 400 µm), a total thickness of 7.2 mm is reached. The lens and quasi-optical THz setup were optimized for aplanatic configuration minimizing internal reflection losses inside the substrate lens [120], [121]. Therefore, a pre-focused THz beam is used in the experiments (see below). For our optical configuration we estimate Fresnel reflection losses of roughly 30% at the air-Si-interface. Assuming a Gaussicity of approximately 90% at 600 GHz [121] we calculate a Gaussian beam coupling efficiency of $\sim$ 63% for our TeraFET modules.

Note that in certain experimental environments, external electromagnetic parasitic signals can constitute a significant noise source in the TeraFET characterization setup. We experienced such problems in particular with Q-switching lasers, motion controllers and pulsed electrooptical THz sources. We therefore developed a smaller version of the presented detector modules enclosed in a shielded housing, which could overcome some of the external influences. For further improvement, integration of low-noise amplifiers on the module's PCB is currently being realized.

6.3 AlGaN/GaN TeraFETs

This section presents characterization results for broadband AlGaN/GaN TeraFETs. A number of generations of detectors were fabricated over the course of this work to yield optimized sensitivity and broadband performance based on experimental evaluation and modeling of devices with the TeraFET models presented in this thesis. The design and fabricaton of AlGaN/GaN TeraFETs was part of a joint funded research project of Goethe-University Frankfurt and the Ferdinand-Braun-

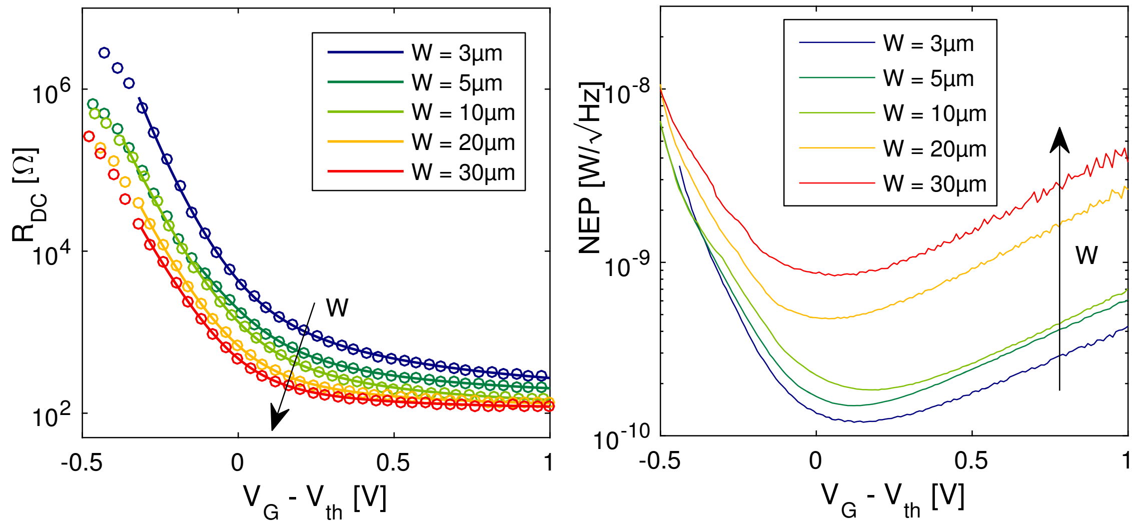

Fig. 6.8: Left: DC drain-source resistance R_{DC} and resistance fits for TeraFETs with different gate width. Right: Optical NEP measured at 590 GHz.

Institut, Leibniz-Institut für Höchstfrequenztechnik (FBH), Berlin. Devices were produced by FBH and most of the characterization experiments were carried out at Goethe-University.

There are several reasons why GaN in particular was chosen as material system for the implementation of the TeraFETs. Most prominently, GaN provides high break through voltages and can be operated at much higher powers than, e.g., conventional Si CMOS technology. An exceptional radiation hardness make GaN electronics in particular interesting for application in harsh environments, for example in space applications. From an electronic transport point-of-view, GaN offers high saturation velocities and significantly higher mobilities than, e.g., silicon. Those are some of the reason why we chose GaN as a material for our TeraFET implementation. Some further discussion on GaN material in the context of HF application can be found in [50], [132], [133].

6.3.1 First detector generation, variation of gate width

A first generation of AlGaN/GaN devices was produced to investigate the influence of the gate width on the TeraFET sensitivity. The results of the THz characterization presented in this section have previously been published in Ref. [15]. It should be mentioned that these detectors were designed prior to the in-depth development of the presented detection model and device design was the result of thourough considerations and experience from TeraFET fabrication in other materials, mostly Si CMOS [7], [19], [42], rather than based on detailed device simulations. Nevertheless, we could achieve high detection sensitivities at 0.6 THz down to 120 pW/$\sqrt{\text{Hz}}$, which compared well to similar results obtained with TeraFETs fabricated in Si CMOS with a resonant antenna design and comparable device parameters [15].

TeraFETs with different gate widths of $W = 3, 5, 10, 20$, and 30 µm were fabricated in an inhouse-developed 0.25 µm AlGaN/GaN process at FBH [134] on semi-insulating SiC substrate, which offers good THz transparency for backside illumination through

a Si substrate lens. A schematic of device design and AlGaN/GaN HEMT technology is shown on the left in Fig. 6.7. This first generation of GaN-TeraFETs was designed as a differential two-transistor layout, ensuring asymmetric boundary conditions of radiation coupling from the source side only[38] by placing the drain output at the antenna's AC ground at the center node. The rectified THz signal was read out at this same point from the transistor's drain port.

The right side of Fig. 6.7 shows a drawing of the experimental setup for THz characterization of the TeraFETs. An all-electronic, multiplier-based THz source similar to the one described in the previous section but operating in resonant configuration at 590 GHz was used. The source was electronically chopped with a rectangular modulation signal at 333 Hz and the detection signal was recorded with a lock-in amplifier at the same reference frequency. The diverging THz beam was collimated by a 10 cm Picarin lens and pre-focused by a 4" off-axis paraboloidal gold mirror. The available power in the THz beam was 22 µW at the position of the detector module employing a Si substrate lens with 12 mm diameter and height of 6.8 mm in aplanatic configuration [120], [121] to focus the beam onto the TeraFETs through the SiC substrate. Contacting of the TeraFETs was achieved with needle probes on a probe station, which was built inhouse and which allowed alignment - and thereby selection of individual devices on a single die - perpendicular to the impinging THz beam.

Fundamental device parameters were extracted by fitting measured DC drain-source resistances following the fit procedure[39] as described in Section 4.2.2. The obtained fit curves along with the mesurement data are plotted in the left graph of Fig. 6.8. Besides minor deviations between individual devices, in particular the overall reduction of channel resistance with increasing gate width is observed (comp. Eq. (2.25)). The extracted device parameters are listed in Table 6.1 together with obtained values for optical NEP. Notice that some of the parameter variations seem to indicate a problem with the measured DC data and/ or the parameter extraction by the fit routine, respectively. In particular, one would expect a monotonically increasing ungated resistance R_{ug} for narrower transistors. To this point the exact cause of this unexpected behaviour could not be determined conclusively. Nevertheless, the extracted carrier mobilities μ and threshold voltages V_{th}yield reasonable physical parameters in accordance with technological parameters obtained from other experiments (not presented here).

Figure 6.8 shows the measured optical NEPs of the fabricated TeraFETs characterized at 590 GHz. We observe an increasing NEP (decreasing sensitivity) with increasing gate width. This is in qualitative agreement with theoretical considerations [3]. It can be shown easily that the (quasi-static) current responsivity of the intrinsic TeraFET transistor is independent of the channel width W (comp. Eq. (2.20)). On the other hand, the DC channel resistance depends on the inverse channel width according to Eq. (2.25). Consequently, the thermal current noise spectral density

[38]Note that this is similar to the drain coupling boundary conditions from previous chapters, since labelling of source and drain is arbitrary.

[39]No special adaptions of the fit procedure were made to account for possible differences of the two-transistor layout.

Table 6.1: Device parameters and measured $\mathrm{NEP}^{\mathrm{opt}}$ for AlGaN/GaN TeraFETs with different gate widths W.

Channel width W [µm]	Mobility μ [cm^2/Vs]	η_1/η_2	V_{th} [V]	R_{ug} [Ω]	$\mathrm{NEP}^{\mathrm{opt}}$ [pW/$\sqrt{\mathrm{Hz}}$]
3	1236	2.9/2.0	-1.67	82	120
5	1651	0.2/2.4	-1.85	121	150
10	1206	1.9/2.2	-1.62	88	184
20	1274	2.0/2.4	-1.68	105	473
30	1337	1.6/2.3	-1.68	103	836

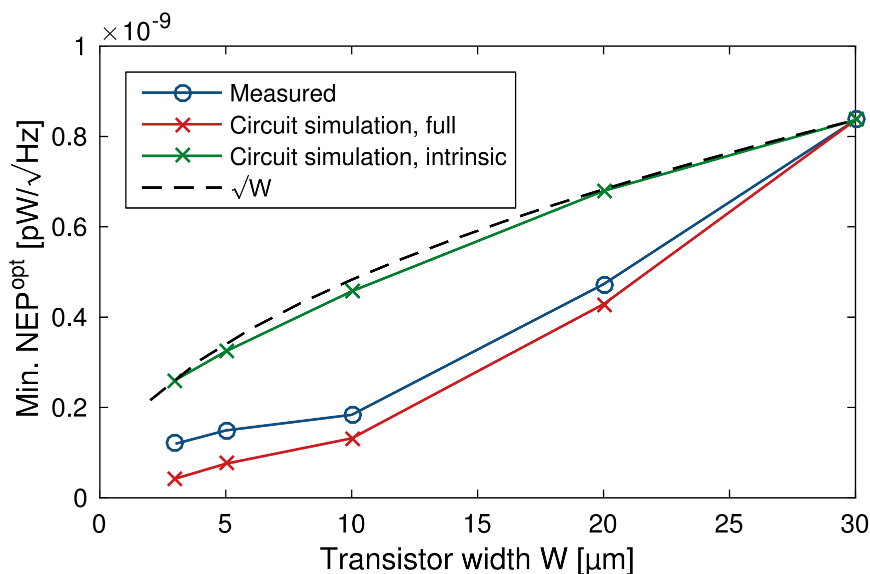

Fig. 6.9: Simulated versus measured NEPs at 0.6 THz of TeraFETs with different gate widths. The values are extracted at gate bias points of optimal detector operation determined from the experimental NEPs. Crossed lines show simulation results with the circuit implementation for intrinsic model only (green) and for full TeraFET model (red) including ungated regions and a fixed antenna impedance of 75 Ω.

and therefore the NEP (comp. Eq. (6.5)) should scale with the square root $\sqrt{W}$ of the channel width. Figure 6.9 as green line shows circuit simulations of the intrinsic transistor region for device paramters as given in Table 6.1. The square root dependence of the NEP on the channel width is indicated as dashed black line and the dependence is well reproduced by the simulation (simulation data was normalized to the measured optical NEP for the TeraFET with 30 µm width).

Notice, however, that the above consideration assumed perfect matching of the integrated antenna to the channel. The investigated devices were designed with the same antenna structure varying only the width of the metal contact of source and drain terminal but keeping the geometry of the antenna bows unaltered. Decreasing of the channel width leads to an increased channel impedance and impedance matching to the antenna cannot be achieved for all devices with different gate widths. In

particular, the power transfer to the intrinsic channel region is not optimized. Hence, the current responsivity shows variation with gate width in contrast to intrinsic TeraFET theory (data shown in [15]). Figure 6.9 gives measured optical NEP (circle line) and simulated NEP from the circuit implementation (red crossed line), where ungated regions have been included in the simulation, as well as a fixed antenna impedance of $Z_{\mathrm{ant}} = 75\ \Omega$. Circuit simulation an measured data show a good agreement. Furthermore, the overall trend of increasing NEP for wider channels is confirmed. However, a difference in functional dependence on W can be observed and must be attributed to imperfect matching conditions.

In conclusion, optimal detection performance in a real device should be reached for a trade-off between reduction of the channel width and retaining close-to impedance matching conditions[3]. This underlines once more the need for a careful design of TeraFET detectors including extrinsic influences on the device performance as enabled by the presented equivalent circuit model implementation. Some further discussion on the topic of optimal transistor width-to-length ratio for CMOS-based devices can be found in Refs. [43], [135]. THz characterization experiments yielded best device performance for the smallest feasible device geometry with a transistor width of $W = 3$ µm. The best achieved optical NEP of 120 $\mathrm{pW}/\sqrt{\mathrm{Hz}}$ compares well with competing Si CMOS technology of the same device geometry[15].

6.3.2 Improved detectors, bow-tie and log-spiral design

A second, optimized generation of AlGaN/GaN TeraFETs was designed with two different layouts of integrated antenna structures for broadband THz detection. The transistor gate length remained at $L_{\mathrm{g}} = 0.25$ µm in a similar GaN MMIC process as before [134]. However, improved fabrication technology allowed for a reduction of the access regions to an ungated channel length of $L_{\mathrm{ug}} = 0.35$ µm in the bow-tie TeraFETs. The transistor width was chosen as $W = 3$ µm following the experimental findings presented in the previous section. Characterization results of devices with integrated broadband bow-tie antennas have in parts been published before in Refs. [13]. A second antenna design was implemented, namely a log-spiral antenna for circular polarization of the THz beam. First measured values for optical NEPs at several distinct THz frequencies were reported in Ref. [3].

Figure 6.10 shows a simplified schematic (not to scale) of the TeraFET layout and technology together with miscroscopic photographs of two fabricated devices, one with bow-tie and one with log-spiral antenna design. Special emphasis during the design phase of the detectors was laid on two main aspects. First, the TeraFETs were embedded in an electric stabilization environment. Large-area *metal-insulator-metal* (MIM) capacitors and series resistances in the electric feed lines were included for DC decoupling of the HF antenna structure. A grounded ring surrounding the antenna was added to prevent cross-talk between neighboring circuits on the same die and to yield a defined area of illumination for the integrated antenna. Second, optimized drain-coupling boundary conditions were aimed for by introducing capacitive coupling between gate and source. For this purpose, both the gate and source contact were laid out as large-area metal sheets in the shape of one of the bow-tie wings and separated by a 200 nm $\mathrm{SiN_x}$ dielectric ($\epsilon \approx 7 - 7.5$) forming an additional MIM

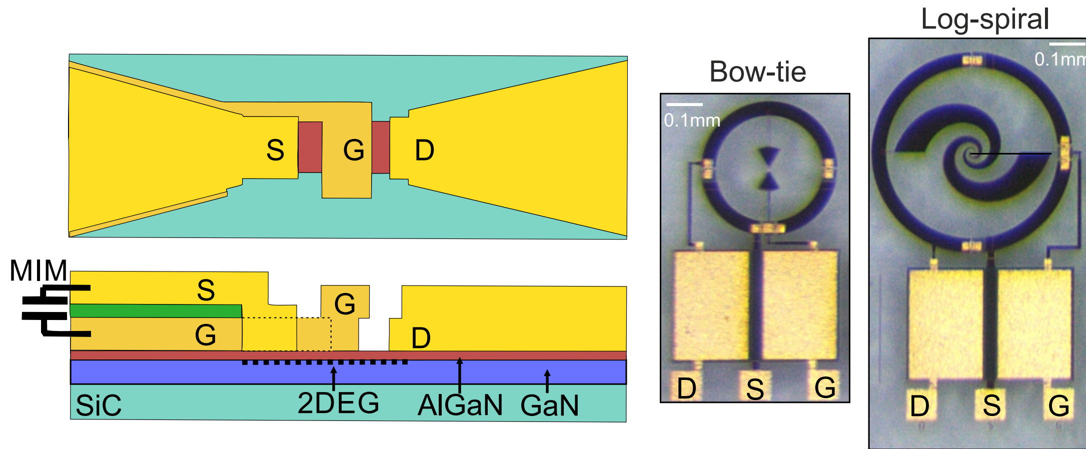

Fig. 6.10: Schematic of the optimized AlGaN/GaN TeraFET design with integrated broadband bow-tie antenna. A similar MIM coupling scheme was implemented for the log-spiral antenna design. The magnified photographs show the TeraFETs integrated in an electric stabilization environment with shielding ground ring and large DC decoupling capacitors.

capacitor between the two terminals as illustrated in Fig. 6.10. The bow-tie antenna was designed with an opening angle of the bow-tie wings of 60 degrees and a single bow length of 60 µm. The log-spiral design had a radius of 208 µm and, similar to the bow-tie design, a gate-source capacitance was implemented as MIM capacitor under one of the antenna arms. Device parameters were extracted from DC drain-source resistance measurements with the fit routine described in Section 4.2.2. A resistance fit of one of the bow-tie TeraFETs together with extracted parameters was shown before in Fig. 4.2. The electron mobility was determined independently at FBH by Hall measurements, where a mobility of roughly $\mu \approx 0.16\ \mathrm{m^2/Vs}$ was found, which compares well to our result from parameter extraction.

We performed broadband THz characterization of the fabricated TeraFETs with the photomixer-based THz source in the frequency range from 0.15 to 1.18 THz. The experimental setup was slightly modified compared to the one described previously. Here, we employed a combination of two lenses to collimate and pre-focus the THz beam onto the detector module described in Section 6.2.3. The experiments were performed with both the photomixer THz source for broadband characterization and two all-electronic sources for power-calibrated reference measurements working at 210 to 360 GHz and at 590 GHz, respectively (comp. Section 6.2.2). A schematic drawing of the experimental setup is depicted in Fig. 6.11. For the electronic sources setup two PTFE lenses with 10 cm focal length were used, while for the photomixer system - for reasons of THz beam characteristics - the first lens was replaced by a PTFE lens with 5 cm focal length. The lenses as well as the detector module could be translated perpendicular to the THz beam for fine adjustment of the optical setup.

Figure 6.12 shows optical current responsivities measured with a TeraFET with integrated bow-tie antenne over a broad range of frequencies from 0.15 to 1.18 THz. The detection signal was optimized by realignment to the maximum response at each single frequency. It it observed that the maximum peak of the responsivity does not shift significantly with frequency, although small shifts can be recognized and are

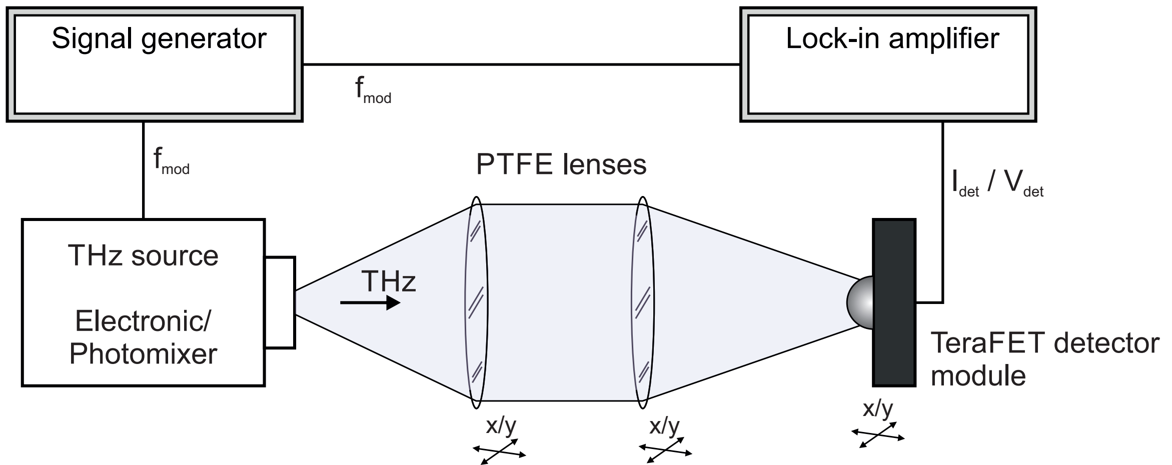

Fig. 6.11: Experimental setup for TeraFET characterization. Characterization of the TeraFETs was performed with three different THz sources, namely two all-electronic THz sources, one working from 210 to 360 GHz and one from 480 to 590 GHz, and the broadband photomixer-based THz system (see Section 6.2.2) working at frequencies from 0.1 to 1.18 THz. The THz beam was electronically modulated at $f_mod = 333$ Hz. A two-lens optical system was employed for collimation and pre-focusing of the beam. The detection signal was read-out with a lock-in amplifier.

attributed to details of impedance matching at the individual frequencies. In the inset, the maximum current responsivities are plotted versus frequency. Besides a strong dip caused by a parasitic, resonant antenna feature around 0.3 THz (see discussion below), the TeraFET exhibits a reasonably flat response over the investigated frequency range. For high gate voltages above threshold, signal contribution are observed which can be identified to be of thermoelectric origin. A detailed discussion is presented in Chapter 7.

For absolute power calibration of the broadband measurements with the photomixer THz source, the relative frequency dependence of the power of the photomixer source was recorded with a Golay cell with assumed flat frequency response over the region of interest. Standing waves in the optical setup as well as the diamond window and gas cavity of the Golay cell, however, produced significant resonances in the measurement. We therefore fitted the data as an exponential decay of THz power. Figure 6.13 shows the raw data as blue curve and the corresponding exponential fit function as red line. Pronounced water vapor lines[40] in the Golay cell data are clearly visible and proof that the signal power lay well above noise level of the cell. In order to calibrate to absolute power levels, reference measurements were performed with the photoacoustic calibrated powermeter (see Section 6.2.2) and are shown together with the noise level as black lines in the figure. Finally, the exponential fit data was scaled to the calibrated power measurement in the region between 0.4 and 0.5 THz. Absolute power levels for the evaluation of the TeraFET's optical responsivity and NEP could then be read out from the exponential fit curve. We critically note here,

[40]Located at 0.557, 0.752, 0.988, 1.097, 1.113, and 1.163 THz [136], indicated by black arrows in the figure.

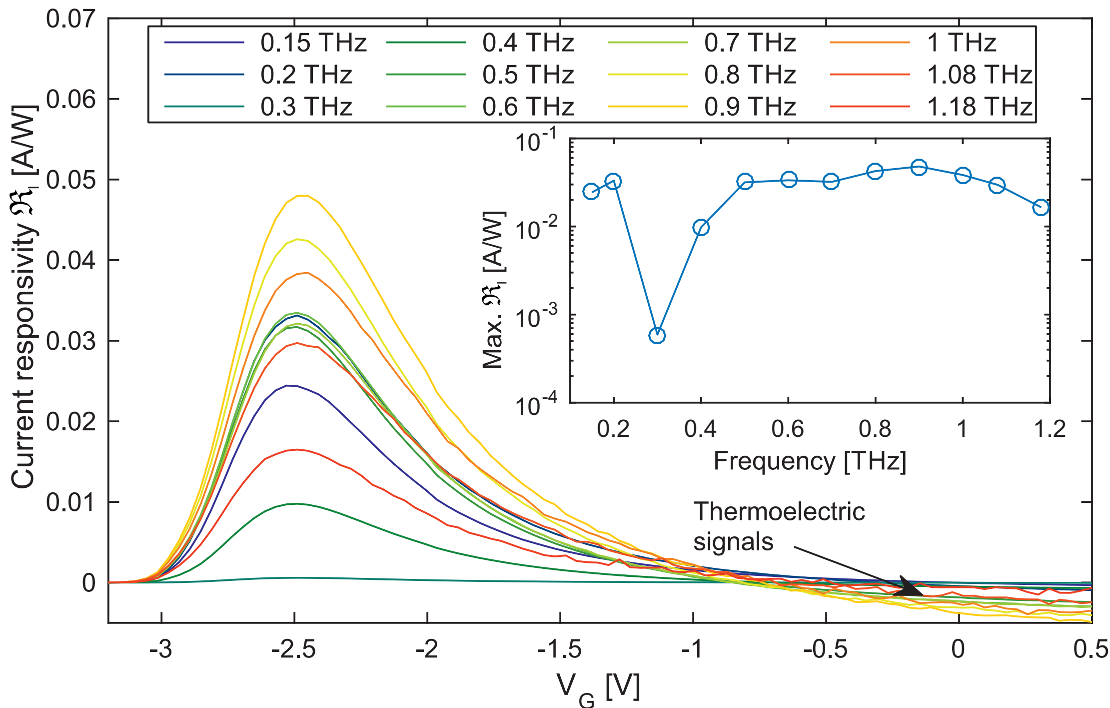

Fig. 6.12: Current responsivities $\mathfrak{R}_I$ measured with a bow-tie design TeraFET over a frequency range from 0.15 to 1.18 THz. Thermoelectric contributions to the detection signal manifest at high V_{G} above threshold at $V_{\mathrm{th}} = -2.51$ V. Inset: Maximum $\mathfrak{R}_I$ versus radiation frequency.

that an uncertainty in the powers used for the calibration of the measurement results may be present. This is first and foremost due to strong Fabry-Pérot resonances inside the golay cell cavity and remains unsatisfactory to some extent. Improvements on power calibration are therefore essential to overcome these residual uncertainties in the evaluation of device performance.

The plot in Figure 6.14 shows measured minimum optical NEPs for a number of distinct frequencies with corresponding values listed in the table below the graph. The values are the minimum NEPs from gate voltage sweeps at each individual frequency carried out to determine the best gate bias point of TeraFET operation. The inset of the plot shows as an example the optical current responsivity $\mathfrak{R}_I$ and NEP versus applied gate voltage at 0.9 THz for the bow-tie TeraFET. The best sensitivity (minimum NEP) is found at a gate voltage of $V_G = -2.6$ V.

At this point it should be noted from this exemplary gate sweep measurement that the gate bias operation point of best NEP in general not coincides with the point of best current (or voltage) responsivity. This becomes obvious when we recall from Section 6.1 that the responsivity is merely a measure for the effciency of the intrinsic detection process whereas the sensitivity in terms of NEP takes the detector's noise into account (comp. Eqs. (6.3) and (6.5)). Optimal TeraFET operation is therefore found for the applied gate voltage where the ratio of exhibited thermal noise and measured detection signal is lowest. When operated in current mode, TeraFETs

[41]Note that this is strictly true only for the intrinsic detection signal.

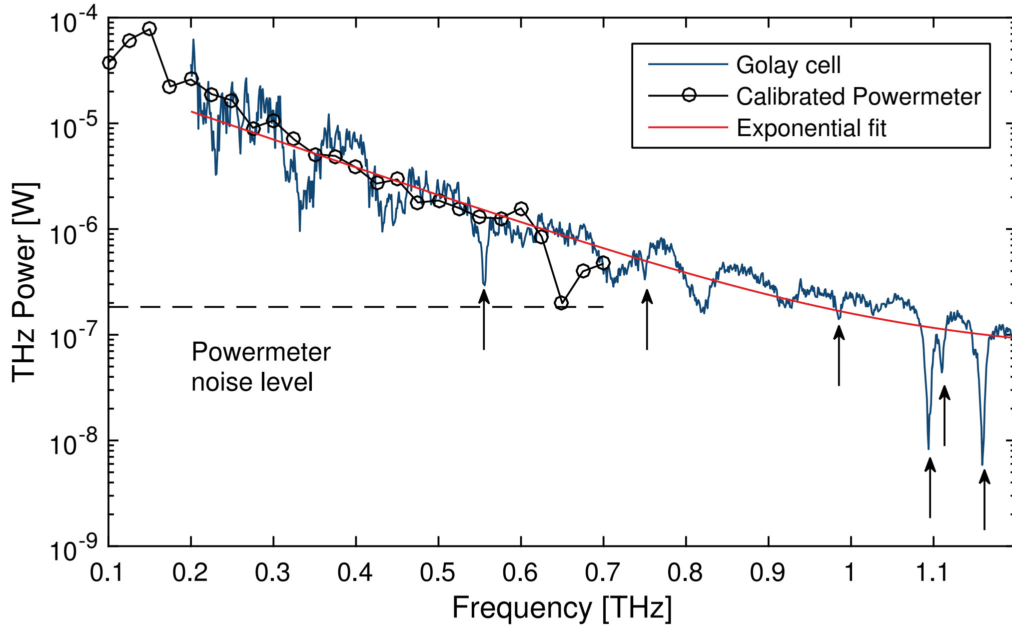

Fig. 6.13: THz power of the photomixer source. The measured signal of a Golay cell (blue line) was scaled to an absolute power measurement with the calibrated photoacoustic powermeter. Power levels were extracted from an exponential fit (red line). The arrows indicate spectral absorption lines of water vapor.

exhibit higher signals for higher gate voltages above threshold[41] while at the same time the current thermal noise rises (comp. Eq. (6.4)). The lowest NEP is hence found on the rising slope for gate biases lower than the bias point of maximum responsivity (here $V_{\mathrm{G,minNEP}} = -2.65$ V and $V_{\mathrm{G,maxRI}} = -2.45$ V). For voltage read-out the situation is reversed and minimum NEP is found at higher gate biases than the maximum responsivity.

In terms of absolute detection performance, both TeraFET designs exhibit a reasonably flat frequency dependence of NEP with high sensitivities below 100 pW/$\sqrt{\mathrm{Hz}}$ over more than one octave from 0.5 to 1.08 THz. Best NEPs of 57 pW/$\sqrt{\mathrm{Hz}}$ at 0.9 THz for the bow-tie and 39 pW/$\sqrt{\mathrm{Hz}}$ at 0.7 THz for the log-spiral design are found. To the author's knowledge, the presented sensitivities where record optical values for GaN-based TeraFETs at the time of publication [13], in particular for broadband devices. While this was aready the case for the bow-tie antenna design, it is known that these antennas show strong variations in directivity, beam shape and antenna efficiency[137] over broad bandwidths. We therefore also implemented TeraFETs with integrated log-spiral antennas which commonly exhibit a more stable beam pattern over the investigated frequency range. The directly measured NEPs even surpass the excellent values of the bow-tie design up to 0.8 THz. It must be mentioned, however, that the radiation patter of log-spiral planar antennas has circular polarization. On the other hand, the employed photomixer-based THz source was linearly polarized because of the bow-tie photoconductive antenna. Therefore, about 50% of the available THz beam power at the detector position is "lost". Since here we give optical NEPs without any assumptions on optical coupling this has not been corrected for in the data presented in Fig. 6.14. The shown values for the

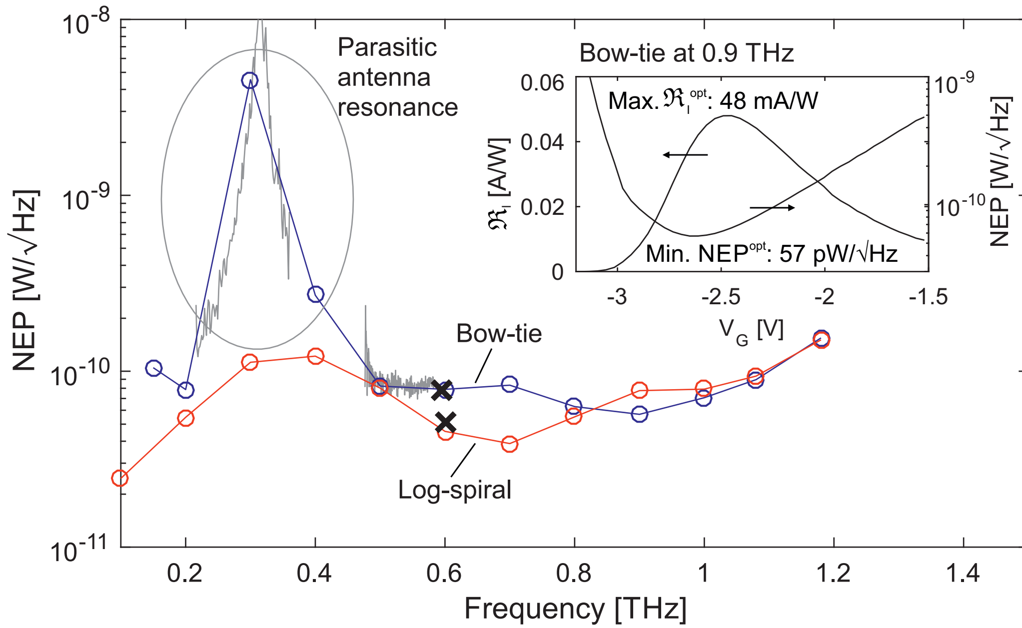

Frequency [THz]	0.1	0.2	0.3	0.4	0.5	0.6	0.7	0.8	0.9	1	1.08	1.18
Bow-tie	105	79	4544	270	82	79	83	63	57	71	90	155
Log-spiral	25	55	112	122	80	46	39	55	76	80	94	151

Fig. 6.14: Measured sensitivity of AlGaN/GaN TeraFETs with bow-tie (blue) and log-spiral (red) antenna design. Inset: Responsivity and optical NEP of the bow-tie TeraFET at 0.9 THz versus gate voltage. The table gives the NEP values (in pW/$\sqrt{\text{Hz}}$) at the data points marked in the plot.

log-spiral design should therefore be even lower by a factor of 2 with an approximate lowest optical NEP of 21 pW/$\sqrt{\text{Hz}}$ at 0.7 THz.[42]

For the bow-tie antenna design we observe a strong resonant drop in sensitivity (high NEP) centered at 0.3 THz with an approximate bandwidth of 2.5%. Detailed simulations of the integrated antenna embedded in the electric stabilization circuit revealed that at these frequencies, the shielding ground ring (diameter 360 µm) acts as a parasitic resonant structure interacting with the actual bow-tie antenna and preventing effective power coupling to the transistor. The feature is not observed for the log-spiral design in the investigated frequency range, since the ring has a significantly larger diameter in this design and parasitic resonances are expected at lower frequencies.

For further verification of the absolute evaluated detector sensitivities obtained with the photomixer source, the NEPs of the TeraFET's were independently measured at several frequencies with two all-electronic THz sources and evaluated from the calibrated, photoacoustic power measurement shown in Fig. 6.13. Results from these

[42]It has been shown that the polarization of log-spiral antennas can be elliptical rather than circular in some cases. We therefore refrain from assuming perfect circular beam shape over the whole frequency range. Comparative measurements with the detector rotated by 90 degrees should be performed to experimentally verify the factor of roughly 50% signal loss.

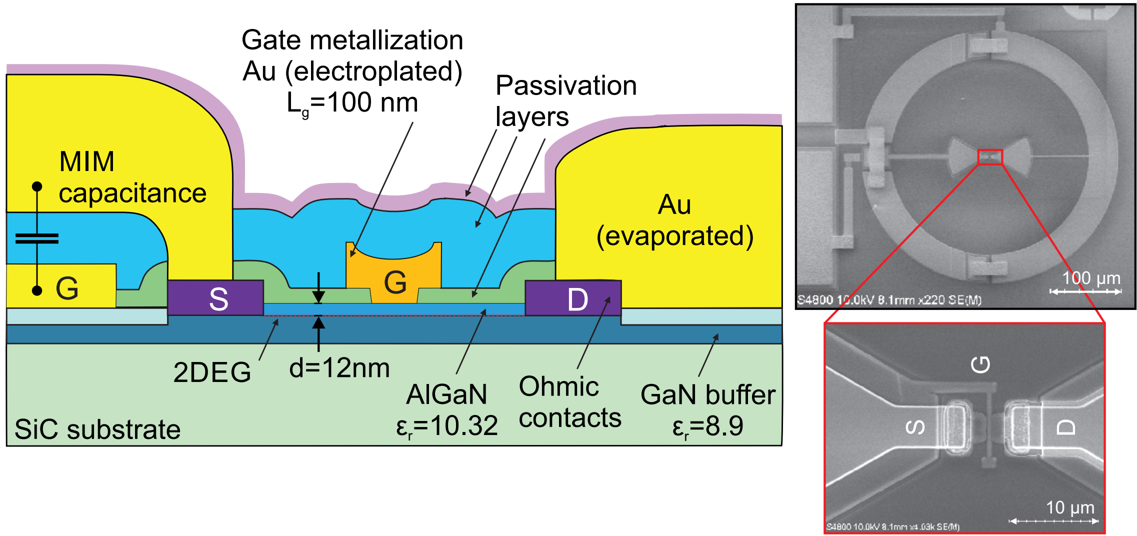

Fig. 6.15: Left: Technological parameters and schematic structure of fabricated AlGaN/GaN TeraFETs in an improved GaN MMIC process with reduced gate length $L_g = 100$ nm and thinner gate-to-channel separation $d = 12$ nm. Right: Scanning electron microscopy images of the integrated bow-tie antenna with surrounding ground ring and magnified center area with transistor structure and visible MIM capacitor.

calibrated measurements at 210 to 360 GHz and 480 to 590 GHz are plotted as light gray lines and black crosses in Fig. 6.14. The evaluated optical NEPs from both measurements show excellent agreement and in particular the parasitic resonance feature around 0.3 THz is clearly reproduced.

To conclude this section, TeraFETs with two types of integrated broadband antennas were fabricated and characterized. Record performance in terms of optical NEP of 57 pW/$\sqrt{Hz}$ at 0.9 THz for a bow-tie and 39 pW/$\sqrt{Hz}$ at 0.7 THz for a log-spiral antenna design were found and a flat frequency dependence over at least one octave could be observed. The values were cross-verified in two different measurement setups for absolute NEP evaluation and yielded good agreement.

6.3.3 Highly sensitive broadband AlGaN/GaN TeraFETs

Technological optimization of an alternate GaN MMIC process recently developed at FBH allowed the design and fabrication of a third improved generation of AlGaN/GaN TeraFETs. In the optimized fabrication process, the transistor dimensions could be even further reduced compared to the devices described above. The gate length was shortened by a factor of 2.5 down to only $L_g = 100$ nm and furthermore, the gate-to-channel dielectric could be thinned down to 12 nm. This should have an immediate effect on plasma wave generation in the FET channel, where in general, the gated plasmon frequency is directly proportional to the square root of the gate-to-channel separation [138]. The carrier density in the channel is controlled more effectively with a thinner gate dielectric as the gate capacitance rises (comp. Eq. 2.34).

A schematic of the improved GaN technology is shown in Fig. 6.15 on the left. Again, the structures were grown on SiC substrate of roughly 470 µm thickness for backside THz illumination. We incorporated most of the design features of the

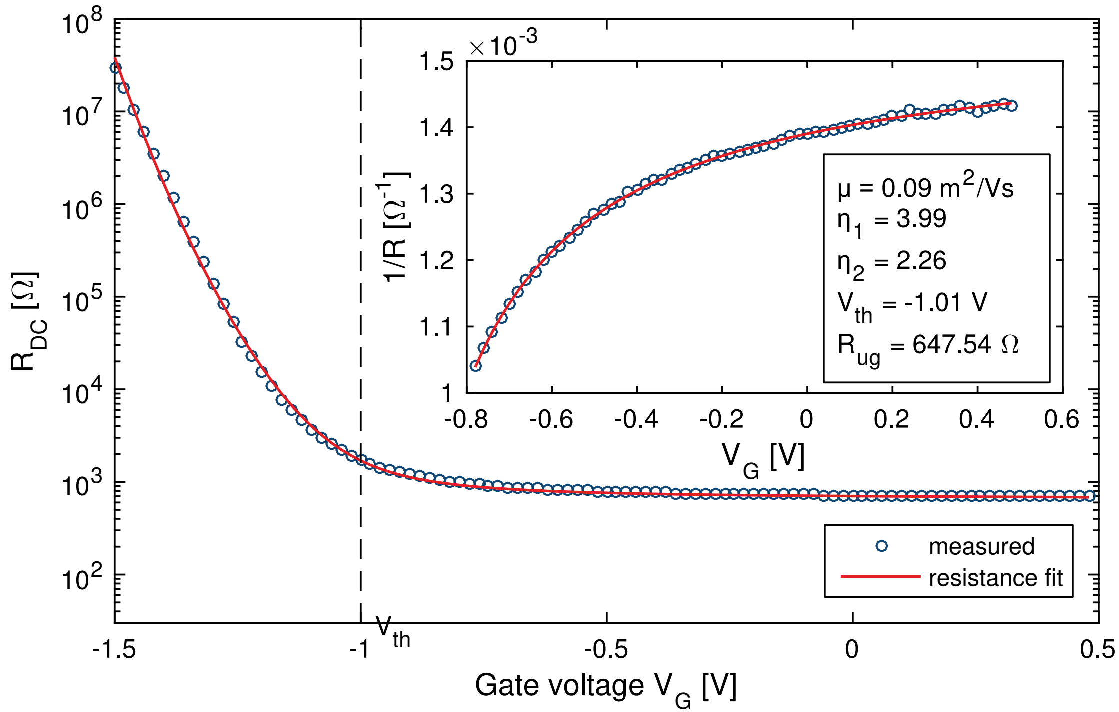

Fig. 6.16: Fit of measured DC drain-source resistance of a TeraFET with reduced gate length of 100 nm. The inset shows the result of the first fit stage. Extracted device parameters are listed in the box.

detector generation described above choosing again a broadband bow-tie antenna design. A MIM capacitor was implemented between the transistor's source an gate terminals to realize drain coupling boundary conditions, and the metal sheets were laid out in the shape of one of the bows of the integrated bow-tie antenna. The length of the source and drain side ungated access could be further reduced to $L_{\mathrm{ug}} = 300$ nm. The gate width was kept at 3 µm. The scanning electron microscopy image on the right of Fig. 6.15 show the bow-tie antenna design embedded in an eletric stabilization circuit as introduced before. In the magnified detail, the transistor structure with source, gate, and drain contacts as well as the implemented MIM capcitor can be recognized.

Figure 6.16 presents the fitted DC resistance of a 100 nm TeraFET with extracted device parameters in the inset box. Improved ohmic contacting was achieved by evaporation of the drain and source metals while the gate metal was deposited by electroplating. In total, the contact resistance was slightly reduced compared to the devices presented before and amounted to $r_{\mathrm{c}} = 0.8\ \Omega{\times}\mathrm{m}$, while the sheet resistance of the $\mathrm{Al_0.32Ga_0.68N}$ gate dielectric barrier was determined at FBH[43] to be $r_{\mathrm{s}} = 610\ \Omega/\mathrm{sq}$. From the device geometry we calculate a total contact resistance (together for both source and drain side) of $R_{\mathrm{C}} = 2r_{\mathrm{c}}/W \approx 533\ \Omega$ and a sheet resistance of $R_{\mathrm{S}} = 2r_{\mathrm{s}}(L_{\mathrm{ug}}/W) \approx 61\ \Omega$. With these values we calculate an expected total ungated resistance of approximately $R_{\mathrm{ug}} = R_{\mathrm{S}} + R_{\mathrm{C}} \approx 655\ \Omega$ which is reasonably

[43]Measurement of the specific sheet and contact resistances at FBH were performed by the so-called *van der Pauw method*.

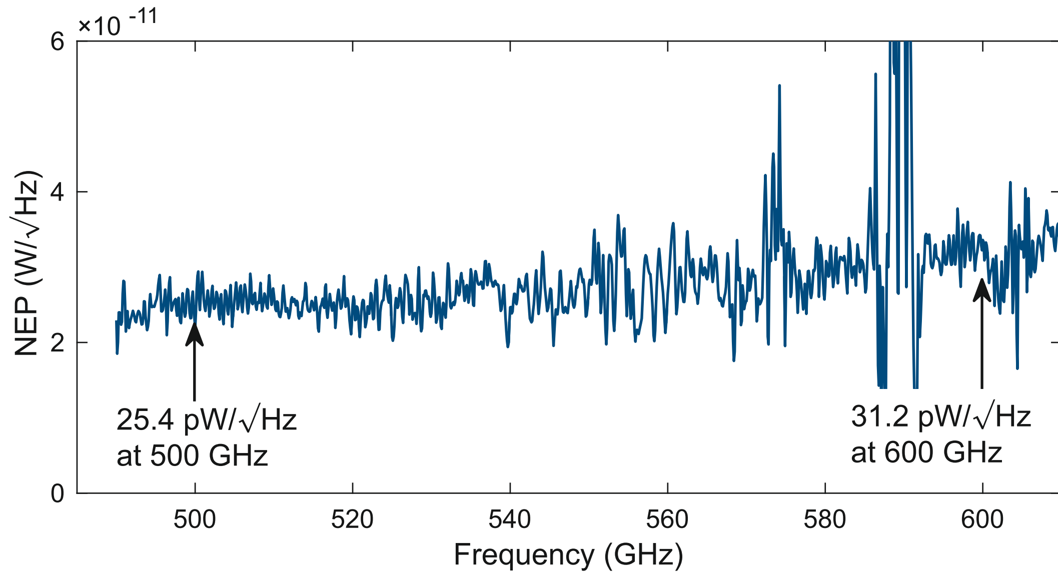

Fig. 6.17: Absolute optical characterization measurement of the optimized AlGaN/GaN TeraFET between 490 and 610 GHz. The achieved values in optical sensitivity constitute record values for GaN-based TeraFETs in the investigated frequency region, in particular, for broadband devices.

well reproduced by parameter extraction from the DC resistance fit.

A measurement setup similar to the one described in the previous section was used to characterize the TeraFET's broadband performance. A detailed measurement of the TeraFET's optical NEP in the region between 490 and 610 GHz performed with the tunable, all-electronic source described in Section 6.2.2 is shown in Fig. 6.17. The optical power in the THz beam was measured with a photoacoustic calibrated powermeter. To give a reference, we obtained power levels of 75 and 18 µW at 500 and 600 GHz, respectively, measured after the two PTFE lenses at the position of the TeraFET detector module. With these powers TeraFETs optical NEPs of 25.4 and 31.2 pW/$\sqrt{\text{Hz}}$ were determined at the above two frequencies assuming again thermal noise as the dominating noise source in our detectors. To the authors knowledge, these constitute record values for broadband-designed AlGaN/GaN HEMT-based TeraFETs in the investigated frequency range. Roughly comparable performance was reported in Ref. [116] employing a floating antenna design working around 900 GHz. Recently, optimized detectors were presented by the same group with optical NEPs of 30 to 300 $pW/\sqrt{\text{Hz}}$ at 0.7 to 1.1 THz, respectively [70]. It should be critically mentioned though that the exact procedure of power calibration is not further elucidated in the reference.

To give an estimate for the electrical NEP of our TeraFETs we assume THz optical coupling as discussed above in Section 6.2.3 including conservative estimates for the Gaussicity with respect to the employed Si substrate lens as well as reflection losses on the Si surface. The detectors were operated in aplanatic optical configuration an no losses due to internal reflection are considered. With these assumptions we calculate a frequency-independent total beam coupling efficiency of 63%. The electrical NEPs of the fabricated AlGaN/GaN TeraFETs is evaluated to yield 16 and 19.7 pW/$\sqrt{\text{Hz}}$

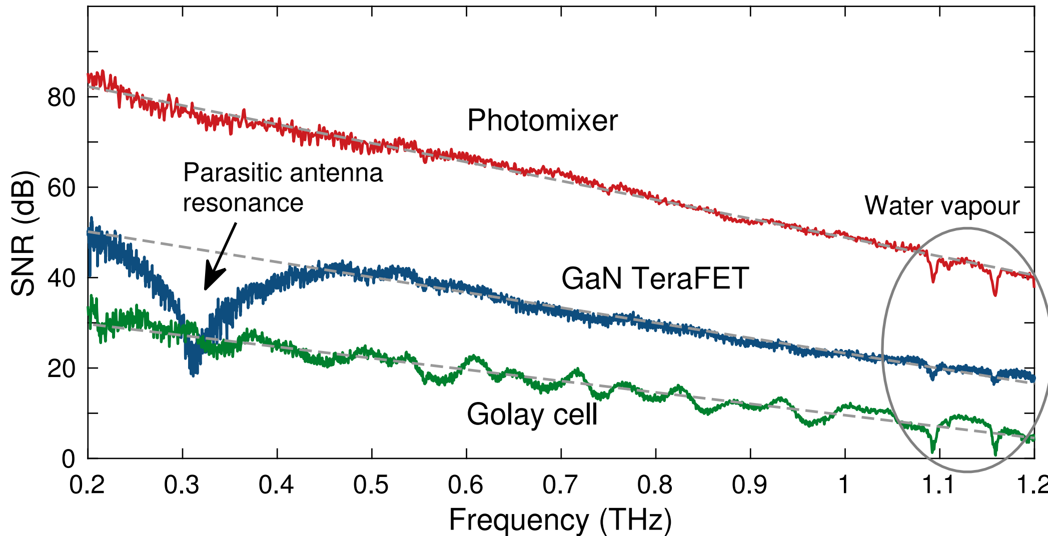

Fig. 6.18: Comparison of the SNRs of THz detection with three different detectors, namely, the AlGaN/GaN TeraFET (blue), a Golay cell (green), and the coherent photomixer receiver (red). The gray dashed lines represent linear fits reflecting the exponential power decay of the Photomixer THz source.

at 0.5 and 0.6 THz, respectively. These values compare well to state-of-the-art Si CMOS-based TeraFETs [37] and even are almost comparable to resonant TeraFETs in the same technology [24], [139].

We further characterized the TeraFET's over a broader frequency range from 0.2 to 1.2 THz. For this purpose, the all-electronic source was replaced with the photomixer-based tunable THz source. In the specific experimental setup, calibrated measurements of the THz power at the detector position could no be reliably performed because the power levels over the largest part of the frequency region lay at the noise level of the calibrated, large-area, photo-acoustic powermeter. We therefore determined the detector's performance in terms of SNR and then compared the obtained results to THz detection measurements with two other detectors, namely, a commercial Golay cell and a photomixer detector module identical to the transmitting photoconductive antenna of the photomixer THz source. Fig. 6.18 shows the obtained SNRs for our TeraFET (blue), the photomixer (red) and the Golay cell (green). The measurement with the TeraFET and photomixer were performed at a modulation frequency of the THz source of $f_{\mathrm{mod}} = 12$ kHz and a lock-in integration time constant of 100 ms. Measurements with the Golay cell at lower modulation frequency of $f_{\mathrm{mod}} = 20$ Hz had to be performed at a much longer integration time of 2 ms due to a significantly higher noise level. The equivalent SNR at 100 ms was calculated based on the equivalent noise bandwidth (ENBW) for the applied filter slope setting of the lock-in amplifier from a measured noise voltage of 17.5 $\mu\mathrm{V}/\sqrt{\mathrm{Hz}}$. The TeraFET's gate bias voltage of best sensitivity was determined as $V_{\mathrm{G}} = -1.09$ V from measurements of THz response versus gate voltage at a number of single frequencies. No significant shift of the optimal gate bias point was observed, which allowed sweeping of the THz frequency while keeping the gate bias fixed.

For all three detector's, an overall linearly (in dB) decreasing SNR reflects the ex-

ponential decay of output power of the THz source, where the approximate slopes were extracted from linear regression and amounted to -0.034, -0.025, and -0.042 dB/GHz for TeraFET, Golay cell, and photomixer, respectively. Note that again, as discussed in the previous section, a drop in the TeraFET's SNR around 300 GHz is observed, caused by a parasitic resonance of the ground ring surrounding the actual broadband bow-tie antenna, because the detector's circuit design was mostly adopted from the preceding TeraFET generation. In terms of device performance, THz detection with the TeraFET yielded an SNR from 50 dB down to 17 dB over the investigated frequency range. The only noise source in the detector was assumed to be thermal noise based on the discussion in Section 6.1.1. The measured TeraFET SNRs exceeded the Golay cell's SNR by roughly 20 dB. On the other hand, the photomixer detector showed significantly higher sensitivity at SNRs from 82 dB down to 41 dB. The reason for the higher SNR is that the photomixer was operated in coherent detection mode while the TeraFET worked as a direct power detector (comp. Eq. (2.15)). It was shown that TeraFET can as well be operated as coherent detectors in heterodyne configurations, and an enhancement of detection sensitivity of approximately 25 dB was reported [140].

Some remarks should be made about the presented data of broadband detector characterization. First, note that the fluctuations visible in all presented measurements - with the TeraFET and also the two reference detectors - are not to be confused with noise but rather reflect resonant standing waves in the optical setup. The noise level of all three detectors lies well below the respective measurement signals in the investigated frequency range. Second, spectral absorption lines can be well recognized with all three detectors around 1 THz. However, the lines seem to be significantly more pronounced in the Golay cell's SNR curve despite the lowest total sensitivity of this detector. The reason for this behavior could not be determined conclusively up to this point. We assume that spurious signals were emitted by the laser-driven photomixer source due to possible sidebands of the fundamental laser oscillation frequency. The signals are expected to be located at lower GHz frequencies and are still effectively picked up by both, the TeraFET and the photomixer detector. It should be investigated further if the unexpected observation can decisively be attributed to a faulty operation of the THz source. A possible approach would be the implementation of an adjustable aperture in the THz path to implement a spatial frequency filter to suppress low frequency parasitic signals in the experimental setup.

6.4 Graphene TeraFETs

Graphene can offer enhanced possibilities for the fabrication of THz detectors due to its specific properties of electronic transport, in particular a theoretically high mobility with respect to electronic and HF application, as well as high mechanical flexibility. From a physics point-of-view, graphene as a novel material offers a fascinating test bed to investigate electronic transport in real tow-dimensional systems. Ever since the first mechanical fabrication of graphene by Novoselov and Geim [141], [142] in 2004, graphene has emerged as an extensively studied *novel* electronic material in recent years. While these pioneering works are often cited for the sheer fabrication of single and multi-layer graphene by mechanical exfoliation, which certainly deserves high

appreciation on its own, the probably even greater achievement lies in the successful contacting of the fabricated graphene by gating contacts to enable investigation of electric field-dependent electronic transport properties of the new material [143]. A multitude of literature on both theoretical and experimental studies of graphene-based electronics exists and a comprehensive discussion far beyond the scope of this thesis.

6.4.1 Differences for graphene TeraFET model

Four fundamental physical differences between single-layer graphene and 2DEGs in conventional semiconductors were identified as predominant sources of different carrier transport behavior of the two categories of materials in Ref. [143]. First of all, energy dispersion in single-layer graphene is linear while most semiconductors exhibit quadratic dispersion. The profound consequence is that while the transport of carriers in conventional 2DEGs is governed by the non-relativistic Schrödinger equation, the appropriate transport equation for carriers in graphene sheets is the relativistic Dirac equation [142]. Second, graphene is always conducting due to its gapless band structure and electronic transport can be switched from electron-dominated to hole-dominated by tuning the Fermi level to lie either in the conduction or the valence "band" of the Dirac cones. Third, graphene layers in contrast to 2DEGs in semiconductors are chiral systems, which imposes further consequences on carrier transport. And fourth, single-layer graphene constitutes a "true" two-dimensional material with precise confinement of carriers, while semiconductor 2DEGs are induced by external fields and must be considered quasi-two-dimensional. Extensive analysis of the impact of these qualitative differences on the transport properties of carriers in graphene can be found, e.g., in Refs. [143]–[147] and numerous references given therein.

The hydrodynamic model and circuit implementation of the same was developed in thesis mainly in the light of TeraFETs based on AlGaN/GaN HEMTs. In particular, the hydrodynamic transport equations were derived from a parabolic band approximation (comp. Eq. (3.4) and Appendix B). It can therefore not be expected that the above details and their impact on the transport properties of graphene are readily covered by the investigated detector model. A thorough derivation of hydrodynamic transport equations for graphene should therefore be performed along the line given, e.g., in Refs. [146], [147]. The formal steps in the derivation follow the same logic in applying the method of moments to the fundamental Boltzmann equation. The derivation must consider both types of carriers - electrons and holes - and a the linear energy dispersion

$$E(\boldsymbol{k}) = \hbar |k| v_{\mathrm{F}} \tag{6.13}$$

must be employed in the distribution function Eq. (3.6). Here, $v_{\mathrm{F}} \approx 1 \cdot 10^{6}\,\mathrm{m/s}$ is the Fermi velocity [143].

Up until this point, these fundamental modifications have not been incorporated in the circuit model implementation. We introduced a number of modifications to the presented semiconductor model accounting for the ambipolarity of electronic transport via electrons and holes in graphene. The analysis of experimental data and

modeling of graphene TeraFETs was then based on an adaptation of the detector model presented in the previous chapters. We do, however, incorporate a carrier density-dependent effective electron and hole mass, thereby considering to some extent the linear energy dispersion relation of graphene [147]. All other quantities were defined similar to the semiconductor case. We found that this simplified approach to a reasonable level accounted qualitatively for the observations we made in THz detection experiments with our fabricated graphene TeraFETs - in particular the influence of thermoelectric currents on the detection signal. Device parameters extracted from DC device analysis yielded reasonable physical values. The reader should always keep in mind, however, that an extension of the employed model considering the above fundamental differences in electronic transport must be pursued in the future. In the context of this work, additional literature on the topic of plasma wave phenomena in graphene exists, some valuable examples are Refs. [146]–[152].

6.4.2 Graphene DC parameter extraction and modifications of transport model

Graphene TeraFETs with integrated broadband bow-tie antennas were fabricated in a collaboration with Chalmers Technical University, Göteborg, Sweden. The conducting graphene layer was grown by *chemical vapor deposition* (CVD) on a wafer-scale. The antenna design, being loosely based on the layout of the GaN-based devices presented above, was limited two only two available gold layers for the implementation of the FET with integrated antenna. We therefore chose a bow-tie antenna structure and introduced a split bow geometry in one of the antenna wings to realize again capacitive coupling, this time between gate and drain contacts[44] to yield source-coupling boundary conditions. A schematic of the TeraFET design together with a microscopic photograph is shown in Fig. 6.19.

A single layer of graphene was CVD-grown on copper foil and then transferred to a Si/SiO_2 substrate via the so-called PMMA frame-assisted H_2 *bubbling transfer method* [153], [154]. The thickness of the SiO_2 was approximately 300 nm on high-resistivity Si with reasonable THz transparency for backside illumination. Wafer dies of 10x10 mm^2 were fabricated and source and drain metal stacks of Ti/Pd/Au with thickness 1/15/300 nm were deposited via electron beam lithography and graphene was plasma-etched outside the transistor region. A 17 nm thick Al_2O_3 gate oxide layer was grown by *atomic layer deposition* (ALD) and finally the gate metal stack consisting of 1 nm Ti/300 nm Au was deposited. Multiple devices were patternd on the wafer (2x32 in total), which was then sub-diced into smaller pieces each containing 8 individual TeraFETs. The dies were wire-bonded and mounted in a detector module as described in Section 6.2.3 and integrated with a silicon substrate lens of same geometry as described above for aplanatic THz beam coupling. Different FET layouts were implemented with varying gate length and width. Here, we present results of THz characterization of samples with a gate length of $L_\mathrm{g} = 2.5$ µm and widths of $W_\mathrm{g} = 2$ µm (Device 1) and 5 $L_\mathrm{g} = 5$ µm (Device 2). THz measurements performed at 0.6 THz with Device 1 have been published before in Ref. [5].

[44]Recall that labelling of drain and source contacts is arbitrary.

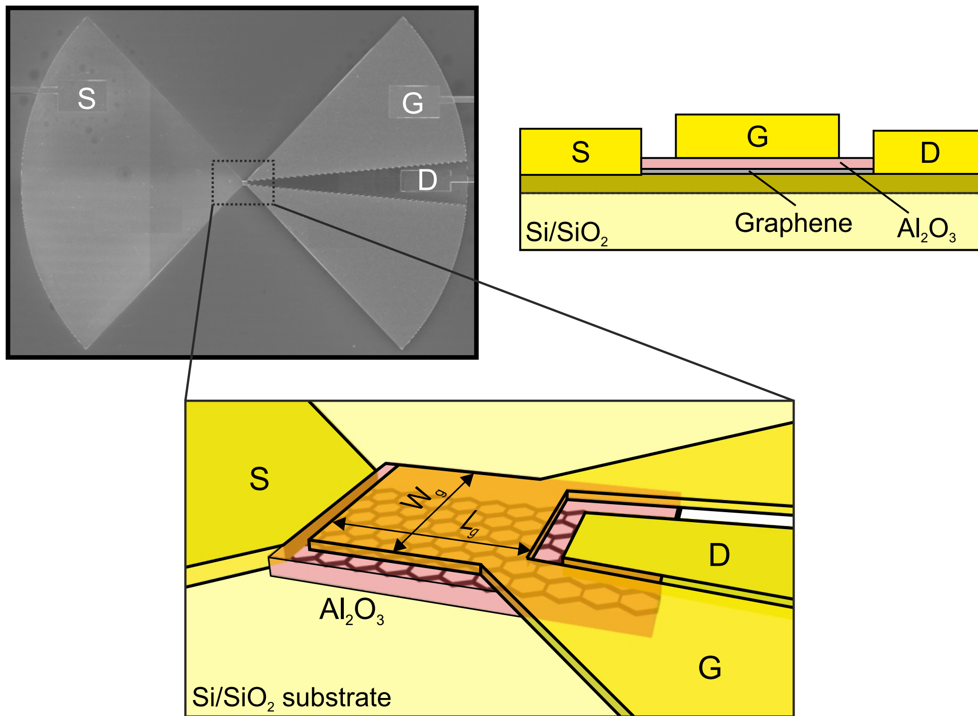

Fig. 6.19: Schematic layout, desing and microscopic photograph of the CVD-graphene TeraFET with integrated broadband bow-tie antenna. The graphene was grown on copper foil and bubble-transferred the Si/SiO_2 substrate. The transistor contacts and integrated antenna were deposited via electron beam lithography. We introduced a split bow-tie geometry to achieve asymmetric radiation coupling. The transistor's gate length was $L_g = 2.5$ µm and devices with two different widths of 2 µm (Device 1) and 5 µmu (Device 2) were fabricated.

Figure 6.20 presents measurements of the DC drain-source resistance (symbols) and resistance fits of the two graphene TeraFETs. The shift of the Dirac point of charge neutrality (V_{Dirac}) away from $V_G = 0$ V reflects unintentional n and p-doping for devices 1 and 2, respectively. We fitted the resistance curves with a simplified resistance model largely based on the fit routine explained in Section 4.2.2 for the GaN-based TeraFETs, however, employing only a single fit stage for the total carrier density $n(V_G)$.[45] This can only be considered a simplified approach since carrier transport in graphene has some fundamental differences to electronic transport in conventional semiconductor two-dimensional inversion layers, which should also reflect in the functional dependence of $n(V_G)$.

Graphene is an ambipolar material and hole transport must be incorporated in the transport description. A consequence of the ambipolarity of transport in gapless graphene is that there is always a finite number of charge carriers - electrons and/ or holes - contributing to the total charge density in a graphene-based FET channel. The resistance can be tuned by an external gate bias voltage, however, it does not diverge as in conventional semiconductor-based FETs but exhibits a maximum at the gate bias where the number of holes equals the number of electrons.

[45]as opposed to the prior two-stage fit routine to extract the threshold voltage and ungated resistance.

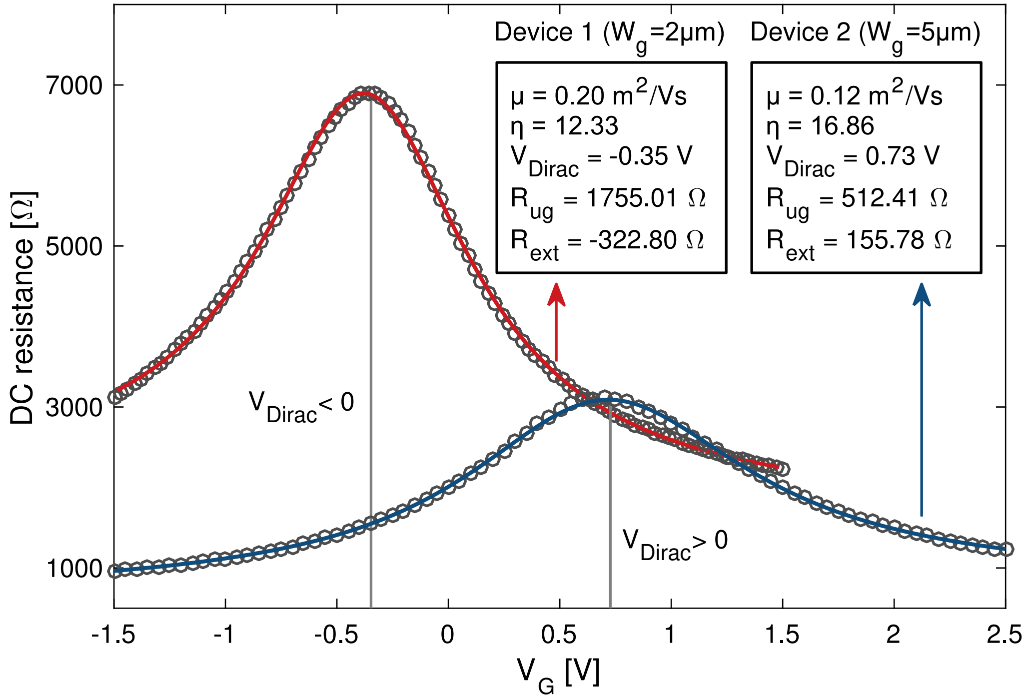

Fig. 6.20: Measurements and fits of the DC drain-source resistance of two investigated CVD-graphene TeraFETs. Both devices were fabricated with a gate length of $L_g = 2.5$ µm, but differed in channel width, namely $W = 2$ µm for Device 1 (red) and $W = 5$ µm for Device 2 (blue). The increased gate width for Device 2 reflects in an overall reduced resistance. The fits were obtained using a modified version of the fit routine employed for the GaN TeraFETs. The single-mobility model was extended to account for the ambipolarity of electronic transport and the formation of an additional contact resistance R_{ext} for one type of carriers leading to the slight asymmetry in resistance with respect to V_{Dirac}.

The carrier density at this point is often called a *residual* carrier density. The bias point is referred to as the *charge neutrality point* (CNP) and the corresponding gate voltage is denoted as V_{Dirac} the *Dirac voltage*. The most profound difference between graphene and conventional semiconductors is its linear dispersion relation being a truly two-dimensional material.

The total charge carrier density in our graphene model is calculated as the sum of the individual densities of electrons and holes[146]

$$n = n_e + n_h \tag{6.14}$$

where both n_e and n_h are assumed to individually satisfy a functional dependence as given in Eq. 4.15 for GaN, where V_{th} is substituted by V_{Dirac}. The inverse sign of elementary charge of both types of carriers is accounted for by adding a minus sign in the argument of the exponential function replacing $V_G - V_{Dirac}$ by $-(V_G - V_{Dirac})$ for holes. In addition, we drop the gate voltage-dependence of the non-ideality factor η treating it as constant over the whole range of gate biases below and above V_{Dirac}. Note that an exact derivation of a graphene transport model based on Eq. (6.13) should yield a different functional dependence of carrier density on Fermi energy than the one found for AlGaN/GaN in Eq. (4.14) and (B.10), respectively. This is not included in the present stage of model implementation.

For the inclusion of diffusive current contributions in the transport description, the derivative of the carrier density with respect to applied gate voltage $\partial n/\partial V_{\mathrm{G}}$ must be calculated (comp. Eq. (4.10)). Since we evaluate current contributions for electron and hole transport separately, we account for the inverse sign of holes via

$$\frac{\partial n}{\partial V} = \frac{\partial n_{\mathrm{e}}}{\partial V} - \frac{\partial n_{\mathrm{h}}}{\partial V} \tag{6.15}$$

A close look at the experimental data in Fig. 6.20 reveals another peculiarity of graphene FETs, namely, an asymmetry of hole branch ($V_{\mathrm{G}} < V_{\mathrm{Dirac}}$) and electron branch ($V_{\mathrm{G}} > V_{\mathrm{Dirac}}$) in the DC resistance. It was discussed before that this in an effect of the ohmic contacting of the conducting graphene layer by the drain and source metal electrodes. An additional p-n barrier can form when the type of majority of carriers in the graphene channel is opposite to the charge in the contacts [155], [156], leading to a non-negligible resistance contribution for one of the two conduction branches. We included this effect by adding an additional resistance R_{ext} as fit parameter, where the asymmetry is modeled by a smooth Fermi-Dirac-like transition function centered around V_{Dirac} to account for carrier type dependency of R_{ext}.[46] Negative and positive values for the respective fit parameter correspond to an additional resistance in the hole and electron branch, respectively. Finally, it must be mentioned that in general, the mobility of electrons μ_{e} and holes μ_{h}in graphene is not equal. This is not considered in the model implementation, where we assume a single mobility μ for both types of carriers, which has been reported before to yield satisfactory fits and device parameters [157].

Recall that the carrier density-controlling gate capacitance C in the transmission line equivalent circuit model was implemented as the time derivative of the total charge in the FET channel (comp. Eq. (4.1)). For graphene, on the other hand, the influence of positive and negative charges must be considered, and the capacitive coupling between gate and channel was described by

$$Q = qW\Delta x(n_{\mathrm{e}} - n_{\mathrm{h}}) \tag{6.16}$$

with the value of $(n_{\mathrm{e}} - n_{\mathrm{h}})$ depending on the applied gate voltage. We did not include additional effects of quantum capacitance in our modeling, since the influence should be negligible for our device geometry, in particular the thickness of the Al_2O_3 gate oxide, as was discussed in Ref. [143], [158].

With the above modification to the fit model of DC drain-source resistance, we obtained the device parameters displayed in Fig. 6.20 for the two graphene devices with different channel width, which seem to yield reasonable values for the physical quantities. Note that a significantly lower ungated channel resistance was obtained for the wider channel. We extracted mobilities of 2000 and 1200 $\mathrm{cm}^2/\mathrm{Vs}$ for the two devices under test, which is within expectations for CVD-grown graphene on

[46]Another functional dependence for R_{ext} was proposed in [156], however, introducing an additional fit parameter.

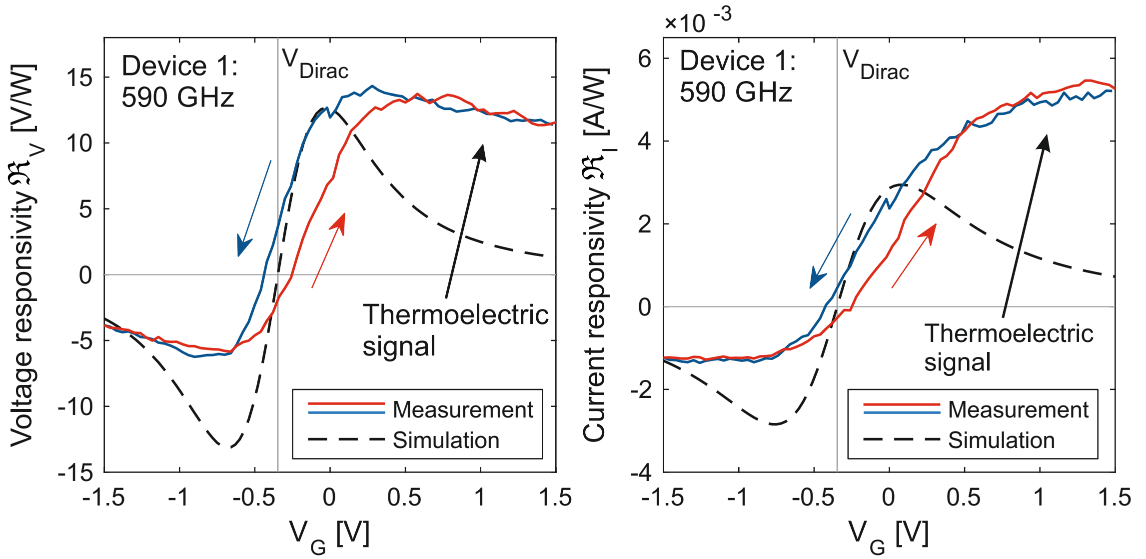

Fig. 6.21: Measurements of the voltage (left) and current (right) responsivity of a graphene TeraFET (Device 1 from Fig. 6.20). The arrows denote the sweep direction of V_G and a pronounced hysteresis can be recognized. The dashed lines represent device simulations with the circuit model implementation without diffusive transport. Strong signal contribution at high gate voltages and, in particular, a non-vanishing THz response at V_{Dirac} indicate the presence of an additional thermoelectric detection mechanism in the measured signals (for further discussion, see Chapter 7).

Si/SiO_2[156] .[47] The Dirac voltage as the maximum of the resistance curve is well reproduced by the fit function, as well.

The same modifications to the model described in the previous chapters were incorporated in the equivalent circuit implementation for the HF simulations of the graphene FET's THz response. Here, an additional important difference is the definition of carrier mass required for the calculation of the momentum scattering time $\tau_p = m\mu/q$ showing up in the convection current densities responsible for the non-linear plasmonic mixing mechanism (comp. Eq. (4.7)). The mass of carriers in graphene is defined as the cyclotron mass depending on the gate voltage-controlled Fermi energy (see Appendix C). In the model, the constant mass of carriers is therefore replaced by the voltage-dependent cyclotron mass and the voltage-dependent momentum relaxation time is introduced as

$$\tau_p(V_G) = \frac{\mu m(V_G)}{q} = \frac{\mu \hbar}{q v_F} \sqrt{\pi n(V_G)} \tag{6.17}$$

[47] While extremely high mobilities can be calculated for intrinsic graphene sheets, strong mobility degradation due to lattice and impurity effects and other substrate interactions was discussed and experimentally observed, in particular for CVD-grown graphene [143], [159]. Possible ways to enhance the mobility are the use of dielectrics with higher refractive index (e.g., BN [160] or SiN [161]) or suspension of the graphene sheet [162].

6.4.3 THz detection with graphene TeraFETs

THz detection was performed with the fabricated TeraFETs at 590 GHz with an all-electronic THz source and between 0.2 and 1 THz with the photomixer-based source, where the experimental setup and optical configuration was largely identical to the situation describe before for the characterization of the AlGaN/GaN TeraFETs (see Section 6.2.3 and Fig. 6.11). Again, a silicon substrate lens in aplanatic configuration was used for backside illumination of the integrated bow-tie antennas. Measurement results of the THz optical voltage and current responsivity of graphene Device 1 are shown in Fig. 6.21, where absolute power calibration was achieved using the large-area photoacoustic powermeter at the position of the detector module yielding a total THz beam power of 29.3 µW. Two important features of the detected signals versus applied gate voltage can be observed.

First, a significant hysteresis is present in the investigated devices. The direction of gate voltage sweeping is indicated by the arrows next to the measured curves corresponding to sweeping upwards from negative to positive gate biases (red arrow and curve) and downwards vice versa (blue arrow and curve). The presence of hysteresis in graphene is a well-known effect and is mainly attributed to charging effects of impurities [25], [117]. For CVD-grown graphene FETs using Al_2O_3 as gate dielectric layer, in particular the diffusion of ambient air oxygen through the oxide into the graphene layer is assumed to be the predominant mechanism causing hysteresis [117]. It was reported that current annealing of the material can improve sample stability to a large extent [163]. The issue of charging effects in TeraFETs was mentioned before in Section 6.1.1 and is currently under investigation [10]. When evaluating the absolute performance of graphene TeraFETs, special attention must be paid to hysteresis in device resistance when calculating the thermal noise spectral density for the determination of NEP after Eq. (6.5). We limit further evaluation of the measured data to the downward sweep direction, however, for reasons of completeness, the other sweep direction is included in the figures.

Another highly interesting aspect are strong thermoelectric signals at high gate bias voltages. The dashed curve in Fig. 6.21 shows results from a device simulation performed with the hydrodynamic circuit model implementation presented earlier, however, with diffusive transport contributions switched off. The obtained model curves were scaled to the measured data at the gate bias point of maximum voltage and current response in the simulation, respectively.[48] The measured THz response deviates significantly from expectations for the plasmonic detection mechanism. This becomes in particular pronounced at the CNP (V_{Dirac}) and at higher positive gate biases but differences are evident at almost all values of V_{G}. The qualitative nature of differences in measured and anticipated THz response suggests the presence of an additional physical detection mechanism in the device. In Chapter 7 we will see from comparison with device simulations that the signals are indeed most probably of thermoelectric origin.

[48] Recall that the THz amplitude at the TeraFET's transistor ports is not accessible in the experiment, the simulation was therefore performed for an arbitrary signal amplitude of 1 mV and scaled to the measured data. It should be noted that inconsiderate scaling of the curves can have an effect on the perception of signal trends.

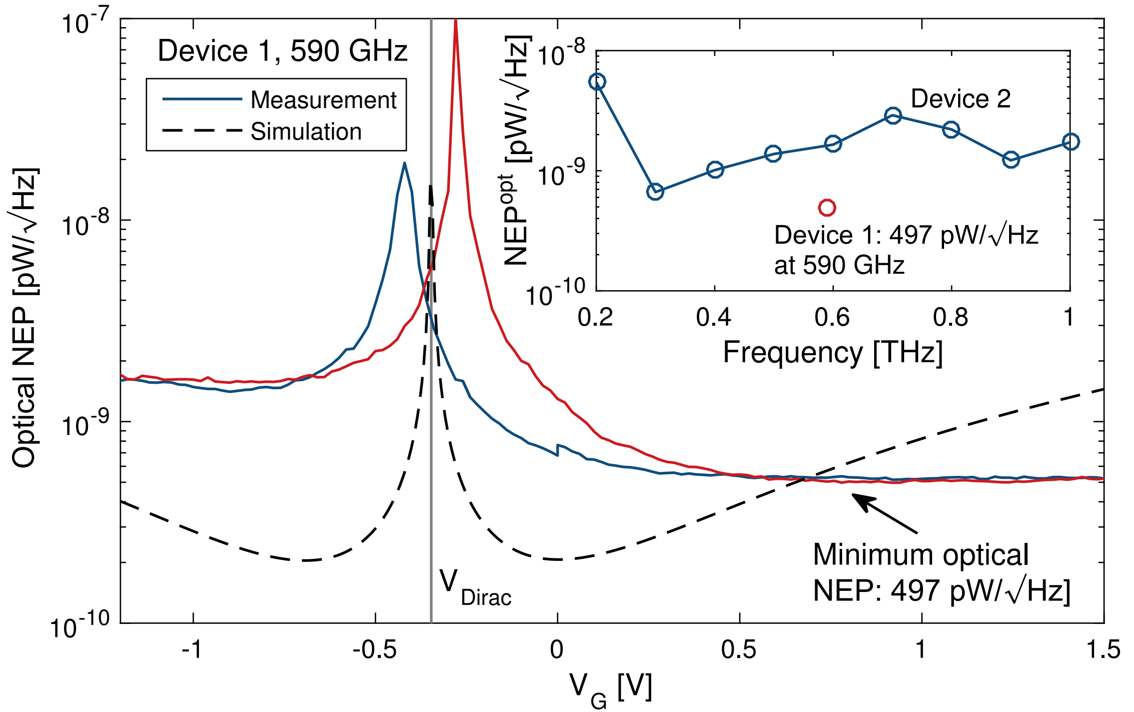

Fig. 6.22: Measured (solid lines) optical NEP versus gate voltage for graphene Device 1 and versus THz frequency for Device 2. A relatively flat frequency response was achieved over the range from 0.3 to 1 THz. The best measured NEP amounted to 497 pW/$\sqrt{\text{Hz}}$ at 590 GHz. A strong thermoelectric contribution shifted the bias point of best sensitivity significantly away to a higher voltage with respect to the simulated minimum in NEP of plasmonic detection (thermoelectric currents not included in the simulation).

From the measured voltage or current responsivity, the optical NEP of the graphene TeraFETs was calculated after Eq. (6.12) and is plotted in Fig. 6.22 for Device versus gate bias voltage in the main graph and for Device 2 versus THz frequency in the inset. The frequency sweep was performed by replacing the all-electronic with the photomixer-based THz source. The dashed line shows the simulated device NEP obtained from a circuit simulation with an integrated 75 Ω antenna. Again, thermoelectric contributions to the detection signal were switched off in the simulation and a plasma wave mixing-based sensitivity significantly deviating qualitatively from the measured data can be seen. Note that we achieve the best device performance in terms of lowest optical NEP at a gate bias far away from the Dirac voltage V_{Dirac}, whereas the minimum NEP for the simulated plasmonic response is found close to V_{G}. Furthermore, the NEP at this point of device operation is even lower than the one at the best point expected from simulations. Again, this is explained by additional thermoelectric detection leading to a flattening trend of the NEP towards higher gate biases, at least up to a measured gate voltage of 1.5 V. The thermal noise (voltage) decreases towards higher gate biases as the channel resistance is reduced (comp. Eq. (6.4)). In combination with an almost constant (voltage) detection signal (see Fig. 6.21 above) at the same voltages, an improved NEP compared to anticipated optimal point of device operation is obtained.

The optical NEP measured in the frequency range from 0.2 to 1 THz shows a

reasonably flat frequency-dependence for the bow-tie integrated broadband TeraFETs. We find again, in accordance with the observations presented in the previous Sections on GaN-based devices, that a lower NEP - i.e., a higher sensitivity - is measured with the TeraFET with smaller device geometry. With our best device, we measured a minimum NEP of 497 $\mathrm{pW}/\sqrt{\mathrm{Hz}}$ at 590 GHz. Up until this date, this value represents a record optical sensitivity for graphene TeraFETs, in particular, for CVD-grown single-layer graphene. THz detection with graphene TeraFETs was demonstrated before with exfoliated single and bi-layer graphene devices [30], [152], [164], where NEP values of on the order of a few 10^{-9} $\mathrm{pW}/\sqrt{\mathrm{Hz}}$ were reported, however, measured at lower frequencies around 300 GHz.

Chapter 7

Thermoelectrics in TeraFETs

So far we presented THz detection experiments with TeraFETs in the context of device performance regarding detection responsivity and NEP. It was shown that by careful device design taking into account intrinsic plasmonic mixing effects, HF influences of extrinsic detector components, as well as stabilization of the detector environment and implementation of defined boundary conditions we succeeded in the fabrication of highly sensitive TeraFETs which exhibited record performance in both material systems, namely AlGaN/GaN HEMTs and graphene FETs.

During the TeraFET characterization experiments, we observed significant qualitative deviations of the measured signals from what is to be expected from the plasmonic mixing mechanism. Recall from the simple quasi-static picture Eq. (2.20) that the detector response should level off to zero for high gate voltages above the threshold as the channel conductivity saturates in the strong inversion regime and the derivative $\partial n/\partial \phi$ vanishes. It is in particular at these high gate voltages were signal contributions could be measured indicating the presence of other physical detection mechanisms than conventional plasmonic mixing. We discussed before that the fluid-dynamic transport model Eqs. (2.1) and (2.2) is a reduced one in the sense that pressure terms have been neglected. A hydrodynamic transport model including diffusive contributions to the carrier transport (see Chapter 3) was therefore implemented in the circuit solver.

In this chapter we investigate the contribution of thermoelectric signals to detection signals measured in the course of the experimental characterization of our TeraFETs. Consider the schematic shown in Fig. 7.1. The implemented asymmetry of coupling conditions by capacitive HF shunting of the gate and source contacts (for a discussion, see Section 2.5) leads to a concentration of input power on the drain side of the transistor channel. The yellow line represents the spatial power distribution along the device as obtained in a circuit simulation for realistic AlGaN/GaN TeraFET device parameters. The local concentration of incident radiation power induces a local electric field, which in turn leads to a local heated distribution of charge carriers since $T_{\mathrm{C}} \propto \mathcal{E}^2$. Carriers on the drain side acquire energy from the electric field and form a hot carrier distribution while the electrons on the source side experience only a small electric field and remain at thermal equilibrium with the lattice. A gradient in carrier temperature over the gated region of the transistor is the result. Diffusion of hot carriers to the cold region then induces a thermoelectric

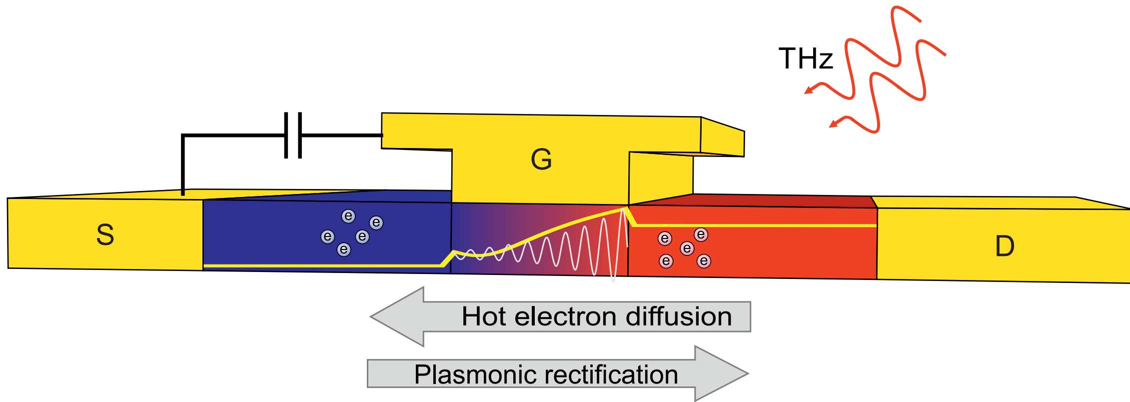

Fig. 7.1: Illustration of the origin of thermoelectric signals in a TeraFET with a built-in asymmetry under THz illumination. Carriers in the drain end of the channel (ungated region and transition to the gated region) are effectively heated by the electric field with respect to cold carriers on the source side, which remain at the equilibrium lattice temperature. A diffusion of hot carriers from drain to source against the temperature gradient is the result. Plasmonic self-mixing of the induced charge density wave produces a rectified signal of opposite direction.

signal which can be measured as a DC rectified signal. The diffusion contributions to the current density Eq. (3.30) is to some extent (details see below) contained in the hydrodynamic transport model as $j_{\text{diff}} = \mu k_{\text{B}} \partial_x (n T_{\text{C}})$. We show in this chapter that adding these diffusive contributions can - at least qualitatively, at the current stage of implementation - account for the measured additional signals. This strongly indicates that they are indeed of thermoelectric nature.

It should be mentioned at this point that thermoelectric contributions in TeraFETs have been suggested before based on both theoretical and experimental findings. First THz detection graphene-based TeraFETs working at 0.3 THz was presented in 2012 [30]. The measured voltage responsivities exhibited an additional zero-crossing besides vanishing signal at the CNP, which could not be explained in the context a plasma wave mixing model. It was suggested that an additional thermoelectric signal contribution due to a local heating of carriers near the transition between gated and ungated graphene regions could be the reason for this behavior. A similar effect was observed sometime later, however, the measured signals were attributed to bolometric processes [31]. Recently, thermoelectric signals were measured in TeraFETs based on black phosphorus nano-transistors [32], [36], [165]. On the theoretical side, suggestions have been made to include pressure gradients in the fluid-dynamic model equations, however, for the investigated GaAs HEMTs diffusion currents were considered negligible compared to electric field terms [35], [146]. An fluid-dynamic transport model extended by an energy transport equation was investigated in some detail with focus on the propagation of oblique plasma waves in the channel and formation of shock waves [33], [34].

7.1 Origin of thermoelectric signals in TeraFETs

It was argued in Section 2.5 that efficient exploitation of the plasmonic mixing principle requires the implementation of asymmetric boundary conditions. To prevent partial or full canceling of plasma oscillations by reverse, counteracting waves in the channel, one end of the transistor should be pinned to DC and AC ground, while the other end should be exposed to the full amplitude of an incoming THz signal. In this way, a wave is launched from one transistor end only and a maximum mixing signal is generated under homogenous illumination of the integrated antenna structure (comp. Fig. 2.4) [2].

On the other hand, a gradient in local electric field, and therefore energy distribution over the transistor channel, is a direct consequence of such a built-in asymmetry. We discussed before in Section 3.2.3 that in a situation when electron-electron scattering dominates energy relaxation by phonon scattering, an elevated carrier temperature can be the result - a hot electron distribution evolves. The efficiency of thermalization of excited carriers to form a hot carrier ensemble is mainly determined by underlying scattering processes in a material. In most cases, energy is exchanged between the electronic system and the crystal lattice mainly by electron-phonon or impurity scattering, associated with an energy relaxation time τ_{e} while thermalization of carriers is achieved by electron-electron scattering described in our model by the momentum relaxation time τ_{p}. This fact was reflected in the expression Eq. (4.13) for the carrier temperature by a factor $\tau_{\mathrm{e}}/\tau_{\mathrm{p}}$. An implicit assumption we make in this thesis is that carriers gain their energy solely from the electric field induced by the incoming THz radiation.

When heating of carriers is localized and a gradient in electronic temperature forms, a thermoelectric current can be the result. The phenomenon of the generation of a diffusion current due to a temperature gradient inside a material is known as the *thermoelectric effect*. I an open circuit, a respective voltage $V = S\Delta T$ is generated[166], which is commonly refered to as the *thermovoltage*. The factor S is the so-called *Seebeck coefficient* and is a material parameter depending on the Fermi level under specific operation conditions.

7.1.1 Derivation of Seebeck coefficient from transport equations

In a general formalis, the current density induced by an electric field $\mathcal{E}$ and temperature gradient ∇T is given as (comp. Eq. (3.30))

$$j = L_{11}\mathcal{E} + L_{12}\nabla T \tag{7.1}$$

in a slightly generalized formalism[49][91, CH. 13]. The coefficients L_{11} and L_{12} and their relation have physical meaning and, e.g., $L_{11} = \sigma$ is the conductivity as defined before. The Seebeck coefficient is in general given as the ratio $S = -L_{12}/L_{11}$ and a full expression is derived in Appendix B.3. We assume here a constant mobility and

[49]employing a diffusion matrix after Onsager's principle [54][83, Chapter1]

write the Seebeck coefficient as

$$S = -\frac{k_\mathrm{B}}{q}\left(1 + \frac{T_\mathrm{C}}{n}\frac{\partial n}{\partial T_\mathrm{C}}\right) \tag{7.2}$$

Assuming Maxwell-Boltzmann statistics in three dimensions and evaluating the derivative in Eq. (7.2), we obtain the common form of the three-dimensional Seebeck coefficient (see Appendix B.3) [84]

$$S_\mathrm{3D} = -\frac{k_\mathrm{B}}{q}\left(\frac{5}{2} - \ln\frac{n_\mathrm{3D}}{N_\mathrm{C,3D}}\right) \tag{7.3}$$

Since we investigate in this work a 2DEG, the according expression for the carrier density was derived as given in Eq. (B.11) with $N_\mathrm{C} = mk_\mathrm{B}T_\mathrm{C}/\pi\hbar^2$. The Seebeck coefficient in our case therefore takes the form

$$S_\mathrm{2D} = -\frac{k_\mathrm{B}}{q}\left(2 - \ln\frac{n}{N_\mathrm{C}}\right) \tag{7.4}$$

but the analytic form of S is maintained. The according coefficients for Fermi-Dirac statistics take a slightly more complicated form, since the Fermi integral $\mathcal{F}_0(\epsilon_\mathrm{F})$ in n must be considered, while the general expression Eq. (7.2) holds. In Appendix (B.3), the according expression is given for the sake of completeness.

The model implementation presented in this thesis does up to this point not consider the temperature dependence of the carrier density n. To some extent this also requires some conceptual consideration as to where additional charges are generated when an electric field is applied. One can assume that the metallic contacts provide carriers to account for a change in n. However, this has not been investigated in the course of this work and recall that carrier generation and recombination rates were omitted in the derivation of the transport model. A further detailed investigation is beyond the scope of this thesis but a dependence on T_C of the carrier density should be implemented in the future, because it is required to model the Seebeck coefficient correctly. As a consequence of this simplified approach, the derivative in Eq. (7.2) vanishes and the Seebeck coefficient simply becomes a constant

$$S = -\frac{k_\mathrm{B}}{q} \tag{7.5}$$

This presents a strong simplification to the physical situation in an FET, where clearly, the Seebeck coefficient of the 2DEG material should depend on the (gate voltage-controlled) Fermi energy. However, even with the reduced form of constant S we find that our simulations show a remarkable level of qualitative agreement with experimental observations.[50]

[50] Note that a constant Seebeck coefficient is not to be confused with constant amount of thermoelectric signal at all gate voltages. The total thermoelectric current still depends on V_G via the electric field, the carrier density and the carrier temperature in Eq. (4.10).

7.1.2 Direction of thermoelectric signals

While the classical thermoelectric effect was investigated experimentally by conventional heating of a material, i.e., locally increasing the lattice temperature,[51] in particular research dedicated to semiconductor devices led to a widespread investigation of thermoelectric currents or voltages induced by local field gradients. Because of the analogy of both phenomena, the latter is usually referred to as the *hot carrier thermoelectric effect*[23].

While the diffusion of carriers from hot to cold regions of a device is a universal effect, actual measurement of an induced current or voltage requires a transition region between two different materials with different Seebeck coefficient. When a homogenous material is locally heated, diffusion will be isotropic in all directions and in particular, opposite diffusive currents will cancel and prevent the observation of a net thermoelectric effect. In a common classical realization of a Seebeck measurement, two different metals are used and brought to contact at two distinct points, where one contact region is heated while the other remains cold [166][91, Chapter13]. A thermoelectric voltage can then be measured between the two contact regions. Recent thermoelectric measurements, e.g., on graphene, employ an intense laser beam for laser scanning over a sample and measuring the induced photocurrent at metal contacts on the edges (see, e.g., Refs. [27], [167]). It was observed in these spatially resolved experiments that a thermoelectric signal could only be recorded when either a transition region between bilayer and single-layer graphene was illuminated, or the region close to the metal contacts was heated by the laser.

In our devices, heating always occurs at the contacts of the FET where the radiation is coupled from the receiving antenna to the channel. Hence, the build-up of a temperature gradient and induced carrier diffusion can always be observed by measurement of either an induced thermoelectric current or voltage at the output terminals - in our case the drain end - of the device. A very comparable method of *electrical injection* of hot carriers has recently been employed on graphene flakes [29]. An additional “contact” region is formed in our devices at the boundaries of the gated and ungated channel regions, since the Seebeck coefficient of gated and ungated regions is different $S_{\mathrm{g}}(V_{\mathrm{G}}) \neq S_{\mathrm{ug}}$ unless $V_{\mathrm{G}} = 0$. Note finally, that these transitions are not a necessary condition for the build-up of a thermoelectric signal in TeraFETs as sometimes stated [30], [36], although the heating of the ungated channel regions plays an important role in the magnitude effect. A hot carrier distribution induced close to one of the metal contacts in the case of a FET without ungated access regions will also induce a measurable thermoelectric signal. This is, for example, the case in Si CMOS TeraFETs, where we also observed strong indications for thermoelectric signals, which are qualitatively similar to the ones in the AlGaN/GaN TeraFETs. There however, the contributions to the plasmonic detection signal become evident only at cryogenic temperatures (unpublished measurements).

We want to conclude this introduction by carefully investigating the direction of the thermoelectric signals with respect to the plasma wave detection, which was indicated already in the schematic Fig. 7.1. Figure 7.2 presents actual simulation

[51] This is the classical textbook situation for the conventional Seebeck effect.

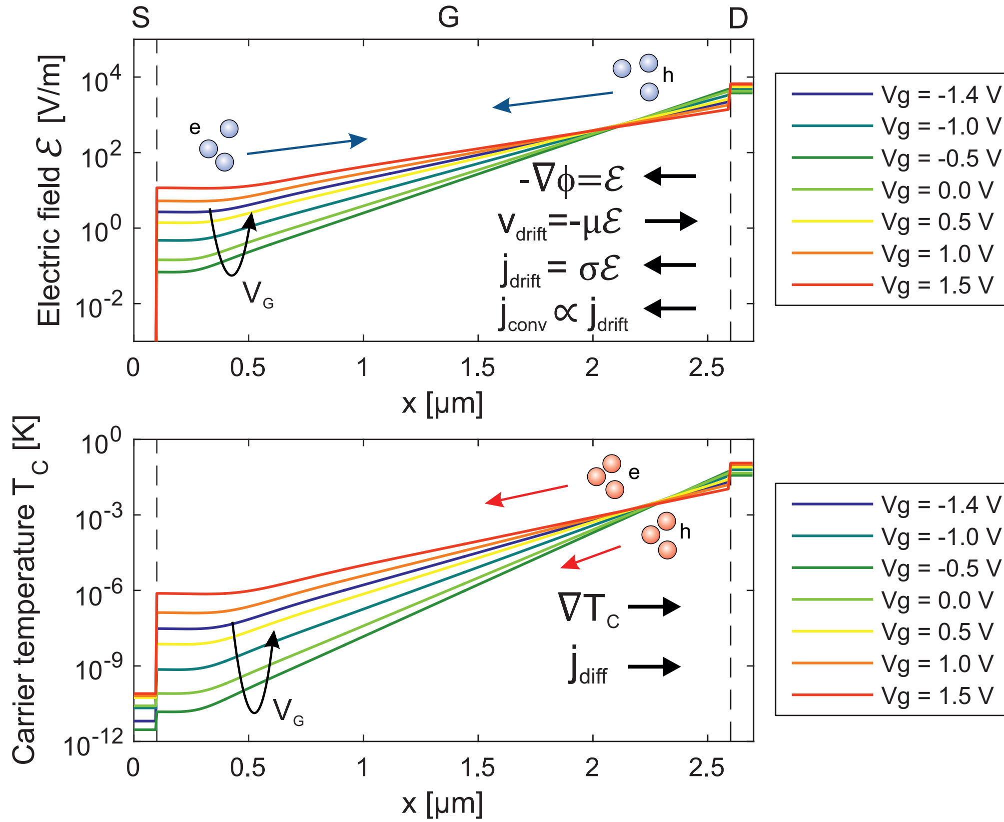

Fig. 7.2: Illustration of charge transport in the FET channel at the example of a field gradient in a graphene TeraFET. Top: Electric field. Electrons move with, holes move against the field gradient. The inset arrows indicate directions for electron transport. Note that the current density by definition is always opposite to the direction of movement of charge carriers. Bottom: Local carrier temperature. Here, holes and electrons both diffuse from the hot to the cold end of the channel. In total, for electrons the contributions of drift current density and diffusion current density are of opposite sign.

results performed for the local electric field and the local carrier temperature distribution along the transistor channel of a TeraFET. The top graph in the figure plots the electric field for a number of gate voltages against the spatial coordinate in the channel. The ungated regions, are indicated by the dashed vertical lines and amounted to 100 nm each in this specific technology.[52] Since the simulated device was a graphene FET, we observe as expected a similar dependence of the field strength in the transistor for voltages below and above the CNP ($V_{\mathrm{Dirac}} = -0.35$ V), indicated by the looped arrow in the plot. Let us consider the now the currents (current densities), which are induced by the two detection mechanisms - the plasmonic mixing and the thermoelectric effect, respectively.

The plotted local electric field in the figure is the result of a gradient of the gate-to-channel potential $-\nabla\phi = \mathcal{E}$. Its direction is indicated by the arrow on the right. The direction of drift velocity of electrons - at this point a distinction

[52]Simulations were performed for the graphene TeraFET presented in Chapter 6 at a frequency of 0.6 THz. Similar results were obtained for the GaN-based devices.

between electrons and holes becomes important - is opposite to the electric field and $v_{\text{drift}} = -\mu\mathcal{E}$ (comp. Eq. (B.43) in Appendix B). In the example, electrons drift from the source to the drain side of the FET. Because of the definition of the current density $j = -qnv$, a drift current $I_{\text{drift}} = j_{\text{drift}}W$ from drain to source is the result. The plasmonic mixing signal, given by the convective current density j_{conv} in the transport equation points in the same direction (cp., e.g., Eq. (3.34)).

The bottom graph in Fig. 7.2 shows the distribution of carrier temperature over the device. Note that the scale is logarithmic and the gradient along the channel is not a linear one. The temperature gradient points from source to drain, as the source side of the channel is on ground and the potential is shunted by an external capacitance to ensure the asymmetric boundary conditions discussed before. The sign of the diffusion term in the velocity density equation is negativ with respect to v (again, cp. Eq. (B.43) in Appendix B). In accordance with intuition, the hot electrons diffuse against the temperature gradient from the hot to the cold end of the channel to achieve thermal equilibrium. Once more, the respective current density has reverse sign of the velocity and a diffusion current pointing along the temperature gradient results. In conclusion, the resistive and plasmonic mixing signal should have opposite sign with respect to a thermoelectric signal induced by the same electric field distribution. Both detection mechanisms counteract, which, e.g., leads to the observed sign switch in the THz measurements with the GaN TeraFETs, a more detailed discussion following below.

Note finally, that the above situation is fundamentally different in graphene, where the direction of plasmonic mixing is mainly determined by the type - electrons or holes - of the majority of charge carriers in the channel. The drift and convective currents reverse sign for hole-dominated transport whereas carriers diffuse from hot to cold channel regions independent of the sign of their charge. The thermoelectric contribution to the total detected signal can therefore be additive or subtractive depending on the applied gate voltage with respect to the CNP.

7.2 Experimental evidences

Thermoelectric signal contributions were observed in the context of TeraFET characterization experiments, which added to the motivation to implement a comprehensive hydrodynamic transport model in a circuit solver. We expect that thermoelectric detection should always be present in TeraFETs for optimized asymmetric signal coupling boundary conditions. On the other hand, close to the threshold where TeraFETs are commonly characterized and where the best operation point of device sensitivity is expected for most materials, thermoelectric signals are mostly masked by the plasmonic THz response and cannot be investigated independently. In particular at higher gate voltages above threshold, where the signal of plasma wave mixing decays to zero, thermoelectric signals can become evident. It was found in the carried out THz detection experiments that the signals constituted merely a side effect in the investigated AlGaN/GaN detectors but emerged as significant detection signals in graphene TeraFETs at the same order of magnitude as the plasma wave responses.

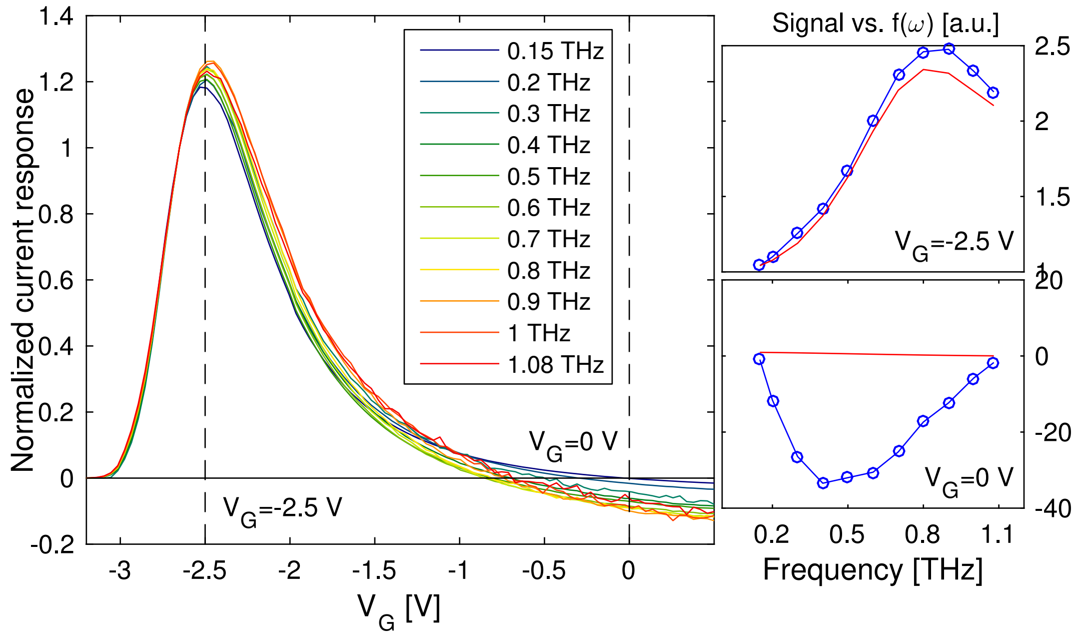

Fig. 7.3: Left: Measured current responses normalized to operation points of best optical NEP ($V_G = -2.7$ V). Right: Frequency-dependence of the normalized current responses with respect to the plasmonic enhancement factor $f_D(\omega)$ at two distinct gate voltages marked by the dashed vertical lines in the left graph. The signal evolves as expected from plasma wave mixing theory close to the threshold ($V_{th} \approx -2.5$ V) where the response is maximum. At higher gate voltages above threshold, a significant deviation from expected vanishing response and a thermoelectric signal with negative sign is observed.

7.2.1 AlGaN/GaN TeraFETs

Signal contributions to measured TeraFET current responses, which deviate from expected plasmonic mixing signals, could already be recognized in the respective chapter on TeraFET characterization, e.g., in Fig. 6.12, at high gate voltages above threshold. To emphasize the effect, the same current responses from THz measurements with the AlGaN/GaN bow-tie TeraFET are plotted versus radiation frequency in the main graph in Fig. 7.3, but normalized for each single frequency to the gate bias point of minimum NEP. The responses are seen to almost monotonically increase towards higher positive values close to the maximum and along the falling edge for higher gate voltages above threshold ($V_{th} = -2.5$ V). However, at a certain point, the behavior is reversed and a sign switch in the detected signal is identified, which seems to saturate for even higher gate biases. In order to confirm that the observed signals at these high voltages above threshold are indeed the manifestation of an additional physical mechanism, which is different from plasma wave mixing, we compare the frequency dependence of the signals to the anticipated frequency dependence of plasmonic enhancement. The small plots on the right of Fig. 7.3 were obtained from multiplication of the normalized current response at the lowest frequency for two distinct gate voltages by the plasmonic enhancement factor $f_D(\omega)$ calculated after Eq. (2.17) for device parameters of this particular TeraFET. It is clearly recognized that the increase of the normalized detection signal versus frequency at the point of maximum responsivity ($V_G = -2.5$ V) follows $f_D(\omega)$ to

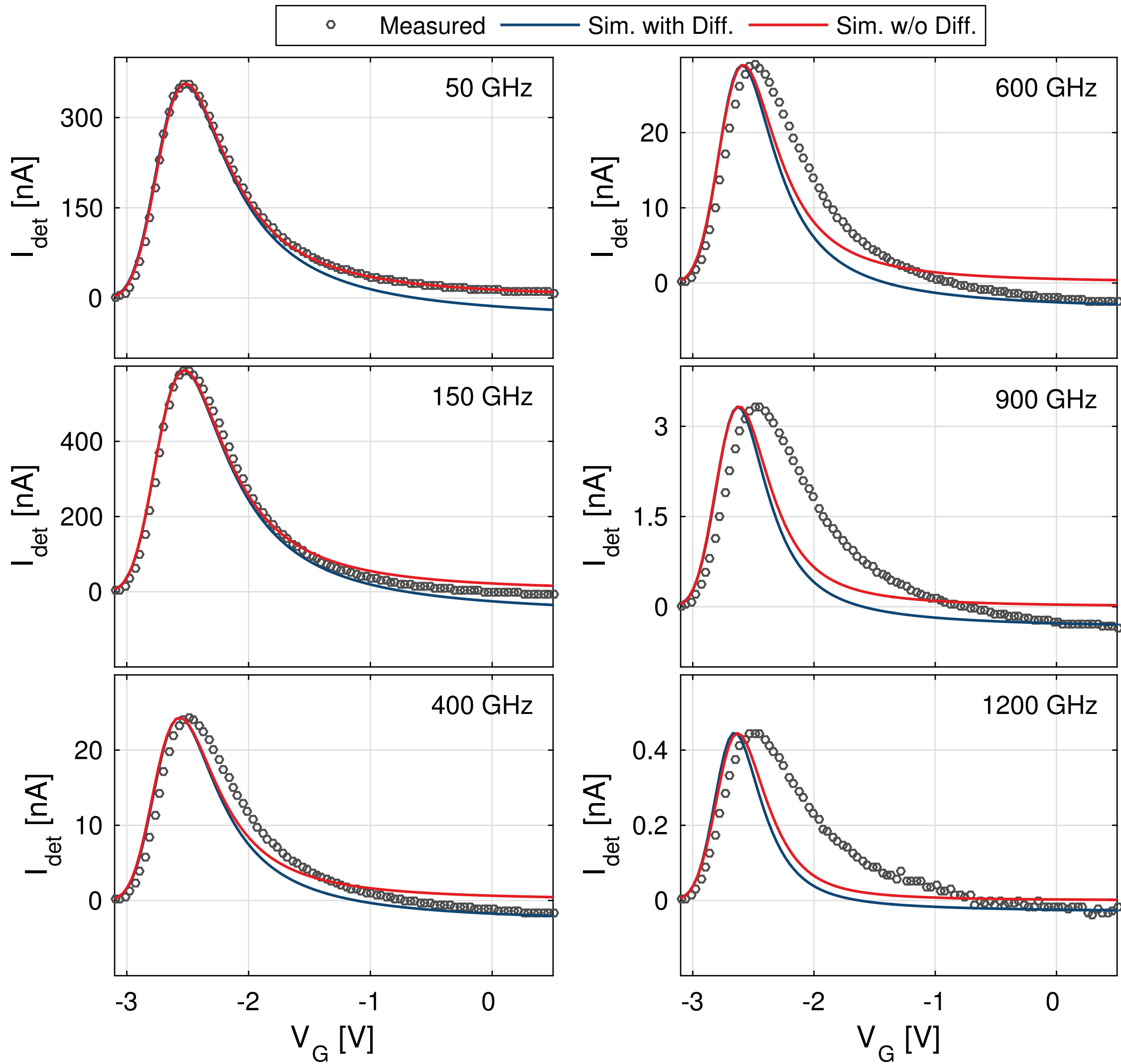

Fig. 7.4: Simulation and measured signal of the AlGaN/GaN TeraFET at different frequencies versus gate voltage. The red curves are simulated data without thermoelectric contribution, while the blue curve includes the effect. The symbols represent the measured signals. The simulated data can clearly be recognized to deviate from the pure plasmonic behavior with frequency as thermoelectric conributions set in. For high frequencies, the contribution start to decrease again. The simulation with diffusive contribution follows this trend (cp. Fig. 7.5 below), however, the plasmonic and thermoelectric signals seem to be overpronounced.

a remarkable degree. In contrast, for the signal at high gate bias ($V_{\mathrm{G}} = 0$ V), an entirely different behavior compared to the anticipated plasma wave response is observed. While the enhancement factor remains close to zero and no plasmonic mixing signal is expected, the measured signals with negative sign build up to reach a maximum around 0.4 THz and then decrease again. This observation presents clear empirical evidence that an additional physical mechanism besides conventional plasma wave mixing is responsible for the observed signal at high gate biases. Note also, that the enhancement factor $f_{\mathrm{D}}(\omega)$ cannot account for a switch in signal sign for the specific device under test and frequency regime of interest - for a rough

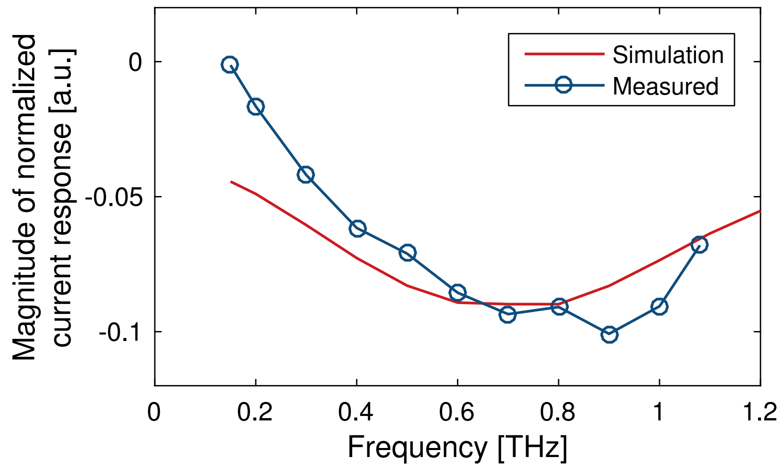

Fig. 7.5: Measurement and simulation of the GaN TeraFET detection signal extracted from the data in Fig. 7.4 at a gate voltage of $V_G = 0$ V where thermoelectric contributions are pronounced. We find a qualitative agreement of the signal trend between simulation and measurement, however, the thermoelectric signal seems to degrade fast, especially towards lower frequency, than the simulated one.

comparision see Fig. 2.3 where the enhancement shows first indications of a sign switch at significantly higher frequencies than the measured ones.

In order to reinforce the above implications, Fig. 7.4 presents results from a circuit simulation based on the hydrodynamic transport model presented in Chapter 4. Simulations were performed at distinct frequencies of 50, 150, 400, 600, 900, and 1200 GHz and the resulting curves were normalized to the peak measured current response at each single frequency. The measured responses are plotted in gray. The implementation of the circuit model as described in Chapter 4 allowed for diffusive contributions to the total detection signal to be switched on and off for the simulations. The graphs in the figure show simulated THz responses without thermoelectric diffusive currents as green lines and simulations with the full hydrodynamic model as red lines. We find as a first evidence that for simulations without contributions from diffusive terms the rectified signals level off to zero for high gate voltages, in contrast to the measured current responses above 50 GHz, as expected within the plasma wave mixing picture. When diffusive and in particular thermoelectric[53] current contributions are switched on in the simulations, the responses exhibit a sign switch and an additional, frequency-dependent signal contribution emerges at high gate voltages above threshold, which begins to saturate towards even higher biases. We therefore conclude that the observed signals are indeed of thermoelectric origin.

Some remarks must be made about the simulation results presented in Fig. 7.4. First, a pronounced shift with respect to applied gate voltage of the maximum current signal is observed versus radiation frequency in the simulated data, which is not present in the measured THz responses. It can be assumed that this behavior is due to an overestimation of the plasmonic mixing mechanism in the device simulation. The n-n^+ transition from gated to ungated channel regions was not modeled in

[53]It is observed that diffusive signals due to the $\partial_x n$-term in Eq. (3.30) play a minor role only.

detail and is therefore implemented as a sharp boundary rather than a smeared out transistion. As a consequence, reflections of plasma waves at the intrinsic channel boundaries are more pronounced than expected in a real device situation. This observation contains another implication, i.e., the plasma wave enhancement of distributed resistive mixing seems to be of minor influence to the THz response in the particular device under test over the investigated regime of frequencies. It was proposed to include fringing effects in a device simulation by introducing a gate "extension" with an exponentially growing gate-to-channel separation $d(1+\exp(d))$ to model effects of a smooth transistion region [47]. Another important aspect is that the ungated resistance is assumed to be independent of frequency. However, the largest amount in R_{ug} is due to the contact resistance (cp. discussion in Section 6.3.3). It must be assumed that a strong frequency dependence can exist for this part of R_{ug}, which is not modeled in our implementation, and which should diminish the influence of the ungated parts in the simulation.

Second, the frequency dependence of the thermoelectric signals of the measured TeraFET responses is only reproduced on a qualitative level in the simulations. Fig. 7.5 shows again the frequency dependence of the thermoelectric signals at $V_{\mathrm{G}} = 0$ V for the measured (blue line and symbols) compared to the simulated (red line) normalized current responses. The overall trend of frequency-dependence of the measured thermoelectric signal is clearly reproduced by the simulation.[54] However, the thermoelectric contribution to the THz response decays more rapidly in the measurement than predicted by the device simulation. The decrease of the thermoelectric signal towards lower or towards higher frequencies, reflects two different mechanisms. On the low frequency side, the asymmetry in the device is strongly dominated by the efficiency of asymmetric coupling of the incident radiation. In particular, the HF signal path due to capacitive gate-source coupling was illustrated earlier in Fig. 5.5. For low frequencies, more power is distributed to the source-side ungated region of the transistor channel leading to a reduced asymmetry and a homogeneous heating of both ungated regions of the FET. The gradient in electronic temperature is thereby reduced and the thermoelectric signal disappears. For growing frequencies, the asymmetry is enhanced and the thermoelectric signal increases - in an ideal drain coupling situation, only the drain-side ungated channel region is heated and the charge carrier ensemble on the source side remains in equilibrium with the crystal lattice. As the frequency rises further, heating of the charge carrier ensemble becomes increasingly inefficient. The carrier temperature in frequency domain is easily shown to decrease according to[11] $T_{\mathrm{C}} \propto 1/\sqrt{1+\omega^2\tau_{\mathrm{p}}^2}$ in analogy to a classical driven harmonic oscillator with damping. When the driving frequency significantly exceeds the resonance frequency, energy transfer to the system is suppressed and in conclusion, the thermoelectric signal contributions in our TeraFETs disappear.

Third, calculations were based on an estimated energy relaxation time of $\tau_{\mathrm{e}} = 1$ ps [168], [169]. An exact determination of the electron scattering times is far beyond the scope of this thesis and τ_{e} is referred to literature values. Note that the hot

[54] Note that again an additional frequency dependence of the contact resistances could be responsible for some of the differences here. Note also, that the deviations could also be interpreted as an overall vertical shift of the simulated curve.

electron energy relaxation time has been investigated at low temperatures in the given references. The momentum scattering rates are found from parameter extraction of DC resistance measurements to be $\tau_\mathrm{p} \approx 180$ fs. Hence we employ a ratio of $\tau_\mathrm{e}/\tau_\mathrm{p}$ of roughly 5:1, which is within reasonable boundaries. In general, a higher ratio of $\tau_\mathrm{e}/\tau_\mathrm{p}$ should lead to a more effective heating of charge carriers (comp. Eq. (4.13)). The carrier mobility, however, is merely a fit parameter in our analysis being independent of the applied gate bias, which is assumed as a valid simplification for low electric fields. Detailed modeling of the energy dependent carrier mobility should be performed for further insight on these matters.

7.2.2 Graphene TeraFETs

Pronounced thermoelectric signals were also measured in the graphene TeraFETs, which were presented in the previous chapter. A major difference with respect to the GaN-based devices was that the contributions did not show up as a mere side-effect of the plasmonic mixing signal. The typical roll-off of the plasmonic THz response with high gate voltages above threshold[55] was almost entirely masked by thermoelectric signals on the same order of magnitude as the maximum of the detector's plasmonic responsivity. Respective measurements were shown earlier in Fig. 6.21 and the observed signals were compared to a purely plasmonic TeraFET device simulation with the implemented detector model but with the diffusive terms switched off. Evaluation of the TeraFET's NEP even showed that the best point of bias operation was shifted far into the strong inversion regime due to the distinct thermoelectric response. In voltage read-out mode, the noise of TeraFETs reduces with increasing gate bias voltage as the FET's resistance is decreased. In combination with the observed thermoelectric detection mechanism the prospect arises that a new type of detectors could be realized, whose sensitivities of the thermoelectric mixing mechanism can exceed the plasma wave-based detection principle.

We already discussed above that the origin of thermoelectric signals in TeraFETs is the local generation of hot carriers in the FET's channel due to an asymmetric heating of channel regions by the incoming HF signal. Such a distribution can be excited with great efficiency in graphene[27], [29], [85], [86], [170]. In a number of experimental studies in 2011, Gabor and Song found that based on an effective decoupling of the heated electronic system from the crystal lattice, the thermoelectric effect is particularly pronounced in graphene and indeed dominates the direct photoresponse of the material [27], [28]. In previous optical/IR pump-probe spectroscopy investigations, thermalization of excited carriers within the carrier ensemble on an ultrafast 1 to 100 fs timescale was reported [171]–[174]. This leads to an initial formation of a hot carrier distribution [27]–[29], [170], [175], [176]. After thermalization, carrier energy relaxation via optical phonons slows down and the electronic system becomes thermally decoupled from the lattice - this has been referred to as *quenching* of electron-lattice relaxation [27]. Further relaxation of carrier energy happens mainly via scattering of acoustic phonons and impurities, which are significantly slower

[55] In graphene, the classical transistor threshold voltage is substituted by the Dirac voltage at the CNP.

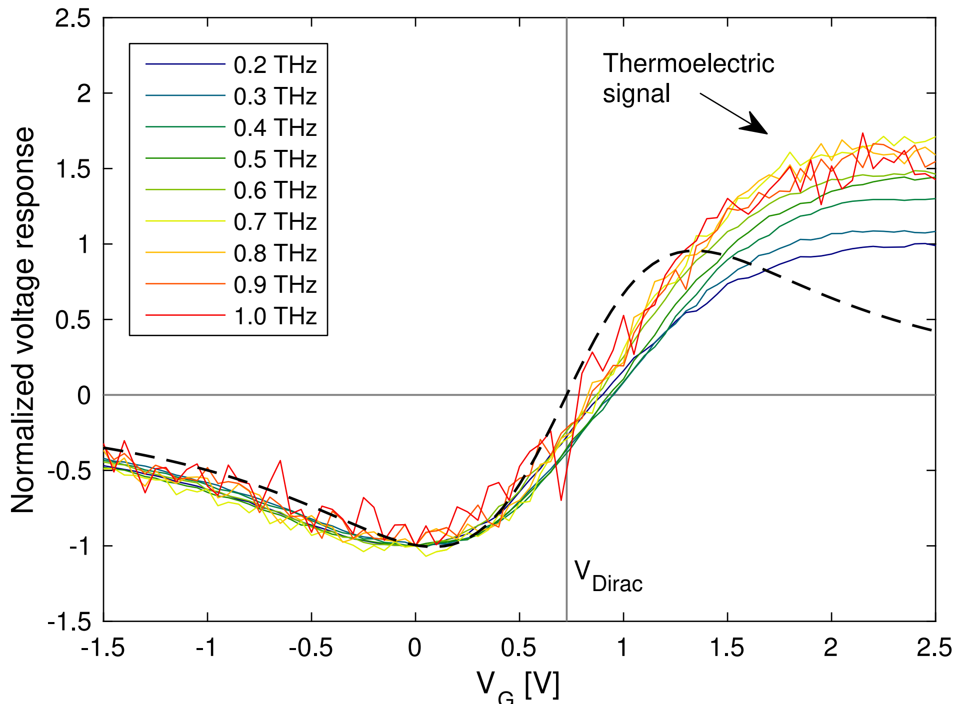

Fig. 7.6: Frequency dependence of the THz response of one of the graphene TeraFETs (Device 2). The measured signals where normalized at $V_\mathrm{G} = 0V$. The dashed line shows the simulated, anticipated device response from purely plasmonic mixing. A strong thermoelectric signal with pronounced frequency dependence can be recognized at voltages $V_\mathrm{G} > 1$.

processes[38]. It was shown that cooling of hot carriers occurs on a 1 to 100 ps timescale and associated mean free paths of carriers can extend to several micrometers at room temperature [86], [170]. For typical nanometer to micrometer device dimensions this implies that carriers can travel along the entire device without experiencing a significant energy loss.

When the described heating of the carrier ensemble is local - resulting in the build-up of pronounced gradients in electronic temperature - strong hot carrier thermoelectric currents can be the result and were measured by laser scanning photocurrent miscroscopy [27], [28], [176], photoemission spectroscopy [177], and recently by a non-local electrical injection method [29]. A multitude of literature exists on the topics of carrier dynamics and the thermoelectric effect in graphene, which cannot be listed here comprehensively. Some valuable review-type sources are Refs. [29], [85], [86], [170]. A summary of recent thermoelectric measurements in graphene is given in Ref. [178].

A gradient in carrier temperature T_C in our TeraFETs evolves due to the implementation of asymmetric boundary conditions for efficient plasma wave mixing. For idealized drain-coupling, the incident radiation energy is concentrated as an electric field at the drain side of the transistor. A simulation of electric field and carrier temperature in the channel of one of our graphene TeraFETs was shown earlier in Fig. 7.2. We discussed that the contribution of thermoelectric signals to the total rectified THz signal can be additive or subtractive depending on the applied gate bias voltage.

Figure 7.6 shows signals from a THz detection experiment with the graphene FET (Device 2), which was introduced before in Chapter 6. Measurements were performed at different frequencies and the obtained response curves versus frequency normalized at $V_{\mathrm{G}} = 0$ V. The dashed line shows the modeled detector response from a circuit simulation performed without thermoelectric contributions. The normalization reveals again strong thermoelectric contributions and a pronounced frequency dependency of the latter. Also, at high frequencies, the effect seems to decrease again and one can speculate if a reversal of the dependence starts to set in, despite the growing noise in the detection signals. The normalization can be misleading to the false premise that a thermoelectric contribution is only present at positive high gate voltages. Recall, however, the measurements presented in Section 6.4 in Fig. 6.21. There we observed, in particular, a detection signal at $V_{\mathrm{G}} = V_{\mathrm{Dirac}}$ where the plasmonic mixing signals should vanish, because the derivative of the channel conductance in the quasi-static responsivity Eq. (2.20) becomes zero. This is probably the strongest evidence of an additional detection mechanism besides the plasma wave-enhanced resistive mixing.

We finally demonstrate that the implementation of the modified graphene model including diffusive current contributions also can largely account qualitatively for the observed signals. Figure 7.7 shows again the measured voltage (left) and current (right) responsivity of graphene TeraFET Device 1 from Chapter 6. The measured data are plotted as open symbols. The dashed line represents a simulation with the circuit model implementation at 600 GHz but with diffusive contributions to the total rectified signal switched off. Note that this does not correspond to the quasi-static detection limit alone, which THz measurement signals were previously compared to, e.g., in Refs. [5], [30], [31], but already includes plasmonic enhancement as well as HF impedances of gated and ungated channel regions, which is an essential improvement in modeling of the detector's response. The simulated signals reflect the expected overall $\propto (1/\sigma)(\partial\sigma/\partial V_{\mathrm{G}})$ trend (cp. Eq. (2.20)) leading to a vanishing THz response for high positive or negative gate voltages where the channel conductance saturates. In particular, the responsivities become zero at the CNP where $V_{\mathrm{G}} = V_{\mathrm{Dirac}}$ for the same reason, the derivative of the channel conductivity vanishing at this point.

The solid red line in Fig. 7.7 gives the result of a simulation with the full hydrodynamic model as presented in this thesis. At voltages $V_{\mathrm{G}} > V_{\mathrm{Dirac}}$ above the CNP, the trend of the measured signal is clearly reproduced in the investigated region of bias voltages. On the other side of the CNP for $V_{\mathrm{G}} < V_{\mathrm{Dirac}}$, the simulation data show a lower THz responsivity as predicted from a purely plasmonic simulation (dashed line) and hence reflects the experimental obesrvation. Most important, the non-vanishing detector response at the CNP is also reproduced by the model, accounting for a general shift of the measurement curve with respect to the plasma wave signal. This behavior was observed before [30], [31]. Altogether, including diffusive, and particularly thermoelectric signals[56] in the detector model can largely account for the measured THz rectified signals in graphene TeraFETs.

From a detection efficiency point-of-view the thermoelectric effect in graphene

[56]We observe for graphene TeraFET, similar to the investigated AlGaN/GaN devices, that the diffusion due to a gradient in carrier temperature has only minor influence on the simulated detection signal.

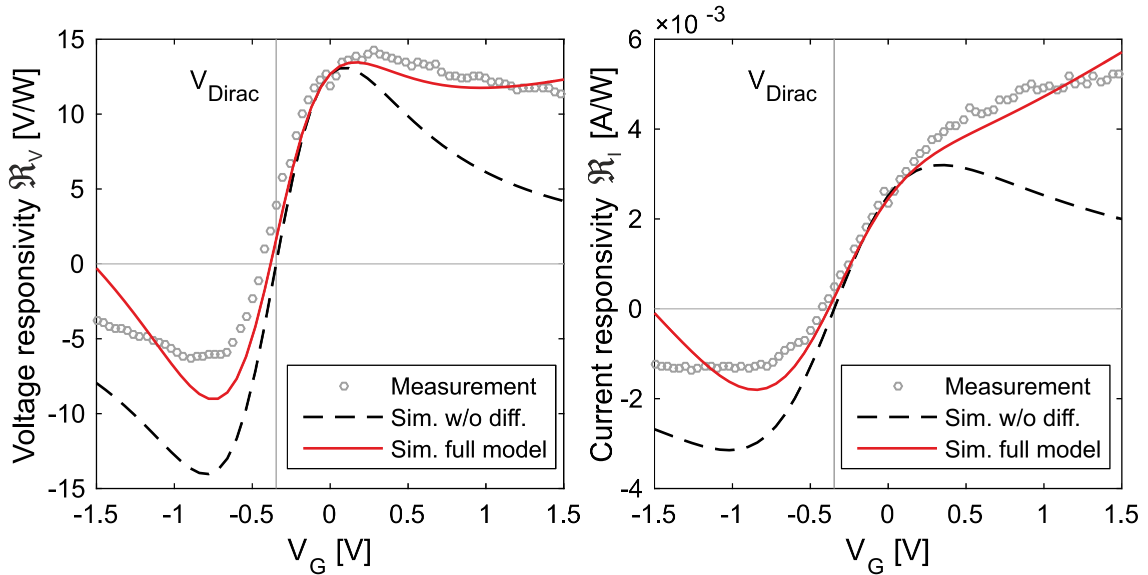

Fig. 7.7: Comparison of simulation and measurement of the voltage (left) and current (right) responsivity of graphene TeraFET (Device 1) measured at 590 GHz. The data for the simulation were scaled to the point of maximum responsivity in the curve with the diffusive contributions switched off. Again, thermoelectric signals are overpronounced due to additional frequency-dependent factors (see discussion).

TeraFETs is of particular interest because of two aspects. First, the measured signals of thermoelectric origin were observed to be on the same order of magnitude as the plasmonic-enhanced resistive mixing signal. Second, the contribution to the total detection signal was additive for gate voltages $V_G > V_{Dirac}$, hence, an enhancement of plasma wave mixing takes place in graphene FETs. To further substantiate these promising premises, Fig. 7.8 shows simulations of the frequency-dependence of the total efficiency factor $f_{tot}(\omega)$ - as introduced earlier in Section 5.2 - including besides the plasmonic mixing efficiencythe influence of extrinsic, ungated detector parts. Again, simulations were performed with and without thermoelectric contributions, indicated in the Figure as solid and dashed lines, respectively. The simulation was performed at three different gate voltages of $V_G = -1.5, +1.5$, and 0 V, the latter corresponding to a bias point close to maximum expected plasmonic response.

We observe the same expected behavior as simulated before for the GaN TeraFETs (cp. Fig. 5.7). The efficiency of detection relative to quasi-static mixing drops below unity for increasing frequency, because an increasing amount of incident power is distributed to the ungated channel regions. When thermoelectric contributions are added to the simulated detection signal, the falling trend in f_{tot} is found to be significantly weaker at the high voltages below and above the CNP at $V_{Dirac} = -0.35$ V, the regions where thermoelectric contributions were most prominent in the THz detection experiments. After an initial drop, the detection efficiency almost reaches unity again around 1 THz before the onset of another roll-off with frequency becomes apparent. This behavior is in accordance with the observations made in the AlGaN/GaN TeraFETs (see Fig. 7.5), where also an increase of thermoelectric detection up to roughly 1 THz was found, followed by a roll-off towards higher input frequency. We can therefore assume that the observed detection mechanism is the same in TeraFETs

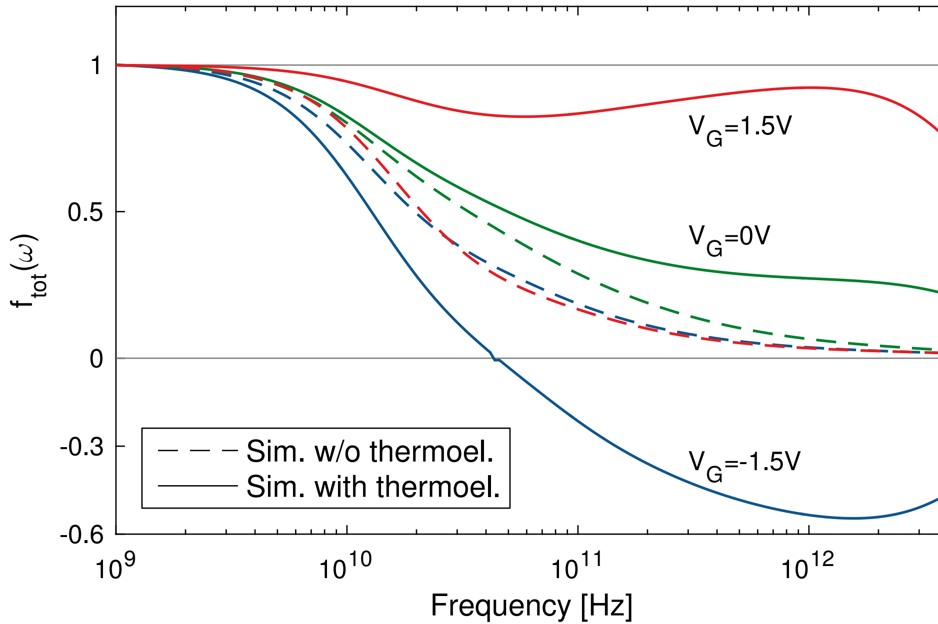

Fig. 7.8: Signal trend versus frequency for a device simulation of graphene Device 1 with thermoelectric contributions switched on (solid lines) and off (dashed lines) at the given gate voltages. The efficiency factor is strongly degraded below unity due to the influence of ungated channel parts. When the thermoelectric signal is switched on, however, the efficiency almost reaches unity again. This shows that for the graphene device, the measured response is mainly thermoelectric.

in both material systems and the simulated data strongly supports the suggestion that the physical basis for the signals is the hot carrier thermoelectric effect.

Some closing remarks should be made about the simulated curves presented above. It appears that the simulated thermoelectric signals in Fig. 7.7 seem to be overpronounced, in particular, in regions of relatively high negative gate voltage around $V_G = -1.5$ V. It is up to this point not clear what is the exact reason of this behavior. It must also be mentioned, that the general HF behavior of the implemented model, i.e., also the frequency-dependence of the channel impedance and plasmonic enhancement of resistive mixing appears too strong in the simulations. In the previous section, we addressed one possible explanation - the influence of sharp boundaries at the transition region between gated and ungated channel parts. Another highly probable effect, which is not exactly covered in the model is the frequency-dependence of the ungated resistance in general. The value for R_{ug} employed in our simulation was extracted from DC measurements of the channel conductance with R_{ug}. We discussed in Chapter 6 in the context of the GaN devices that $R_{ug} = R_C + R$S contains both the actual sheet resistance of the ungated channel parts, as well as the contact resistance at the transistor terminals. In fact, with the especially short ungated region in the graphene devices of only $L_{ug} = 100$ nm on each side, it must be assumed that the largest part of R_{ug} indeed stems from the contacts. Those are in general not purely ohmic and a dependence of decreasing R_C over frequency must be assumed. The calculations above were therefore performed with an empirically determined reduction of the ungated resistance by roughly a factor of 5 at THz

frequencies. We did not model this mechanism in detail, which should be a main focus in future development of the implemented model.

Another important factor already discussed in the previous section are the exact scattering times footnoteand mechanisms, for that matter. The efficiency of carrier heating is determined by the individual scattering times of τ_p and τ_e and their ration (cp. Eq. (4.13)). On the other hand, here we did not conduct additional measurements of τ_e or included a detailed theoretical modeling. An energy relaxation time $\tau_\mathrm{e} \approx 75\tau_\mathrm{p}$ times larger than the momentum relaxation time was assumed in the simulation. The momentum relaxation time τ_p in the simulations lay in the range of 20 to 60 fs[57] and τ_e was therefore assumed to be on the order of a few ps, which is in reasonable agreement with theoretical and experimental observations [86], [170]. A detailed modeling of scattering times should be a major direction of improvement of the current state of the model implementation.

Finally, note that the thermoelectric effect for gate biases below the CNP can lead to a second sign switch in the total detection signal, which is almost indicated in the presented simulation in Fig. 7.7. Although the slope of the detected signal in the figure is not steep enough to exhibit such behavior in the investigated range of gate voltages, we observed sign switches in some of our investigated devices. Similar observation where reported in Ref. [30], where also the presence of thermoelectric signals was suggested. This aspect is analogous to the sign switch we found in the AlGaN/GaN TeraFETs with unipolar charge transport and emphasizes once more the same underlying physical principle in both materials.

[57] Recall that the momentum scattering time is not fixed but depends on the applied gate voltage in graphene (cp. Eq. (6.17)).

Chapter 8

Summary and Outlook

In this thesis, the modeling and experimental characterization of antenna-coupled field-effect transistors for the detection of THz radiation (TeraFETs) was investigated. The main focus lay on the formulation of a hydrodynamic model and its implementation in a circuit model to describe charge carrier transport in the FET's channel under consideration of both, the plasma wave mixing mechanism and diffusive, thermoelectric currents in the devices. Both effects originate in an asymmetric coupling of the incident THz radiation via the integrated antennas to achieve a maximum electric field amplitude on one end of the transistor channel while pinning the potential to zero (AC ground) on the other end. We discussed in Chapter 2 that such an asymmetry in excitation is essential in the realization of efficient plasmonic THz detection to prevent a counteracting detection mechanism, which would degrade the total rectified DC measurement signals.

The localized electric field distribution, in turn, gives rise to a local heating of the charge carrier ensemble of the FET's two-dimensional electron gas (2DEG). The high charge carrier density in the 2DEG promotes energy distribution within the electronic system by frequent carrier-carrier collision over comparably slow energy relaxation by phonon and impurity scattering to the crystal lattice. A gradient in carrier Temperature evolves over the transistor channel, in particular, between the ungated regions on the hot and cold side of the device. Such a gradient has been shown to be accompanied by a diffusion of charge carriers against the spatial gradient of carrier temperature from hot to cold regions. This hot carrier thermoelectric effect presents a second detection mechanism in TeraFETs and was investigated in some detail in this work based on experimental observations and device modeling.

Formulation of the TeraFET model equations

We reviewed in Chapter 2 the classical plasmonic detection mechanism in THz radiation in TeraFETs by non-linear self-mixing of plasma waves in the FET's intrinsic gated channel region. A calculation of the plasmonic enhancement of distributed resistive mixing in the quasi-static approximation was presented in some detail and the deducted plasmonic efficiency factors were discussed using as an example device parameters of a AlGaN/GaN TeraFET, which was produced during the time of this work. We presented the requirement of asymmetric radiation coupling based on

measurements, which were performed with TeraFETs with different levels of device asymmetry [2]. Over the course of this work we found that implementation of the asymmetric coupling is efficiently achieved by drain-feeding of the THz signals from the integrated antennas and additional gate-source shunting with the help of an external capacitance. Such a capacitance was realized as a metal-insulator-metal (MIM) structure in fabricated AlGaN/GaN TeraFETs and by inducing a split-bow geometry in single metal-layer bowtie antenna structures in graphene TeraFETs (see Chapter 6). Both approaches yielded excellent results in detector sensitivity.

The basis for the theoretical calculations of the detection in TeraFETs by plasma wave mixing is a fluid-dynamic description of the charge carrier transport in the FET's 2DEG. Such a model was formulated by Dyakonov and Shur in the early 1990s [18] as has since been widely applied in literature dedicated to modeling and theoretical analysis of THz detection with TeraFETs. A number of recent experimental observations revealed, however, that additional detection by thermoelectric signals can yield significant contributions to the total rectified THz signal, which are not readily covered by this theoretical description. Highly efficient TeraFETs had mostly been investigated in mature Si CMOS technology before, where the influence of such effects is minor due to practically non-existing ungated channel regions. We observed similar signal contributions only in cryogenic THz measurements (unpublished data, not shown here). With emerging technology of fabrication of TeraFETs, in particular, in high electron mobility transistors (HEMTs) in GaN, single-layer graphene FETs and recently TeraFETs with CNTs (unpublished data) and black phosphorus [165], thermoelectric signals could be measured in room-temperature THz detection experiments. The observation of these effects was the major motivation to extend the classical plasmonic detection model to account for thermoelectric detection.

A closer investigation of the fluid-dynamic transport description by Dyakonov and Shur shows that the transport model is a reduced one in the sens that hydrodynamic pressure terms were omitted in the formalism. In particular, extension of the model by spatial gradients in local carrier density and local carrier temperature adds diffusive carrier transport phenomena including the thermoelectric effect. In Chapter 3 of this thesis we presented the deduction of a full hydrodynamic transport model for charge carriers in a 2DEG from the fundamental Boltzmann transport equation. Comparison with the original formulation of transport equations revealed that indeed the hydrodynamic pressure is commonly omitted in the classical TeraFET theoretical description. By making a number of assumptions of the exact form of the individual terms in the model equations and using an analogy of to a transmission line equivalent circuit formalism, we presented the implementation of the device model in commercial numerical circuit simulation software. Let us consider here the most important simplifications we applied in this implementation.

Current simplifications in the implementation of the hydrodynamic device model

First, derivation of the hydrodynamic equations was presented in a generalized formalism employing a displaced Fermi-Dirac distribution for carrier statistics. For the implementation, however, we reduced ourselves to the approximation of the full degenerate case by the simpler Maxwell-Boltzmann distribution describing non-

degenerate semiconductors. When our devices are operated close to the threshold, such an assumption seems reasonable. For an operation in the strong inversion regime far above threshold, a modification of, in particular, the carrier density and the kinetic energy density becomes important and should be incorporated in future development of the model.

Second, the equation for the evolution of energy density in the hydrodynamic model was simplified by omitting non-stationary terms and neglecting the drift velocity component in the averaged kinetic energy. An evolution of the energy is therefore not included in our model and the carrier temperature is calculated directly from the stationary, local electric field in the channel. This simplified approach is sometimes referred to as an energy transport model - however, we do consider convective transport in the current density equation, which is commonly neglected in such models. We also showed that these convective contributions are the origin of the plasmonic enhancement of distributive resistive mixing (cp. Section 4.2). Nevertheless, it should be aimed for an inclusion of the full energy transport equation in the implementation of the transport model in the future.

Third, concerning the thermoelectric effect in particular, we showed that the current stage of model implementation does not account for a temperature dependence of the carrier energy and mobility (cp. Section 7.1.1). The result is a constant Seebeck coefficient independent of material and Fermi energy (applied gate voltage). This certainly presents a strong simplification and should be the main point of investigation for an improvement of the current TeraFET device model. We showed in Chapter 7 in a number of comparisons of measurement results and numerical simulations with the implemented circuit model that despite this approximation, the thermoelectric signals in our TeraFETs could to a large extent be reproduced qualitatively.

Fourth, derivation of the transport model was based on a parabolic band approximation for the energy dispersion in conventional semiconductors. The model was adapted by a number of modifications to simulate the graphene TeraFETs produced in the course of this work (cp. Sections 6.4.1 and 6.4.2). While we still obtain reasonably good agreement of simulations with experimental data, it cannot be expected that this modification is sufficient to account for the linear energy dispersion in gapless graphene and merely constitutes a strong approximation. Formulation of a full hydrodynamic transport model for graphene follows the same logic as presented for here for semiconductors and the transport equations largely maintain their form, however, some profound differences in the individual transport terms exist (cp., e.g., [147]) for graphene. A modification of the present model implementation is therefore essential and must be the primary goal of future investigations.

Device simulations

We performed a number of device simulations with the implemented TeraFET model to investigated the influence of power coupling and extrinsic device elements, such as ungated channel regions. A remarkable result concerns the efficiency of plasmonic mixing by resonant enhancement in the gate-source coupling case promoted by Dyakonov and Shur [18]. Their initial work had given rise to the prospect of strongly enhanced THz detection in FETs due to a possible formation of standing wave resonances in the FET channel. Our simulations in Chapter 5 of the device sensitivity

in terms of miminum NEP showed, however, that such resonances merely reflect in the enhancement factor of plasma wave mixing but are countered by respective resonant behavior of the intrinsic HF channel impedance. Enhanced power coupling at frequencies of plasma wave resonances leads in total to a device NEP, which is, if at all, only marginally improved compared to the strong enhancement in the efficiency factor. Indeed we found that the best NEP is achieved when the resonances disappear and a situation close to the long-channel approximation is reached. This observation should have profound implications on future device design, where the strive for resonant plasmonic detection should no longer be the aim from a perspective of best detection performance.

We also investigated in Chapter 5 the influence of ungated channel regions on power distribution and overall mixing efficiency in TeraFETs. Our simulation results showed that significant amount of incident radiation power can be lost to the ungated channel regions for the plasmonic detection mechanism, which reduces the total efficiency factor (plasmonics + influence of ungated regions) significantly below unity relative to the quasi-static case. Note however, that the same argument of detection efficiency is not true for the thermoelectric signals. An effective heating of charge carriers can still exist in the ungated channel regions and a temperature gradient over the device is independent of the exact location of the hot carrier distribution. For this reason, the thermoelectric signals are observed most pronounced at high gate biases above threshold, where most of the incident power is coupled to the ungated region (in our case, the drain side) of the channel. The plasmonic signal disappears under such conditions but the thermoelectric signal remains. We observe this behavior in both, graphene and GaN, as well as initial studies on CNT FETs (unpublished data, not shown here). In Chapter 7, according simulations of the mixing efficiency with thermoelectric signals switched on showed, that the additional detection mechanism adds to total efficiency factor in particular at these high gate voltages an an efficiency close to unity was simulated.

Experimental results of TeraFET performance

Several generations of TeraFETs were designed and fabricated over the course of this work. We presented results of THz measurements with the detectors in Chapter 6. Three generations of optimized AlGaN/GaN HEMTs with were produced [1], [13], [15]. The TeraFETs were designed as broadband detectors with integrated bow-tie and spiral planar antennas and were characterized with calibrated all-electronic THz sources and a broadband photomixer-based THz system. Studies on the variation of detector dimensions were performed and fed into the design phase of subsequent detector generations. In general, smaller FET dimensions - made possible by technological improvement of the GaN fabrication processes at FBH - yielded better results in the investigated devices in terms of maximum responsivity and minimum NEP. By careful design of the electric circuits in terms of radiation coupling boundary conditions, close as possible impedance matching for broadband devices, as well as electric stabilization of the detector environment, highly sensitive THz detectors were realized, which exhibited record optical NEPs between 25.4 and 31.2 $\mathrm{pW}/\sqrt{\mathrm{Hz}}$ from 0.5 to 0.6 THz for broadband GaN-based TeraFETs and showed flat frequency-dependence in the range of 0.2 to 1.2 THz. From the measured optical

NEPs we deduced electrical NEPs of 16 to 19.7 pW/$\sqrt{\text{Hz}}$ by making reasonable assumptions on THz beam coupling in our detection modules. The dynamic range of TeraFETs of the latest detector generation was measured and the devices showed superior SNR compared to a Golay cell, while a photomixer receiver exhibited significantly higher dynamic range due to coherent operation. Finally, the achieved sensitivities prove that with proper device design, GaN-based TeraFETs are able to compete with state-of-the-art TeraFET technology and are slowly approaching Schottky diode-based THz detectors, which up until today are still superior for lower THz frequencies [20], [21], [43], [71].

Single-layer graphene TeraFETs with integrated broadband bow-tie antennas were fabricated in the course of this work. We measured a flat THz response versus frequency between 0.2 and 1 THz and found for the best device an optical NEP of 497 pW/$\sqrt{\text{Hz}}$ at 590 GHz [5]. This performance is roughly a factor two higher than other reported values in the literature [30], [164], [179]. In particular, the devices were fabricated in a CVD-growth process, showing that wafer scale production of sensitive THz detectors based on graphene TeraFETs is feasible. Capacitive coupling for asymmetric radiation coupling boundary conditions was introduced by employing a split bow-tie design in one of the integrated antenna's wings. As a final note, we achieved even slightly better sensitivities with single devices based on exfoliated graphene (420 pW/$\sqrt{\text{Hz}}$ at 590 GHz, unpublished data, not shown here), where in particular, significantly weaker hysteresis effects were observed.

Pronounced thermoelectric signals were observed in our graphene measurements and also as a side-effect in the experiments of GaN TeraFET characterization. In particular in graphene, such signals have been reported before[30], [31]. In Chapter 7 we investigated the thermoelectric signals in some detail and found that in both materials the inclusion of diffusive transport in the model equations could largely account qualitatively for the observations both with respect to applied gate voltage and THz frequency. We found on the other hand that the simulations seem to quantitatively overestimate both the thermoelectric and the plasmonic mixing with respect to frequency. We assume two possible explanations. First, the transitions between gate and ungated channel regions were modeled as sharp boundaries, which should produce a much stronger reflection of plasma waves as expected in a real device with smeared out transition regions. Note however, that this effect should play only a minor role in the comparably long graphene channel. A second aspect is the assumption of a frequency independent ungated resistance. The parameter for the ungated resistance was obtained from DC parameter extraction and it was estimated that the largest part stems from the contact resistances. Those should exhibit strong decrease with rising frequency, which would lead to a significantly lower influence of the ungated parts in the simulations. For the graphene we found that an empirical reduction of the ungated resistance significantly improved the modeling results. We suggest that this matter should be one of the main points of investigation for model improvement.

Outlook

Based on the investigations presented in this work, future work on TeraFETs should consider two main directions. First, an improvement of the device model following

the ideas mentioned above should be aimed for. In particular the experimental results achieved in the course of this work showed that careful device design and modeling can eventually lead to highly efficient real devices. From the design point-of-view, the goal for an efficient plasmonic detection is the reduction of ungated channel regions and other parasitic influences as well as best possible impedance matching [3], [43]. While this is in general hard to achieve over a broad range of frequencies, our studies have shown that broadband TeraFETs can still almost reach the performance of resonant device designs in, e.g., Si CMOS technology. An option would be to push the sensitivity limit by implementing such resonant TeraFETs also in GaN.

The situation is to a significant extent different for the graphene TeraFETs, in particular with respect to the ungated channel regions. The presented measurements showed that the thermoelectric signals showed up as an enhancement of detection sensitivity and the best values were found at gate biases where the plasmonic response had already decayed. This implicates that highly efficient graphene-based detectors can be realized, designed to exploit the thermoelectric effect - solely or in addition to plasma wave mixing. Graphene offers ideal material parameters for such purpose. In order to further investigate the fundamental physics and the device realization of thermoelectric graphene detectors, we are currently working on devices relying only on this effect. The aim is to achieve a localized field enhancement by intentionally introducing an asymmetry in the geometry of the graphene material. Triangular structuring of the graphene should lead to a large field concentration at the tip of the structure and a strong thermoelectric signal should be the result. The respective devices are currently being processed. Altogether, future theoretical and experimental work should be dedicated to the prospect of a new generation of graphene-based THz detectors employing the hot carrier thermoelectric effect.

Acknowledgment

The experimental studies presented in this thesis were carried out with TeraFETs produced in fruitful collaborations with other research institutes. The AlGaN/GaN devices were designed and fabricated in a funded SAW project in close cooperation with Ferdinand-Braun-Institut, Leibniz-Institut für Höchstfrequenztechnik (FBH), Berlin, Germany. The group there is led by Prof. Dr. Wolfgang Heinrich and device design was mainly carried out by Adam Rämer.

The CVD-grown TeraFETs were produced in collaboration with the group of Prof. Dr. Jan Stake at Chalmers Technical University, Göteborg, Sweden. The devices were fabricated by Dr. Michael Andersson and Audrey Zak, who also took part in the experimental characterization at Goethe-University Frankfurt.

Appendix A

Plasma wave mixing model

A.1 Plasma velocity and plasma wavevector

Fundamental properties of the plasma waves in the gated region of the transistor channel can be derived from the model equations Eqs. (2.1) and (2.2) by first order harmonic analysis [18], [42]. Assume a modulation of the gate-to-channel potential by an external oscillation with angular frequency ω. The potential ϕ, the charge density n and the carrier velocity v can be expanded in orders of ω as

$$n = n_0 + \frac{1}{2}\left[n_1 e^{i(\omega t - kx)} + n_1^* e^{i(\omega t - kx)}\right] + ... \tag{A.1}$$

$$v = v_0 + \frac{1}{2}\left[v_1 e^{i(\omega t - kx)} + v_1^* e^{i(\omega t - kx)}\right] + ... \tag{A.2}$$

$$\phi = \phi_0 + \frac{1}{2}\left[\phi_1 e^{i(\omega t - kx)} + \phi_1^* e^{i(\omega t - kx)}\right] + ... \tag{A.3}$$

with complex wavevector $k = k_\mathrm{r} - ik_\mathrm{i}$. Note that for zero-drain bias operation considered in this work, the initial DC component of the velocity $v_0 = 0$ but $\phi_0, n_0 \neq 0$ since a DC gate bias and residual charge density can be present. Inserting into Eqs. (2.1) and (2.2), applying the spatial and time derivatives, and eliminating the exponential terms leads to the linearized transport equations

$$i\omega v_1 + ik\frac{q}{m}\phi_1 + \frac{v_1}{\tau_\mathrm{p}} = 0 \tag{A.4}$$

$$i\omega n_1 - n_0 ikv_1 = 0 \tag{A.5}$$

Solving Eq. (A.4) for v_1 and inserting into Eq. (A.5) yields the plasmon dispersion relation in general form

$$\omega^2 - i\frac{\omega}{\tau_\mathrm{p}} + \frac{k^2 q n_0 \phi_1}{m n_1} = 0 \tag{A.6}$$

The Fourier component of the electrostatic potential can be written in the form

$$\phi_1 = -\frac{q n_1}{2\epsilon_0 \bar{\epsilon}(k + k_s)} \tag{A.7}$$

With $k_s = (q/2\epsilon_0\bar{\epsilon}) \cdot \partial n/\partial \phi$ being the Thomas-Fermi screening parameter [61] and $\bar{\epsilon}$ the effective relative permittivity depending on the thickness of the dielectrics

surrounding the 2-DEG layer. In the long-wavelength approximation $k + k_s \approx k_s$ and $\bar{\epsilon} \approx (\epsilon + \epsilon_s)/2$ and

$$\phi_1 \approx -n_1 \frac{\partial \phi}{\partial n} \tag{A.8}$$

To find the velocity of the plasma wave, Eq. (A.8) is inserted into Eq. (A.6) and in the limit of $\tau_\mathrm{p} \to \infty$:

$$\omega^2 = \frac{k^2 q n_0}{m} \frac{\partial \phi}{\partial n} \equiv k^2 s^2 \tag{A.9}$$

where a linear dispersion for the plasma wave exists and the plasma velocity is defined as [42]

$$s = \sqrt{\frac{q}{m} n_0 \frac{\partial \phi}{\partial n}} \tag{A.10}$$

Taking again the full form of Eq. (A.6) the complex wavevector of the plasma wave is then found to be

$$\begin{aligned} \omega^2 - i\frac{\omega}{\tau_\mathrm{p}} - k^2 s^2 = 0 \\ \Leftrightarrow k = \frac{\omega}{s}\sqrt{1 - \frac{i}{\omega \tau_\mathrm{p}}} \end{aligned} \tag{A.11}$$

With the above definition of wavevector and velocity, a wave equation in the first order in ω of the potential ϕ can be formulated. Retaining the spatial derivatives of ϕ_1 and v_1 in the linearized Eqs. (A.4) and (A.5) and eliminating v_1 yields

$$\begin{aligned} & - i\omega \frac{\partial n}{\partial \phi}\phi_1 + \frac{q}{m} n_0 \frac{\tau_\mathrm{p}}{i\omega\tau_\mathrm{p}} \partial_x^2 \phi_1 = 0 \\ & \Leftrightarrow k^2 \phi_1 + \partial_x^2 \phi_1 = 0 \end{aligned} \tag{A.12}$$

where relation Eqs. (A.8), (A.10) and (A.11) were already applied. The solution to differential equations of the form of Eq. (A.12) are well known to be propagating waves with $\phi_1 \propto e^{-ikx}$, which verifies that s, ω, and k indeed represent velocity, angular frequency and wavevector of charge density waves in the transistor channel.

Solution of the wave equation is subject to specific boundary conditions. Employing drain-coupling boundary conditions as defined in Eq. (2.7). leads to solutions for the electrostatic potential and carrier velocity

$$\phi_1(x) = V_\mathrm{a} \frac{\sin(kx)}{\sin(kL_\mathrm{g})} \tag{A.13}$$

$$v_1(x) = V_\mathrm{a} \frac{q\omega}{iks^2 m} \frac{\cos(kx)}{\sin(kL_\mathrm{g})} \tag{A.14}$$

Note that in the above derivation we have omitted time dependence for reasons of simplified notation only and recall that $\phi_1, v_1, n_1 \propto e^{i(\omega t - kx)}$.

For open gate-source coupling boundary conditions as defined in Eq. (2.11) the above quantities can be derived in a similar way to take and take the form [43]

$$\phi_{1,\mathrm{GS}}(x) = -V_\mathrm{a} \frac{\cos(k(L_\mathrm{g} - x))}{\cos(kL_\mathrm{g})} \tag{A.15}$$

$$v_{1,\mathrm{GS}}(x) = V_\mathrm{a} \frac{q\omega}{iks^2 m} \frac{\sin(k(L_\mathrm{g} - x))}{\sin(kL_\mathrm{g})} \tag{A.16}$$

A.2 THz response

The THz response of an FET can be derived from second order analysis of the transport equations Eqs. (2.1) and (2.2). Expanding as in Eqs. (A.1)-(A.3) but retaining only non-oscillatory DC terms, i.e., stationary quantities n_0 and ϕ_0 (recall that $v_0 = 0$ for zero-drain bias), mixing terms of first order quantities $v_1, \phi_1, n_1 \propto e^{i\omega t}$ as well a second order velocity $\bar{v} \propto e^{2i\omega}$ yields

$$\partial_x \left(\frac{v_1 v_1^*}{4} - \frac{q}{m}\phi_0 \right) + \frac{\bar{v}}{\tau_\mathrm{p}} = 0 \tag{A.17}$$

$$\partial_x \left(n_0 \bar{v} + \frac{v_1 n_1^* + v_1^* n_1}{4} \right) = 0 \tag{A.18}$$

The term in parentheses in Eq. (A.18) must equal a constant, in particular, a DC current $\bar{j} = -(q) n_0 \bar{v}$ will be induced only when an electric field is present, i.e., the constant must be zero and using the relations Eqs. (A.8) and (A.10) we find

$$\begin{aligned} \bar{v} &= -\frac{v_1 n_1^* + v_1^* n_1}{4 n_0} \\ &= \frac{q}{m} \frac{v_1 \phi_1^* + v_1^* \phi_1}{4 s^2} \end{aligned} \tag{A.19}$$

Equation (A.19) is inserted into Eq. (A.17) and integrated over the gate length from $x = 0$ to $x = L_\mathrm{g}$ to yield the detector's induced voltage response. For the first two terms integration and derivatives cancel so that [18], [42]

$$\begin{aligned} V_\mathrm{det} &= V(L_\mathrm{g}) - V(0) \\ &= -\frac{m}{q} \frac{v_1 v_1^*}{4} \bigg|_{x=0}^{x=L_\mathrm{g}} - \frac{1}{4 s^2 \tau_\mathrm{p}} \int_{x=0}^{x=L_\mathrm{g}} (v_1 \phi_1^* + v_1^* \phi_1) \mathrm{d}x \\ &= \frac{q}{m} \frac{V_a^2}{4 s^2} f(\omega). \end{aligned} \tag{A.20}$$

After a lengthy calculation the above general solution is derived where the frequency dependent terms have been condensed into the factor $f(\omega)$, which is the plasmonic enhancement factor discussed in Section 2.4.3 and whose exact form depends on the specific boundary conditions for ϕ_1 and v_1.

For drain coupling, using velocity and charge density components v_1 and ϕ_1 from Eqs. (A.13) and (A.14) and applying the trigonometric identities

$$\begin{aligned} \cos^2(ix) &= \cosh^2(x) \\ \sin^2(ix) &= -\sinh^2(x) \\ \sin(kL_\mathrm{g}) \sin(k^* L_\mathrm{g}) &= \cosh^2(k_\mathrm{i} L_\mathrm{g}) - \cos^2(k_\mathrm{r} L_\mathrm{g}) \\ \cos(kL_\mathrm{g}) \cos(k^* L_\mathrm{g}) - 1 &= \sin^2(k_\mathrm{r} L_\mathrm{g}) - \sinh^2(k_\mathrm{i} L_\mathrm{g}) \end{aligned} \tag{A.21}$$

as well as

$$kk^* = |k|^2 = \frac{\omega^2}{s^2} \sqrt{1 + \frac{1}{\omega^2 \tau_\mathrm{p}^2}} \tag{A.22}$$

and

$$k_{\mathrm{r}} k_{\mathrm{i}} = \frac{\omega}{2 s^2 \tau_{\mathrm{p}}} \tag{A.23}$$

the enhancement factor is derived as [42]

$$f_{\mathrm{D}}(\omega) = 1 + \beta \frac{\sinh^2 (k_{\mathrm{i}} L_{\mathrm{g}}) - \sin^2 (k_{\mathrm{r}} L_{\mathrm{g}})}{\cosh^2 (k_{\mathrm{i}} L_{\mathrm{g}}) - \cos^2 (k_{\mathrm{r}} L_{\mathrm{g}})} \tag{A.24}$$

with

$$\beta = \frac{2}{\sqrt{1 + \left(\frac{1}{\omega \tau_{\mathrm{p}}}\right)^2}} \tag{A.25}$$

A similar calculation for gate-source coupling boundary conditions leads to [18]

$$f_{\mathrm{GS}}(\omega) = 1 + \beta - \frac{1 + \beta \cos (2 k_{\mathrm{r}} L_{\mathrm{g}})}{\sinh^2 (k_{\mathrm{i}} L_{\mathrm{g}}) + \cos^2 (k_{\mathrm{r}} L)} \tag{A.26}$$

A.2.1 Quasi-static TeraFET response

In quasi-static approximation, the oscillation frequency ω is assumed to be small. The complex wavevector reduces to

$$k_{\mathrm{QS}} = \frac{1}{s} \sqrt{\frac{\omega}{i \tau_{\mathrm{p}}}} \tag{A.27}$$

and likewise becomes small proportional to $\sqrt{\omega}$. Trigonometric expressions are approximated as

$$\begin{aligned} \sin(kL_{\mathrm{g}}) &= \tan(kL_{\mathrm{g}}) = kL_{\mathrm{g}} \\ \cos(kL_{\mathrm{g}}) &= \cos^2(kL_{\mathrm{g}}) = \cosh^2(kL_{\mathrm{g}}) = 1 \\ \sin^2(kL_{\mathrm{g}}) &= \sinh^2(kL_{\mathrm{g}}) = 0 \end{aligned} \tag{A.28}$$

Derivation of the TeraFET response can be performed by either following the procedure in Section A.2 using the quasi-static first order velocity and potential (comp. Eqs. (A.13) and (A.14)). For drain coupling boundary conditions these read

$$\begin{aligned} \phi_{1,\mathrm{QS}}(x) &= V_{\mathrm{a}} \frac{x}{L_{\mathrm{g}}} \\ v_{1,\mathrm{QS}}(x) &= V_{\mathrm{a}} \frac{q \omega}{i k^2 s^2 m L_{\mathrm{g}}} \end{aligned} \tag{A.29}$$

Again, the detector response V_{QS} is found by integration according to Eq. (A.20). The solution takes a similar form as before

$$V_{\mathrm{QS}} = \frac{q}{m} \frac{V_{\mathrm{a}}^2}{4 s^2} f_{\mathrm{QS}}(\omega) = \frac{q}{m} \frac{V_{\mathrm{a}}^2}{4 s^2} \tag{A.30}$$

where the plasmonic enhancement is calculated to be $f_{\mathrm{D,QS}}(\omega) = 1$. Alternatively, the same result is obtained by taking the limit for small ω in Eqs. (A.24). For gate-source coupling, the quasi-static limit leads to a vanishing response $f_{\mathrm{GS,QS}} \to 0$ as $\omega \to 0$ (comp. Fig. 2.3).

When the carrier mobility is assumed constant, i.e., independent of the channel potential, employing Eqs. (A.10) and the definition for channel conductivity $\sigma = qn_0\mu$ leads to

$$V_{\mathrm{QS}} = \frac{V_{\mathrm{a}}^2}{4}\frac{1}{n_0}\frac{\partial n}{\partial \phi} = \frac{V_{\mathrm{a}}^2}{4}\frac{1}{\sigma}\frac{\partial \sigma}{\partial \phi} \tag{A.31}$$

which was derived before in Ref. [74] using a purely resistive mixing approach.

Appendix B

Derivation of transport models from the Boltzmann transport equation

B.1 Method of moments

The definition of Eq. (3.13) allows to evaluate average quantities when an explicit form for the distribution function $f(\boldsymbol{r}, \boldsymbol{k}, t)$ is chosen. The probability distribution for charge carriers in a semiconductor under applied electric field is described by a displaced Fermi-Dirac distribution

$$f_0 = \frac{1}{e^{\frac{\hbar^2 |\boldsymbol{k}-\boldsymbol{k}_\mathrm{d}|^2}{2mk_B T_\mathrm{C}} - \epsilon_\mathrm{F}} + 1} \tag{B.1}$$

in general and by the displaced Maxwellian

$$f_0 \approx \frac{1}{e^{\frac{\hbar^2 |\boldsymbol{k}-\boldsymbol{k}_\mathrm{d}|^2}{2mk_B T_\mathrm{C}} - \epsilon_\mathrm{F}}} \tag{B.2}$$

for a non-degenerate situation. We further assumed here a parabolic band approximation for the energy dispersion

$$E(\boldsymbol{r}, \boldsymbol{k}) = \frac{\hbar^2 k^2}{2m} + E_\mathrm{c}(\boldsymbol{r}) \tag{B.3}$$

For the following derivations, the following definition of Fermi-Dirac integrals

$$\mathcal{F}_j(x) = \frac{1}{\Gamma(j+1)} \int_0^\infty \frac{t^j}{e^{t-x}+1} \, \mathrm{d}t \tag{B.4}$$

is useful. References [54], [55], [94], [146] are some of the sources, which were used in the preparation of this appendix.

B.1.1 Charge carrier density

The charge carrier density is calculated applying $\Phi = 1$ in Eq. (3.13)

$$n = \langle 1 \rangle = \frac{g_s g_v}{(2\pi)^2} \int_0^\infty \int_0^{2\pi} f k \, \mathrm{d}k \, \mathrm{d}\theta \tag{B.5}$$

For reasons of simplicity in the following discussions we use $g_s = 2$ and $g_v = 1$ for the spin and valley degeneracy for Wurtzite GaN. To explicitly perform the integration in $\boldsymbol{k}$-space we choose two-dimensional polar coordinates and rewrite Eq. 3.14

$$n = \frac{1}{2\pi^2} \int_0^\infty \int_0^{2\pi} f k \, \mathrm{d}k \, \mathrm{d}\theta = \frac{1}{2\pi^2} \int_0^\infty \int_0^{2\pi} \frac{1}{e^{\frac{\hbar^2 (k - k_d \cos\theta)^2}{2 m k_B T_C} - \epsilon_F} + 1} k \, \mathrm{d}k \, \mathrm{d}\theta \tag{B.6}$$

where we have already employed that $\boldsymbol{k}_d = k_d \cos\theta$ for vector quantities.[58] A substitution of variables is applied

$$\begin{aligned} t &\rightarrow \frac{\hbar^2 (k - k_d \cos\theta)^2}{2 m k_B T_C} \\ \Leftrightarrow \quad k &\rightarrow \sqrt{\frac{2 m k_B T_C t}{\hbar^2}} + k_d \cos\theta \end{aligned} \tag{B.7}$$

and

$$\begin{aligned} \frac{dt}{dk} &= \frac{\hbar^2}{2 m k_B T_C} 2k \\ \Leftrightarrow \quad k \, \mathrm{d}k &\rightarrow \frac{m k_B T_C}{\hbar^2} \, \mathrm{d}t \end{aligned} \tag{B.8}$$

and Eq. (B.6) simplifies to

$$\begin{aligned} n &= \frac{m k_B T_C}{2\pi^2 \hbar^2} \int_0^\infty \int_0^{2\pi} \frac{1}{e^{t - \epsilon_F} + 1} \, \mathrm{d}t \, \mathrm{d}\theta \\ &= \frac{m k_B T_C}{\pi \hbar^2} \int_0^\infty \frac{1}{e^{t - \epsilon_F} + 1} \, \mathrm{d}t \\ &= \frac{m k_B T_C}{\pi \hbar^2} \mathcal{F}_0(\epsilon_F) \end{aligned} \tag{B.9}$$

Here, $\mathcal{F}_0(\epsilon_F)$ is the first Fermi integral, which can be evaluated explicitly, and finally

$$n = \frac{m k_B T_C}{\pi \hbar^2} \ln\left(1 + e^{\epsilon_F}\right) = N_C \ln\left(1 + e^{\epsilon_F}\right) \tag{B.10}$$

When Maxwell-Boltzmann statistics are assumed, the expression simplifies to

$$n = \frac{m k_B T_C}{\pi \hbar^2} e^{\epsilon_F} = N_C \, e^{\epsilon_F} \tag{B.11}$$

[58] We use only one $\cos\theta$ term in $|\boldsymbol{k} - \boldsymbol{k}_d|$ considering only the relative angle between $\boldsymbol{k}$ and $\boldsymbol{k}_d$.

B.1.2 Carrier momentum density and drift velocity

With the same procedure as above, the average carrier momentum density is calculated using $\Phi = \boldsymbol{p} = \hbar\boldsymbol{k}$ in Eq. (3.13)

$$n\boldsymbol{p}_\mathrm{d} = \langle \boldsymbol{p} \rangle \frac{1}{2\pi^2} \int_0^\infty \int_0^{2\pi} \hbar\boldsymbol{k} f k \;\mathrm{d}k\,\mathrm{d}\theta = \frac{1}{2\pi^2} \int_0^\infty \int_0^{2\pi} \hbar k \cos(\theta) f k \;\mathrm{d}k\,\mathrm{d}\theta \tag{B.12}$$

where we used that $\boldsymbol{k}$ is a vector quantity. Again, the substitutions Eqs. (B.8) and (B.9) are used. Note that the integral over θ vanishes for odd powers of $\cos\theta$. We find for the momentum density

$$np_\mathrm{d} = \hbar k_\mathrm{d} \frac{m k_\mathrm{B} T_\mathrm{C}}{\hbar^2 \pi} \int_0^\infty \frac{1}{e^{t-\epsilon_\mathrm{F}} + 1} \;\mathrm{d}t = \hbar k_\mathrm{d} n \tag{B.13}$$

A similar calculation for $\Phi = \boldsymbol{v} = \hbar\boldsymbol{k}/m$ yields the average velocity

$$v_\mathrm{d} = \frac{1}{n} \frac{1}{2\pi^2} \int_0^\infty \int_0^{2\pi} \frac{\hbar\boldsymbol{k}}{m} f k \;\mathrm{d}k\,\mathrm{d}\theta = \frac{\hbar k_\mathrm{d}}{m} = \frac{p_\mathrm{d}}{m} \tag{B.14}$$

This result is expected, since no net current is present in equilibrium and the average velocity and momentum are solely due to the shifted component. Hence, the subsript "d" indeed denotes a drift velocity of the carrier ensemble caused by an external force.

B.1.3 Energy density

The average energy density is obtained employing $\Phi = E = \boldsymbol{pv}/2 = \hbar^2 k^2/2m$ in Eq. (3.13). Note here that the energy is a scalar quantity and no additional $\cos\theta$ terms must be added in the integrals.

$$nw = \left\langle \frac{\boldsymbol{pv}}{2} \right\rangle = \frac{1}{2\pi^2} \int_0^\infty \int_0^{2\pi} \frac{\hbar^2 k^2}{2m} f k \;\mathrm{d}k\,\mathrm{d}\theta \tag{B.15}$$

Application of the substitution of variables after Eqs. (B.8) and (B.9) and using $2\int_0^{2\pi} \cos^2(\theta)\,\mathrm{d}\theta = \int_0^{2\pi} \mathrm{d}\theta = 2\pi$ yields two integrals

$$nw = k_B T \frac{m k_B T_\mathrm{C}}{\pi\hbar^2} \int_0^\infty \frac{t}{e^{t-\epsilon_\mathrm{F}} + 1} \;\mathrm{d}t + \frac{1}{2} \frac{k_\mathrm{d}^2 k_B T_\mathrm{C}}{\pi} \int_0^\infty \frac{1}{e^{t-\epsilon_\mathrm{F}} + 1} \;\mathrm{d}t \tag{B.16}$$

We rewrite both terms with the help of the Fermi-Dirac integrals $\mathcal{F}_0(\epsilon_\mathrm{F})$ and $\mathcal{F}_1(\epsilon_\mathrm{F})$

$$nw = k_B T_\mathrm{C} \frac{m k_B T_\mathrm{C}}{\pi\hbar^2} \mathcal{F}_1(\epsilon_\mathrm{F}) + \frac{1}{2} \frac{k_\mathrm{d}^2 k_\mathrm{B} T_\mathrm{C}}{\pi} \mathcal{F}_0(\epsilon_\mathrm{F}) \tag{B.17}$$

and using the above result for the carrier density Eq. (B.10) we calculate the average energy density

$$nw = \langle E \rangle = n k_\mathrm{B} T_\mathrm{C} \frac{\mathcal{F}_1(\epsilon_\mathrm{F})}{\mathcal{F}_0(\epsilon_\mathrm{F})} + \frac{1}{2} n m v_\mathrm{d}^2 \tag{B.18}$$

or the average kinetic energy

$$w = \frac{\langle E \rangle}{n} = k_\mathrm{B} T_\mathrm{C} \frac{\mathcal{F}_1(\epsilon_\mathrm{F})}{\mathcal{F}_0(\epsilon_\mathrm{F})} + \frac{1}{2} m v_\mathrm{d}^2 \tag{B.19}$$

as the sum of a thermal and a drift velocity component [55]. When Maxwell-Boltzmann statistics apply, which is valid unless the Fermi energy is close to or below the conduction band edge, the Fermi-Dirac integrals disappear and $\mathcal{F}_1(\epsilon_\mathrm{F})/\mathcal{F}_0(\epsilon_\mathrm{F}) \approx 1$. For better readability in further discussions, we use this reduced form keeping in mind that the full Fermi-Dirac statistic has to be employed in a degenerate case

$$w = \frac{\langle E \rangle}{n} = k_\mathrm{B} T_\mathrm{C} + \frac{1}{2} m v_\mathrm{d}^2 \tag{B.20}$$

B.2 Transport models

Transport model can be derived from the fundamental BTE

$$\frac{\partial f}{\partial t} + \boldsymbol{v} \cdot \nabla_{\boldsymbol{r}} f + \frac{\boldsymbol{F}}{\hbar} \cdot \nabla_{\boldsymbol{k}} f = -\frac{f - f_0}{\tau} \tag{B.21}$$

with the help of the method of moments following the calculation of averaged quantities as presented above. In general, balance equations are obtained by multiplying Eq. (B.21) with a weighting function Φ and integrating over $\boldsymbol{k}$-space. A generalized balance equation as given in Eq. (3.21) then formulated as

$$\begin{aligned} \frac{1}{2\pi^2} \int_0^\infty \Phi(\boldsymbol{k}) \partial_t f \, \mathrm{d}^2 k + \frac{1}{2\pi^2} \int_0^\infty \Phi(\boldsymbol{k}) (\boldsymbol{v} \partial_x f) \, \mathrm{d}^2 k + \frac{1}{2\pi^2} \int_0^\infty \Phi(\boldsymbol{k}) \left(\frac{\boldsymbol{F}}{\hbar} \partial_{\boldsymbol{k}} f \right) \mathrm{d}^2 k \\ = -\frac{1}{2\pi^2} \int_0^\infty \Phi(\boldsymbol{k}) \frac{f - f_0}{\tau_\Phi} \, \mathrm{d}^2 k \end{aligned} \tag{B.22}$$

We outline here the derivation of a simple drift-diffusion and a more comprehensive hydrodynamic transport model. Detailed calculations and in-depth discussions can be found, e.g., in Refs. [54], [55].

B.2.1 Charge continuity equation

The fundamental charge continuity equation is derived from the BTE by application of the simplest weighting function $\Phi = 1$. We give here the evaluation of the individual terms in in Eq. (3.21)/(B.22).

- In the first term (time derivative term) on the LHS, the time derivation can be exchanged with the integration because $\partial_t \Phi = 0$. The resulting moment $\langle 1 \rangle$ was discussed in Section B.1.1 to yield the carrier density. Hence, the first term gives

$$\partial_t n \tag{B.23}$$

- In the second term (velocity term) on the LHS, again, the derivation can be exchanged with the integration because $\partial_x \boldsymbol{v} = 0$. The moment $\langle \boldsymbol{v} \rangle$ is obtained from the result in Section B.1.2 and we obtain

$$\partial_x (n v_\mathrm{d}) \tag{B.24}$$

- The third term (force term) on the LHS can be shown to vanish because $f \propto e^{-k^2}$ drops to zero rapidly for increasing k and the integral $\int \partial_{\boldsymbol{k}} f \mathrm{d}k \approx 0$ unless the electric field becomes extremely large [55, p. 214].

- The collision term on the RHS after Eq. (B.6) becomes

$$-\frac{n - n_0}{\tau} = 0 \tag{B.25}$$

because the number of carriers is constant.

Collecting the above terms we obtain the balance equation for $\Phi = 1$

$$\partial_t n + \partial_x (n v_\mathrm{d}) = 0 \tag{B.26}$$

which is the charge continuity equation. Multiplication by $-q$ and using $j = -q n v_\mathrm{d}$ leads to the current formulation of the continuity equation

$$\partial_t n = \frac{1}{q} \partial_x j \tag{B.27}$$

B.2.2 Drift-diffusion model

To derive the standard drift-diffusion equation, the weight function $\Phi = \boldsymbol{p}$ of first order in k is applied to the BTE. We again discuss the evaluation of the individual terms in Eq. (3.21)/(B.22).

- The time derivative term is neglected in the steady-state assumption of the drift-diffusion formalism.

- The velocity term becomes a third moment in k of the distribution function. Again, the spatial derivative can be moved outside the integral because $\partial_x \boldsymbol{p}\boldsymbol{v} = \partial_x (\hbar^2 k^2 / m) = 0$. Calculation of $\langle \boldsymbol{p}\boldsymbol{v} \rangle /2$ was shown in Section B.1.3 and yielded the energy density. In the drift-diffusion model, the contribution of drift velocity to the carrier energy is commonly neglected[95], [101]

$$\partial_x \langle \boldsymbol{p}\boldsymbol{v} \rangle = \partial_x \left(n k_B T_\mathrm{C} \frac{\mathcal{F}_1(\epsilon_\mathrm{F})}{\mathcal{F}_0(\epsilon_\mathrm{F})} + m n v_\mathrm{d}^2 \right) \approx \partial_x \left(n k_B T_\mathrm{C} \frac{\mathcal{F}_1(\epsilon_\mathrm{F})}{\mathcal{F}_0(\epsilon_\mathrm{F})} \right) \tag{B.28}$$

- The force term on the LHS is rewritten applying the product rule for derivatives to

$$\begin{aligned} \frac{1}{2\pi^2} \frac{F}{\hbar} \int \boldsymbol{p} \partial_{\boldsymbol{k}} f \, \mathrm{d}^2 k &= \frac{1}{2\pi^2} \frac{F}{\hbar} \int \partial_{\boldsymbol{k}} (\boldsymbol{p} f) \, \mathrm{d}^2 k - \frac{1}{2\pi^2} \frac{F}{\hbar} \int f \partial_{\boldsymbol{k}} \boldsymbol{p} \, \mathrm{d}^2 k \\ &\approx \frac{1}{2\pi^2} \frac{F}{\hbar} \int f \partial_{\boldsymbol{k}} \boldsymbol{p} \, \mathrm{d}^2 k \end{aligned} \tag{B.29}$$

where again, with the same argument as above, it can be shown that the integral $\int \partial_{\boldsymbol{k}}(\boldsymbol{p}f)$ vanishes [55, p. 214]. We finally obtain

$$-\frac{F}{\hbar}\langle\partial_{\boldsymbol{k}}\boldsymbol{p}\rangle = -nF \tag{B.30}$$

- The collision term on the RHS yields after Section B.1.2 becomes

$$-\frac{np_{\mathrm{d}} - np_{\mathrm{d},0}}{\tau_{\mathrm{p}}} = -\frac{np_{\mathrm{d}}}{\tau_{\mathrm{p}}} \tag{B.31}$$

  because the average momentum in equilibrium $p_{\mathrm{d},0}$ is zero.

Collecting all terms, multiplication by τ_{p}/m yields the drift-diffusion equation in velocity formulation (assuming again Maxwell-Boltzmann statistics for convenience of notation)

$$-nv_{\mathrm{d}} = -n\tau_{\mathrm{p}}\frac{F}{m} + \frac{\tau_{\mathrm{p}}}{m}\partial_x\left(nk_BT_{\mathrm{C}}\right) \tag{B.32}$$

By additional multiplication with charge q and using the definition for current density $j = -qnv_{\mathrm{d}}$ and Eq. (3.1) for the electric force, the drift-diffusion current density model is obtained

$$j = qn\mu\mathcal{E} + \mu k_B\partial_x\left(nT_{\mathrm{C}}\right) \tag{B.33}$$

B.2.3 Hydrodynamic transport model

A hydrodynamic transport model can be derived from the Boltzmann equation using the weighting function $\Phi = 1$, $\Phi = \boldsymbol{p}$, and $\Phi = \boldsymbol{p}\boldsymbol{v}/2$ retaining time derivatives. We evaluate again individually the terms in Eq. (3.21)/(B.22).

$\Phi = 1$:

- For the first order weighting function, the continuity equation Eq. (B.26) is obtained following the derivation in Section B.2.1.

$\Phi = \boldsymbol{p}$:

- In the time derivative term, derivation and integration commute, because $\partial_t\boldsymbol{p} = 0$. We obtain the time derivative of the average carrier momentum density as derived in Section B.1.2, rewritten in terms of drift velocity

$$\partial_t\langle\boldsymbol{p}\rangle = \partial_t np_{\mathrm{d}} = m\partial_t(nv_{\mathrm{d}}) \tag{B.34}$$

- The velocity and force terms are evaluated as presented in Section B.2.2. Note that this time, the drift component in $\langle\boldsymbol{p}\boldsymbol{v}\rangle$ is retained

$$\partial_x\langle\boldsymbol{p}\boldsymbol{v}\rangle - \frac{F}{\hbar}\langle\partial_{\boldsymbol{k}}\boldsymbol{p}\rangle = \partial_x\left(nk_BT_{\mathrm{C}}\frac{\mathcal{F}_1(\epsilon_{\mathrm{F}})}{\mathcal{F}_0(\epsilon_{\mathrm{F}})} + mnv_{\mathrm{d}}^2\right) - nF \tag{B.35}$$

- The collision term transforms as shown in Section B.2.2 and becomes

$$-\frac{np_{\mathrm{d}}}{\tau_{\mathrm{p}}} \tag{B.36}$$

$\Phi = \boldsymbol{pv}/2$:

- The first term yields the time derivative of the kinetic energy density as derived in Section B.1.3
$$\partial_t \left\langle \frac{\boldsymbol{pv}}{2} \right\rangle = \partial_t \langle E \rangle = \partial_t(nw) \tag{B.37}$$
- For the velocity term, the third moment of the distribution function must be calculated after moving the spatial derivative outside the integral
$$\partial_x \left\langle \frac{\boldsymbol{p}v^2}{2} \right\rangle = \partial_x \frac{1}{2\pi^2} \int_0^\infty \int_0^{2\pi} \frac{\hbar^3 k^3}{2m^2} \cos\theta f k \, \mathrm{d}k \, \mathrm{d}\theta \tag{B.38}$$
and is evaluated to
$$\partial_x \left(\frac{1}{2} m n v_\mathrm{d}^3 + \frac{3}{2} n v_\mathrm{d} k_\mathrm{B} T_\mathrm{C} \frac{\mathcal{F}_1(\epsilon_\mathrm{F})}{\mathcal{F}_0(\epsilon_\mathrm{F})} \right) = \partial_x \left[n v_\mathrm{d} \left(w + k_\mathrm{B} T_\mathrm{C} \frac{\mathcal{F}_1(\epsilon_\mathrm{F})}{\mathcal{F}_0(\epsilon_\mathrm{F})} \right) \right] \tag{B.39}$$
- The force term is transformed with the same argument as given in Section B.2.2 and $\int \partial_{\boldsymbol{k}}(\boldsymbol{pv}f) \approx 0$. The remaining integral is calculated to yield
$$-\frac{n p_\mathrm{d} F}{m} = -n v_\mathrm{d} F \tag{B.40}$$
- Finally, the collision term is simply given as
$$-\frac{n(w - w_0)}{\tau_\mathrm{e}} = -\frac{n\left(w - k_B T_\mathrm{L} \frac{\mathcal{F}_1(\epsilon_\mathrm{F})}{\mathcal{F}_0(\epsilon_\mathrm{F})}\right)}{\tau_\mathrm{e}} \tag{B.41}$$
since in equlibrium, the drift velocity component is zero and the carrier temperature equals the lattice temperature $T_{\mathrm{C},0} = T_\mathrm{L}$.

Collecting all above terms, multiplying the second order ($\Phi = \boldsymbol{p}$) equation by τ_p/m and applying $F = -q\mathcal{E}$ in the third order $\Phi = E$ equation, we obtain the hydrodynamic transport model in velocity formulation
$$\partial_t n + \partial_x(n v_\mathrm{d}) = 0 \tag{B.42}$$
$$-n v_\mathrm{d} = \mu n \mathcal{E} + \tau_\mathrm{p} \partial_x(n v_\mathrm{d}^2) + \frac{k_\mathrm{B}}{q} \mu \partial_x(n T_\mathrm{C}) + \tau_\mathrm{p} \partial_t(n v_\mathrm{d}) \tag{B.43}$$
$$\partial_t(nw) + \partial_x \left[n v_\mathrm{d} \left(w + k_\mathrm{B} T_\mathrm{C} \right) \right] + q n v_\mathrm{d} \mathcal{E} = -\frac{n \left(w - k_\mathrm{B} T_\mathrm{L} \right)}{\tau_\mathrm{e}} \tag{B.44}$$
where we have already introduced the carrier mobility $\mu = q\tau_\mathrm{p}/m$ after Eq. (2.26). Additional multiplication of Eq. (B.43) by the charge q and using $j = -q n v_\mathrm{d}$ yields the hydrodynamic transport model as given in Eqs. (3.29)-(3.31) in current density formulation
$$\partial_t n = \frac{1}{q} \partial_x j \tag{B.45}$$
$$j = q n \mu \mathcal{E} + \frac{\tau_\mathrm{p}}{q} \partial_x \left(\frac{j^2}{n} \right) + \mu k_\mathrm{B} \partial_x(n T_\mathrm{C}) - \tau_\mathrm{p} \partial_t j \tag{B.46}$$
$$\partial_t(nw) = \frac{1}{q} \partial_x \left[j \left(w + k_\mathrm{B} T_\mathrm{C} \right) \right] + j\mathcal{E} - \frac{n(w - k_\mathrm{B} T_\mathrm{L})}{\tau_\mathrm{e}} \tag{B.47}$$

with the kinetic energy density in velocity or current formulation, respectively

$$w = \frac{1}{2} m v_{\mathrm{d}}^2 + k_{\mathrm{B}} T_{\mathrm{C}} = \frac{m}{2q^2} \frac{j^2}{n^2} + k_{\mathrm{B}} T_{\mathrm{C}} \tag{B.48}$$

B.3 Diffusion constant and Seebeck coefficient

The thermoelectric effect is included in the hydrodynamic transport model containing a current density contribution due to a gradient in carrier temperature and density $\mu k_{\mathrm{B}} \partial_x (n T_{\mathrm{C}})$. The carrier density depends on T_{C} via the distribution function f. In addition, the carrier mobility μ may in general be a function of T_{C}.

$$j = q n \mu \mathcal{E} + k_{\mathrm{B}} \partial_x (\mu n T_{\mathrm{C}}) \tag{B.49}$$

and expanding with the help of the product rule for derivatives yields

$$j = q n \mu \mathcal{E} + \mu k_{\mathrm{B}} T \partial_x n + n \mu k_{\mathrm{B}} \partial_x T_{\mathrm{C}} + n k_{\mathrm{B}} T_{\mathrm{C}} \partial_x \mu \tag{B.50}$$

Without giving an explicit expression, the temperature dependence of the mobility can be expressed as $\partial_x \mu = (\partial \mu / \partial T_{\mathrm{C}}) \partial_x T_{\mathrm{C}}$. Rearrangement then leads to the well-established form as derived, e.g., by Stratton [81]

$$\begin{aligned} j &= q n \mu \mathcal{E} + \mu k_{\mathrm{B}} T \partial_x n + n \mu k_{\mathrm{B}} \left(1 + \frac{T_{\mathrm{C}}}{\mu} \frac{\partial \mu}{\partial T_{\mathrm{C}}} \right) \partial_x T_{\mathrm{C}} \\ &= q n \mu \mathcal{E} + \mu k_{\mathrm{B}} T \partial_x n + q n D^T \partial_x T_{\mathrm{C}} \end{aligned} \tag{B.51}$$

with the diffusion coefficient defined as $D^T = (\mu k_{\mathrm{B}}/q)[1 + (T_{\mathrm{C}}/\mu)(\partial \mu / \partial T_{\mathrm{C}})]$.

We express now the temperature dependence of n in a similar way as $\partial_x n = (\partial n / \partial T_{\mathrm{C}}) \partial_x T_{\mathrm{C}}$. Further rearrangement of term leads to the full expression for current density

$$j = \sigma \mathcal{E} + \frac{\sigma k_{\mathrm{B}}}{q} \left(1 + \frac{T}{n} \frac{\partial n}{\partial T_{\mathrm{C}}} + \frac{T_{\mathrm{C}}}{\mu} \frac{\partial \mu}{\partial T_{\mathrm{C}}} \right) \partial_x T_{\mathrm{C}} \tag{B.52}$$

where we have also used the conductivity $\sigma = q n \mu$. As discussed in Chapter 7, the general definition of the Seebeck coefficient is then

$$\sigma S \equiv -\frac{\sigma k_{\mathrm{B}}}{q} \left(1 + \frac{T_{\mathrm{C}}}{n} \frac{\partial n}{\partial T_{\mathrm{C}}} + \frac{T_{\mathrm{C}}}{\mu} \frac{\partial \mu}{\partial T_{\mathrm{C}}} \right) \tag{B.53}$$

in accordance with the expression given by Cutler and Mott in Ref. [180]. Note once more, that the derivation assumes Maxwell-Boltzmann statistics and an additional factor $\mathcal{F}_1(\epsilon_{\mathrm{F}}) / \mathcal{F}_0(\epsilon_{\mathrm{F}})$ must be included for a Fermi-Dirac distribution function.

For a constant carrier mobility, the third term on the RHS of Eq. (B.53) vanishes. The Seebeck coefficient can then be calculated as [84]

$$S_{\mathrm{3D}} = -\frac{k_{\mathrm{B}}}{q} \left(\frac{5}{2} - \ln \frac{n_{\mathrm{3D}}}{N_{\mathrm{C,3D}}} \right) = -\frac{k_{\mathrm{B}}}{q} \left(\frac{5}{2} - \epsilon_{\mathrm{F}} \right) \tag{B.54}$$

with [54]

$$n_{3\mathrm{D}} = 2\left(\frac{mk_\mathrm{B}T_\mathrm{C}}{2\pi\hbar^2}\right)^{\frac{3}{2}} e^{\epsilon_F} = N_{\mathrm{C,3D}} e^{\epsilon_F} \tag{B.55}$$

and in two dimensions as

$$S = -\frac{k_\mathrm{B}}{q}\left(2 - \ln\frac{n}{N_\mathrm{C}}\right) = -\frac{k_\mathrm{B}}{q}\left(2 - \epsilon_\mathrm{F}\right) \tag{B.56}$$

with n, N_C as given in Eq. (B.11).

Using a Fermi-Dirac distribution we obtain for the two-dimensional Seebeck coefficient the slightly more complicated form

$$S = -\frac{k_\mathrm{B}}{q}\left[2 - \frac{\ln\left(e^{\frac{n}{N_\mathrm{C}}} - 1\right)}{\mathcal{F}_0(\epsilon_\mathrm{F})}\frac{1}{e^{-\epsilon_\mathrm{F}} + 1}\right] = -\frac{k_\mathrm{B}}{q}\left[2 - \frac{\epsilon_\mathrm{F}}{\mathcal{F}_0(\epsilon_\mathrm{F})(e^{-\epsilon_\mathrm{F}} + 1)}\right] \tag{B.57}$$

This result is consistent with the full *Mott formula* in integral form given in Ref. [180]

$$S_\mathrm{Mott} \propto -\frac{\int_0^\infty (E - \epsilon_\mathrm{F})\left(\frac{\partial}{\partial E} f\right) g(E)\,\mathrm{d}E}{\int_0^\infty f\,\mathrm{d}E} \tag{B.58}$$

where $g(E)$ is the density of states and where we have dropped all prefactors for reasons of simplicity.

Appendix C

Graphene TeraFET model

C.1 Cyclotron mass

Carriers in graphene, due to the linear energy dispersion relation

$$E = \hbar v_{\mathrm{F}} |\boldsymbol{k}| \tag{C.1}$$

are described as relativistic particles by the Dirac equation [144]. Here, k_{F} and v_{F} are the Fermi wavevector and velocity, respectively. In graphene, v_{F} is independent of the carrier density [143] and can be calculated from tight binding description to yield approximately $v_{\mathrm{F}} \approx 1 \cdot 10^6$ m/s. As a consequence, the carrier's mass is defined as the cyclotron mass depending on the Fermi energy, which is controlled in a graphene FET by the applied external gate voltage V_{G}. Within semiclassical approximation, the cyclotron mass is defined as

$$m = \frac{\hbar^2}{2\pi} \frac{\partial A(E)}{\partial E}\bigg|_{E=E_{\mathrm{F}}} \tag{C.2}$$

with A the cross-sectional area in $\boldsymbol{k}$-space enclosed by the orbiting particle. With Eq. (C.1), the area is calculated as

$$A(E) = \pi k^2 = \pi \frac{E^2}{\hbar^2 v_{\mathrm{F}}^2} \tag{C.3}$$

Using Eq. (C.3) in Eq. (C.2) yields

$$m = \frac{\hbar^2}{2\pi} \frac{E_{\mathrm{F}}}{\hbar^2 v_{\mathrm{F}}^2} = \hbar k_{\mathrm{F}} / v_{\mathrm{F}} \tag{C.4}$$

The Fermi wavevector in two-dimensional systems is given by [61]

$$k_{\mathrm{F}} = \sqrt{\frac{4\pi n(V_{\mathrm{G}})}{g_{\mathrm{s}} g_{\mathrm{v}}}} = \sqrt{\pi n(V_{\mathrm{G}})} \tag{C.5}$$

with $g_{\mathrm{s}} = g_{\mathrm{v}} = 2$ the spin and valley degeneracy in graphene. Finally, the mass of carriers is calculated from the voltage-dependent carrier density as

$$m(V_{\mathrm{G}}) = \frac{\hbar \sqrt{\pi n(V_{\mathrm{G}})}}{v_{\mathrm{F}}} \tag{C.6}$$

List of own publications

Journal articles

[1] M. Bauer, A. Rämer, S. Chevtchenko, *et al.*, “A high-sensitivity AlGaN/GaN HEMT Terahertz Detector with Integrated Broadband Bow-tie Antenna”, *IEEE Transactions on Terahertz Science and Technology*, 2017, invited for submission.

[2] S. Boppel, M. Ragauskas, A. Hajo, *et al.*, “0.25- GaN TeraFETs Optimized as THz Power Detectors and Intensity-Gradient Sensors”, *IEEE Transactions on Terahertz Science and Technology*, vol. 6, no. 2, pp. 348–350, Mar. 2016.

[3] M. Bauer, S. Boppel, J. Zhang, *et al.*, “Optimization of the Design of Terahertz Detectors Based on Si CMOS and AlGaN/GaN Field-Effect Transistors”, *International Journal of High Speed Electronics and Systems*, vol. 25, no. 03n04, p. 1 640 013, Sep. 2016.

[4] J. Zdanevičius, M. Bauer, S. Boppel, *et al.*, “Camera for High-Speed THz Imaging”, *Journal of Infrared, Millimeter, and Terahertz Waves*, Jun. 2015.

[5] A. Zak, M. A. Andersson, M. Bauer, *et al.*, “Antenna-Integrated 0.6 THz FET Direct Detectors Based on CVD Graphene”, *Nano Letters*, vol. 14, no. 10, pp. 5834–5838, Oct. 2014.

[6] A. Lisauskas, M. Bauer, S. Boppel, *et al.*, “Exploration of Terahertz Imaging with Silicon MOSFETs”, *Journal of Infrared, Millimeter, and Terahertz Waves*, vol. 35, no. 1, pp. 63–80, Jan. 2014.

[7] M. Bauer, R. Venckevičius, I. Kašalynas, *et al.*, “Antenna-coupled field-effect transistors for multi-spectral terahertz imaging up to 4.25 THz”, *Optics Express*, vol. 22, no. 16, p. 19 235, Aug. 2014.

[8] F. Friederich, W. von Spiegel, M. Bauer, *et al.*, “THz Active Imaging Systems With Real-Time Capabilities”, *IEEE Transactions on Terahertz Science And Technology*, vol. 1, no. 1, pp. 183–200, Sep. 2011.

Conference proceedings

[9] K. Ikamas, A. Lisauskas, M. Bauer, *et al.*, "Efficient detection of short-pulse THz radiation with field effect transistors", in *Noise and Fluctuations (ICNF), 2017 International Conference on*, IEEE, 2017, pp. 1–4.

[10] D. Čibiraitė, M. Bauer, A. Lisauskas, *et al.*, "Thermal noise-limited sensitivity of FET-based terahertz detectors", in *Noise and Fluctuations (ICNF), 2017 International Conference on*, IEEE, 2017, pp. 1–4.

[11] A. Lisauskas, M. Bauer, A. Rämer, *et al.*, "Terahertz rectification by plasmons and hot carriers in gated 2d electron gases", in *Noise and Fluctuations (ICNF), 2015 International Conference on*, IEEE, 2015, pp. 1–5.

[12] M Bauer, M Andersson, A Zak, *et al.*, "The potential for sensitivity enhancement by the thermoelectric effect in carbon-nanotube and graphene Tera-FETs", in *Journal of Physics: Conference Series*, vol. 647, Oct. 2015, p. 012 004.

[13] M. Bauer, A. Rämer, S. Boppel, *et al.*, "High-sensitivity wideband THz detectors based on GaN HEMTs with integrated bow-tie antennas", in *Microwave Integrated Circuits Conference (EuMIC), 2015 10th European*, IEEE, 2015, pp. 1–4.

[14] M. Bauer, A. Lisauskas, P. Sakalas, M. Schröter, and H. G. Roskos, "Terahertz detection at 240 GHz with a semiconducting carbon-nanotube field-effect transistor", in *Infrared, Millimeter, and Terahertz waves (IRMMW-THz), 2014 39th International Conference on*, IEEE, Sep. 2014, pp. 1–2.

[15] M. Bauer, A. Lisauskas, S. Boppel, *et al.*, "Bow-tie-antenna-coupled terahertz detectors using AlGaN/GaN field-effect transistors with 0.25 micrometer gate length", in *Microwave Integrated Circuits Conference (EuMIC), 2013 8th European*, Dec. 2013, pp. 212–215.

[16] M. Bauer, S. Boppel, A. Lisauskas, V. Krozer, and H. G. Roskos, "Real-time CMOS terahertz camera employing plane-to-plane imaging with a focal-plane array of field-effect transistors", in *Infrared, Millimeter, and Terahertz Waves (IRMMW-THz), 2013 38th International Conference on*, 2013, pp. 1–2.

[17] A. Brahm, M. Bauer, T. Hoyer, *et al.*, "All-electronic 3d computed THz tomography", in *Infrared, Millimeter, and Terahertz Waves (IRMMW-THz), 2011 36th International Conference on*, IEEE, Oct. 2011, pp. 1–2.

Bibliography

[18] M. Dyakonov and M. Shur, “Detection, mixing, and frequency multiplication of terahertz radiation by two-dimensional electronic fluid”, *Electron Devices, IEEE Transactions on*, vol. 43, no. 3, pp. 380–387, Mar. 1996.

[19] A. Lisauskas, U. Pfeiffer, E. Öjefors, *et al.*, “Rational design of high-responsivity detectors of terahertz radiation based on distributed self-mixing in silicon field-effect transistors”, *Journal of Applied Physics*, vol. 105, no. 11, p. 114 511, Jun. 2009.

[20] M. Sakhno, A. Golenkov, and F. Sizov, “Uncooled detector challenges: Millimeter-wave and terahertz long channel field effect transistor and Schottky barrier diode detectors”, *Journal of Applied Physics*, vol. 114, no. 16, p. 164 503, Oct. 2013.

[21] W Knap, S Rumyantsev, M. S. Vitiello, *et al.*, “Nanometer size field effect transistors for terahertz detectors”, *Nanotechnology*, vol. 24, no. 21, p. 214 002, May 2013.

[22] T. Otsuji and M. Shur, “Terahertz Plasmonics: Good Results and Great Expectations”, *IEEE Microwave Magazine*, vol. 15, no. 7, pp. 43–50, Nov. 2014.

[23] E. M. Conwell and J. Zucker, “‘‘Thermoelectric Effect” of Hot Carriers”, *Journal of Applied Physics*, vol. 36, no. 7, pp. 2192–2196, Jul. 1965.

[24] F. Schuster, D. Coquillat, H. Videlier, *et al.*, “Broadband terahertz imaging with highly sensitive silicon CMOS detectors”, *Optics express*, vol. 19, no. 8, pp. 7827–7832, 2011.

[25] H. Wang, Y. Wu, C. Cong, J. Shang, and T. Yu, “Hysteresis of Electronic Transport in Graphene Transistors”, *ACS Nano*, vol. 4, no. 12, pp. 7221–7228, Dec. 2010.

[26] R. I. Harrison and J. E. Zucker, “Hot-carrier microwave detector”, *Proceedings of the IEEE*, vol. 54, no. 4, pp. 588–595, 1966.

[27] N. M. Gabor, J. C. W. Song, Q. Ma, *et al.*, “Hot Carrier – Assisted Intrinsic Photoresponse in Graphene”, *Science*, vol. 334, no. 6056, pp. 648–652, Nov. 2011.

[28] J. C. W. Song, M. S. Rudner, C. M. Marcus, and L. S. Levitov, “Hot Carrier Transport and Photocurrent Response in Graphene”, *Nano Letters*, vol. 11, no. 11, pp. 4688–4692, Nov. 2011.

[29] J. F. Sierra, I. Neumann, M. V. Costache, and S. O. Valenzuela, “Hot-Carrier Seebeck Effect: Diffusion and Remote Detection of Hot Carriers in Graphene”, *Nano Letters*, vol. 15, no. 6, pp. 4000–4005, Jun. 2015.

[30] L. Vicarelli, M. S. Vitiello, D. Coquillat, *et al.*, “Graphene field-effect transistors as room-temperature terahertz detectors”, *Nature Materials*, vol. 11, no. 10, pp. 865–871, Sep. 2012.

[31] A. V. Muraviev, S. L. Rumyantsev, G. Liu, *et al.*, “Plasmonic and bolometric terahertz detection by graphene field-effect transistor”, *Applied Physics Letters*, vol. 103, no. 18, p. 181 114, 2013.

[32] L. Viti, J. Hu, D. Coquillat, *et al.*, “Efficient Terahertz detection in black-phosphorus nano-transistors with selective and controllable plasma-wave, bolometric and thermoelectric response”, *Scientific Reports*, vol. 6, p. 20 474, Feb. 2016, ISSN: 2045-2322.

[33] G. Rupper, S. Rudin, and F. J. Crowne, “Effects of oblique wave propagation on the nonlinear plasma resonance in the two-dimensional channel of the Dyakonov-Shur detector”, *Solid-State Electronics*, vol. 78, pp. 102–108, Dec. 2012.

[34] S. Rudin, G. Rupper, A. Gutin, and M. Shur, “Theory and measurement of plasmonic terahertz detector response to large signals”, *Journal of Applied Physics*, vol. 115, no. 6, p. 064 503, Feb. 2014.

[35] S. Rudin and M. Dyakonov, “Edge and strip plasmons in a two-dimensional electron fluid”, *Physical Review B*, vol. 55, no. 7, p. 4684, 1997.

[36] L. Viti, J. Hu, D. Coquillat, *et al.*, “Black Phosphorus Terahertz Photodetectors”, *Advanced Materials*, vol. 27, no. 37, pp. 5567–5572, Oct. 2015.

[37] U. R. Pfeiffer, J. Grzyb, H. Sherry, A. Cathelin, and A. Kaiser, “Toward low-NEP room-temperature THz MOSFET direct detectors in CMOS technology”, in *Infrared, Millimeter, and Terahertz Waves (IRMMW-THz), 2013 38th International Conference on*, IEEE, 2013, pp. 1–2.

[38] R. Bistritzer and A. H. MacDonald, “Electronic Cooling in Graphene”, *Physical Review Letters*, vol. 102, no. 20, p. 206 410, May 2009.

[39] M. Dyakonov and M. Shur, “Shallow water analogy for a ballistic field effect transistor: New mechanism of plasma wave generation by dc current”, *Physical Review Letters*, vol. 71, no. 15, pp. 2465–2468, Oct. 1993.

[40] M. I. Dyakonov and M. S. Shur, “Two dimensional electronic flute”, *Applied Physics Letters*, vol. 67, no. 8, p. 1137, 1995.

[41] W. Knap, M. Dyakonov, D. Coquillat, *et al.*, “Field effect transistors for terahertz detection: Physics and first imaging applications”, *Journal of Infrared, Millimeter and Terahertz Waves*, vol. 30, no. 12, pp. 1319–1337, Aug. 2009.

[42] S. Boppel, A. Lisauskas, M. Mundt, *et al.*, “CMOS Integrated Antenna-Coupled Field-Effect Transistors for the Detection of Radiation From 0.2 to 4.3 THz”, *IEEE Transactions on Microwave Theory and Techniques*, vol. 60, no. 12, pp. 3834–3843, Dec. 2012.

[43] S. Boppel, “Field-Effect-Transistor-Based Detection of Terahertz Radiation: Modelling, Implementation and Application”, PhD thesis, Johann Wolfgang Goethe-Universität, Frankfurt am Main, Germany, 2013.

[44] P. J. Burke, I. B. Spielman, J. P. Eisenstein, L. N. Pfeiffer, and K. W. West, “High frequency conductivity of the high-mobility two-dimensional electron gas”, *Applied Physics Letters*, vol. 76, no. 6, pp. 745–747, Feb. 2000.

[45] F. J. Crowne, “Microwave response of a high electron mobility transistor in the presence of a Dyakonov–Shur instability”, *Journal of Applied Physics*, vol. 91, no. 8, p. 5377, 2002.

[46] I. Khmyrova and Y. Seijyou, "Analysis of plasma oscillations in high-electron mobility transistorlike structures: Distributed circuit approach", *Applied Physics Letters*, vol. 91, no. 14, p. 143 515, 2007.

[47] I. Khmyrova, "Study of Plasma Effects in HEMT-like Structures for THz Applications by Equivalent Circuit Approach", in *Advanced Microwave and Millimeter Wave Technologies Semiconductor Devices Circuits and Systems*, M. Mukherjee, Ed., InTech, Mar. 2010.

[48] S. Preu, S. Kim, R. Verma, *et al.*, "An improved model for non-resonant terahertz detection in field-effect transistors", *Journal of Applied Physics*, vol. 111, no. 2, p. 024 502, 2012.

[49] A. Gutin, S. Nahar, M. Hella, and M. Shur, "Modeling terahertz plasmonic Si FETs with SPICE", *IEEE Transactions on Terahertz Science and Technology*, vol. 3, no. 5, pp. 545–549, 2013.

[50] M. Shur, "AlGaN/GaN plasmonic terahertz electronic devices", *Journal of Physics: Conference Series*, vol. 486, p. 012 025, Mar. 2014.

[51] Advanced Design System, Version 2016, Keysight Technologies, Santa Rosa, Ca, USA.

[52] F. Bloch, "Bremsvermögen von Atomen mit mehreren Elektronen", *Zeitschrift für Physik A Hadrons and Nuclei*, vol. 81, no. 5, pp. 363–376, 1933.

[53] L. Euler, "Principes généraux du mouvement des fluides", *Histoire de l'Académie Royale des Sciences et des Belles-Lettres de Berlin*, pp. 274–315, 1755.

[54] A. Jüngel, *Transport equations for semiconductors*, ser. Lecture notes in physics 773. Berlin: Springer, 2009.

[55] M. Lundstrom, *Fundamentals of Carrier Transport.* New York: Cambridge Univ Pr, 2009.

[56] L. Tonks and I. Langmuir, "Oscillations in Ionized Gases", *Physical Review*, vol. 33, no. 2, pp. 195–210, Feb. 1929.

[57] S. Raimes, "The theory of plasma oscillations in metals", *Reports on Progress in Physics*, vol. 20, no. 1, p. 1, 1957.

[58] F. Stern, "Polarizability of a two-dimensional electron gas", *Physical Review Letters*, vol. 18, no. 14, p. 546, 1967.

[59] A. V. Chaplik, "Possible Crystallization of Charge Carriers in Low-density Inversion Layers", *Journal of Experimental and Theoretical Physics*, vol. 35, no. 2, pp. 395–398, Feb. 1972.

[60] ——, "Absorption and emission of electromagnetic waves by two-dimensional plasmons", *Surface Science Reports*, vol. 5, no. 7, pp. 289–335, 1985.

[61] T. Ando, A. B. Fowler, and F. Stern, "Electronic properties of two-dimensional systems", *Reviews of Modern Physics*, vol. 54, no. 2, p. 437, 1982.

[62] S. J. Allen Jr, D. C. Tsui, and R. A. Logan, "Observation of the two-dimensional plasmon in silicon inversion layers", *Physical Review Letters*, vol. 38, no. 17, p. 980, 1977.

[63] G. C. Dyer, N. Q. Vinh, S. J. Allen, *et al.*, "A terahertz plasmon cavity detector", *Applied Physics Letters*, vol. 97, no. 19, p. 193 507, 2010.

[64] A. El Fatimy, F. Teppe, N. Dyakonova, *et al.*, "Resonant and voltage-tunable terahertz detection in InGaAs/InP nanometer transistors", *Applied Physics Letters*, vol. 89, no. 13, p. 131 926, 2006.

[65] W. Knap, Y. Deng, S. Rumyantsev, and M. S. Shur, "Resonant detection of subterahertz and terahertz radiation by plasma waves in submicron field-effect transistors", *Applied Physics Letters*, vol. 81, no. 24, p. 4637, 2002.

[66] F. Teppe, W. Knap, D. Veksler, *et al.*, "Room-temperature plasma waves resonant detection of sub-terahertz radiation by nanometer field-effect transistor", *Applied Physics Letters*, vol. 87, no. 5, p. 052 107, 2005.

[67] W. Knap, V. Kachorovskii, Y. Deng, *et al.*, "Nonresonant detection of terahertz radiation in field effect transistors", *Journal of Applied Physics*, vol. 91, no. 11, pp. 9346–9353, Feb. 2002.

[68] R. Al Hadi, H. Sherry, J. Grzyb, *et al.*, "A broadband 0.6 to 1 THz CMOS imaging detector with an integrated lens", in *Microwave Symposium Digest (MTT), 2011 IEEE MTT-S International*, IEEE, 2011, pp. 1–4.

[69] S. Regensburger, M. Mittendorff, S. Winnerl, *et al.*, "Broadband THz detection from 01 to 22 THz with large area field-effect transistors", *Optics Express*, vol. 23, no. 16, p. 20 732, Aug. 2015.

[70] H. Qin, X. Li, J. Sun, *et al.*, "Detection of incoherent terahertz light using antenna-coupled high-electron-mobility field-effect transistors", *Applied Physics Letters*, vol. 110, no. 17, p. 171 109, Apr. 2017.

[71] S. Preu, M. Mittendorff, S. Winnerl, *et al.*, "Ultra-fast transistor-based detectors for precise timing of near infrared and THz signals", *Optics Express*, vol. 21, no. 15, p. 17 941, Jul. 2013.

[72] M. I. Dyakonov, "Boundary instability of a two-dimensional electron fluid", *Semiconductors*, vol. 42, no. 8, pp. 984–988, Aug. 2008.

[73] M. Shur, "Plasma wave terahertz electronics", *Electronics Letters*, vol. 46, no. 26, s18–s21, 2010.

[74] M. Sakowicz, M. B. Lifshits, O. A. Klimenko, *et al.*, "Terahertz responsivity of field effect transistors versus their static channel conductivity and loading effects", *Journal of Applied Physics*, vol. 110, no. 5, p. 054 512, Sep. 2011.

[75] D. M. Pozar, *Microwave engineering.* New Delhi: John Wiley & Sons, 2010.

[76] S. J. Orfanidis, *Electromagnetic Waves and Antennas.* Copyright (c) 1996-2016 by Sophocles J. Orfanidis, 1996.

[77] H.-G. Krekels, B. Schiek, and E. Menzel, "Power detector with GaAs field effect transistors", in *Microwave Conference, 1992. 22nd European*, vol. 1, IEEE, 1992, pp. 174–179.

[78] S. M. Sze and K. K. Ng, *Physics of semiconductor devices*, 3. ed. Hoboken, NJ: Wiley-Interscience, 2007.

[79] S. Boppel, A. Lisauskas, and H. G. Roskos, "Terahertz array imagers: Towards the implementation of terahertz cameras with plasma-wave-based silicon MOS-FET detectors", in *Handbook of terahertz technology for imaging, sensing and communications*, Woodhead Publishing Limited, Jan. 2013, pp. 231–271.

[80] A. Lisauskas, S. Boppel, M. Mundt, V. Krozer, and H. G. Roskos, “Subharmonic mixing with field-effect transistors: Theory and experiment at 639 GHz high above f_t”, *IEEE Sensors Journal*, vol. 13, no. 1, pp. 124–132, Jan. 2013.

[81] R. Stratton, “Diffusion of Hot and Cold Electrons in Semiconductor Barriers”, *Physical Review*, vol. 126, no. 6, pp. 2002–2014, Jun. 1962.

[82] S. H. Koenig, “Hot and warm electrons — A review”, *Journal of Physics and Chemistry of Solids*, vol. 8, pp. 227–234, Jan. 1959.

[83] F. J. Blatt, P. A. Schroeder, C. L. Foiles, and D. Greig, *Thermoelectric Power of Metals*. Boston, MA: Springer US, 1976.

[84] M. Wagner, “Simulation of Thermoelectric Devices”, PhD thesis, Technische Universität Wien, Wien, Nov. 2007.

[85] T. A. Amollo, G. T. Mola, M. S. K. Kirui, and V. O. Nyamori, “Graphene for Thermoelectric Applications: Prospects and Challenges”, *Critical Reviews in Solid State and Materials Sciences*, pp. 1–25, May 2017.

[86] W.-K. Tse and S. Das Sarma, “Energy relaxation of hot Dirac fermions in graphene”, *Physical Review B*, vol. 79, no. 23, Jun. 2009.

[87] G. R. Aizin and G. C. Dyer, “Transmission line theory of collective plasma excitations in periodic two-dimensional electron systems: Finite plasmonic crystals and Tamm states”, *Physical Review B*, vol. 86, no. 23, Dec. 2012.

[88] J.-X. Yang, F. Agahi, D. Dai, *et al.*, “Wide-bandwidth electron bolometric mixers: A 2deg prototype and potential for low-noise THz receivers”, *IEEE transactions on microwave theory and techniques*, vol. 41, no. 4, pp. 581–589, 1993.

[89] V. V. Popov, A. N. Koudymov, M. Shur, and O. V. Polischuk, “Tuning of ungated plasmons by a gate in the field-effect transistor with two-dimensional electron channel”, *Journal of Applied Physics*, vol. 104, no. 2, p. 024 508, Jul. 2008.

[90] J. Mateos and T. Gonzalez, “Plasma Enhanced Terahertz Rectification and Noise in InGaAs HEMTs”, *IEEE Transactions on Terahertz Science and Technology*, vol. 2, no. 5, pp. 562–569, Sep. 2012.

[91] N. W. Ashcroft and N. D. Mermin, *Solid state physics*. South Melbourne: Brooks/Cole Thomson Learning, 2012.

[92] G. Chen, *Nanoscale energy transport and conversion: a parallel treatment of electrons, molecules, phonons, and photons*, ser. MIT-Pappalardo series in mechanical engineering. Oxford: Oxford University Press, 2005.

[93] C. Jacoboni, *Theory of electron transport in semiconductors: a pathway from elementary physics to nonequilibrium green functions*, ser. Springer series in solid-state sciences 165. Heidelberg: Springer, 2010, ISBN: 978-3-642-10585-2 978-3-642-10586-9.

[94] S Selberherr, *Analysis and simulation of semiconductor devices*. Wien: Springer, 2013, ISBN: 978-3-7091-8752-4.

[95] T. Grasser, Ting-Wei Tang, H. Kosina, and S. Selberherr, “A review of hydrodynamic and energy-transport models for semiconductor device simulation”, *Proceedings of the IEEE*, vol. 91, no. 2, pp. 251–274, Feb. 2003.

[96] G. K. Wachutka, “Rigorous thermodynamic treatment of heat generation and conduction in semiconductor device modeling”, *IEEE Transactions on Computer-*

Aided Design of Integrated Circuits and Systems, vol. 9, no. 11, pp. 1141–1149, 1990.

[97] W. v. Roosbroeck, "Theory of the flow of electrons and holes in germanium and other semiconductors", *Bell System Technical Journal*, vol. 29, no. 4, pp. 560–607, 1950.

[98] R. Stratton, "Semiconductor current-flow equations (diffusion and degeneracy)", *IEEE Transactions on Electron Devices*, vol. 19, no. 12, pp. 1288–1292, 1972.

[99] R. Minixhofer, "Integrating Technology Simulation into the Semiconductor Manufacturing Environment", PhD thesis, Technische Universität Wien, Wien, Mar. 2006.

[100] K. Blotekjaer, "Transport equations for electrons in two-valley semiconductors", *IEEE Transactions on Electron Devices*, vol. 17, no. 1, pp. 38–47, 1970.

[101] A. Bringer and G. Schön, "Extended moment equations for electron transport in semiconducting submicron structures", *Journal of Applied Physics*, vol. 64, no. 5, p. 2447, 1988.

[102] T. Grasser, "Closure relations for macroscopic transport models", in *Semiconductor Device Research Symposium, 2003 International*, IEEE, 2003, pp. 504–505.

[103] M. Shur, T. A. Fjeldly, T. Ytterdal, and K. Lee, "Unified MOSFET model", *Solid-state electronics*, vol. 35, no. 12, pp. 1795–1802, Dec. 1992.

[104] S. Khandelwal, N. Goyal, and T. A. Fjeldly, "A Physics-Based Analytical Model for 2deg Charge Density in AlGaN/GaN HEMT Devices", *IEEE Transactions on Electron Devices*, vol. 58, no. 10, pp. 3622–3625, Oct. 2011.

[105] ——, "A precise physics-based compact model for 2-DEG charge density in GaAs HEMTs applicable in all regions of device operation", *Solid-State Electronics*, vol. 79, pp. 22–25, Jan. 2013.

[106] R. Weikle, J.-Q. Lu, M. S. Shur, and M. I. Dyakonov, "Detection of microwave radiation by electronic fluid in high electron mobility transistors", *Electronics Letters*, vol. 32, no. 23, pp. 2148–2149, 1996.

[107] J.-Q. Lü, M. S. Shur, J. L. Hesler, L. Sun, and R. Weikle, "Terahertz detector utilizing two-dimensional electronic fluid", *IEEE Electron Device Letters*, vol. 19, no. 10, pp. 373–375, 1998.

[108] J.-Q. Lü and M. S. Shur, "Terahertz detection by high-electron-mobility transistor: Enhancement by drain bias", *Applied Physics Letters*, vol. 78, no. 17, pp. 2587–2588, Apr. 2001.

[109] W. Knap, F. Teppe, Y. Meziani, *et al.*, "Plasma wave detection of sub-terahertz and terahertz radiation by silicon field-effect transistors", *Applied Physics Letters*, vol. 85, no. 4, p. 675, 2004.

[110] R. Tauk, F. Teppe, S. Boubanga, *et al.*, "Plasma wave detection of terahertz radiation by silicon field effects transistors: Responsivity and noise equivalent power", *Applied Physics Letters*, vol. 89, no. 25, p. 253 511, Dec. 2006, ISSN: 00036951.

[111] W. Knap, Y. Deng, S. Rumyantsev, *et al.*, "Resonant detection of subterahertz radiation by plasma waves in a submicron field-effect transistor", *Applied Physics Letters*, vol. 80, no. 18, pp. 3433–3435, May 2002.

[112] W. Schottky, “Über spontane Stromschwankungen in verschiedenen Elektrizitätsleitern”, *Annalen der physik*, vol. 362, no. 23, pp. 541–567, 1918.

[113] J. B. Johnson, “Thermal agitation of electricity in conductors”, *Physical Review*, vol. 32, no. 1, p. 97, 1928.

[114] H. Nyquist, “Thermal agitation of electric charge in conductors”, *Physical Review*, vol. 32, no. 1, p. 110, 1928.

[115] E. Öjefors, U. R. Pfeiffer, A. Lisauskas, and H. G. Roskos, “A 0.65 THz Focal-Plane Array in a Quarter-Micron CMOS Process Technology”, *IEEE Journal of Solid-State Circuits*, vol. 44, no. 7, pp. 1968–1976, Jul. 2009.

[116] J. D. Sun, Y. F. Sun, D. M. Wu, *et al.*, “High-responsivity, low-noise, room-temperature, self-mixing terahertz detector realized using floating antennas on a GaN-based field-effect transistor”, *Applied Physics Letters*, vol. 100, no. 1, p. 013 506, Jan. 2012.

[117] C. G. Kang, Y. G. Lee, S. K. Lee, *et al.*, “Mechanism of the effects of low temperature Al2O3 passivation on graphene field effect transistors”, *Carbon*, vol. 53, pp. 182–187, Mar. 2013.

[118] M. Von Haartman and M. Östling, *Low-frequency noise in advanced MOS devices*. Dordrecht: Springer, 2007.

[119] C. A. Balanis, “Antenna theory: A review”, *Proceedings of the IEEE*, vol. 80, no. 1, pp. 7–23, 1992.

[120] J. Van Rudd and D. M. Mittleman, “Influence of substrate-lens design in terahertz time-domain spectroscopy”, *Journal of the Optical Society of America B*, vol. 19, no. 2, pp. 319–329, Feb. 2002.

[121] D. F. Filipovic, S. S. Gearhart, and G. M. Rebeiz, “Double-slot antennas on extended hemispherical and elliptical silicon dielectric lenses”, *Microwave Theory and Techniques, IEEE Transactions on*, vol. 41, no. 10, pp. 1738–1749, 1993.

[122] J. H. Booske, R. J. Dobbs, C. D. Joye, *et al.*, “Vacuum Electronic High Power Terahertz Sources”, *IEEE Transactions on Terahertz Science and Technology*, vol. 1, no. 1, pp. 54–75, Sep. 2011.

[123] E. R. Brown, J. R. Söderström, C. D. Parker, *et al.*, “Oscillations up to 712 GHz in InAs/AlSb resonant-tunneling diodes”, *Applied Physics Letters*, vol. 58, no. 20, pp. 2291–2293, May 1991.

[124] K. Okada, K. Kasagi, N. Oshima, S. Suzuki, and M. Asada, “Resonant-Tunneling-Diode Terahertz Oscillator Using Patch Antenna Integrated on Slot Resonator for Power Radiation”, *IEEE Transactions on Terahertz Science and Technology*, vol. 5, no. 4, pp. 613–618, Jul. 2015.

[125] M. Asada, S. Suzuki, and N. Kishimoto, “Resonant tunneling diodes for sub-terahertz and terahertz oscillators”, *Japanese Journal of Applied Physics*, vol. 47, p. 4375, 2008.

[126] S. Preu, G. H. Döhler, S. Malzer, L. J. Wang, and A. C. Gossard, “Tunable, continuous-wave Terahertz photomixer sources and applications”, *Journal of Applied Physics*, vol. 109, no. 6, p. 061 301, Mar. 2011.

[127] RPG Radiometer Physics GmbH, DE-53340 Meckenheim, Germany.

[128] Thomas Keating Ltd., RH14 9SH Billingshurst, United Kingdom.

[129] TOPTICA Photonics AG,DE-82166 Gräfelfing, Germany.

[130] A. J. Deninger, A. Roggenbuck, S. Schindler, and S. Preu, "2.75 THz tuning with a triple-DFB laser system at 1550 nm and InGaAs photomixers", *Journal of Infrared, Millimeter, and Terahertz Waves*, vol. 36, no. 3, pp. 269–277, Mar. 2015.

[131] E. R. Brown, K. A. McIntosh, K. B. Nichols, and C. L. Dennis, "Photomixing up to 3.8 THz in low-temperature-grown GaAs", *Applied Physics Letters*, vol. 66, no. 3, pp. 285–287, Jan. 1995.

[132] Y. Hao, L.-A. Yang, and J.-C. Zhang, "GaN-based semiconductor devices for terahertz technology", *Terahertz Science and Technology*, vol. 1, no. 2, pp. 51–64, 2008.

[133] U. Mishra, Shen Likun, T. Kazior, and Yi-Feng Wu, "GaN-based RF power devices and amplifiers", *Proceedings of the IEEE*, vol. 96, no. 2, pp. 287–305, Feb. 2008.

[134] S. A. Chevtchenko, F. Brunner, J. Würfl, and G. Tränkle, "Effect of buffer thickness on DC and microwave performance of AlGaN/GaN heterojunction field-effect transistors", *physica status solidi (a)*, vol. 207, no. 6, pp. 1505–1508, Feb. 2010.

[135] S. Kim, D.-W. Park, K.-Y. Choi, and S.-G. Lee, "MOSFET Characteristics for Terahertz Detector Application From On-Wafer Measurement", *IEEE Transactions on Terahertz Science and Technology*, vol. 5, no. 6, pp. 1068–1077, Nov. 2015.

[136] M. v. Exter, C. Fattinger, and D. Grischkowsky, "Terahertz time-domain spectroscopy of water vapor", *Optics Letters*, vol. 14, no. 20, pp. 1128–1130, 1989.

[137] T. K. Nguyen, T. A. Ho, H. Han, and I. Park, "Numerical Study of Self-Complementary Antenna Characteristics on Substrate Lenses at Terahertz Frequency", *Journal of Infrared, Millimeter, and Terahertz Waves*, vol. 33, no. 11, pp. 1123–1137, Nov. 2012.

[138] T. N. Theis, "Plasmons in inversion layers", *Surface Science*, vol. 98, no. 1-3, pp. 515–532, Aug. 1980.

[139] R. Al Hadi, H. Sherry, J. Grzyb, *et al.*, "A 1 k-Pixel Video Camera for 0.7-1.1 Terahertz Imaging Applications in 65-nm CMOS", *IEEE Journal of Solid-State Circuits*, vol. 47, no. 12, pp. 2999–3012, Dec. 2012.

[140] D. Glaab, S. Boppel, A. Lisauskas, *et al.*, "Terahertz heterodyne detection with silicon field-effect transistors", *Applied Physics Letters*, vol. 96, no. 4, p. 042 106, Jan. 2010.

[141] K. S. Novoselov, "Electric Field Effect in Atomically Thin Carbon Films", *Science*, vol. 306, no. 5696, pp. 666–669, Oct. 2004.

[142] K. S. Novoselov, A. K. Geim, S. V. Morozov, *et al.*, "Two-dimensional gas of massless Dirac fermions in graphene", *Nature*, vol. 438, no. 7065, pp. 197–200, Nov. 2005.

[143] S. Das Sarma, S. Adam, E. H. Hwang, and E. Rossi, "Electronic transport in two-dimensional graphene", *Reviews of Modern Physics*, vol. 83, no. 2, pp. 407–470, May 2011.

[144] A. H. Castro Neto, N. M. R. Peres, K. S. Novoselov, and A. K. Geim, "The electronic properties of graphene", *Reviews of Modern Physics*, vol. 81, no. 1, pp. 109–162, Jan. 2009.

[145] N. M. R. Peres, “The transport properties of graphene: An introduction”, *Reviews of Modern Physics*, vol. 82, no. 3, pp. 2673–2700, Sep. 2010.

[146] S. Rudin, “Non-linear plasma oscillations in semiconductors and graphene channels and application to the detection of terahertz signals”, *International Journal of High Speed Electronics and Systems*, vol. 20, no. 03, pp. 567–582, Sep. 2011.

[147] D. Svintsov, V. Vyurkov, V. Ryzhii, and T. Otsuji, “Hydrodynamic electron transport and nonlinear waves in graphene”, *Physical Review B*, vol. 88, no. 24, Dec. 2013.

[148] V. Ryzhii, “Terahertz plasma waves in gated graphene heterostructures”, *Japanese Journal of Applied Physics*, vol. 45, no. 9L, p. L923, 2006.

[149] E. H. Hwang and S. Das Sarma, “Dielectric function, screening, and plasmons in two-dimensional graphene”, *Physical Review B*, vol. 75, no. 20, May 2007.

[150] M. Polini, R. Asgari, G. Borghi, *et al.*, “Plasmons and the spectral function of graphene”, *Physical Review B*, vol. 77, no. 8, Feb. 2008.

[151] L. Ju, B. Geng, J. Horng, *et al.*, “Graphene plasmonics for tunable terahertz metamaterials”, *Nature Nanotechnology*, vol. 6, no. 10, pp. 630–634, Sep. 2011.

[152] A. Tomadin and M. Polini, “Theory of the plasma-wave photoresponse of a gated graphene sheet”, *Physical Review B*, vol. 88, no. 20, Nov. 2013.

[153] Jie Sun, N. Lindvall, M. T. Cole, *et al.*, “Low Partial Pressure Chemical Vapor Deposition of Graphene on Copper”, *IEEE Transactions on Nanotechnology*, vol. 11, no. 2, pp. 255–260, Mar. 2012.

[154] C. J. L. de la Rosa, N. Lindvall, M. T. Cole, *et al.*, “Frame assisted H2o electrolysis induced H2 bubbling transfer of large area graphene grown by chemical vapor deposition on Cu”, *Applied Physics Letters*, vol. 102, no. 2, p. 022 101, Jan. 2013.

[155] E. J. H. Lee, K. Balasubramanian, R. T. Weitz, M. Burghard, and K. Kern, “Contact and edge effects in graphene devices”, *Nature Nanotechnology*, vol. 3, no. 8, pp. 486–490, Aug. 2008.

[156] O. Habibpour, J. Vukusic, and J. Stake, “A large-signal graphene FET model”, *Electron Devices, IEEE Transactions on*, vol. 59, no. 4, pp. 968–975, 2012.

[157] S. Kim, J. Nah, I. Jo, *et al.*, “Realization of a high mobility dual-gated graphene field-effect transistor with Al2o3 dielectric”, *Applied Physics Letters*, vol. 94, no. 6, p. 062 107, 2009.

[158] J. Xia, F. Chen, J. Li, and N. Tao, “Measurement of the quantum capacitance of graphene”, *Nature Nanotechnology*, vol. 4, no. 8, pp. 505–509, Aug. 2009.

[159] S. Adam, E. H. Hwang, V. M. Galitski, and S. D. Sarma, “A self-consistent theory for graphene transport”, *Proceedings of the National Academy of Sciences*, vol. 104, no. 47, pp. 18 392–18 397, 2007.

[160] W. Gannett, W. Regan, K. Watanabe, *et al.*, “Boron nitride substrates for high mobility chemical vapor deposited graphene”, *Applied Physics Letters*, vol. 98, no. 24, p. 242 105, Jun. 2011.

[161] O. Habibpour, S. Cherednichenko, J. Vukusic, and J. Stake, “Mobility Improvement and Microwave Characterization of a Graphene Field Effect Transistor With Silicon Nitride Gate Dielectrics”, *IEEE Electron Device Letters*, vol. 32, no. 7, pp. 871–873, Jul. 2011.

[162] K. Bolotin, K. Sikes, Z. Jiang, *et al.*, “Ultrahigh electron mobility in suspended graphene”, *Solid State Communications*, vol. 146, no. 9-10, pp. 351–355, Jun. 2008.

[163] J. Moser, A. Barreiro, and A. Bachtold, “Current-induced cleaning of graphene”, *Applied Physics Letters*, vol. 91, no. 16, p. 163 513, Oct. 2007.

[164] D. Spirito, D. Coquillat, S. L. De Bonis, *et al.*, “High performance bilayer-graphene terahertz detectors”, *Applied Physics Letters*, vol. 104, no. 6, p. 061 111, Feb. 2014.

[165] L. Viti, A. Politano, and M. S. Vitiello, “Black phosphorus nanodevices at terahertz frequencies: Photodetectors and future challenges”, *APL Materials*, vol. 5, no. 3, p. 035 602, Mar. 2017.

[166] D. M. Rowe, Ed., *Thermoelectrics handbook: macro to nano*. Boca Raton, Fla.: CRC/Taylor & Francis, 2006.

[167] X. Xu, N. M. Gabor, J. S. Alden, A. M. van der Zande, and P. L. McEuen, “Photo-Thermoelectric Effect at a Graphene Interface Junction”, *Nano Letters*, vol. 10, no. 2, pp. 562–566, Feb. 2010.

[168] N. Balkan, M. C. Arikan, S. Gokden, *et al.*, “Energy and momentum relaxation of hot electrons in GaN/AlGaN”, *Journal of Physics: Condensed Matter*, vol. 14, no. 13, p. 3457, 2002.

[169] A. Matulionis, J. Liberis, L. Ardaravicius, *et al.*, “Hot-electron energy relaxation time in AlGaN/GaN”, *Semiconductor science and technology*, vol. 17, no. 3, p. L9, 2002.

[170] J. C. W. Song and L. S. Levitov, “Energy flows in graphene: Hot carrier dynamics and cooling”, *Journal of Physics: Condensed Matter*, vol. 27, no. 16, p. 164 201, Apr. 2015.

[171] E. H. Hwang, B. Y.-K. Hu, and S. Das Sarma, “Inelastic carrier lifetime in graphene”, *Physical Review B*, vol. 76, no. 11, Sep. 2007.

[172] J. M. Dawlaty, S. Shivaraman, M. Chandrashekhar, F. Rana, and M. G. Spencer, “Measurement of ultrafast carrier dynamics in epitaxial graphene”, *Applied Physics Letters*, vol. 92, no. 4, p. 042 116, Jan. 2008.

[173] P. A. George, J. Strait, J. Dawlaty, *et al.*, “Ultrafast Optical-Pump Terahertz-Probe Spectroscopy of the Carrier Relaxation and Recombination Dynamics in Epitaxial Graphene”, *Nano Letters*, vol. 8, no. 12, pp. 4248–4251, Dec. 2008.

[174] D. Sun, Z.-K. Wu, C. Divin, *et al.*, “Ultrafast Relaxation of Excited Dirac Fermions in Epitaxial Graphene Using Optical Differential Transmission Spectroscopy”, *Physical Review Letters*, vol. 101, no. 15, Oct. 2008.

[175] J. H. Strait, H. Wang, S. Shivaraman, *et al.*, “Very Slow Cooling Dynamics of Photoexcited Carriers in Graphene Observed by Optical-Pump Terahertz-Probe Spectroscopy”, *Nano Letters*, vol. 11, no. 11, pp. 4902–4906, Nov. 2011.

[176] D. Sun, G. Aivazian, A. M. Jones, *et al.*, “Ultrafast hot-carrier-dominated photocurrent in graphene”, *Nature Nanotechnology*, vol. 7, no. 2, pp. 114–118, Jan. 2012.

[177] S. Ulstrup, J. Christian Johannsen, A. Crepaldi, *et al.*, “Ultrafast electron dynamics in epitaxial graphene investigated with time- and angle-resolved photoemission spectroscopy”, *Journal of Physics: Condensed Matter*, vol. 27, no. 16, p. 164 206, Apr. 2015.

[178] N. S. Sankeshwar, S. S. Kubakaddi, and B. G. Mulimani, “Thermoelectric power in graphene”, in *Advances in Graphene Science*, InTech, 2013, pp. 217–271.

[179] F. H. L. Koppens, T. Mueller, P. Avouris, *et al.*, “Photodetectors based on graphene, other two-dimensional materials and hybrid systems”, *Nature Nanotechnology*, vol. 9, no. 10, pp. 780–793, Oct. 2014. (visited on 07/25/2016).

[180] M. Cutler and N. F. Mott, “Observation of Anderson localization in an electron gas”, *Physical Review*, vol. 181, no. 3, p. 1336, 1969.

Zusammenfassung

Die vorliegende Arbeit befasst sich mit der Modellierung und der experimentellen Charakterisierung von Feldeffekttransistoren (FET) mit integrierten breitbandigen planaren Antennenstrukturen. Zur Unterscheidung der vollen Bauelemente von dem intrinsischen gegateten Teil des Transistors werden diese im Folgenden als TeraFETs bezeichnet. TeraFETs zeigen zwei dominante Mechanismen der Strahlungsdetektion, insbesondere im THzbereich, der etwa von 0.3 bis 10 THz veranschlagt wird. Zum einen kann einfallende Strahlung Ladungsträgerdichtewellen (Plasmawellen) im zweidimensionalen Elektronengas des Transistors induzieren, welche nichtlineare, gleichrichtende Eigenschaften mit sich bringen. Dieses Prinzip der Detektion ist daher auch als *plasmonisches Mischen* bekannt geworden und wird seit ca. zwanzig Jahren intensiv untersucht. Zum anderen kann eine lokale Konzentration des elektrischen Felds im Kanal des Transistors, die einhergeht mit notwendigen asymmetrischen Randbedingungen der Strahlungseinkopplung für ein effektives plasmonisches Mischen, zu einem Diffusionsstrom führen, welcher ebenfalls als gleicherichtetes Signal gemessen werden kann. Durch die lokale Anheizung der Ladungsträger des zweidimensionalen Elektronengas entstehen Gradienten der Temperatur des Gases, welche wiederum zu einen Thermoelektrischen Effekt induzieren. Im Zusammenhang einer Verteilung von heißen Ladungsträgern wird dieser Effekt als *hot carrier thermoelectric effect* bezeichnet. Beide untersuchten Effekte basieren somit auf der gleichen asymmetrischen Einkopplung der auftreffenden Strahlung durch die integrierten Antennen. Der Fokus der vorliegenden Arbeit lag auf der Formulierung eines hydrodynamischen Transportmodells für die Ladungsträger des zweidimensionalen Elektronengases und dessen Implementierung in einem äquivalenten Schaltungsmodell in einer kommerziellen Simulationssoftware [51].

Nach einer allgemeinen Einleitung in Kapitel 1 folgt in Kapitel 2 eine Aufbereitung der Theorie des Mischens durch Plasmawellen in TeraFETs auf der Basis eines fluiddynamischen Transportmodells, welches zu Beginn der 1990er Jahre von Dyakonov und Shur formuliert wurde [18]. Die Diskussion fokussiert dabei auf den intrinsischen Teil des Transistors, in dem das eigentliche Mischen stattfindet. Die Herleitung eines Effizienzfaktors der plasmonischen Gleichrichtung wird teilweise vorgeführt. Dieser Faktor ergibt sich als Erhöhung des sogenannten klassischen resistiven Mischens bei quasi-stationären Frequenzen durch die gleichrichtenden Eigenschaften der induzierten Plasmawellen. Die Notwendigkeit asymmetrischer Randbedingungen wird erörtert anhand einer Messungen mit TeraFETs in denen unterschiedliche Grade der Asymmetrie realisiert wurden [2]. Im Zuge der experimentellen Arbeit dieser Promotion erwies es sich als besonders effektiv eine Asymmetrie durch geeignete Einspeisung der Antennensignale, sowie durch das Einbringen einer zusätzlichen

kapazitiven Kopplung zwischen Trasistor-Gate und einem der Kontakte zu realisieren.

Die Basis der theoretischen Beschreibung des plasmonischen Mischen in TeraFETs ist wie erwähnt ein fluiddynamisches Transportmodell, welches in der Literatur weit verbreitet ist. Eine Reihe von jüngeren Experimenten zeigte jedoch, dass zusätzliche Detektion durch den Thermoelektrischen Effekt signifikante Beiträge zu den gemessenen Signalen liefern kann. Zuvor wurden hocheffiziente TeraFETs vornehmlich in Si CMOS Technologie untersucht, aufgrund der technologischen Reife dieses Materialsystems. Dort sind geringe thermoelektrische Beiträge schwer auszumachen, vor allem aufgrund der fehlenden ungegateten Transistorregionen. Untersuchungen in neueren Materialsystemen, so etwa AlGaN/GaN HEMTs und Graphen-FETs lassen diese Beiträge jedoch schon bei Raumtemperatur deutlich hervortreten.

Die Beobachtung der thermoelektrischen Signale war eine hauptsächliche Motivation einer tieferen Untersuchung des Detektormodells. Diese ergeben, dass das Modell als "reduziertes" hydrodynamisches Modell verstanden werden kann, bei welchem hydrodynamische Druckterme vernachlässigt werden. Kapitel 3 dieser Arbeit präsentiert die Formulierung eines vollständigen hydrodynamischen Modells auf Basis der Herleitung aus der Boltzmann-Transportgleichung. Eine Reihe von Vereinfachung liefert ein Modell, welches in einer Formulierung für die Ladungsträger-Strondichte in eine Schaltungsmodell überführt werden kann.

Kapitel 4 der vorliegenden Arbeit beschreibt einige Details der Implementierung. Einige Vereinfachung des theoretischen Transportmodells wurden in dem derzeitigem Stand der Implementierung angewendet. Zum einen wurden die Modellgleichungen auf Basis einer Maxwell-Boltzmann Wahrscheinlichkeitsverteilung beschrieben. Dies ist für den Betrieb der TeraFETs nahe deren Threshold-Spannung gerechtfertigt. Für größer werdende Spannung in Bezug auf den Threshold, also für den Betrieb im sogenannten *strong inversion regime* muss je nach Materialsystem aber eine Erweiterung der Beschreibung in Betracht gezogen werden. Die mögliche Entartung des System würde dann durch eine Fermi-Dirac-Statistik beschrieben. Zweitens wurde die Energiegleichung des hydrodynamischen Modells vereinfacht, in dem nichtstationäre Terme sowie ein Drift-Anteil der gemittelten kinetischen Energie vernachlässigt wurden. Somit enthät das Modell keine Evolution der Energiedichte, sondern betrachtet den Aufbau einer Verteilung heißer Ladungsträger lediglich auf Basis des lokalen elektrischen Felds. Zum dritten wird bisher keine Abhängigkeit der Dichte sowie Beweglichkeit der Ladungsträger von deren Temperatur angenommen. Dies führt zu einem Konstanten Seebeckkoeffizienten des thermoelektrischen Effekts. Eine Erweiterung des Modells in dieser Hinsicht sollte daher angestrebt werden.

Das implementierte Modell wurde auf Basis eines Vergleichs mit analytisch berechneten charakteristischen Größen des plasmonischen Mischens verifiziert. Dabei zeigte sich sowohl für den Hochfrequenzeinfluss auf die Kanalimpedanz sowie den plasmonischen Effizienzfaktor eine hervorragende Übereinstimmung. Die Rechnungen basierten auf einer Reihe von Parametern eines realistischen TeraFET Bauelements, und die Prozedur zur Extraktion der Parameter aus DC Messungen des Kanalwiderstands wird ebenfalls in Kapitel 4 dargestellt.

Kapitel 5 dieser Arbeit zeigt eine Reihe von Simulationsergebnissen, welche mit dem Implementierten Schaltungsmodell auf Basis des hydrodynamischen Ladungsträgertransportmodells angefertigt wurden. Der erste Abschnitt des Kapitels befasst

sich dabei mit der Überhöhung der Effizienz des plasmonischen Mischens unter Randbedingungen, wie sie in der ursprünglichen Arbeit von Dyakonov und Shur vorgeschlagen wurden [18]. Bei einer Kopplung der einfallenden Strahlung zwischen den Gate und Source Kontakten des FETs zeigt sich abhängig von den konkreten Materialparametern eine starke Überhöhung des Effizienzfaktor für Frequenzen, bei denen die induzierten Plasmawellen sich konstruktiv überlagernde Stehwellen im Kanal ausbilden. Dabei wird nur der intrinsische, also gegatete Teil des Kanals betrachtet. Die theoretische Vorhersage dieser Überhöhungen hat in der folgenden Forschung zu einer fragwürdigen Prämisse geführt. Diese wird bis heute getrieben von der Aussicht auf Hocheffiziente THz Detektion unter den o.g. Bedingungen. Anhand von Simulationsergebnissen wird in dieser Arbeit jedoch gezeigt, dass in diesem Fall keine erhöhte Sensitivität der Detektoren zu erwarten ist. Die reine erhöhte Effizienz des Mischens wird begleitet von einer stark abfallenden Kanalimpedanz bei den gleichen Frequenzen. Somit findet eine erhöhte Leistungseinkopplung statt. Da die Effizienz eines Detektors immer auf die relevante, dem Detektionsmechanismus zur Verfügung stehende Leistung bezogen werden muss, ergibt sich nur eine marginale Erhöhung der Sensitivität, unter bestimmten Voraussetzung sogar eine Verschlechterung. Als Fazit dieser Beobachtungen muss - im Gegensatz zur verbreiteten Vorstellung - geschlossen werden, dass zur Implementierung effizienter TeraFETs resonantes plasmonisches Mischen zu vermeiden ist.

In weiteren Simulationen wird der Einfluss extrinsischer Komponenten der Bauteile gezeigt. Dies können ungegatete (sogenannte *access regions*) des FETs sein, sowie andere parasitäre Widerstände und Kapazitäten in der jeweiligen Technologie. Auch muss die Impedanz der integrierten Antennen berücksichtigt werden. Die Simulationen zeigen, dass ein signifikanter Anteil der eingestrahlten Leistung je nach Betriebsspannung (hin zu größeren Spannungen über dem Threshold) und Frequenz der TeraFETs and diese extrinsischen Komponenten "verloren" geht. Ziel bei der Entwicklung effizienter plasmonischer Detektoren muss also die Reduzierung dieser Einflüsse und geeignete Leistunganpassung der integrierten Antennen sein.

Es sollte hier bemerkt werden, dass diese Prämisse nicht in gleicher Weise für die thermoelektrischen Signalbeiträge gilt. Dort zeigt sich, dass auch ein reines Anheizen der Elektronenverteilung in den ungegateten Kanalregionen einen Temperaturgradienten und somit thermoelektrischen Strom erzeugen kann. Insbesondere in den durchgeführten Messungen zeigt sich dieser Beitrag im Fall großer Spannungen über dem Threshold besonders ausgeprägt. Unter diesen Betriebsbedingungen verschwindet die Effizienz des plasmonischen Mischens und das thermoelektrische Signal tritt isoliert hervor.

Experimentelle Ergebnisse von THz-Detektionsmessungen mit einer Reihe von TeraFETs, welche im Laufe dieser Promotion untersucht wurden, werden in Kapitel 6 gezeigt. Dies erfolgt hier insbesondere im Hinblick auf die maximale erreichte Sensitivität. Zuvor werden einige Details der verwendeten Messaufbauten erläutert. Drei Generationen von sukzessive optimierten AlGaN/GaN TeraFETs wurden realisiert und deren Entwicklung und Sensitivitäten werden vorgestellt. Die Detektoren wurde mit integrierten breitbandigen Antennen realisiert. Durch gründliches Design und Modellierung der Detektoren sowie Verbesserungen der Technologie zur Prozessierung der Bauelemente konnten hochsensitive TeraFETs realisiert werden. Die Detektoren

wurden im Bereich von 0. bis 1.2 THz vermessen und zeigen einen weitgehend flachen Frequenzverlauf. Mit der dritten optimierten Detektorgeneration konnten maximale optische Sensitivitäten - in Bezug auf die sogenannte äquivalente Rauschleistung (*noise equivalent power*, NEP) - von 25.4 und 31.2 pW/$\sqrt{\text{Hz}}$ bei 0.5 und 0.6 THz gemessen werden. Diese Werte stellen zum gegenwärtigen Zeitpunk Rekordwerte für GaN-basierte breitbandige TeraFETs in dem Untersuchten Frequenzbereich dar. Vergleichbare Werte wurden bei etwas höheren Frequenzen berichtet[70]. Es wurde somit gezeigt, dass TeraFETs auf der Basis von AlGaN/GaN HEMTS Sensitivitäten erreichen können, welche nahezu die der vorherrschenden Si CMOS Technologie erreichen. Damit erreichen auch GaN TeraFETs beinahe die Sensitivitäten von Detektroen auf Basis von Schottky-Dioden, welche nach wie vor den aktuellen Höchststand der Technik in Bezug auf sensitive elektronische THz-Detektion darstellen [20], [21], [43], [71].

Es wurden außerdem Graphen-basierte TeraFETs hergestellt, die ebenfalls mit breitbandigen Antennen integriert wurden. Es wurde ein ähnlich flacher Frequenzverlauf festgestellt wie bei den GaN TeraFETs. Die kapazitive Kopplung der Randbedingungen wurde hier durch ein Aufsplitten eines der Antennenflügel erreicht. Bei 590 GHz konnte eine minimale optische NEP von 497 pW/$\sqrt{\text{Hz}}$ gemessen werde, was ebenfalls einen Rekordwert für diese Technologie darstellt, und etwas einen Faktor 2 unter bisher berichteten Werten liegt [30], [164], [179]. Die Bauelemente wurde insbesondere in CVD-gewachsenem Graphen realisiert. Somit wurde gezeigt, dass eine Produktion von hochsensitiven Graphen TeraFETs auf Waferskala erreicht werden kann.

Neben den gemessenen guten NEP Werten zeigte sich in Graphen ein besonders ausgeprägter thermoeletrischer Effekt. Die Diskussion der Thermoelektrik in TeraFETs dindet in Kapitel 7 dieser vorliegenden Arbeit statt. Der starke thermoelektrische Effekt in Graphen kann auf die äußert effiziente Entkopplung heißer Ladungsträger von dem umgebenden Kristallgitter zurückgeführt werden [27]. In den durchgeführten Messungen zeigte sich, dass die thermoelektrischen Signale, im Gegensatz zu denen gemessen in GaN TeraFETs, die gleiche Größenordnung hatten, wie die Signale des plasmonischen Mischens. Zudem kann, je nach Art der dominierenden Ladungsträger, eine Addition beider Detektionsmechanismen auftreten. Tatsächlich wurde der o.g. beste Wert der Detektorsensitivität für eine Betriebsspannung gemessen, bei der das plasmonische Mischsignal bereits stark abgeklungen sein sollte. Dieser Zusammenhang wird anhand von Bauelementsimulationen mit dem implementierten Schaltungsmodell untermauert. Ebenso werden die Messergebnisse der THz-Detektion mit den GaN Bauelementen in Hinblick auf die thermoelektrischen Signalbeiträge untersucht und mit entsprechenden Detektor-Simulationen verglichen.

An dieser Stelle sollte erwähnt werden, dass das eingesetzte Simulationsmodell nicht speziell auf die Simulation von Graphen TeraFETs umgeschrieben wurde. So wurden insbesondere die Transportgleichungen in der gleichen Form implementiert wie sie für die GaN TeraFETs verwendet wurden. Graphen zeigt jedoch ein lineare anstelle einer quadratischen Energiedispersion, was grundlegende Einflüsse auf die spezifische Form der einzelnen Terme des hydrodynamischen Transportmodells hat [147]. In dieser Arbeit wurde lediglich ein angepasstes Modell für die Simulation verwendet, welches insbesondere zwei Modifikationen enthält. Zum Einen findet der

Ladungsttransport in Graphen stets unter Beteiligung von Elektronen und Löchern statt. Dieser Beobachtung wird Rechnung getragen, indem die Ladungsträgerdichte als Summe der beiden Ladungsträger modelliert wird. Unter Berücksichtigung eines zusätzlichen p-n Übergangs für eine der beiden Sorten (je nach Dotierung des Materials) und einem dadurch zusätzlich auftretenden Widerstand, liefert dieser Ansatz äußerst vernünftige Werte in der Extraktion der DC Bauelementparameter. Zum Anderen wird die Streuzeit in Abhängigkeit der Ladungsträgerdichte modelliert, da sich für Graphen keine konstante Masse definieren lässt. Mit diesen beiden Anpassungen des Modells liefern die Detektor-Simulationen eine gute qualitative Übereinstimmung mit den gemessenen Detektionssignalen, sowohl in Spannungs als auch Frequenzverlauf.

Für die zukünftige Weiterentwicklung des vorgestellten Detektormodells sollten insbesondere die o.g. Vereinfachungen der Transportgleichungen sowie die Einbindung der Notwendigen Modifikationen der grundlegenden Transportgleichungen des Graphenmodells verfolgt werden. In Bezug auf weitere experimentelle Untersuchungen des thermoelektrischen Effekts empfiehlt sich die Herstellung von Bauelementen, welche vorrangig auf diesen Effekt hin ausgelegt sind. Derzeit werden in unserer Arbeitsgruppe Bauelemente hergestellt, welche die lokale Überhöhung des elektrischen Feldes nicht durch asymmetrische Einkopplung, sondern vielmehr durch eine eingebrachte geometrische Asymmetrie erreichen sollen. Die Bauteile werden auf Graphen-Basis hergestellt. Durch eine dreiecksförmige Strukturierung desselben sollte eine Feldüberhöhung and der Spitze entstehen und sich ein thermoelektrisches Signal unabhängig von plasmonischer Detektion beobachten lassen.

Zusammenfassen wurde in dieser Arbeit ein Detektormodell für TeraFETs vorgestellt und dessen Implementierung als äquivalente Schaltung in einer Simulationssoftware gezeigt. Aus den getätigten Simulationen gingen drei Hauptaspekte hervor. Zum einen konnte der Einfluss ungegateter Bereiche auf die Leistungsverteilung im Transistorkanal simuliert werden. Zum zweiten wurde anhand einer Simulation des intrinsischen Detektionsmechanismus gezeigt, dass eine resonante Überhöhung der Detektorsensitivität im Falle resonanter plasmonischer Detektion nicht erwartet werden kann. Schließlich wurde gezeigt, dass sich in Messungen auftretende Signalbeiträge zu dem plasmonischen Mischen aufgrund eines zusätzlichen physikalischen Detektionsmechanismus qualitativ durch eine Erweiterung des theoretischen Modells um diffusive Anteile reproduzieren lassen. Somit wurde die These, dass es sich bei diesen Beiträgen um thermoelektrische Signale handelt stark untermauert. Die besondere Überhöhung dieser Beiträge in Graphen-basierten Bauelementen verspricht die Möglichkeit einer Optimierung von THz Detektoren auf den thermoelektrischen Effekt um möglicherweise eine neue Art von hochsensitiven THz-Detektoren realisieren zu können.

Eidesstattliche Erklärung

Hiermit erkläre ich gemäß §7 Abs. 2 der Promotionsordnung, dass ich die vorliegende Arbeit selbständig verfasst und nur die angegebenen Hilfsmittel, unter Beachtung der Grundsätze der guten wissenschaftlichen Praxis, verwendet habe.
Ich versichere weiterhin, dass ich bisher noch keinen Versuch zur Promotion unternommen habe.

Frankfurt am Main, den 7. September, 2017

(Maris Bauer)